

Optical Heterodyne Analogue Radio-over-Fibre Links for Next Generation Millimetre Wave Wireless Systems

Amol Delmade

B. Tech, MS (by Research)

A dissertation submitted in fulfilment of the
requirements for the award of
Doctor of Philosophy (Ph.D.)



School of Electronic Engineering
Faculty of Engineering and Computing
Dublin City University


Supervisor: Prof. Liam Barry

Co-Supervisor: Dr. Colm Browning

December 2022

Declaration

I hereby certify that this material, which I now submit for assessment on the programme of study leading to the award of Doctor of Philosophy is entirely my own work, and that I have exercised reasonable care to ensure that the work is original, and does not to the best of my knowledge breach any law of copyright, and has not been taken from the work of others save and to the extent that such work has been cited and acknowledged within the text of my work.



Signed: Amol Delmade

ID No.: 17213687

Date: 09/12/2022

*To my grandparents, parents
and entire family*

You have to dream before your dreams can come true. – Dr. A. P. J. Abdul Kalam

Acknowledgements

First and foremost, I would like to use this opening to express my sincere gratitude to everyone who has contributed and helped me throughout this wonderful PhD research journey. Without their constant support, it would not have been possible to accomplish this research.

I would like to thank my supervisor, Prof. Liam Barry, for giving me an opportunity to pursue my PhD research in his Radio and Optical Communication Lab at DCU. His continuous support, guidance and encouragement helped me a lot in both my professional and personal life and I will be forever indebted for it. His research skills, passion for research and accessibility to researchers will serve as a good example for leading my future research life. I also owe special gratitude to my co-supervisor Dr. Colm Browning for his mentorship, fruitful discussions and continuous support. His innovative way of training me on how to handle lab equipment/components and to think out of the box for solving research problems helped me to lead the PhD research. I could not think of a better supervisor and co-supervisor for my PhD. I also owe special thanks to Liam and Colm for their critical review and suggestions to improve my research papers and thesis.

My sincere gratitude to all the collaborators who shared their research expertise with me. I would like to thank Dr. Arman Farhang, Dr. Theo Verolet, Dr. Philip Perry, Dr. Eamonn Martin, Dr. Aleksandra Kaszubowska and Prof. Deepa Venkitesh for working with me on some of the experiments during the course of my PhD.

I would also like to thank my labmates/colleagues, past and present, from the Radio and Optical Communication Lab and the Photonics Systems and Sensing Lab, who made my PhD research experience very special and memorable: Dr. Prince Anandarajah, Dr. Sean O'Duill, Dr. Yi Lin, Dr. Prajwal, Dr. Mohab, Dr. Lakshmi Narayanan V., Devika Dass, Dr. Gaurav Jain, Alison, Marcos, Ankit, Dr. Syed, Dr. Manas, Haixuan Xu and others. My thanks also go out to the invaluable support I received from technicians: Robert Clare, Conor Maguire, Liam Meany, and other support staff of DCU.

My deepest appreciation goes to the friends who stood with me throughout my PhD journey and are my support system during tough times: Shree Krishnamoorthy, Lakshmi Narayanan V., Kavita Sharma, Sagun Shrestha, Khushi and Sunnee Shrestha, Lisanne Peters, Vinod Bajaj, Rohan R, Pankaj Arora, Rob Furlong, Lana Camilli, Srikant Jayaram, Laura Reidy, Aish Manik, Aneesh Sobhanan, Hasan Bhatti and Anne Marieke Mooji.

I would like to acknowledge the Irish Photonics Research Centre (IPIC) of Science Foundation Ireland (SFI) for providing the funding for my PhD studies, which gave me an opportunity to come to Ireland for pursuing research and enabled me to travel across the world for attending conferences and network with

wonderful researchers. I would also like to acknowledge the IEEE Photonics Society, OPTICA, CONNECT SFI Centre and EU Microwave Photonics Cost Action program for being valuable partners in my PhD research journey.

The most important gratitude goes to my grandparents: Nagorao Delmade and Shivgangabai Delmade, my parents: Sanjay Delmade and Mayabai Delmade, uncle: Shivaji Delmade, Ashok Delmade and Ganesh Delmade and my entire family for their unconditional love, trust, support and encouragement throughout my life. I could have never imagined being at this stage of my life without them.

This PhD work would not have been possible without you all. I'll always be grateful to all of you.

Table of Content

Declaration	I
Acknowledgements	III
Table of Content	V
List of Figure	VIII
List of Table	XII
List of Acronyms	XIII
Abstract	XVI
Introduction	1
1. Optical Access Networks for the Next Generation Wireless Systems	6
1.1 Trends in Data Consumption	6
1.2 Overview of Cellular Wireless Communication System	8
1.2.1 Evolution of Cellular Wireless System from 1G to 5G	11
1.2.2 5 th Generation Cellular System	12
1.2.3 Millimetre and THz Frequency Bands for Wireless Systems	14
1.3 Optical Backhauling for Cellular System	16
1.3.1 Centralized Radio Access Network and Optical Fronthauling	18
1.3.2 Fronthaul Possibilities and Digital Radio-over-Fibre	19
1.3.3 Common Public Radio Interface Fronthaul	20
1.3.4 RAN Functional Split and Fronthaul for 5G	21
1.4 Optical Generation of Millimetre/THz Carriers	24
1.4.1 Summary of Electronics Techniques for Millimetre/THz Wave Carriers Generation	25
1.4.2 Optical Heterodyning for Millimetre/THz Wave Carriers Generation	26
1.4.3 Frequency Fluctuations and Phase Noise in Optical Heterodyning	28
1.5 Research Objectives	31
References	31
2. Analogue Radio-over-Fibre for Fronthauling of 5G Signals	35
2.1 Fronthaul Possibilities	35
2.1.1 Digital RoF Fronthaul Possibilities	37
2.1.2 Analogue RoF Fronthaul Possibilities	38
2.2 Analogue Intermediate Frequency over Fibre Fronthauling and Components	39
2.2.1 Signals: Single Carrier and Multicarrier	40
2.2.2 Optical Modulation and Detection	43

2.2.3	Optical Fibre	45
2.3	Capacity of AIFoF Fronthaul Link	47
2.3.1	Experimental Setup	47
2.3.2	Experimental Results and Discussion	50
2.4	Power Difference Penalty over AIFoF Fronthaul Link	53
2.4.1	Experimental Results and Discussion	54
2.5	Conclusion	55
	References	56

3. Optical Heterodyne Millimetre Wave Analogue Radio-over-Fibre Fronthauling with Free Running Lasers 59

3.1	Optical Heterodyne Analogue RoF Link for Millimetre Wave/THz System	60
3.1.1	A general schematic of Optical Heterodyne Analogue RoF Link	60
3.1.2	Summary of frequency offset and phase noise compensation techniques	63
3.1.3	Literature summary of Optical Heterodyne demonstrations using free-running lasers	65
3.2	Analogue mm-wave Receiver for the FO and PN Compensation	66
3.2.1	Experimental Details	66
3.2.2	Receiver Structure and Compensation Mechanism	68
3.2.3	System Performance	70
3.3	DSP Receiver for the FO and PN Compensation	73
3.3.1	FO and PN Compensation Mechanism	74
3.3.2	System Performance	75
3.4	Discussion	78
3.5	Conclusion	80
	References	80

4. Optical Heterodyne Millimetre Wave Analogue Radio-over-Fiber Fronthauling with Optical Frequency Comb Sources 84

4.1	Optical Frequency Combs & Properties	85
4.1.1	Types of OFC Sources	86
4.2	Optical Heterodyning with OFC Source	88
4.2.1	Phase Noise Analysis due to Path Length Mismatch	90
4.2.2	Literature summary of Optical Heterodyne demonstrations using OFC Sources	91
4.3	Gain Switched Laser OFC Source based Optical Heterodyne A-RoF System	92

4.3.1	Experimental Details	92
4.3.2	Phase Noise Analysis and Effect of Path Length Difference	95
4.3.3	System Performance	98
4.4	Multi-Frequency 5G NR mm-wave signal generation with GSL OFC	100
4.4.1	Phase Noise Analysis	101
4.4.2	System Performance	102
4.4.3	Simultaneous Multi-Frequency Signal Generation	103
4.5	MLL OFC based Optical Heterodyne A-RoF System	104
4.5.1	QD-P-MLL OFC Source and System Description	104
4.5.2	Experimental Results – System Performance	106
4.6	Conclusion	108
	References	109
5.	Advanced Optical Techniques for the Next Generation Millimetre-Wave Wireless Systems	112
5.1	Millimetre-Wave A-RoF System employing Optical Injection Locking and Direct Modulation of a DFB Laser	112
5.1.1	Active De-multiplexing and Simultaneous Data and RF LO modulation	113
5.1.2	Experimental Setup	115
5.1.3	System Performance	118
5.2	Bidirectional Millimetre Wave Analog-RoF System employing Remote Down-Conversion and Wavelength Reuse	120
5.2.1	Experimental Setup and Details	120
5.2.2	System Performance	122
5.3	Conclusion	124
	References	124
6.	Conclusion and Future Work	126
6.1	Conclusion	126
6.2	Future Work	129
	References	130
	Appendix	131
	List of Publications	131

List of Figure

Fig. 1.1 (i) Number of internet users over the last two decades [8] and (ii) Mobile and fixed data consumption prediction between 2019-2026 [10].	7
Fig. 1.2 Schematic of a typical cellular wireless communication system with different types of backhaul possibilities, i.e., wireless, optical and hybrid.	9
Fig. 1.3 Physical layer properties of different generations of cellular communication systems.	11
Fig. 1.4 Figure of merits for 5G system in terms of various physical layer parameters [21].	13
Fig. 1.5 Atmospheric attenuation coefficient vs frequency over wireless channel due to oxygen and water vapour absorption.	14
Fig. 1.6 Architecture of a traditional distributed backhaul network showing X2 interfaces required for coordination between adjacent cells.	17
Fig. 1.7 C-RAN architecture showing the CO, Backhaul, C-BBU, Fronthaul and RRH.	18
Fig. 1.8 Architecture of D-RoF and A-RoF Fronthaul scheme connecting C-BBU and RRH sites.	19
Fig. 1.9 Flow Chart of operations followed by DBBoF based CPRI protocol for fronthaul data transmission between C-BBU and RRH site over optical fibre.	20
Fig. 1.10 RAN functional split options as adopted in CPRI fronthaul standard for 4G LTE and various fronthaul possibilities for 5G.	22
Fig. 1.11 Different fronthaul architecture possibilities arising from the location of CU and DU units for 5G [38].	23
Fig. 1.12 Schematic of an Optical Heterodyning for mm-wave/THz carrier generation with free running lasers and optical frequency comb sources.	26
Fig. 1.13 Frequency fluctuations of photo-mixing generated 48 GHz carrier with heterodyning of different types of free-running lasers.	28
Fig. 1.14 Phase noise of photo-mixing generated 48 GHz carrier with heterodyning of different types of free running lasers.	29
Fig. 2.1 Schematic of a general fronthaul link with (i) digital and (ii) analogue data modulation at (iii) baseband, (iv) intermediate and (v) radio frequency with respect to the optical carrier.	36
Fig. 2.2 Architecture of the ARFoF fronthaul link with data transmission between C-BBU and RRH site.	40
Fig. 2.3 Spectral representation of single carrier and multicarrier baseband signals.	41
Fig. 2.4 Block diagram of baseband OFDM transceiver.	41
Fig. 2.5 Baseband spectra of 200 MHz BW (i) OFDM and (ii) UF-OFDM signals.	42
Fig. 2.6 Schematic of a (i) direct and (ii) external modulation system with respective P-I and P-V characteristics.	44
Fig. 2.7 Power fading introduced by optical fibre chromatic dispersion over (i) EML and (ii) DML systems.	46
Fig. 2.8 Experimental setup to demonstrate the AIFoF fronthauling through the intensity modulation direct detection system.	48
Fig. 2.9 (i) P-I characteristics and (ii) frequency response of the G&H DFB laser diode.	48
Fig. 2.10 Spectrum of the RTS captured 16 UF-OFDM signal bands after transmission over a 25 km SSMF AIFoF IMDD link using a DFB laser i) with and ii) without isolator.	50

Fig. 2.11 (i) Constellation of the single UF-OFDM signal band and (ii) spectrum of the received 16 UF-OFDM signal bands after transmission over a 25 km SSMF OSSB AIFoF IMDD link.	51
Fig. 2.12 EVM performance of 1 (flourocent green), 8 (red), and 16 (blue and green) UF-OFDM signal bands over OSSB AIFoF fronthaul link.	52
Fig. 2.13 (i) Schematic of uplink fronthaul transmission scenario and (ii) spectra of 4 UF-OFDM signal bands showing power difference between transmitted bands.	54
Fig. 2.14 EVM performance of (i) 2 band transmission with power difference and (ii) power varying band in 2, 4, and 8 band transmission scenarios over an O-SSB AIFoF uplink fronthaul link.	55
Fig. 3.1 A general schematic of Analogue RoF fronthaul link with remote optical heterodyning for mm-wave/THz frequency signal generation and distribution.	60
Fig. 3.2 Architecture of (i) a standard external local oscillator heterodyne receiver and (ii) direct detection diode receiver used in the wireless system for frequency down-conversion in the end user.	62
Fig. 3.3 (i) A portion of the transmitted (red) and received (blue) IF OFDM signal spectra showing non-overlap due to FO and (ii) Constellation of the demodulated signal in an optical heterodyne A-RoF link with free running lasers and fixed frequency external LO down-conversion receiver.	62
Fig. 3.4 Schematic of (i) Optical Injection Locking and (ii) Optical Phase-Locked Loop techniques for correlating the frequency and phase fluctuations of free-running lasers.	64
Fig. 3.5 Schematic of Optical heterodyne with analogue RoF fronthauling for remote mm-wave carrier generation and distribution.	66
Fig. 3.6 (i) Schematic and (ii) combined spectrum of photonics integrated hybrid InP-Si ₃ N ₄ micro ring resonator external cavity lasers and (iii) combined signal spectrum at the input of fibre.	67
Fig. 3.7 Analogue mm-wave receiver architecture for FO & PN compensation over optical heterodyne A-RoF system using independent laser sources.	69
Fig. 3.8 (i) A portion of the transmitted (red) and received (blue) IF signal spectra showing exact overlap and (ii) Constellation of the demodulated signal in an optical heterodyne A-RoF link with free-running lasers source and standalone analogue mm-wave receiver.	71
Fig. 3.9 (i) BER vs received optical power for a single UF-OFDM signal band; (ii) spectrum of captured 5 band signal and (iii) measured EVM for the five signal bands over an optical heterodyne A-RoF link with free-running lasers source and standalone analogue mm-wave receiver.	71
Fig. 3.10 The flow chart of offline DSP operations for demodulation of the signal; Constellation of the received signal after (i) FO compensation only (ii) FO & PN compensation and (iii) all the DSP processing.	74
Fig. 3.11 (i) BER vs received optical power and (ii) EVM vs subcarrier spacing/ baud rate performance of the optical heterodyne mm-wave analogue RoF system with DSP impairment compensation.	75
Fig. 3.12 EVM vs Subcarrier Spacing/Baud rate for DSP compensation based Optical heterodyne mm-wave analogue RoF link.	77
Fig. 4.1 Time and Frequency domain representation of an optical frequency comb.	85
Fig. 4.2 Types of optical frequency comb sources and their properties.	86
Fig. 4.3 OFC source based optical heterodyning with a delay between two optical carrier paths.	88
Fig. 4.4 Power spectral density of the heterodyne generated 64 GHz mm-wave carrier for the case of (i) different path length differences (25 MHz linewidth) and (ii) different linewidth OFC tones (20 cm path difference).	90

Fig. 4.5 OFC source based optical heterodyne mm-wave analogue RoF fronthaul link showing the C-BBU, RRH and user unit architecture along with GSL OFC schematic in inset (a).....	92
Fig. 4.6 Optical spectrum of (i) GSL OFC output, (ii) Two OFC tones filtered by WSS and (iii) Combined signal at the input of optical fibre.	93
Fig. 4.7 (i) Simulated and experimental power spectral density and (ii) phase noise of the photo-mixing generated 64 GHz mm-wave carrier for the path matched and mismatched cases over an optical heterodyne A-RoF link.....	95
Fig. 4.8 EVM vs relative path length difference performance for 244 kHz subcarrier spacing 59 GHz mm-wave OFDM signal over an optical heterodyne A-RoF link.	97
Fig. 4.9 (i) EVM vs received optical power performance of 200 MHz bandwidth 59 GHz mm-wave OFDM signal; Constellation of the (ii) 400 MHz and (iii) 800 MHz bandwidth 60.6 GHz mm-wave OFDM signals over a GSL OFC source based optical heterodyne A-RoF system.	98
Fig. 4.10 EVM vs relative path length difference performance of 60.6 GHz mm-wave OFDM signal with variable subcarrier spacing over an optical heterodyne A-RoF link.....	99
Fig. 4.11 Combined signal optical spectrums for the (i) 27 GHz and (ii) 43 GHz mm-wave signal generation case over an optical heterodyne A-RoF link.....	100
Fig. 4.12 Phase noise of the photo-mixing generated 32 GHz, 48 GHz and 64 GHz mm-wave carriers after beating different pairs of GSL OFC tones on the PD.....	101
Fig. 4.13 (i) Constellations and (ii) EVM vs received optical power performance of the 27 GHz and 43 GHz mm-wave OFDM signal over a GSL OFC based optical heterodyne A-RoF link.	102
Fig. 4.14 Combined optical signal spectrum for simultaneous generation of mm-wave OFDM signals at 27 GHz, 43 GHz and 59 GHz frequencies over an optical heterodyne A-RoF system.....	103
Fig. 4.15 (i) Schematic of a QD-MLL; (ii) Optical spectrum at the output of QD-MLL with blue circles showing different sets of operating frequencies used for the heterodyning, and (iii) combined optical signals spectrum at the input of optical fibre.	104
Fig. 4.16 Constellation of the demodulated OFDM signal over an mm-wave A-RoF heterodyne system employing a QD-P-MLL OFC (i) without and (ii) with a free space optical feedback; (iii) RF spectra of a frequency down-converted mm-wave carriers showing phase noise reduction with feedback.	105
Fig. 4.17 EVM vs subcarrier baud rate performance for OFDM signals over a QD-MLL OFC mm-wave A-RoF system.....	106
Fig. 5.1 (i) Schematic of an active de-multiplexer for simultaneously filtering and amplification of GSL OFC tones and (ii) combined optical spectrum of slave laser and OFC tone showing the detuning.	113
Fig. 5.2 A schematic of the optical heterodyne system based on simultaneous data and RF LO modulation and optical injection locking for mm-wave signal generation.	114
Fig. 5.3 Experimental testbed of the optical heterodyne A-RoF link based on simultaneous data and RF LO modulation and remote active demultiplexing for mm-wave signal generation.	115
Fig. 5.4 Optical spectrum of the DFB laser simultaneously modulated with the data signal and RF LO.....	116
Fig. 5.5 Optical spectrum (i) at the output of slave laser (DFB-2) after injection locking and (ii) of a combined signal at the input of PD.....	117
Fig. 5.6 (i) Phase noise of the photo-mixing generated 25.4 GHz and 38.1 GHz mm-wave carriers, (ii) RF spectrum of the generated 35.3 GHz mm-wave signals and (iii) constellation of the 28.2 GHz demodulated mm-wave signal over an optical heterodyne A-RoF system employing OIL and direct modulation of a DFB laser.	118

Fig. 5.7 (i) EVM vs subcarrier spacing and (ii) constellation of the 256-QAM data modulated OFDM signals over mm-wave A-RoF system employing OIL and direct modulation of a DFB laser. 119

Fig. 5.8 Bidirectional mm-wave A-RoF systems experimental testbed with remote frequency down-conversion and wavelength reuse concept. 121

Fig. 5.9 BER vs received optical power performance of (i) 61 GHz mm-wave OFDM downlink signal and (ii) 5 GHz IF OFDM uplink signal for the cases of transmission through different (unidirectional) and same (bidirectional) optical fibre spools over an optical heterodyne A-RoF system. 122

List of Table

Table. 1.1. IEEE nomenclature for bands in the 18 to 300 GHz frequency range.	15
Table. 3.1. Summary of various heterodyne demonstrations reported in the literature.	65
Table. 4.1. Summary of various heterodyne demonstrations reported in the literature using OFC sources.	91

List of Acronyms

1G	1 st Generation
2G	2 nd Generation
3G	3 rd Generation
4G	4 th Generation
5G	5 th Generation
5G NR	5 th generation new radio
6G	6 th Generation
ADC	Analog to Digital Converter
AIFoF	Analogue Intermediate Frequency over Fibre
A-RoF	Analogue Radio-over-Fibre
AWG	Arbitrary Waveform Generator
BB	Baseband Frequency
BBU	Baseband Unit
BER	Bit Error Rate
BS	Base Station
BW	Bandwidth
C-BBU	Centralized/Cloud- BBU
CO	Central Office
CP	Cyclic Prefix
CPRI	Common Public Radio Interface
C-RAN	Centralized Radio Access Network
CU	Central Unit
DAC	Digital to Analog Converter
DBBoF	Digital Baseband-over-Fiber
DD-LMS	Decision Directed Least Mean Square
DFB	Distributed Feedback Laser
DML	Direct Modulation Laser
D-RoF	Digital Radio-over-Fibre
DSP	Digital Signal Processing
DU	Distribution Unit

EBPF	Electrical Bandpass Filter
EDFA	Erbium Doped Fiber Amplifier
EOM	Electro-Optic Modulator
ESA	Electrical Spectrum Analyzer
EVM	Error Vector Magnitude
FBG	Fibre Bragg Grating
FEC	Forward Error Correction
FFT	Fast Fourier Transform
FO	Frequency Offset
FSR	Free Spectral Range
GSL	Gain Switched Laser
IEEE	Institute of Electrical and Electronics Engineers
IF	Intermediate Frequency
IFFT	Inverse Fast Fourier Transform
IM-DD	Intensity Modulation Direct Detection
InP	Indium Phosphide
ITU	International Telecom Union
LO	Local Oscillator
LTE	Long Term Evolution
MIMO	Multiple Input Multiple Output
MLL	Mode Locked Laser
mm-wave	Millimetre-Wave
MZM	Mach Zehnder Modulator
OBPF	Optical Band Pass Filter
ODSB	Optical Double Sideband
OFC	Optical Frequency Comb
OFDM	Orthogonal Frequency Division Multiplexing
OIL	Optical Injection Locking
OLT	Optical Line Terminal
ONU	Optical Network Unit
OOK	On-Off Keying

OPLL	Optical Phase Locked Loop
OSSB	Optical Single Sideband
PA	Power Amplifier
PAPR	Peak-to-Average Power Ratio
PD	Photodetector
PN	Phase Noise
PON	Passive Optical Network
PSD	Power Spectral Density
PSK	Phase Shift Keying
QAM	Quadrature Amplitude Modulation
RAN	Radio Access Network
RF	Radio Frequency
RIN	Relative Intensity Noise
RN	Remote Node
RRH	Remote Radio Head
RTS	Real time oscilloscope
RU	Radio Unit
S&C	Schmidl and Cox
SNR	Signal to Noise Ratio
SSMF	Standard Single Mode Fibre
THz	Terahertz
UF-OFDM	Universally filtered OFDM
VCO	Voltage Controlled Oscillator
VOA	Variable Optical Attenuator
WDM	Wavelength Division Multiplexing
Wi-Fi	Wireless Fidelity
WSS	Wavelength Selective Switch

Optical Heterodyne Analogue Radio-over-Fibre Links for Next Generation Millimetre Wave Wireless Systems

By: Amol Sanjay Delmade

Abstract

Data transmission in the millimetre wave (mm-wave: 30 – 100 GHz), sub-terahertz (sub-THz: 100 GHz – 300 GHz) and THz (300 GHz – 3 THz) frequency bands will be a key aspect of the 5th generation (5G) and 6th generation (6G) wireless systems in order to achieve more than 1 Gb/s and 10 Gb/s per user data rates, respectively. An efficient mm-wave/THz signal generation technique and a spectrally efficient fronthaul distribution network are two important elements to fulfil the demand for such high data rates. This research thesis focuses on the optical heterodyne analogue radio-over-fibre link to simultaneously generate and distribute the mm-wave signals to the increased number of remote antenna sites.

The choice of the optical fronthaul scheme should facilitate the centralization of resources and simplify the remote antenna site. The first part of the thesis focuses on analysing the capacity of spectrally efficient analogue intermediate frequency over fibre fronthaul scheme by simultaneously transmitting multiple 5G signals over a directly modulated 25 km fibre link influenced by multiple impairments. The analogue RoF link is then combined with an optical heterodyne technique to demonstrate the generation and distribution of the mm-wave signals. The performance of a such fibre-wireless system is majorly limited by the frequency drift and phase offset between the optical carriers, obtained from the use of free running lasers, and techniques that ease these restrictions with minimal additional complexity are of paramount importance for wide deployment. Two innovative solutions are demonstrated, in the second part, to compensate for the effect of laser frequency fluctuations and phase noise on the performance of low sub-carrier spacing multicarrier mm-wave signals such as those provisioned in the 5G standard.

In the third part, two different types of optical frequency comb sources are employed in the optical heterodyne A-RoF link to demonstrate a frequency fluctuation-free mm-wave signal generation. The flexibility of this link is demonstrated by generating multi-frequency mm-wave signals using a single device, while the wavelength flexibility is demonstrated using a wide bandwidth photonic integrated OFC source. In the last part, advanced optical techniques such as active demultiplexing, wavelength reuse and bi-directional signal transmission through the same fibre are demonstrated to assist the efficient expansion of optical heterodyne A-RoF link.

The successful demonstration of 5G compatible mm-wave signal generation using a combination of different types of sources and impairment compensation techniques in this thesis makes a strong case for the deployment of optical heterodyne A-RoF link in the next generation millimetre wave wireless systems.

Introduction

The introduction of multiple internet-based applications such as social media apps, video streaming platforms, online gaming and other have increased data consumption over the last three decades. The reliable data transmission in the low to medium mobility scenario has made the cellular wireless system more popular for use in short distance and moderate data rate communication system, while the low loss and wide bandwidth capabilities of the optical fibre wireline system have made them popular for the long distance and high speed communications [1]. The introduction of the 2nd, 3rd and 4th generation (2G, 3G and 4G) cellular systems increased data rates from tens of kbps to several tens of Mbps for the wireless end users [2], however, these speeds are not sufficient for the emerging data hungry applications such as virtual reality (VR), live ultra-high definition (UHD)/4K/8K videos and autonomous vehicles. The 5th and 6th generation (5G and 6G) cellular wireless systems aim to achieve high data rates in the order of several hundreds of Mbps to Gbps by transmitting the data over high bandwidth wireless channels in the millimetre, sub-THz and THz frequency bands. However, such high carrier frequency wireless systems suffer from limited range due to higher propagation loss - requiring the deployment of multiple antenna sites for seamless connectivity. An optical fibre based back/front-haul network is being actively introduced to connect and feed the data to remote antenna sites from the central office (CO) and achieve reliable and ubiquitous connectivity [3].

In order to efficiently deploy the high frequency wireless systems, advanced technologies need to be developed to address the challenges of low phase noise mm-wave/THz carrier and signal generation, filtering, frequency conversion and beamforming [2]. In this thesis, the foremost challenge of mm-wave/THz carrier and signal generation is addressed using an optical heterodyne technique, while a spectrally efficient analogue radio-over-fibre (A-RoF) technique is demonstrated for the fronthaul network implementation. An optical heterodyne technique facilitates the generation of RF carriers by beating of two optical carriers with the desired mm-wave/THz carrier frequency difference on a high speed photodetector [4]. Combining it with the analogue intermediate frequency over fibre (AIFoF) fronthaul link can achieve the simultaneous generation and distribution of the mm-wave signals to the remote antenna site. The frequency fluctuations and phase noise of the generated mm-wave carrier, arising from the use of different types of free-running lasers and an optical frequency comb (OFC) source, have been shown to be a performance limiting factor [4] - especially for the small baud rate/subcarrier spacing multicarrier mobile signals as provisioned in 5G and beyond 5G wireless systems. It is important to mitigate the effect of this relative frequency drift and phase offset between the beating optical carriers on the performance of multicarrier signals and achieve frequency stable and low phase mm-wave carrier delivery. Multiple

techniques are demonstrated in this thesis to mitigate the impairments in optical heterodyne A-RoF systems to achieve successful 5G new radio (5G NR) compatible mm-wave signal generation and distribution.

Main Contribution

- **Capacity of Analogue RoF for Fronthauling of 5G Signals**

The capacity of the directly modulated 25 km AIFoF link is investigated by demonstrating the successful transmission of sixteen 201 MHz BW universally filtered orthogonal frequency division multiplexed (UF-OFDM) 5G compatible signals carrying an aggregate data transmission rate of ~19.3 Gb/s. The effect of performance limiting factors such as chromatic dispersion of optical fibre, the interplay between laser chirp and chromatic dispersion and power per signal band is analysed for the AIFoF link. The effect of the power difference between different signals on the performance of the AIFoF link is also analysed - emulating the uplink transmission scenario.

- **Frequency Fluctuation and Phase Noise Impairment Compensation in Optical Heterodyning Analogue RoF Link with free running lasers**

The optical heterodyne analogue RoF link is successfully demonstrated for the generation and distribution of the 5G compatible mm-wave signal in the 60 GHz band. Two innovative techniques are implemented to mitigate the effect of frequency fluctuation/offset (FO) and phase noise (PN) on the performance of low subcarrier spacing multicarrier mm-wave signals generated from the use of free running lasers for heterodyning. The analogue mm-wave receiver exploits the correlation between the photo-mixing generated mm-wave carrier and data signal to compensate for the effect of FO and PN using a hardware based approach. The second approach used standard digital signal processing (DSP) algorithms to compensate for the effect of FO and PN without increasing the hardware complexity of the optical heterodyne analogue RoF system. The successful generation and transmission of 2 MHz subcarrier spacing 60 GHz band mm-wave orthogonal frequency division multiplexed (OFDM) signals is demonstrated with both these techniques. The FO and PN adversely affect the performance of low subcarrier spacing signals compared to the single carrier signals and the successful demonstration here encourage such system deployment in the real network.

- **Multi-frequency 5G NR Millimetre Wave Signal generation with OFC based Optical Heterodyne A-RoF link**

An optical heterodyne A-RoF link is demonstrated using two different types of comb sources, i.e. gain switched laser (GSL) OFC and passive mode locked laser (MLL) OFC, to facilitate a frequency fluctuation-free and low phase noise 60 GHz band 5G compatible data signals generation and transmission. The effect of PN, resulting from the path length mismatch and fibre dispersion induced OFC tones decorrelation, is

analysed on the performance of 61 kHz subcarrier spacing OFDM signal. Furthermore, the multi-frequency mm-wave signal generation capabilities of the optical heterodyne A-RoF system are demonstrated by generating 5G NR compatible signals at 27 GHz, 43 GHz and 59 GHz frequencies using the same GSL OFC device – providing the flexibility and centralization capabilities for the implementation of the link. Additional wavelength flexibility is demonstrated by using a photonics integrated MLL in the optical heterodyne analogue RoF system. The low phase noise and multi-frequency fluctuation-free mm-wave signals generation capabilities in addition to the possibility of the photonics integration make the OFC based optical heterodyne A-RoF system more suitable for use in the high frequency mm-wave wireless systems capable of transporting the 5G compatible low subcarrier spacing signals.

- **Active Demultiplexing, Wavelength Reuse and Bi-directional transmission for Simplifying the Optical Heterodyning**

Optical demultiplexing, a technique for filtering and amplification of OFC tones, and wavelength reuse and bi-directional transmission over the same fibre are demonstrated for reducing the complexity of the OFC based optical heterodyne analogue-RoF link. A 5G NR compatible subcarrier spacing and mm-wave frequency signals successful generation and transmission is demonstrated by simultaneously modulating a DFB laser with OFDM IF data signal and RF sinusoidal LO. The relaxation oscillation non-linearity of the laser is exploited to reduce the power consumption, while the use of an active demultiplexing enabled amplifier free heterodyne system implementation. Furthermore, a passive fibre Bragg grating (FBG) filter was employed to filter one of the optical carriers used for heterodyning and its reuse for the transmission of uplink data is demonstrated. The deployment of such wavelength reuse can enable a laser free remote antenna site, while the bidirectional downlink and uplink signals transmission through the same fibre can lead to further cost efficient system deployment.

In general, the work presented in this thesis supports the ongoing research being done across the world to employ various optical techniques for supporting the next generation of wireless systems and provide high speed connectivity for the progress of humanity.

Thesis Structure

- Chapter 1 provides an overview of the wireless cellular system, optical backhaul techniques (used for feeding the data to remote antenna sites) and optical heterodyne technique used for the generation of high frequency mm-wave and THz carriers. Initially, a detailed summary of the evolution of the cellular technology from the 1st generation to the 5th generation is provided in section 1.2 along with the details of various mm-wave and THz frequency bands. In the second part, a summary of the evolution in the backhaul from the use of distributed radio access network

(RAN) to the introduction of optical fronthaul with centralized RAN and its further functional split for 5G system is provided in section 1.3. An introduction to the digital radio-over-fibre (D-RoF) and analogue RoF schemes is also provided. In the third part, the concept of optical heterodyning is presented (in section 1.4) using two different types of sources, i.e. free running lasers and an optical frequency comb, for the generation of mm-wave/THz carriers. The issues of frequency fluctuation and phase noise arising from the use of different types of free running lasers is presented. The challenges in the optical backhaul and optical heterodyne techniques are presented as the objective of the thesis at the end of chapter 1.

- Chapter 2 details the various optical fronthaul link implementation possibilities with a major focus on analogue-RoF for the transmission of 5G NR compatible signals. The various optoelectronic and optical components used in the fronthaul link are discussed in section 2.2, along with the commonly used orthogonal frequency division multiplexed multicarrier waveform. The capacity of spectrally efficient analogue intermediate frequency over fibre fronthaul link is investigated in section 2.3 for the transmission of multiple 201 MHz bandwidth 5G NR compatible universally filtered orthogonal frequency division multiplexed signals over a 25 km optical fibre. The permissible power difference between signal bands is also analysed in section 2.4 to emulate the uplink transmission scenario.
- Chapter 3 demonstrates two innovative techniques for the compensation of the effect of free running laser's frequency fluctuation and phase noise on the performance of low subcarrier spacing mm-wave OFDM signals generated over an optical heterodyne A-RoF link. Initially, a general schematic of the optical heterodyne A-RoF link is presented in section 3.1 along with a summary of various aspects such as high speed photodetector technologies, traditional frequency fluctuations and phase noise compensation techniques and frequency down-conversion receivers. In the second part, the analogue mm-wave receiver structure is introduced for the compensation of the effect of FO and PN on the heterodyne generated mm-wave signal. The successful generation of five signals at different mm-wave frequencies around 60 GHz is demonstrated by presenting the performance of a 2 MHz subcarrier spacing OFDM signal in section 3.2. In the third part, a digital signal processing algorithm based receiver is introduced for compensating the effect of FO and PN on the performance of the photo-mixing generated 61 GHz mm-wave OFDM signal. The system's EVM performance is presented in section 3.3, with variable received optical power, subcarrier spacing of the OFDM signals and frequency offset introduced by changing the user side external LO.
- Chapter 4 demonstrates the mm-wave carrier generation using two different types of OFC sources, i.e., gain switched laser OFC and passively mode-locked laser OFC, over an optical heterodyne A-

RoF link. The effect of phase noise, arising from the path length difference between beating OFC tones, on the generated mm-wave carrier is analysed in section 4.2. The performance of 244 kHz subcarrier spacing 59 GHz mm-wave OFDM signal is analysed over a GSL OFC based optical heterodyne analogue RoF link, with variable receiver optical power, subcarrier spacing and length difference between two optical carrier's paths in section 4.3. Different pairs of OFC tones were filtered from the output of GSL OFC and multi-frequency mm-wave carrier and signal generation (at 27, 43 and 59 GHz) is demonstrated in section 4.4. The phase noise analysis of the generated mm-wave carriers at 32, 48 and 64 GHz is also presented in section 4.4. A photonic integrated MLL OFC source use is demonstrated for the generation of 59 GHz mm-wave OFDM signal over an optical heterodyne A-RoF link in section 4.5. Its suitability for the transmission of 5G NR compatible low subcarrier spacing OFDM signals is also analysed.

- Chapter 5 demonstrates two innovative techniques, i.e. optical demultiplexing and bi-directional transmission over the same fibre for simplifying the optical heterodyne A-RoF system. A DFB laser is simultaneously modulated with OFDM IF data signal and RF sinusoidal LO and the mm-wave signal generation at 28.2 GHz and 35.3 GHz frequencies is demonstrated by heterodyning of relevant optical components in section 5.1. The relaxation oscillation non-linearity of the laser is exploited to reduce the power consumption, while the use of an active demultiplexing technique, for filtering and amplification of optical carriers, enabled amplifier system implementation. In section 5.2, a bidirectional mm-wave A-RoF system is demonstrated employing remote frequency down-conversion and wavelength reuse. One of the optical carriers used for heterodyning is initially filtered using an FBG filter at the remote antenna site and then frequency down-converted uplink IF data signal is modulated on it for transmission to the C-BBU site over the same fibre.
- Chapter 6 provides a brief conclusion drawn from the results presented in this thesis. The potential future work plan is also presented to further enhance the presented optical techniques and lead toward their deployment in actual optical access networks.

References

- [1] G. P. AGRAWAL, *FIBER-OPTIC COMMUNICATION SYSTEMS*, 5th ed. JOHN WILEY, 2021.
- [2] T. S. Rappaport *et al.*, "Wireless communications and applications above 100 GHz: Opportunities and challenges for 6g and beyond," *IEEE Access*, vol. 7, pp. 78729–78757, 2019, doi: 10.1109/ACCESS.2019.2921522.
- [3] A. Checko *et al.*, "Cloud RAN for Mobile Networks - A Technology Overview," *IEEE Communications Surveys and Tutorials*, vol. 17, no. 1, pp. 405–426, Jan. 2015, doi: 10.1109/COMST.2014.2355255.
- [4] C. Browning *et al.*, "Gain-switched optical frequency combs for future mobile radio-over-fiber millimeter-wave systems," *Journal of Lightwave Technology*, vol. 36, no. 19, pp. 4602–4610, Oct. 2018, doi: 10.1109/JLT.2018.2841365.

1. Optical Access Networks for the Next Generation Wireless Systems

The increased means of communication and introduction of multiple social media apps, video streaming platforms, online gaming and other internet-based applications have increased data consumption over the last three decades. The technological advances in both the wired and wireless data transmission systems and associated technologies led to the development of low-cost end user devices and empowered the masses with easy access to information. Wired data transmission systems moved from the use of lossy and low bandwidth coaxial cables to low loss and wide bandwidth optical fibre cables [1], and the wireless operators also introduced multiple upgrades through the 2nd, 3rd and 4th generation cellular system in order to achieve higher data transfer speed [2], [3]. The reliable data transfer in the medium to high mobility scenario has made the wireless cellular system more popular, however, its limited range due to higher propagation loss requires the deployment of multiple antenna sites for seamless connectivity. The low loss and wide bandwidth optical fibres are being actively introduced in the backhaul network, from the start of the last decade, in order to connect and feed the data to remote antenna sites from the central office and achieve reliable and ubiquitous connectivity [4], [5].

Multiple technological advances such as the use of a centralized radio access network (C-RAN), common public radio interface (CPRI), RAN functional split and other protocols were introduced in the backhaul network for the simple and cost-efficient deployment of remote cellular antenna sites [4], [6]. These advances led to reduced operational expenditure (OPEX) and flexible implementation of the cellular wireless system over the past decade, however, the continuous emergence of many data hungry applications coupled with the current trend of working from home has further increased the demand for high-speed broadband [7]. Further advances are required in both the wireless and optical domains in order to fulfil the increased data demand with next generation transmission systems. This introductory chapter will summarize the trends in data consumption, describe the legacy and next generation cellular wireless systems and enlist the state-of-the-art optical backhaul and fronthaul techniques employed for supporting the cellular transmission systems. Various challenges in different optical techniques currently used for supporting the efficient implementation of the wireless cellular system will be outlined and the key research objectives of this thesis will be presented.

1.1 Trends in Data Consumption

The recent pandemic made it clear that access to reliable and affordable internet is paramount not only for connecting with family and friends but for educational, work and entertainment purposes as well. The

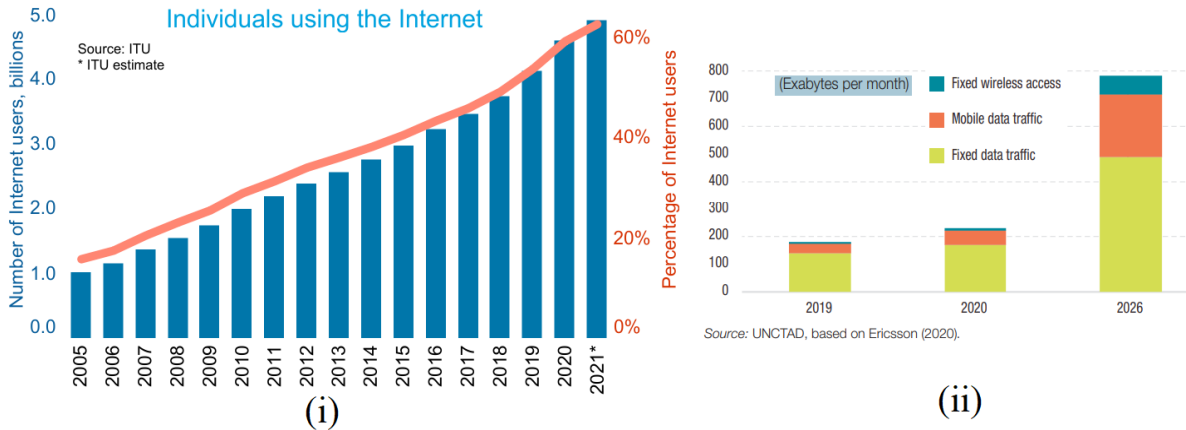


Fig. 1.1 (i) Number of internet users over the last two decades [8] and (ii) Mobile and fixed data consumption prediction between 2019-2026 [10].

increased role of the internet in people’s daily life over the past two decades is reflected in the increased number of internet users across the world. Data from the International Telecommunication Union (ITU), (Fig. 1.1) indicate a continuous increase in the number of internet users over the last two decades [8]. As of 2021, ~62.57% of the world population i.e., 4.95 billion out of 7.91 billion people are connected to the internet [8]. This number is still growing at a compound annual rate (CAGR) of 4% with the latest data showing the addition of around 192 million new users within the past twelve months [9]. Further technological advances especially with the introduction of the 5th generation cellular system, increased fibre penetration to rural areas and the emergence of low earth orbit satellite communication systems will help to increase internet penetration over the coming years and bring the remaining population online.

More than 90% of the users use mobile devices to spend some time of the day on internet, while the share of total online activities using laptops and desktop computers is higher in developed countries [9]. Mobile devices access the internet using both cellular and fixed wireless networks, while desktop and laptop devices majorly use fixed wireless and cable services. Fig. 1.1(ii) shows the global data consumption and prediction done by Ericsson for mobile cellular, fixed wireless and fixed data networks between the period 2019 – 2026 [10], [11]. The total mobile network traffic, which includes cellular and fixed wireless data, reached 80 Exabytes (EB; 1 EB = 10⁶ TB) in 2020 - an increase of 21 EB within a year. This trend is predicted to continue in the coming years and the total data traffic over the mobile network is expected to reach 370 EB by 2027 with a compound annual growth rate of 29% [11]. A comparatively slower CAGR of 17% is expected in the fixed data with traffic hitting 480 EB by 2026. Adding the data traffic from other services such as the Internet of Things (IoT), Machine-to-Machine Communication (M2MC), IP Television (IP TV) and other mediums, to the values mentioned in Fig. 1.1(ii), will further increase the total data traffic to 10s of Zettabytes in the coming years [7].

Currently, smartphones contribute to more than 90% of the traffic over the mobile network [9] and this number is expected to further increase with the introduction of the 5th and 6th generation cellular technologies in the current decade [11]. Video streaming platforms account for close to 68 to 70% of all mobile data traffic, which is forecasted to hit 79% by 2027 [9]. Social media platforms also significantly contribute to mobile traffic with 4.62 billion users spending an average of more than two and a half hours per day. The above-mentioned study from Ericsson [11] has predicted that the monthly global average data usage per smartphone has reached 11.4 GB by the end of 2021 and is forecasted to increase to 41 GB by the end of 2027. These numbers indicate the increased importance of mobile devices and associated network technologies. While the data consumption per smartphone has increased significantly over the past few years, however, the cellular and fixed wireless fidelity (Wi-Fi) data access speeds were expected to be around 20 Mbps and 37 Mbps, respectively, by the end of 2021 [7]. While these speeds are sufficient to access standard definition and high definition videos, social media and general office work requirements, they are not sufficient for data hungry applications such as virtual reality, live ultra-high definition (UHD)/4K/8K videos and online gaming.

In meantime, the number of IoT devices connected to the IP network are expected to increase to more than three times the global population by 2023 [7]. Also, the data speed for fixed broadband users is predicted to double while that of mobile users will triple by 2023 [7]. The expected increase in the number of internet connected devices and their data transfer speed along with the high demand for machine-to-machine communication will necessitate further technological advances in both the wireless and supporting optical backhaul network. In the next section, an overview of cellular communication systems and standards is provided.

1.2 Overview of Cellular Wireless Communication System

A basic cellular communication system consists of a central office, a backhaul link, an antenna site base station, a multi-path fading wireless channel and an end user mobile device/unit as shown in the schematic of Fig. 1.2 [2], [12]. The central office acts as a gateway between the radio and the external network and performs critical operations such as authentication of the subscriber's profile and location and switches the information between voice calls, text messages and mobile data [2]. The central office is connected to multiple antenna base stations (BS) using a physical layer backhaul network. Different transmission approaches are used to implement the backhaul network depending on the availability of transmission media, i.e. high bandwidth wireless channel or optical fibre, the distance between CO and BS and the population density in the cell site [12]. Traditionally a point-to-point link based on either wireless or optical fibre transmission alone was preferred for cost-efficient backhaul network implementation, however, a multi-hop transmission via a macro-cell relay antenna tower has become a more common scenario in rural

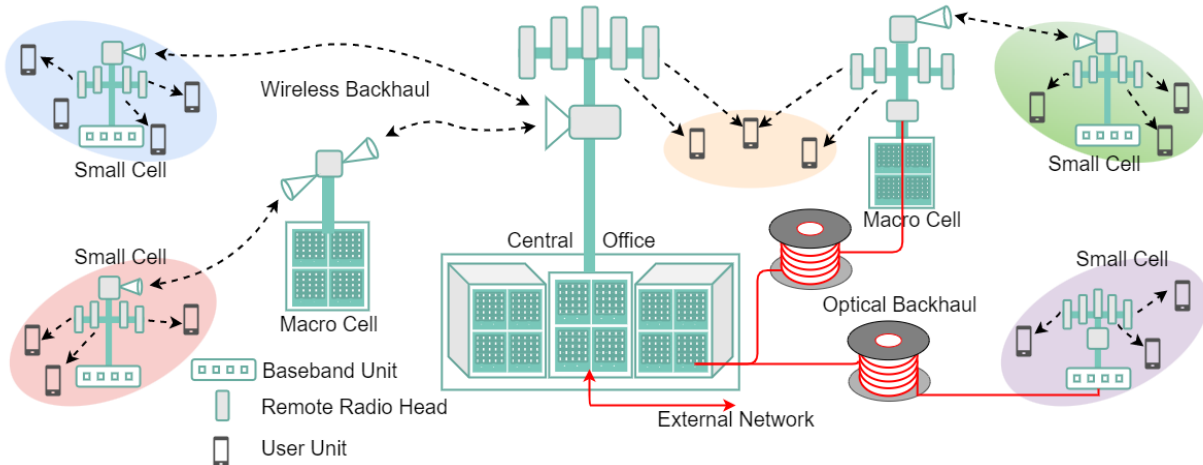


Fig. 1.2 Schematic of a typical cellular wireless communication system with different types of backhaul possibilities, i.e., wireless, optical and hybrid.

and low fibre connectivity urban areas. Some of the backhaul scenarios involving the use of either wireless or optical or both media are shown in Fig. 1.2 [12].

In the case of wireless backhaul, the CO baseband data is transmitted to the small cell site antenna unit over the wireless channel, either directly or via macro cell antenna, as shown by two different links on the left side of Fig. 1.2 [12]. The small cell site antenna received data is first frequency down-converted to the baseband and then processed using a baseband processing unit (BBU). The baseband unit generates the standard specific waveforms and transmits them to the end user over the wireless channel after frequency up-conversion to the appropriate band as specified by various standards. In the case of optical fibre backhauling, the CO baseband data is modulated on optical carriers and transmitted to the small cell site [5], [13], [14]. The photo-detected baseband electrical data is initially processed using the BBU at the small cell antenna site and the standard specific waveform is then transmitted to end users over a wireless channel after frequency up-conversion to the desired RF band [13]. In the case of hybrid backhaul, first optical fibre is used for carrying the data from CO to the macro cell site and then a wireless channel is used to carry the data to a small cell site [12]. The opposite order of transmission media in the hybrid backhauling case is also possible. More details of backhauling techniques are presented in section 1.3 of this chapter.

The remote antenna site base station acts as the last interface between the network and the end user device. Traditionally, the base station consists of two parts i.e., a baseband unit, for signal processing, and a remote radio head (RRH) for performing radio related operations [2], [4], [12], [14] as shown in the schematic of Fig. 1.2. The BBU performs physical layer signal processing on the data received from the backhaul link and converts it into a specific format waveform in compliance with various cellular communication standards. This baseband waveform is frequency up-converted to the desired RF frequency band, using a set of radio frequency electronic components at RRH, and then transmitted to the mobile end

users over an allocated wireless channel using the antenna unit. A typical BS site will host multiple radiating antenna elements in order to serve a large number of users [2]. Advanced techniques such as sectoring, multiple input multiple output (MIMO) antenna beamforming and phased array antennas are employed in typical cellular systems to achieve omni-directional propagation and increase the total throughput [2]. Both the BBU and RRH need to support all the digital and radio processing requirements for these advances, respectively. Also, the same antenna site is generally used for serving users operating with different generations of cellular technologies and the BSs need to handle such heterogeneous deployment [12].

The antenna elements emit radio signals as electromagnetic (EM) waves which travel through air consisting of different gases, moisture, dust, other particles and obstacles such as buildings, trees and mountains. These particles and obstacles typically absorb, scatter, reflect and diffract the radio frequency signals depending on the absorption properties and size [2], [15]. Also, the EM wave gets spread as it propagates through free space – resulting in reduced power at the receiver. The propagation and absorption attenuation effect results in a loss of signal power, which increases with an increase in the frequency of the signal and the distance between the transmitter and receiver [15]. Due to this, low frequency carriers (up to 6 GHz frequency) are usually employed in cellular transmission systems to minimize losses [2]. Also, the scattering and reflection from obstacles result in receiving multiple copies of the signal at the receiver – a phenomenon typically known as a multi-path channel. Typically, a correlation-based rake radio receiver with a maximum ratio combining technique is employed to decode the information and achieve reliable data delivery in multi-path scenarios [2]. Apart from the propagation loss and multi-path reception, wireless signals also experience interference from other services being transmitted on the adjacent channels. In order to accommodate multiple users and different applications, the wireless channel spectrum is divided into multiple frequency bands and different frequency bands are allocated to different services such as mobile cellular, Wi-Fi, military communication, radar, FM radio, etc [2]. All telecommunication services need to adhere to the specific frequency bands as set by standardization bodies such as the ITU, the Institute of Electrical and Electronics Engineers (IEEE), the United Nations (UN) and country specific government organizations.

The end user mobile devices receive the signal using a small antenna unit and frequency down-converts it to the baseband with a chain of RF operations [2]. This standard specific baseband data is then converted to voice, video or other user-friendly formats after processing. A reverse process is followed for uplink data transmission from the end user to the antenna base station and then to the central office in accordance with the employed transmission standard [2]. In the next subsection, the evolution of wireless cellular communication through different generations is summarized.

1.2.1 Evolution of Cellular Wireless System from 1G to 5G

Fig. 1.3 shows the various physical layer properties such as modulation format, multiplexing techniques, achievable data rates, associated parameters and applications of the different generations of the cellular system as it evolved from 1G to 5G. The 1st generation cellular system was based on analogue communication and was primarily used for voice delivery [3], [16]. The limited bit rate between 4.8 – 9.6

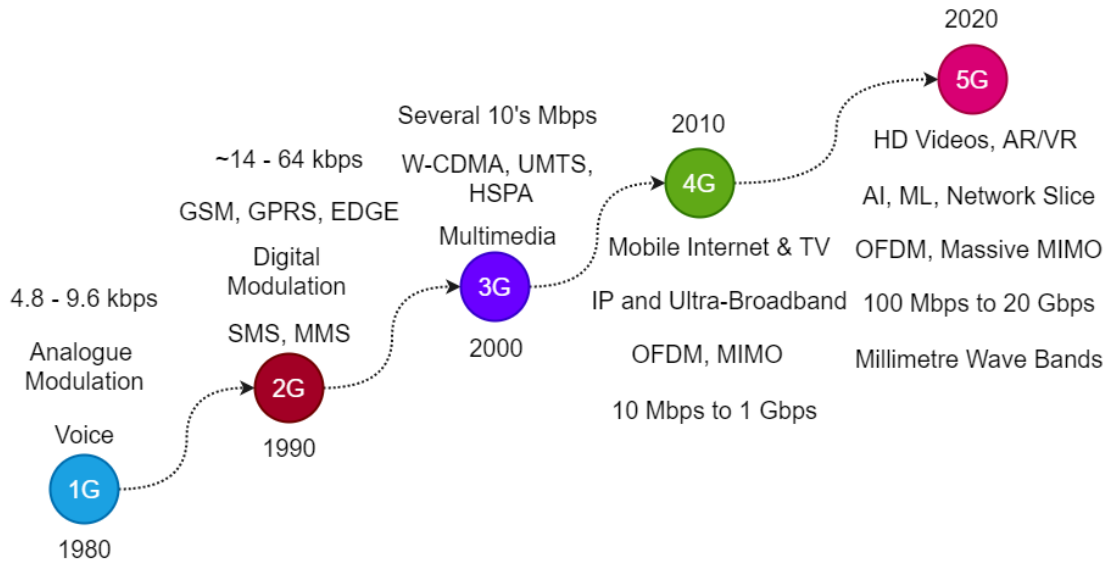


Fig. 1.3 Physical layer properties of different generations of cellular communication systems.

kbps resulted from the use of small channel bandwidths in the 800 – 900 MHz frequency band and inefficient frequency modulation technique for data transmission. The use of analogue modulation made these systems prone to interference, loss and weak security, while the underdeveloped infrastructure resulted in smaller transmission distances, frequent call drops and poor battery life of end user devices - limiting its usage to a smaller population [3]. The use of digital modulation in the 2nd generation system eliminated some of these drawbacks [2], [3]. The discrete nature of the digital signal made it less prone to noise, while encryption made it more secure. The data transfer speeds in the range of 14.4 – 64 kbps enabled the internet access and delivery of short and multimedia messaging services (SMS & MMS) [16]. The 2G system, technically known as the global system for mobile communication (GSM), used both time and code division multiple access (TDMA; CDMA) techniques to combine the data from different users [3], [16]. Higher data speeds, of up to 164 kbps and 473 kbps, were achieved with the introduction of packet switching for data transmission in 2.5G GPRS (general packet radio services) and additional circuit switching for voice transmission in 2.75G EDGE (enhanced data rate GSM Evolution) systems [16], respectively.

Further advances were introduced with the 3rd generation universal mobile terrestrial system (UMTS) developed by the 3rd generation partnership program (3GPP) [2]. The data speeds of up to 384 kbps and 2 Mbps for the moving and fixed receivers, respectively, were sufficient to support multiple applications such

as instant messaging, internet access, video and conference calls, mobile TV and legacy voice, SMS and MMS services. The 3G UMTS is based on the wideband CDMA (W-CDMA) technology, which used frequency division duplexing with a pair of 5 MHz channels and additional time domain duplexing to transmit data in frequency bands around 2 GHz [2], [3], [16]. Higher data speeds up to 14 Mbps and 42 Mbps were achieved in 3.5G HSPA (high speed packet access) and 3.75G HSPA+ (high speed packet access plus) systems, respectively, with the use of advanced modulation formats such as 16 and 64-ary quadrature amplitude modulations (16-QAM; 64-QAM) [17]. MIMO and carrier aggregation were introduced in 3.9G to further increase the data rates [16], [17].

The development of multiple applications and advances in smartphone technology required higher than 3G achievable data rates - resulting in the development of the 4th generation cellular technology (also termed as long term evolution (LTE)) [17], [18]. The 4G system promises to provide an edge data rate of 10 Mb/s for all users, while the maximum rates can reach up to 100 Mb/s and 1 Gb/s for mobility and fixed receivers [17], [18], respectively. In 2021, almost 59.7% of total mobile subscribers were covered by 4G [11], and the median global speed is reported to be ~29.60 Mbps at the end of 2021 [19]. This disparity in data rates arises from the high density of users and limited spectrum availability among multiple operators. 4G supports multiple channel bandwidths ranging from 1.25 MHz to 20 MHz and higher bandwidths up to 100 MHz could be obtained with aggregation of five 20 MHz carrier components [18], [20]. The use of spectrally efficient orthogonal frequency division multiplexed waveform for data transmission and MIMO beamforming improved the spectral efficiency in 4G [18]. RF carriers from 700 MHz to 3.6 GHz are used in the 4G system to transmit signals over the wireless channel with reduced latency of 10 ms for non-roaming users [18]. The 4G system improved the data speed from hundreds of kbps in the 3G era to several tens of Mbps, however, these speeds are not sufficient for emerging data hungry applications and a high density of IoT devices. Further improvement in speed and technology is expected to be achieved with the 5G system, which started deployment in 2020.

1.2.2 5th Generation Cellular System

The 5th generation wireless system focuses on three major aspects, i.e., enhanced broadband (eMBB), massive machine type communication (MMTC) and ultra-reliable low latency communication (URLLC) to serve different applications [21], [22]. The figure of merits in terms of achievable targets for different quantities are depicted in Fig. 1.4 for the 5G system with the inner circle giving the corresponding values of the 4G system. The 5G system promises to provide an edge data rate of 100 Mbps, a 10 times jump from the 4G system, while the peak data rates will increase by 20 times to reach 20 Gb/s [21]. Such high rates will be achieved with a combination of known techniques such as the use of higher order data modulation

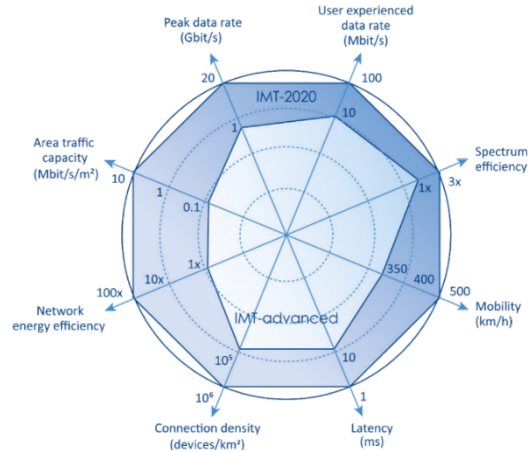


Fig. 1.4 Figure of merits for 5G system in terms of various physical layer parameters [21].

format (to increase the spectral efficiency), higher channel bandwidths, smaller area cell sites (increasing the frequency reusability) and increased order of MIMO configuration (spatial multiplexing) [21], [23]. According to the Shannon capacity theorem [2], an exponential increase in the signal-to-noise ratio (SNR) is required for increasing the order of modulation format. Higher SNRs cannot be always guaranteed over the wireless system – making it difficult to increase the order of modulation beyond a certain limit.

A linear increase in the data rate can be achieved by directly increasing the channel bandwidth [2]. The 5G new radio specification, released by the 3GPP, provisions the use of channel bandwidth up to 400 MHz [24], much higher than the 20 MHz of 4G. Such higher BWs are achieved by moving the data transmission away from the sub-6 GHz frequencies to the millimetre wave band. The 5G NR standard has provisioned the use of mm-wave carriers within 24.25 GHz to 52.6 GHz frequency bands along with some sub-6 GHz bands (with bandwidths up to 50 MHz) for use in the high speed cellular systems [21], [24]. While the move towards the use of higher frequency bands increases the throughput, the higher propagation and atmospheric losses at these frequencies reduce the coverage. Also, an efficient technique for the generation of low phase noise mm-wave carriers and signals need to be employed for successful system deployment. More details about various mm-wave and high frequency THz bands, which might be used for the 6G system, are given in the next subsection 1.1.3.

In the case of MMTTC applications, the 5G network is expected to support around 1 million small-scale IoT devices within a square km area along with improving the network's energy efficiency by 100 times compared to the 4G network [21]. Also, the 5G network design should be made such that time-sensitive applications such as remote surgery and autonomous driving should experience a maximum latency of 1 ms. In order to provide reliable services, the deployed 5G network should be capable of serving the users in high mobility scenarios of up to 500 km/hr speed [21], [22]. The work presented in this thesis is focused on the eMBB aspect of 5G – especially on the use of optical techniques for mm-wave systems.

1.2.3 Millimetre and THz Frequency Bands for Wireless Systems

Theoretically, the mm-wave and terahertz spectra spread over the frequency range from 30 to 300 GHz and 300 GHz to 3 THz, respectively, with corresponding wavelength values ranging from 10 mm to 1 mm and 1 mm to 1 μm in the electromagnetic wave spectrum. In modern engineering, the mm-wave frequency band ranges from 24 GHz to 100 GHz, while the frequencies within the 100 GHz to 300 GHz range are termed as a sub-THz band [25]. Despite such a wide frequency range, all the frequencies within the mm-wave and THz band cannot be used for data transmission in the wireless cellular system. These high-frequency radio carriers suffer from large propagation and atmospheric absorption losses. The propagation loss, between the far spaced transmit and receiver antenna units, increases directly with the square of distance and frequency of the carrier [15]. The higher propagation loss results in reduced coverage and requires the dense deployment of antenna base stations to cover the geographical area. Various telecom operators from different countries have started deploying 5G sites with coverage ranging from a few km with sub 6 GHz carriers to 100s of meters for the mm-wave bands [26].

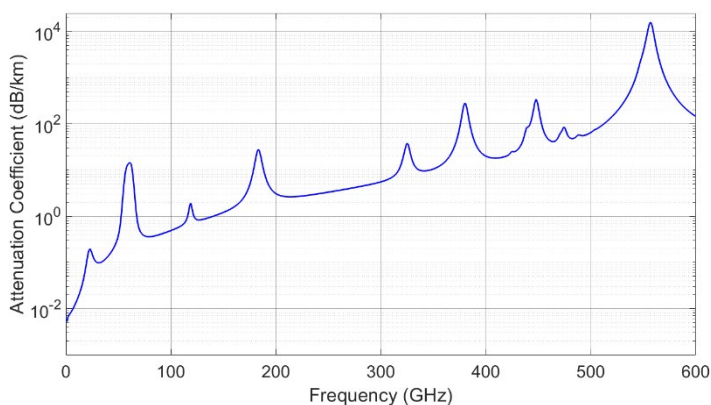


Fig. 1.5 Atmospheric attenuation coefficient vs frequency over wireless channel due to oxygen and water vapour absorption.

The Friis transmission equation [2] which governs the link budget of a wireless link considers the channel as free space. However, the earth's atmosphere contains various gases and particles which absorb electromagnetic radiation - resulting in an additional loss. The variable absorption properties of different gases and particles result in a frequency-dependent loss [15]. The atmospheric attenuation coefficient, due to oxygen and water vapour absorption, is shown in Fig. 1.5 as a function of frequency at room temperature. The absorption peaks are seen at 22 GHz, 60 GHz, 119 GHz, 183 GHz, 325 GHz and higher frequencies - limiting the available mm-wave and THz spectra for the cellular wireless system. The low-loss frequency bands between these peaks are generally assigned for outdoor communication applications, while the frequencies around the absorption peaks are used for indoor or short-distance outdoor communication systems with higher frequency reusability [25].

Table. 1.1. IEEE nomenclature for bands in the 18 to 300 GHz frequency range.

Band Name	Frequency Range
Ka	26.5 to 40 GHz
Q	33 to 50 GHz
V	40 to 75 GHz
E	60 to 90 GHz
W	75 to 110 GHz
D	110 to 170 GHz

The IEEE has divided the Extremely High Frequency (EHF) mm-wave frequency band, spanning from 30 GHz to 300 GHz, into various bands as mentioned in Table 1.1 [27], [28]. The bandwidth occupancy of these bands is very wide, ranging from 13.5 GHz for the Ka-band to 60 GHz for the D-band. It is extremely difficult to have one component working over such a wide range and hence some intermediate bands are created for simplicity. The Q band has frequency overlap with Ka and V bands, while the E band is created with frequencies from V and W bands. A large portion of the spectrum from these bands is assigned for other applications such as sensing, radar, military and space communications to name a few [25]. The Ka and V bands are widely used in satellite systems [29], while some frequencies from the Ka-band will be used in the 5G system. The federal commission for communication (FCC) has completed three auctions for the 24 to 48 GHz frequency bands and is planning to extend it up to 100 GHz in the United States [25].

The unlicensed frequency bands are also being considered for providing high speed connectivity, mostly in indoor settings. The frequency band around 60 GHz has attracted much attention with the availability of a continuous 5 to 7 GHz (57 to 64 GHz) useful spectrum in most countries [30]. In the United States, 14 GHz of unlicensed spectrum is available between 57 to 71 GHz frequencies [25]. Though the high atmospheric attenuation around 60 GHz frequency, as shown in Fig. 1.5, limits its use for short-distance systems, the absence of licensing and availability of such wide bandwidth has made it popular for wireless local area networks such as Wi-Fi. Communication standards like IEEE802.11ad [31] and IEEE802.11ay [32], working in the 60 GHz unlicensed frequency band, have been established to provide throughputs of ~7 Gb/s and more than 100 Gb/s, respectively. Multiple IoT devices working at the 60 GHz band have also come to market in recent times along with Wi-Fi modems. The majority of the work presented in this thesis is also targeted at generating signals in the 60 GHz mm-wave band using optical heterodyning.

The high frequency mm-wave/THz carriers are also used in wireless backhaul, radar, satellite communication, THz imaging and other applications. Currently, Ericsson has wireless backhaul products working in the 15 GHz, 23 GHz, 38 GHz and 70/80 GHz frequency bands [33] and is developing products for beyond 100 GHz frequency bands [34]. The recent emergence of autonomous vehicles and atmospheric

and ocean research has increased the interest in radar systems working in high-frequency bands up to 100 GHz [35]. Satellite communication continues to use frequency carriers in the Ku, K and Ka bands [29], and the shift toward the use of higher frequency carriers is foreseen given the recent newfound interest in the deployment of the constellation with thousands of internet beaming high throughput satellites.

The 6th generation wireless communication system may use carriers beyond 100 GHz for achieving data rates up to and beyond 1 Tb/s [25]. The use of sub-THz and THz frequency carriers will help in terms of increased channel bandwidth, higher directivity with a smaller beamwidth and small antenna aperture due to the low wavelength of radiations. However, multiple challenges in terms of the design of high power amplifiers, low loss mixers and low phase noise RF sources need to be solved for harnessing the full capacity of such systems [36]. The FCC has already identified 21.2 GHz bandwidth of unlicensed spectrum within various frequency bands up to 250 GHz and has granted experimental licenses to use frequencies up to 3 THz [25]. The IEEE has established a task force to develop the Wi-Fi IEEE.802.15.3d [37] standard in the frequency range from 250 to 350 GHz and achieve more than 100 Gbps data rate. With such high data rates, the wireless system can replace fibre optics in applications such as intra-data centre connectivity, intra-device communication and optical fronthaul/backhaul. The precision and accuracy of some traditional applications such as imaging, sensing and positioning can be greatly improved with sub-THz and THz frequency systems [25].

In hindsight, the move towards the use of higher frequency mm-wave, sub-THz and THz frequency carriers is inevitable and technological advancements need to be followed up to address the various challenges. In addition, an efficient backhaul network should be also implemented to serve the increased number of antenna sites in the densely deployed network. An efficient mm-wave carrier generation technique and backhaul network deployment are two important aspects of the next generation wireless system. The work presented in this thesis focuses on both these aspects with a major focus on impairment free mm-wave carrier and signal generation with optical techniques. A summary of various optical backhauling schemes is presented in the next section 1.3, while the technique for mm-wave and THz carrier generation is discussed in section 1.4.

1.3 Optical Backhauling for Cellular System

Different transmission media such as wireless, optical or hybrid of both can be used for the backhaul data transmission to the remote base station site [12], as shown by various possibilities in Fig. 1.2. While the use of wireless channel alone facilitates simple backhaul system deployment and helps to connect the remote areas covering mountains and rivers, their limited range due to higher propagation and atmospheric losses limit the range over which the wireless backhaul can be deployed [34]. Also, some of the frequency bands need to be reserved for backhaul data transmission – limiting the spectrum allocation for serving the

end users and other applications. In contrast, the low loss and wide bandwidth capabilities of optical fibre can extend the reach of the backhaul link to more than several tens of km from the CO and do not occupy the valuable wireless channel bandwidth [5], [6], [14]. While the deployment of optical fibre cables is a cumbersome process, however, once deployed the link and its capacity can be easily upgraded through terminal equipment upgrade. Also, the existing passive optical network (PON) infrastructure can be exploited to transmit the backhaul data to the antenna sites and achieve centralization of resources and cost reduction through converged network deployment [5], [38], [39]. Multiple governments across different continents are deploying fibre cables and leasing the services to increase the use of optical fibres in backhaul services and provide high speed last mile connectivity to remote end users. This section provides a summary of advances in optical backhaul network deployment.

Fig. 1.6 show the architecture of a traditional optical fibre based distributed backhaul network. The CO is connected with the multiple remote small cell site base stations either with a direct optical fibre link or

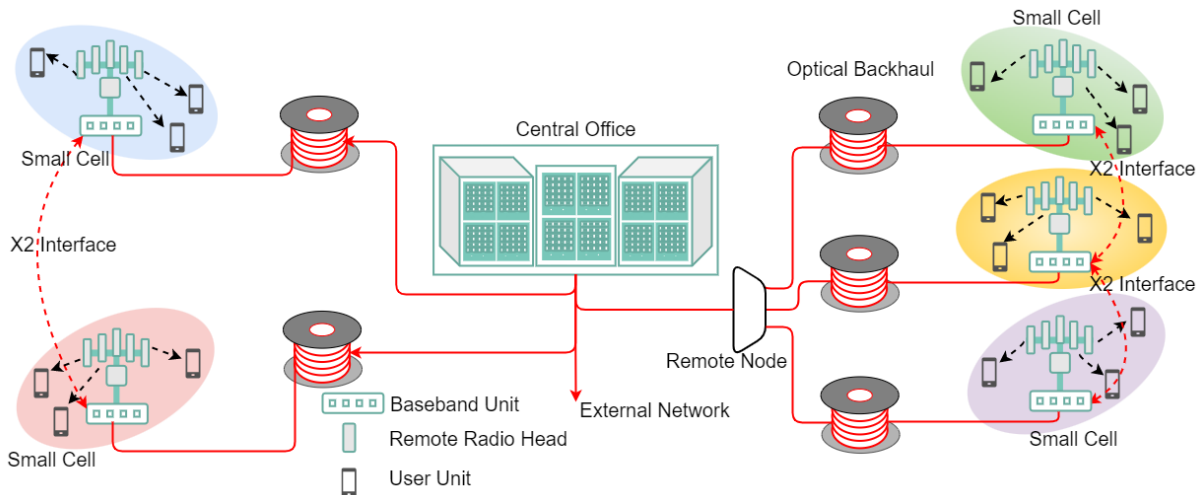


Fig. 1.6 Architecture of a traditional distributed backhaul network showing X2 interfaces required for coordination between adjacent cells.

through a distribution network [40]. A passive splitter remote node is typically used in the case of a distributed network use for connecting the CO to multiple BS sites as shown on the right side of the figure. This architecture is similar to the passive optical network [41], where the optical line terminal (OLT - mimicking the CO) is connected with multiple optical network units (ONUs – mimicking the BBU) via a remote node passive splitter. Data from these ONUs is fed to business centres or residential areas or mobile base stations. The distributed backhaul network shown in Fig. 1.6 is a special case of the “Fiber-to-the-X (FTTX)” PON network, where x stands for antenna [42]. Fig. 1.6 also shows the X2 interface links connecting the base stations of adjacent cell sites. These X2 interfaces (implemented using a physical wireless or optical link) are used for connecting adjacent BSs for better coordination to reduce the interference arising due to coverage overlap and handover process [4] – especially for end users in motion.

As the wireless network shifts toward using the mm-wave frequency carriers, the ultra-dense deployment of the small/pico-cell base station antenna sites will result in a more complex backhaul network architecture with an increase in X2 interfaces, operational cost and energy consumption [18]. Also, the transmission of higher BW signals will increase the traffic over the backhaul network and footprint of the BS as the baseband unit needs higher capabilities for processing. It is necessary to simultaneously improve the backhaul network and reduce the footprint of the antenna site for the simple and cost-effective 5G and next generation wireless cellular system deployment. The solution that is being sought, to reduce BS footprint and simplify the backhaul, is to move some of the radio access network related signal processing functionalities of multiple BSs to a common location and connect it to the antenna site RRH unit with optical fibre based fronthaul link in conjunction with a centralized/cloud radio access network [4].

1.3.1 Centralized Radio Access Network and Optical Fronthauling

The functional split of the traditional base station into BBU and RRH units along with the centralization of the RAN baseband signal processing of multiple BSs provides an efficient solution for simplifying the backhaul link and reducing the footprint of the BS [4]. Centralization of the BBUs, termed as centralized/cloud-BBU (C-BBU), eliminates the long X2 interfaces and simplifies the radio resource management in a complex environment like heterogeneous antenna sites serving various mobile technology (3G/4G/5G) users or using carrier aggregation [4]. Such functionality split requires high speed and low latency connectivity between C-BBU and multiple antenna RRH sites, which is typically provided by an optical fibre. A network connecting the C-BBU to multiple antenna units is termed a fronthaul, while the connection between CO and C-BBU is served by a backhaul link, as shown in the architecture of the C-RAN in Fig. 1.7 [4]. The terms fronthaul and radio-over-fibre are used interchangeably as both serve the same purpose of transmitting wireless signals to the antenna site RRH units over optical fibre.

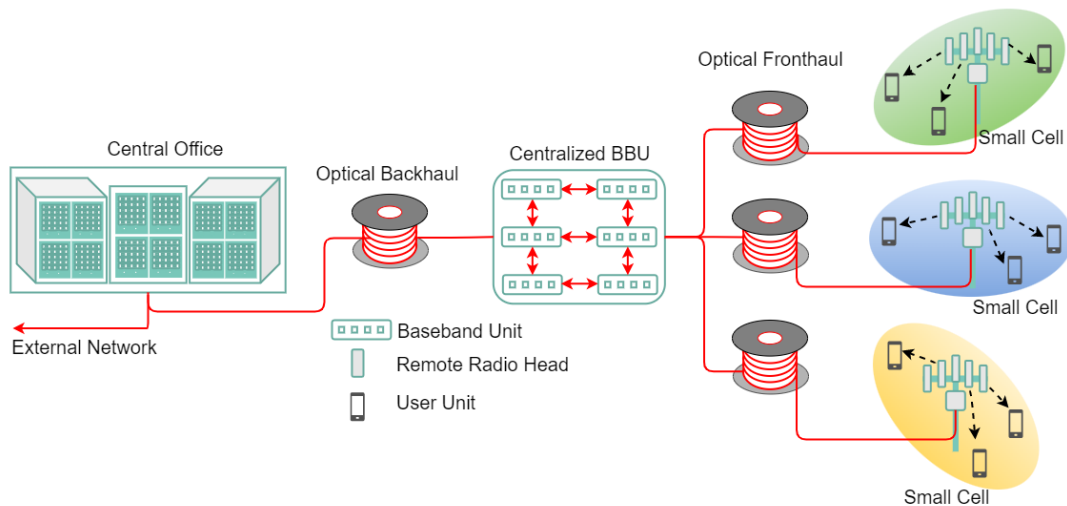


Fig. 1.7 C-RAN architecture showing the CO, Backhaul, C-BBU, Fronthaul and RRH.

Conventionally, the RoF technology refers to the transmission of high frequency radio signals by modulating them on optical carriers but in general, any optical fibre link carrying the wireless signals is termed as an RoF link [13].

All the baseband processing, of multiple BBUs located at the C-BBU site, can be performed on a high speed cloud – improving the processing time and efficiency of the network. Also, any common processing required for the interference mitigation, between the co-located small cell BBUs, can be done efficiently by connecting them with a short link as shown in the architecture of Fig. 1.7 [4]. This will result in a reduction of the BS footprint as only radio related operations will be performed at the antenna sites. The requirement of the various optoelectronic and electronic components at the C-BBU and RRH antenna site depends on the transport protocol used over the fronthaul link [13].

1.3.2 Fronthaul Possibilities and Digital Radio-over-Fibre

The RoF link is fundamentally based on analogue transmission, but most of the conventional optical links employ digital transmission. This creates two possibilities for implementation of the fronthaul link [13], [43], i.e. digital RoF and analogue RoF, as shown in Fig. 1.8. Also, the signals can be transmitted either in the baseband (BB) frequency or intermediate frequency (IF) or wireless radio frequency (RF) over the fronthaul link leading to additional three different transmission schemes [13], [43]. The complexity of the RRH antenna site architecture depends on whether the signal is transmitted in the analogue or digital form, and at the BB, IF or RF frequency with respect to the optical carrier [13], [14].

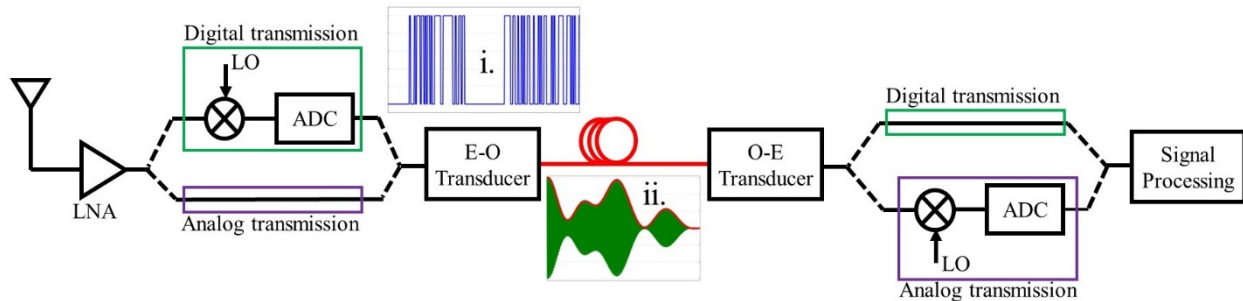


Fig. 1.8 Architecture of D-RoF and A-RoF Fronthaul scheme connecting C-BBU and RRH sites.

In the case of D-RoF, as shown by the upper path in Fig. 1.8, the antenna received signal is first frequency down-converted and then the baseband signal is digitized to bits after quantization and mapping – requiring the use of high speed analogue to digital converter (ADC), and digital to analogue converter (DAC) for uplink, at the remote antenna RRH sites [13], [43]. The quantization of frequency down-converted signal increases the line/data rate over the D-RoF fronthaul link and it scales linearly with the level of quantization and bandwidth of the signal [13], [20], [43]. In contrast, the antenna received signal is directly transmitted over the A-RoF fronthaul link – eliminating the need for ADC and DAC at the antenna site [13], [14], [43]. The direct transmission of wireless signals preserves the spectral efficiency over the optical fronthaul link.

However, the performance of the A-RoF link suffers from limited dynamic range, power fading due to optical fibre dispersion, nonlinearity and other impairments [13]. Also, the bandwidth of optoelectronic components needs to be proportional to the wireless signals carrier frequency. Additional details of all fronthaul possibilities are discussed in chapter 2.

The D-RoF fronthauling scheme has been adopted in the common public radio interface [20], [44] and open base station architecture initiative (OBSAI) [45] standards. The CPRI standard is currently used for carrying the 4G data between the C-BBU and antenna RRH sites, due to its flexibility and higher IQ data capacity compared to OBSAI. The quantization and other processing required in CPRI increases the amount of bandwidth required to transmit the radio signals. Details of the D-RoF based CPRI protocol line rate requirements are given in the next subsection.

1.3.3 Common Public Radio Interface Fronthaul

The CPRI standard uses the D-RoF protocol for the transmission of 4G LTE wireless signals between the C-BBU and RRH site. The 4G LTE standard uses the OFDM waveform, which is complex in nature with in-phase (I) and quadrature (Q) component representation i.e. $I+jQ$ sample, for data transmission to the users. The signal processing unit at C-BBU will generate the I-Q samples of OFDM signal required for transmission and the respective fronthaul protocol will transport them to the RRH antenna site [20]. The flowchart of the operations followed by the CPRI fronthaul protocol is shown in Fig 1.9. Initially, the multiple I-Q samples of OFDM signal are serialized as $I_0Q_0I_1Q_1I_2Q_2\dots\dots I_{N-1}Q_{N-1}$, where N is the number

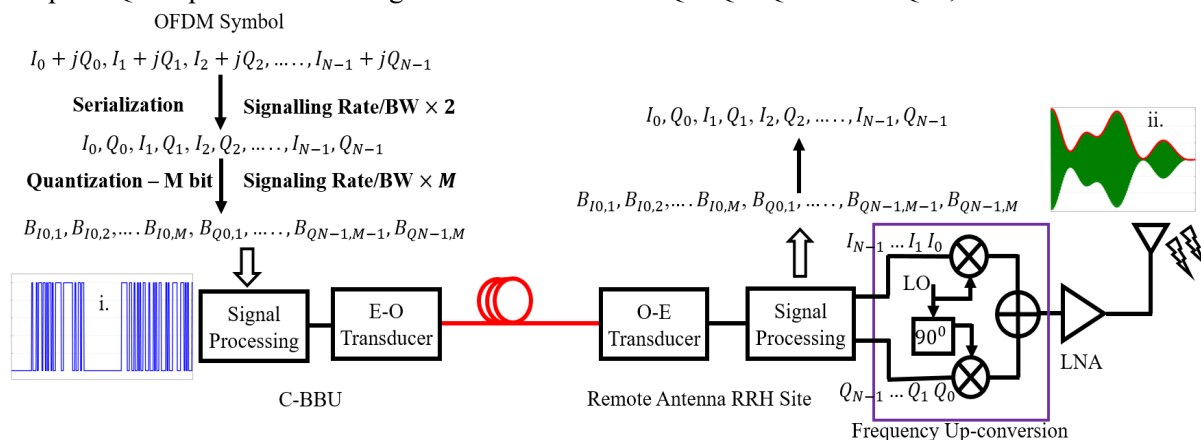


Fig. 1.9 Flow Chart of operations followed by DBBoF based CPRI protocol for fronthaul data transmission between C-BBU and RRH site over optical fibre.

of subcarriers present in the OFDM symbol. The details of OFDM waveform/signal will be discussed in the next chapter. This serialization increases the signalling rate and in turn the bandwidth of the signal by a factor of 2 [20]. The serialized $I_0Q_0I_1Q_1$ samples are then quantized using the ADC and converted to 1's and 0's according to the resolution and quantization level. Each I_0, Q_0 sample will be converted into M bits – resulting in an M factor increase in the signalling rate/bandwidth of the signal as shown in Fig 1.9 [20].

The on-off keying (OOK) 1's and 0's signal (shown in the inset (i) of Fig. 1.9) is converted to the optical domain using an electric-to-optical (E-O) transducer/modulator and then transmitted to the antenna site over the optical fibre. At the remote antenna site, the photo-detected signal is processed (signal processing + DAC) to obtain the I-Q samples of the OFDM signal and then transmitted to the user after frequency up-conversion. The radio frequency modulated OFDM signal is shown in inset (ii) of Fig. 1.9. The OOK signal will get distorted due to the nonlinear response of E-O/O-E transducers and PD noise. The retrieved bits and I-Q samples, in Fig. 1.9, are shown the same as the transmitted one for a simple understanding of the CPRI operation flow. The CPRI digitized transmission link transports the signal in frames requiring additional data overhead [20]. The use of line coding to eliminate the distortion also adds to the data rate overhead leading to increased signal bandwidth over the fronthaul link.

The serialization and quantization required in CPRI increases the amount of bandwidth required to transmit the radio signals. For example, the transmission of a 20 MHz bandwidth 4G LTE OFDM signal will require a data rate of ~ 0.9216 Gb/s over the D-RoF CPRI fronthaul link [20], which increases to ~ 1.0138 Gb/s after considering the frame-wise transmission and line coding overhead. For a typical 8×8 MIMO antenna RRH site covering four sectors (i.e. $32 - 20$ MHz BW signals) this rate increases to ~ 32 Gb/s – showing the overwhelming bandwidth expansion required over the CPRI link [20]. Moreover, in the case of 200 MHz bandwidth 5G NR signal transmission, this same scenario will require ten times (i.e. 320 Gb/s) the 4G CPRI bandwidth – showing the poor spectral efficiency of the link. This data rate requirement can be reduced to some extent by using compression techniques [46], but it leads to additional signal processing complexity and performance degradation.

In order to overcome the problem of increased line rate in CPRI, a further split in the RAN functionality is being introduced for the fronthauling of 5G signals. These advances in the RAN functional split and implementation of fronthaul for 5G systems are discussed in the next subsection.

1.3.4 RAN Functional Split and Fronthaul for 5G

In order to reliably transfer the data to the intended end users, the wireless cellular system performs multiple RAN signal processing operations such as radio resource control (RRC), packet data convergence protocol (PDCP), radio link control (RLC), media access control (MAC), physical layer (PHY) and radio frequency related functions as shown in Fig. 1.10 [38], [39]. These processing operations are traditionally performed by the BS's baseband unit at the remote antenna sites. However, the introduction of the fronthauling moved most of these operations to the C-BBU site and only RF related operations are performed by the RRH unit at the remote antenna site. The data rate and latency values over the fronthaul link vary depending on which operations are performed at the C-BBU site and remote antenna site, i.e. selection of one of the functional split options among the eight potential options shown in Fig. 1.10 [38],

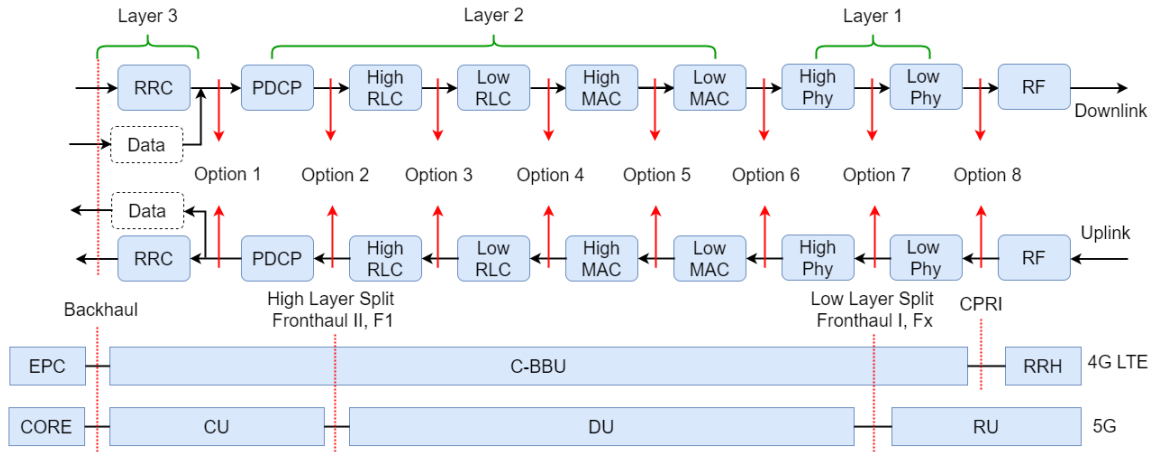


Fig. 1.10 RAN functional split options as adopted in CPRI fronthaul standard for 4G LTE and various fronthaul possibilities for 5G.

[39]. The CPRI standard uses a high layer functional split (option 8), requiring higher line rates for transporting the digitized IQ data from C-BBU to the RRH site. In order to reduce the line rate, a lower option functional split needs to be used – requiring some of the functionalities to be moved to the RRH site [39]. The data rate over the fronthaul link varies from as low as 4 Gb/s with the use of option 1 functional split to 157.3 Gbps with option 8 split for delivering 100 MHz bandwidth signals to 8×8 MIMO and 32 antenna port remote site [39]. This shows how the choice of split option affects the data rate over the fronthaul link. An in-depth review and analysis of the trade-offs among the different split options is provided in [38], [39].

While the use of a low functional split option reduces the data rate over the fronthaul link, it increases the complexity of the RRH site as some of the processing will be shifted to the remote antenna site. In order to keep the remote antenna site architecture simple, the radio processing for 5G is split into the next generation core (NGC – same as core/CO of 4G), centralized unit (CU – same as C-BBU), distributed unit (DU) and radio unit (RU – same as RRH) elements [38]. An additional distribution unit is introduced in the 5G fronthaul as shown in the bottom part of Fig. 1.10. The placement of this additional distribution unit and the choice of functional split used for CU and DU helps to maintain the balance between the complexity of the antenna site RU/RRH unit, line rate and RAN processing latency [39]. The link between CU and DU is termed as Fronthaul-II (F1) and the link between DU and RU is termed as Fronthaul-I (Fx). A general term x-haul also finds mention in the literature, where x stands for back, front or mid possibilities.

Fig. 1.11 shows all the fronthaul possibilities created with the placement of central and distribution units at different locations [38], [39], [47]. The first case, where CU, DU and RU are placed at a remote location, resembles the traditional backhaul network shown in Fig. 1.6. In this case all the RAN processing is done

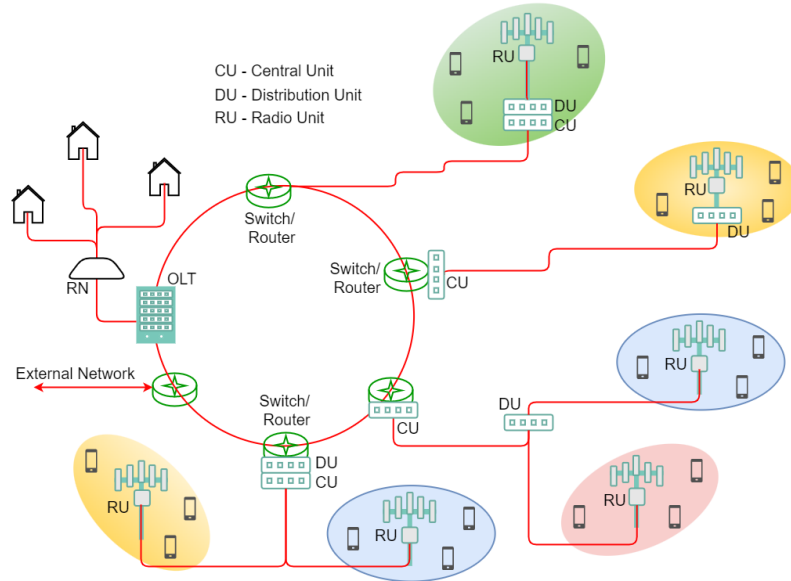


Fig. 1.11 Different fronthaul architecture possibilities arising from the location of CU and DU units for 5G [38].

at the antenna site and is connected to the core with the backhaul link. In the second case, some of the functionalities are moved away from the remote location and will be performed by the CU. Depending on the choice of the functional split, the antenna site will still host some processing – requiring the presence of an intelligence unit. In the third case, CU, DU and RU units are physically separated with most of the processing done by the CU and DU and leaving only RF operations to the RU site [38]. The fourth scenario resembles the fronthaul link shown in Fig. 1.7, where the CU and DU are physically located at the same site (same as C-BBU) and are connected with the RU (same as RRH) over a fronthaul link.

The work presented in this thesis considers the fourth scenario, where CU and DU are co-located physically and a fronthaul link is used for sending the signals to the antenna site, due to its simplicity for experimental demonstration in a research lab environment. As this architecture resembles the fronthaul link, C-BBU and RRH terms are used interchangeably with co-located CU-DU and RU, respectively.

The choice of the CU and DU placement and split options among them depends on each operator's deployment scenarios. In general, two split options, i.e. higher layer split point (F1) and lower layer split point (Fx) are being recommended by various standardization groups [38]. The 3GPP has specified the F1 interface at option 2 split, while Fx could be from variants of option 7 [38]. Different interfaces have been proposed by the eCPRI Group, the Small Cell Forum and the ORAN Alliance [38]. The IEEE has also started a working group P1914, for studying the packet and Ethernet based fronthaul delivery, and task force 802.1CM to look into the time sensitive fronthaul network design [38].

The trade-off in the data rate requirements over the fronthaul link, complexity of the antenna site, and cost of high-speed digital functionality implementation (due to the choice of RAN split point) may result

in operator and/or use case specific fronthaul networks as 5G evolves towards higher bandwidth signal transmission [6]. Hence, it is necessary to move towards a spectrally efficient and simple remote antenna site fronthaul link for higher bandwidth 5G signals transmission between C-BBU and RRH site. As mentioned in subsection 1.3.2, the analogue RoF link retains the inherent bandwidth efficiency of the wireless signals over the fronthaul link and simplifies the remote antenna site architecture. It also avoids the use of a high-speed DAC and ADC at the remote antenna site. Various experiments [48]–[50] have demonstrated the feasibility of A-RoF fronthaul supporting the transmission of multiple intermediate frequency signal bands over the same link. Multiple impairments such as power fading due to fibre dispersion, limited dynamic range and non-linearities from the optoelectronics components limit the performance of the A-RoF link [13], [14]. It is necessary to analyse the capacity of the A-RoF link for the transmission of 5G NR compatible signals for an efficient fronthaul system deployment. In chapter 2, the A-RoF fronthauling scheme is discussed in detail along with its various implementation possibilities and experimental results for downlink and uplink implementations.

The photo-detected signal at the antenna site, after transmission over the fronthaul link from the C-BBU site, will be at either the baseband or intermediate frequency for D-RoF and A-RoF links, respectively [13], [43]. An electrical frequency up-conversion stage needs to be implemented at the remote antenna site to transmit these signals to the end users over the mm-wave/THz frequency band wireless channel [51]. In the case of uplink transmission, an electrical frequency down-conversion stage needs to be implemented at the remote site to bring the antenna captured signal to either the baseband or IF band. This electrical frequency up/down-conversion stage will require the use of either a high-frequency local oscillator (LO) and mixer or a frequency multiplication/division stage – resulting in higher complexity of the remote antenna site. The footprint and energy consumption of the antenna site increase with an increase in the frequency of the mm-wave/THz carrier transmitted over the wireless channel. In order to avoid this, an alternate optically compatible technique, i.e. optical heterodyning [52]–[54], has been proposed for the mm-wave/THz carriers generation in the past and it has gained more interest recently due to the emergence of the possibility to deploy a fully optical solution for both fronthauling and mm-wave/THz carrier generation. An efficient mm-wave/THz carrier generation technique and deployment of a back/front-haul network are two important aspects of the next generation wireless system. In the next section, the optical heterodyne technique is explored for the generation of mm-wave/THz signals and carriers. A summary of the electronics carrier generation technique is also provided.

1.4 Optical Generation of Millimetre/THz Carriers

The move toward the use of higher frequency mm-wave, sub-THz and THz frequency carriers is inevitable for the next generation wireless systems. Technological advancements need to be followed up to

address the challenges of low phase noise mm-wave/THz carrier and signal generation, filtering, frequency conversion and beamforming for harnessing the full potential being offered by the high frequency wireless communication systems [25]. In this thesis, the foremost challenge of mm-wave/THz carrier and signal generation is addressed.

1.4.1 Summary of Electronics Techniques for Millimetre/THz Wave Carriers Generation

The fundamental operating limit for a device technology is defined by the maximum frequency, f_{\max} , at which an electronic device exhibits unity power gain. The widely used silicon integrated technologies such as complementary metal oxide semiconductor (CMOS), bipolar CMOS (Bi-CMOS) and Silicon Germanium (SiGe) operate up to f_{\max} of 300 to 350 GHz owing to their smaller junction breakdown voltage at such high frequencies [55]. The use of III-V materials, with higher bandgap and saturation velocities, can increase the operating frequencies up to 1.5 THz with InP HEMTs (Indium Phosphide High Electron Mobility Transistors) [55]. The f_{\max} values of more than 1 THz have been reported with the InP-DHBTs (double heterojunction bipolar transistor) [56] and InP GaAsSb DHBTs [57]. While such high operating frequency demonstrations are encouraging, this does not guarantee the self-sustaining oscillation required for the generation of stable carriers up to those frequencies. Other parameters such as thermal stability, driving current handling capabilities, noise figure, $1/f$ noise and phase noise are important for the design of such high-frequency synthesizers and voltage controlled oscillators (VCO).

Typically, high-frequency carrier generation is achieved by extracting either a harmonic or mixing component obtained by exploiting the non-linear characteristics of transistors driven by VCOs operating at low frequency [58]. While the power transfer efficiency to a harmonic or mixing component is usually low, however, it allows the generation of carriers beyond the frequency range of VCOs. In [59], a harmonic oscillator is demonstrated for the generation of a 976 GHz carrier by extracting the 8th harmonics of a fundamental LO operating at 122 GHz. A detailed summary of various non-linear phenomena used for harmonics generation and mixing is provided in [58]. Recently, several wireless communication system demonstrations using silicon [60], [61] and InP [62], [63] electronic components operating at 230 to 300 GHz frequencies are reported in the literature achieving data rates ranging from 20 Gbps to 100 Gbps. In most of these demonstrations, single carrier waveforms, for which the requirement of phase noise and other parameters is not that stringent, were transmitted over the link instead of multicarrier signals. Nevertheless, such high-frequency system demonstrations are encouraging and further progress in terms of increasing the signal bandwidth, achieving higher power amplifiers and associated device technologies are needed to achieve Tbps data rates as envisioned with 6G and beyond 6G systems. A summary of emerging graphene-based plasma wave THz devices can be found in [64], [65].

An optical heterodyning technique has emerged as the most promising alternate option for the generation of high frequency mm-wave/THz carriers [52]–[54]. Optical heterodyning facilitates the beating of two laser sources with the desired mm-wave/THz carrier frequency difference on a high speed photodetector – resulting in the generation of the required RF carrier. In the electronic approach, frequency up-conversion operation is performed using a mixer to generate mm-wave/THz carriers, while in the photonics approach higher frequency optical carriers are mixed and frequency down-converted to achieve mm-wave/THz wireless carrier generation.

1.4.2 Optical Heterodyning for Millimetre/THz Wave Carriers Generation

The beating of two optical carriers with the desired frequency spacing on a high speed photodetector results in the generation of a microwave/mm-wave/sub-THz/THz radio carrier [52]. The schematic of a general optical heterodyne concept is shown in Fig. 1.12 with optical carriers obtained from two different

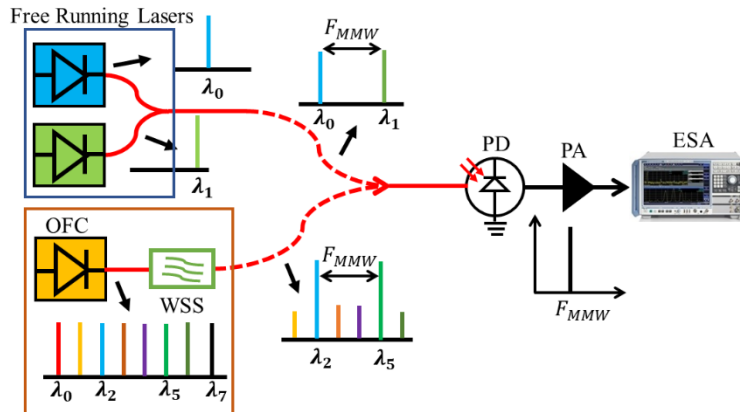


Fig. 1.12 Schematic of an Optical Heterodyning for mm-wave/THz carrier generation with free running lasers and optical frequency comb sources.

types of sources, i.e. free-running lasers and an optical frequency comb source. An OFC source generates multiple optical carriers, which are correlated in frequency and phase, from a single device [54]. The free-running lasers need to be precisely tuneable in order to achieve the exact frequency spacing between the optical carriers, while the free spectral range (FSR) of the OFC source should not be fixed to allow the generation of variable frequencies RF carriers. An additional filtering stage, implemented using a programmable wave shaper (or wavelength selective switch (WSS) as shown in Fig. 1.12), is required to filter out the desired tones from the output of the OFC source.

Mathematically, the magnitude of the electric field of two monochromatic optical carriers can be represented as [1]

$$E_1(t) = E_{01} \exp[j(2\pi f_1 t + \varphi_1(t))] \quad 1.1$$

$$E_2(t) = E_{02} \exp[j(2\pi f_2 t + \varphi_2(t))] \quad 1.2$$

where, E_{01} and E_{02} are the amplitudes, f_1 and f_2 are the frequencies and φ_1 and φ_2 are the phases of the individual optical carriers. In a typical monochromatic laser, the spontaneous emission results in random power and phase fluctuations. The random power fluctuations manifest as a relative intensity noise and the phase fluctuations or noise result in the optical linewidth [1]. The phase noise and linewidth terms convey the same information about the presence of phase/frequency fluctuation in the laser output and are typically used synonymously with each other. For the case of an OFC source, the phase fluctuations of both optical carriers are correlated over a fraction of the coherence length.

When two optical carriers are combined and beat on a high speed photodetector to generate the mm-wave carrier, the PD output current is proportional to the square of the combined signal and is given as

$$\begin{aligned}
 I_{PD}(t) &= RP_{opt} \propto R (E_1(t) + E_2(t)) (E_1(t) + E_2(t))^* \\
 &= R |E_1(t) + E_2(t)|^2 \\
 &= R (E_{01}^2 + E_{02}^2) + 2RE_{01}E_{02} \cos(2\pi(f_2 - f_1)t + (\varphi_2(t) - \varphi_1(t))) \quad 1.3
 \end{aligned}$$

where R is the responsivity of the PD and P_{opt} is the optical power falling on PD. The first term in Eq. 1.3 is the DC component being generated from the individual optical carriers, while the second term represents the generated mm-wave/THz carrier from the mixing of two optical fields. The frequency of the generated carrier is equal to the difference between frequencies of beating optical carriers, i.e. $f_2 - f_1$. Theoretically, any mm-wave or THz frequency can be generated by using the lasers with the desired frequency difference, but the practical limitation arises due to the BW of the photodetector. Higher frequency carriers up to 5 THz have been generated in various lab demonstrations with specially designed high-speed detectors [66]. A summary of various photodetector technologies is provided in chapter 3. The distribution of the generated mm-wave/THz carrier and data signals, to various RRH site antenna units, can be achieved by combining remote optical heterodyning with fronthaul link – especially with the analogue RoF scheme [52], [54].

The random and uncorrelated fluctuations in the lasing frequencies of the free running lasers (majorly due to temperature changes in the gain medium) result in time varying fluctuations in the frequency of generated mm-wave carrier [1]. The phase noise on the generated carrier will be proportional to the sum of the individual laser's phase noise/linewidth. The Gaussian random variable representation of the laser phase noise leads to the addition of variances upon beating [1]. In the case of the use of an OFC source, a fixed spacing between the beating optical carriers results in the generation of a frequency fluctuation-free mm-wave carrier. The phase noise of the generated mm-wave carrier in this case depends on the level of correlation and frequency spacing between the beating optical carriers. The level of correlation between the beating OFC tones reduces with the path length difference between the two beating carriers as they

propagate through the system [67]. Also, the correlation between the comb tones reduces with an increase in the spacing between the tones from the central frequency of the laser [67].

In the wireless communication system, the purity of the carrier in terms of phase noise and frequency fluctuation is very important and both need to be minimal. The frequency fluctuations and phase noise of the generated mm-wave carrier limit the performance of a heterodyne system, particularly for those involving the transport of multicarrier signals typical of mobile communication [54]. For successful system deployment, the frequency fluctuations and phase noise of the generated mm-wave carrier should be much smaller than the subcarrier spacing of the multicarrier signal. It is important to analyse the frequency fluctuations and phase noise of the generated carrier from the use of different types of lasers over an optical heterodyne system and design special solutions/techniques to compensate or cancel their effect on the performance of the system for the successful transmission of mm-wave signals. In the next subsection, the frequency fluctuations and phase noise arising from the use of different types of free-running lasers are analysed. For comparison purposes, the frequency fluctuations and phase noise from the use of a gain-switched laser OFC [54] are also presented.

1.4.3 Frequency Fluctuations and Phase Noise in Optical Heterodyning

In order to study the level of frequency fluctuations and phase noise caused by different types of sources, a mm-wave carrier was generated at 48 GHz frequency over the heterodyne system, shown in Fig. 1.12, using pairs of optical carriers obtained from various free-running sources and a correlated source. Three different pairs of tuneable free-running lasers, i.e. external cavity lasers (ECL), an integrated dual laser module (DLM) and fibre lasers (FL), and an OFC were used separately to obtain the optical carriers for heterodyning. Fig. 1.13 shows the max hold spectrum of the generated 48 GHz carrier captured using an R&S signal and spectrum analyser for the duration of 5 minutes. Results indicate that the RF signal

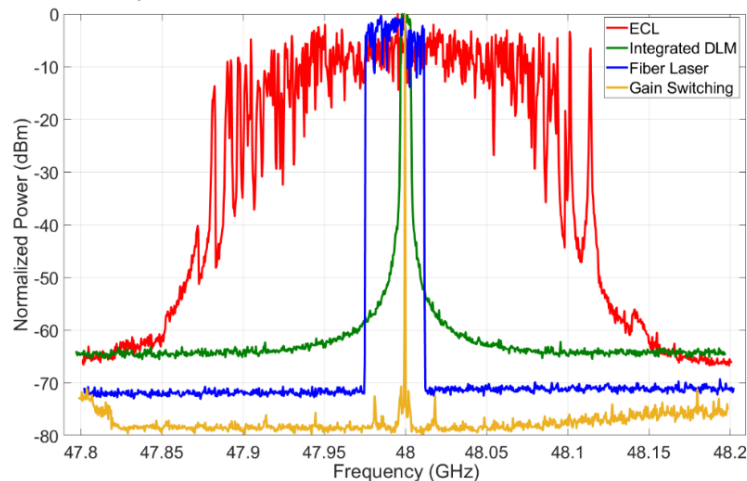


Fig. 1.13 Frequency fluctuations of photo-mixing generated 48 GHz carrier with heterodyning of different types of free-running lasers.

generated using heterodyning of two ECLs exhibits a high level of frequency fluctuation (more than 200 MHz), while employing optical carriers from an integrated dual laser module from LioniX International exhibits [68] less than 10 MHz fluctuation on the generated RF signal; due to the single TEC employed in the integrated device. When employing two fibre lasers from the NKT Photonics the resultant RF beat signal exhibited around 30 MHz of frequency fluctuation. Minimal frequency fluctuation was observed in the case where a GSL OFC source was used, as expected.

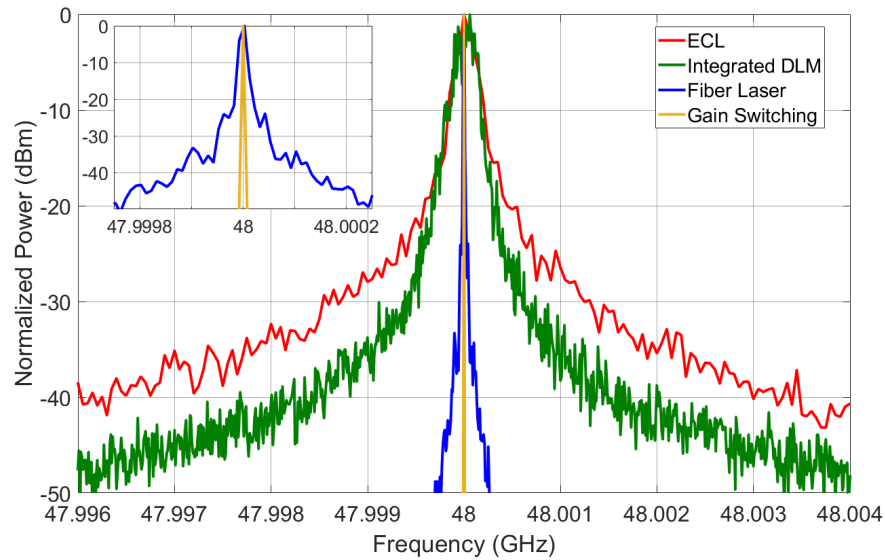


Fig. 1.14 Phase noise of photo-mixing generated 48 GHz carrier with heterodyning of different types of free running lasers.

The linewidth of the generated 48 GHz mm-wave carrier was also observed in order to study the PN arising from heterodyning using the above-mentioned sources. The spectra presented in Fig. 1.14, indicate that the highest phase noise on the carrier generated from heterodyning results from the use of two ECLs. Lower levels of phase noise can be observed in the cases where the integrated DLM and fibre lasers were employed, while the GSL OFC source results in the RF carrier with the minimum phase noise. The RF linewidth of the generated carrier using heterodyning of two independent lasers is the sum of the optical linewidths of the sources employed for heterodyning. In this work, the ECLs had linewidths of ~ 80 kHz and resulted in a mm-wave carrier with ~ 160 kHz linewidth. Similarly, RF linewidth values of ~ 60 kHz and ~ 4 kHz were measured from the beating of 30 kHz and 2 kHz linewidth uncorrelated carriers from DLM and FL, respectively. The beating of ~ 30 MHz optical linewidth correlated optical carriers from the GSL OFC resulted in the cancellation of phase noise, as evident from the narrow RF linewidth, in the order of a few 10s Hz, as seen in Fig. 1.14.

While the maximum optical linewidth from all three free-running lasers described here is less than 100 kHz, the corresponding RF phase noise after optical heterodyning can create significant performance degradation in RF communication systems – especially for the small subcarrier spacing OFDM signals

synonymous with mobile communications. The 5G NR standard has specified the use of OFDM waveforms with subcarrier spacing ranging from as low as 60 kHz to 240 kHz for the mm-wave band data transmission [22]. A previous study [54] has shown that frequency fluctuation-free lasers with less than 900 Hz linewidth would be required in order to achieve the required performance (below the 7% overhead forward error correction (FEC) limit) for 64-QAM data modulated OFDM signals with 60 kHz subcarrier spacing. In addition, the frequency fluctuations of the RF carrier will have a more adverse effect on the signal performance as it will result in the loss of orthogonality; thus, in this case, optical sources with frequency fluctuations well below 60 kHz would be required for distortion-free heterodyne system implementation. Hence, it is necessary to either reduce the frequency fluctuations and phase noise of the mm-wave carrier or compensate for it in some way for successful system implementation.

Traditionally techniques such as optical injection locking [69], optical phase locked loop [70] and optical injection phase-lock loop [71] are used for correlating the frequency and phase fluctuations of the free running lasers to achieve a stable mm-wave/THz carrier generation. However, these techniques increase the electronics and optical complexity of the system – hindering its dense deployment. It is essential to design and investigate more techniques for minimizing the effect of laser frequency and phase fluctuations on the performance of the low subcarrier spacing multicarrier signals such as those provisioned in the 5G standard. Two innovative techniques, i.e., analogue mm-wave receiver [72] and digital signal processing receiver [73], are introduced in chapter 3 of this thesis for compensating the effect of frequency fluctuations and phase noise arising from the use of free running lasers in the heterodyne system.

The use of an OFC source results in the frequency fluctuation-free mm-wave carrier generation upon heterodyning; however, the PN depends on the correlation between the beating optical carriers. The results presented in Fig. 1.14 show a narrow linewidth for the generated mm-wave carrier, however, this was achieved without splitting the two OFC tones into two different paths. For a data signal modulation, on one of the OFC tones (refer to Fig. 1.12), the WSS output is typically split into two paths. The use of an optical modulator and other components, in one of the carrier's paths, leads to a delay between two carrier tones resulting in an increase in the PN. It is essential to analyse the effect of this path length difference induced delay on the PN and eventually on the performance of the low subcarrier spacing multicarrier signals. In chapter 4 of this thesis, an optical heterodyne system is demonstrated with two different types of OFC sources and the effect of phase noise is analysed on the performance of the low subcarrier spacing OFDM signals.

Some of the challenges mentioned in sections 1.3 and 1.4 are listed as the objective of the thesis work.

1.5 Research Objectives

The main objective of this thesis work is to design and analyse efficient optical techniques for supporting the two key aspects of the next generation wireless systems, i.e., mm-wave/THz carrier generation and distribution using heterodyning and optical back-/front-haul networks. The specific research objectives are:

- Analyzing the performance limiting factors of spectrally efficient analogue-RoF fronthaul link and demonstrating its capacity for the transmission of multiple bands of 5G signals.
- Demonstrating an optical heterodyning technique using free running lasers for mm-wave signal generation and designing solutions for mitigating the performance limiting factor, such as frequency fluctuations and phase noise, for efficient system implementation.
- Demonstrating an optical heterodyne technique using an optical frequency comb source for mm-wave signal generation and analyzing the impact of phase noise, arising from the decorrelation between OFC tones, on the performance of low subcarrier spacing multi-carrier signals provisioned in 5G NR standard.
- Demonstrating advanced optical techniques for reducing the complexity of the optical heterodyne system and scaling it for use in high frequency mm-wave/THz bands.

References

- [1] G. P. AGRAWAL, *FIBER-OPTIC COMMUNICATION SYSTEMS*, 5th ed. JOHN WILEY, 2021.
- [2] Rappaport Theodore S., *Wireless Communications Principles and Practice*, Second. Pearson, 2001.
- [3] Sharma P., "Evolution of Mobile Wireless Communication Networks-1G to 5G as well as Future Prospective of Next Generation Communication Network," *International Journal of Computer Science and Mobile Computing*, vol. 2, no. 8, pp. 47–53, Aug. 2013.
- [4] A. Checko *et al.*, "Cloud RAN for Mobile Networks - A Technology Overview," *IEEE Communications Surveys and Tutorials*, vol. 17, no. 1, pp. 405–426, Jan. 2015, doi: 10.1109/COMST.2014.2355255.
- [5] J. Li and J. Chen, "Passive Optical Network Based Mobile Backhaul Enabling Ultra-Low Latency for Communications Among Base Stations," *Journal of Optical Communications and Networking*, Vol. 9, Issue 10, pp. 855–863, vol. 9, no. 10, pp. 855–863, Oct. 2017, doi: 10.1364/JOCN.9.000855.
- [6] P. Assimakopoulos, "Optical Fronthaul Options for Meeting 5G Requirements," *International Conference on Transparent Optical Networks*, vol. 2018-July, Sep. 2018, doi: 10.1109/ICTON.2018.8473762.
- [7] Cisco, "Cisco Annual Internet Report (2018–2023)," 2020.
- [8] International Telecommunication Union, "Measuring digital development, Facts and figures 2021," *ITU Publications*, 2021.
- [9] Data Reportal, We are Social, and Hootsuite, "Digital 2022 Global Overview Report," 2022.
- [10] United Nations, "Digital Economy Report 2021," 2021.
- [11] Ericsson, "Ericsson Mobility Report," Nov. 2021.
- [12] Damian Anzaldo, "BACKHAUL ALTERNATIVES FOR 4G/5G HETNET BASE STATIONS PART 1 - EQUIPMENT TRENDS AND SOLUTION TOOLBOX," APPLICATION NOTE 6544, Aug. 2018.

- [13] C. Lim *et al.*, “Fiber-wireless networks and subsystem technologies,” *Journal of Lightwave Technology*, vol. 28, no. 4, pp. 390–405, Feb. 2010, doi: 10.1109/JLT.2009.2031423.
- [14] C. Lim, Y. Tian, C. Ranaweera, T. A. Nirmalathas, E. Wong, and K. L. Lee, “Evolution of Radio-Over-Fiber Technology,” *Journal of Lightwave Technology*, vol. 37, no. 6, pp. 1647–1656, Mar. 2019, doi: 10.1109/JLT.2018.2876722.
- [15] ITU-R, “Recommendation ITU-R P.676-11: Attenuation by atmospheric gases,” 2016.
- [16] C. Ranaweera, J. Kua, I. Dias, E. Wong, C. Lim, and A. Nirmalathas, “4G to 6G: Disruptions and drivers for optical access [Invited],” *Journal of Optical Communications and Networking*, vol. 14, no. 2, pp. A143–A153, Feb. 2022, doi: 10.1364/JOCN.440798.
- [17] Erik. Dahlman, *3G evolution: HSPA and LTE for mobile broadband*, 2nd ed. Elsevier Academic Press, 2007.
- [18] Christopher Cox, *An Introduction to LTE: LTE, LTE-Advanced, SAE, VoLTE and 4G Mobile*, 2nd ed. John Wiley & Sons Ltd, 2014.
- [19] Speedtest Global Index, “Global Median Speeds June 2022,” Jun. 2022.
- [20] A. de La Oliva, J. A. Hernandez, D. Larrabeiti, and A. Azcorra, “An overview of the CPRI specification and its application to C-RAN-based LTE scenarios,” *IEEE Communications Magazine*, vol. 54, no. 2, pp. 152–159, Feb. 2016, doi: 10.1109/MCOM.2016.7402275.
- [21] ETSI - The European Standards Organization, “5G Technology Specifications,” <https://www.etsi.org/technologies/5G>, 2021.
- [22] 3GPP, “5G Technical specification: NR and NG-RAN Overall Description,” 2020.
- [23] J. G. Andrews *et al.*, “What will 5G be?,” *IEEE Journal on Selected Areas in Communications*, vol. 32, no. 6, pp. 1065–1082, 2014, doi: 10.1109/JSAC.2014.2328098.
- [24] Javier Campos, “Understanding the 5G NR Physical Layer,” Nov. 2017.
- [25] T. S. Rappaport *et al.*, “Wireless Communications and Applications Above 100 GHz: Opportunities and Challenges for 6G and Beyond,” *IEEE Access*, vol. 7, pp. 78729–78757, 2019, doi: 10.1109/ACCESS.2019.2921522.
- [26] M. M. Ahamed and S. Faruque, “5G Network Coverage Planning and Analysis of the Deployment Challenges,” *Sensors 2021, Vol. 21, Page 6608*, vol. 21, no. 19, p. 6608, Oct. 2021, doi: 10.3390/S21196608.
- [27] ITU-R, “Nomenclature of the frequency and wavelength bands used in telecommunications,” 2015.
- [28] IEEE Radar Systems Panel, “IEEE Standard 521: Designations for Radar-Frequency Bands 2019,” IEEE, 2020.
- [29] A. D. Panagopoulos, P.-D. M. Arapoglou, and P. G. Cottis, “Satellite communications at KU, KA, and V bands: Propagation impairments and mitigation techniques,” *IEEE Communications Surveys & Tutorials*, vol. 6, no. 3, pp. 2–14, Dec. 2009, doi: 10.1109/COMST.2004.5342290.
- [30] 3GPP Technical Specification Group Radio Access Network, “Study on Scenarios and Requirements for Next Generation Access Technologies,” 2018.
- [31] B. Schulz, “802.11ad - WLAN at 60 GHz a technology introduction,” 2017.
- [32] Y. Ghasempour, C. R. C. M. da Silva, C. Cordeiro, and E. W. Knightly, “IEEE 802.11ay: Next-Generation 60 GHz Communication for 100 Gb/s Wi-Fi,” *IEEE Communications Magazine*, vol. 55, no. 12, pp. 186–192, Dec. 2017, doi: 10.1109/MCOM.2017.1700393.
- [33] Ericsson, “High-capacity Microwave backhaul for all sites,” 2022.
- [34] Edstam J., Hansryd J., Carpenter S., Emanuelsson T., Li Y., and Zirath H., “Microwave Backhaul Evolution- Reaching Beyond 100 GHz,” *ERICSSON Technology Review, Vol. 2*, Feb. 2017.
- [35] H. Griffiths *et al.*, “Radar spectrum engineering and management: Technical and regulatory issues,” *Proceedings of the IEEE*, vol. 103, no. 1, pp. 85–102, Jan. 2015, doi: 10.1109/JPROC.2014.2365517.
- [36] C. Han, Y. Wu, Z. Chen, and X. Wang, “Terahertz Communications (TeraCom): Challenges and Impact on 6G Wireless Systems,” Dec. 2019, doi: 10.48550/arxiv.1912.06040.

- [37] IEEE Computer Society, “802.15.3d IEEE Standard for High Data Rate Wireless Multi-Media Networks--Amendment 2 : 100 Gb/s Wireless Switched Point-to-Point Physical Layer.,” IEEE, 2017.
- [38] J. S. Wey and J. Zhang, “Passive Optical Networks for 5G Transport: Technology and Standards,” *Journal of Lightwave Technology*, vol. 37, no. 12, pp. 2830–2837, Jun. 2019, doi: 10.1109/JLT.2018.2856828.
- [39] ITU-T, “5G wireless fronthaul requirements in a passive optical network context,” Sep. 2020.
- [40] J. E. Mitchell, “Integrated wireless backhaul over optical access networks,” *Journal of Lightwave Technology*, vol. 32, no. 20, pp. 3373–3382, Oct. 2014, doi: 10.1109/JLT.2014.2321774.
- [41] T. Horvath, P. Munster, V. Oujezsky, and N. H. Bao, “Passive Optical Networks Progress: A Tutorial,” *Electronics 2020, Vol. 9, Page 1081*, vol. 9, no. 7, p. 1081, Jul. 2020, doi: 10.3390/ELECTRONICS9071081.
- [42] K. Borzycki, “FTTx Access Networks: Technical Developments and Standardization,” *Broadband Communications Networks - Recent Advances and Lessons from Practice*, Dec. 2017, doi: 10.5772/INTECHOPEN.71785.
- [43] A. Delmade, D. Venkitesh, and R. D. Koilpillai, “Performance comparison of optical fronthauling techniques for centralized radio access network,” *2016 IEEE International Conference on Advanced Networks and Telecommunications Systems, ANTS 2016*, Jun. 2017, doi: 10.1109/ANTS.2016.7947836.
- [44] CPRI Consortium, “Common Public Radio Interface (CPRI): Interface Specification V 7.0,” Oct. 2015.
- [45] OBSAI Consortium, “Open Base Station Architecture Initiative BTS System Reference Document Version 2.0.,” 2006.
- [46] B. Guo, W. Cao, A. Tao, and D. Samardzija, “LTE/LTE-A signal compression on the CPRI interface,” *Bell Labs Tech J*, vol. 18, no. 2, pp. 117–133, Sep. 2013, doi: 10.1002/BLTJ.21608.
- [47] D. Dass, A. Delmade, L. Barry, C. G. H. Roeloffzen, D. Geuzebroek, and C. Browning, “Wavelength & mm-Wave Flexible Converged Optical Fronthaul With a Low Noise Si-Based Integrated Dual Laser Source,” *Journal of Lightwave Technology*, vol. 40, no. 10, pp. 3307–3315, May 2022, doi: 10.1109/JLT.2022.3169446.
- [48] S. Noor, P. Assimakopoulos, and N. J. Gomes, “A Flexible Subcarrier Multiplexing System with Analog Transport and Digital Processing for 5G (and Beyond) Fronthaul,” *Journal of Lightwave Technology*, vol. 37, no. 14, pp. 3689–3700, Jul. 2019, doi: 10.1109/JLT.2019.2918215.
- [49] H. Xin, H. He, K. Zhang, S. B. Hussain, and W. Hu, “Flexible Baseband-Unit Aggregation Enabled by Reconfigurable Multi-IF over WDM Fronthaul,” *IEEE Photonics J*, vol. 10, no. 1, Feb. 2018, doi: 10.1109/JPHOT.2017.2780090.
- [50] S. H. Cho, H. S. Chung, C. Han, S. Lee, and J. H. Lee, “Experimental Demonstrations of Next Generation Cost-Effective Mobile Fronthaul with IFoF technique,” *Optical Fiber Communication Conference (2015), paper M2J.5*, vol. 2015-June, p. M2J.5, Mar. 2015, doi: 10.1364/OFC.2015.M2J.5.
- [51] E. Ruggeri *et al.*, “A 5G Fiber Wireless 4Gb/s WDM Fronthaul for Flexible 360° Coverage in V-Band massive MIMO Small Cells,” *Journal of Lightwave Technology*, vol. 39, no. 4, pp. 1081–1088, Feb. 2021, doi: 10.1109/JLT.2020.3029608.
- [52] J. Beas, G. Castanon, I. Aldaya, A. Aragon-Zavala, and G. Campuzano, “Millimeter-wave frequency radio over fiber systems: A survey,” *IEEE Communications Surveys and Tutorials*, vol. 15, no. 4, pp. 1593–1619, 2013, doi: 10.1109/SURV.2013.013013.00135.
- [53] T. Nagatsuma, M. Fujita, and L. Yi, “Enabling Device Technologies for Photonics-Assisted Millimeter and Terahertz Wave Applications,” *Technical Digest - International Electron Devices Meeting, IEDM*, vol. 2021-December, pp. 11.5.1-11.5.4, 2021, doi: 10.1109/IEDM19574.2021.9720521.
- [54] C. Browning *et al.*, “Gain-switched optical frequency combs for future mobile radio-over-fiber millimeter-wave systems,” *Journal of Lightwave Technology*, vol. 36, no. 19, pp. 4602–4610, Oct. 2018, doi: 10.1109/JLT.2018.2841365.
- [55] K. Sengupta, T. Nagatsuma, and D. M. Mittleman, “Terahertz integrated electronic and hybrid electronic–photonic systems,” *Nature Electronics 2018 1:12*, vol. 1, no. 12, pp. 622–635, Dec. 2018, doi: 10.1038/s41928-018-0173-2.
- [56] X. Mei *et al.*, “First Demonstration of Amplification at 1 THz Using 25-nm InP High Electron Mobility Transistor Process,” *IEEE Electron Device Letters*, vol. 36, no. 4, pp. 327–329, Apr. 2015, doi: 10.1109/LED.2015.2407193.
- [57] M. Alexandrova, R. Flueckiger, R. Lovblom, O. Ostinelli, and C. R. Bolognesi, “GaAsSb-based DHBTs with a reduced base access distance and fT fMAX 503/780 GHz,” *IEEE Electron Device Letters*, vol. 35, no. 12, pp. 1218–1220, Dec. 2014, doi: 10.1109/LED.2014.2364622.

- [58] H. Aghasi, S. M. H. Naghavi, M. Tavakoli Taba, M. A. Aseeri, A. Cathelin, and E. Afshari, "Terahertz electronics: Application of wave propagation and nonlinear processes," *Appl Phys Rev*, vol. 7, no. 2, p. 021302, Apr. 2020, doi: 10.1063/1.5129403.
- [59] A. Mostajeran and E. Afshari, "An ultra-wideband harmonic radiator with a tuning range of 62GHz (28.3%) at 220GHz," *Digest of Papers - IEEE Radio Frequency Integrated Circuits Symposium*, pp. 164–167, Jul. 2017, doi: 10.1109/RFIC.2017.7969043.
- [60] S. Hara *et al.*, "300-GHz CMOS transceiver for terahertz wireless communication," *Asia-Pacific Microwave Conference Proceedings, APMC*, vol. 2018–November, pp. 429–431, Jan. 2019, doi: 10.23919/APMC.2018.8617468.
- [61] P. Rodriguez-Vazquez, J. Grzyb, B. Heinemann, and U. R. Pfeiffer, "A 16-QAM 100-Gb/s 1-M Wireless Link with an EVM of 17% at 230 GHz in an SiGe Technology," *IEEE Microwave and Wireless Components Letters*, vol. 29, no. 4, pp. 297–299, Apr. 2019, doi: 10.1109/LMWC.2019.2899487.
- [62] F. Boes *et al.*, "Ultra-broadband MMIC-based wireless link at 240 GHz enabled by 64GS/s DAC," *9th International Conference on Infrared, Millimeter, and Terahertz Waves (IRMMW-THz 2014), Tucson, Arizona, USA, 14 - 19 September 2014*, p. 1, Nov. 2014, doi: 10.1109/IRMMW-THZ.2014.6956202.
- [63] H. Hamada *et al.*, "300-GHz. 100-Gb/s InP-HEMT Wireless Transceiver Using a 300-GHz Fundamental Mixer," *IEEE MTT-S International Microwave Symposium Digest*, vol. 2018–June, pp. 1480–1483, Aug. 2018, doi: 10.1109/MWSYM.2018.8439850.
- [64] V. Ryzhii, T. Otsuji, and M. Shur, "Graphene based plasma-wave devices for terahertz applications," *Appl Phys Lett*, vol. 116, no. 14, p. 140501, Apr. 2020, doi: 10.1063/1.5140712.
- [65] A. Singh, M. Andreello, N. Thawdar, and J. M. Jornet, "Design and Operation of a Graphene-Based Plasmonic Nano-Antenna Array for Communication in the Terahertz Band," *IEEE Journal on Selected Areas in Communications*, vol. 38, no. 9, pp. 2104–2117, Sep. 2020, doi: 10.1109/JSAC.2020.3000881.
- [66] K. A. McIntosh, E. R. Brown, K. B. Nichols, O. B. McMahon, W. F. Dinatale, and T. M. Lyszczarz, "Terahertz photomixing with diode lasers in low-temperature-grown GaAs," *Appl Phys Lett*, vol. 67, no. 26, p. 3844, Aug. 1998, doi: 10.1063/1.115292.
- [67] T. Shao *et al.*, "Phase Noise Investigation of multicarrier Sub-THz Wireless Transmission System Based on an Injection-Locked Gain-Switched Laser," *IEEE Trans Terahertz Sci Technol*, vol. 5, no. 4, pp. 590–597, Jul. 2015, doi: 10.1109/TTHZ.2015.2418996.
- [68] R. Guzman *et al.*, "Widely Tunable RF Signal Generation Using an InP/Si3N4 Hybrid Integrated Dual-Wavelength Optical Heterodyne Source," *Journal of Lightwave Technology*, 2021, doi: 10.1109/JLT.2021.3078508.
- [69] K. Balakier *et al.*, "Optical injection locking of monolithically integrated photonic source for generation of high purity signals above 100 GHz," *Optics Express, Vol. 22, Issue 24, pp. 29404-29412*, vol. 22, no. 24, pp. 29404–29412, Dec. 2014, doi: 10.1364/OE.22.029404.
- [70] K. Balakier, L. Ponnampalam, M. J. Fice, C. C. Renaud, and A. J. Seeds, "Integrated Semiconductor Laser Optical Phase Lock Loops," *IEEE Journal of Selected Topics in Quantum Electronics*, vol. 24, no. 1, Jan. 2018, doi: 10.1109/JSTQE.2017.2711581.
- [71] L. A. Johansson and A. J. Seeds, "Millimeter-wave modulated optical signal generation with high spectral purity and wide-locking bandwidth using a fiber-integrated optical injection phase-lock loop," *IEEE Photonics Technology Letters*, vol. 12, no. 6, pp. 690–692, Jun. 2000, doi: 10.1109/68.849086.
- [72] D. Dass, S. O'Duill, A. Delmade, and C. Browning, "Analysis of Phase Noise in a Hybrid Photonic/Millimetre-Wave System for Single and Multi-Carrier Radio Applications," *Applied Sciences 2020, Vol. 10, Page 5800*, vol. 10, no. 17, p. 5800, Aug. 2020, doi: 10.3390/APP10175800.
- [73] A. Delmade, C. Browning, A. Farhang, R. D. Koilpillai, D. Venkitesh, and L. P. Barry, "OFDM Baud Rate Limitations in an Optical Heterodyne Analog Fronthaul Link using Unlocked Fibre Lasers," *2019 IEEE International Topical Meeting on Microwave Photonics, MWP 2019*, Oct. 2019, doi: 10.1109/MWP.2019.8892190.

2. Analogue Radio-over-Fibre for Fronthauling of 5G Signals

The centralized radio access network advocates for the functional split of a traditional base station and simplifies the antenna site architecture by moving the baseband processing to a centralized location [1]. The optical x-haul link connecting the central unit (or centralized baseband unit of 4G) to the distribution unit and onwards to the remote unit (or remote radio head for 4G) antenna site needs to be spectrally and cost efficient as mentioned in the chapter 1. The RAN signal processing functional split and possible positions of DU, either at the same location as CU or RU or as a separate unit along the link, result in different line rates and RAN signal processing requirements [2]. In order to deploy a cost-efficient system, it is essential to simultaneously minimize the line rate over an optical fronthaul link and avoid the DSP processing at RU/RRH – especially for the mm-wave 5G and 6G systems with the dense deployment of cell sites. The co-hosting of CU and DU at a central office and connecting it to remote antenna units with an optical fibre fronthaul link provides a simple architecture. The line rate depends on the nature of the signal being transported over such a fronthaul link. The wireless signals can be modulated at the baseband or intermediate or wireless radio frequencies with respect to the optical carrier [3]. Also, the signals can be transmitted in the wireless channel compatible analogue or modified digital format over the optical fronthaul link leading to various implementation possibilities [3]. The choice of a fronthaul transmission scheme should aid the centralization of resources while facilitating the scalability for future expansion.

In this chapter, various possibilities for the optical fronthaul link implementation are discussed with a major focus on analogue RoF for the transmission of 5G new radio compatible signals. In section 2.2, the various optoelectronic and optical components used in the spectrally efficient analogue intermediate frequency over fibre fronthaul link are discussed along with the commonly used orthogonal frequency division multiplexed multicarrier waveform. The capacity of the directly modulated AIFoF link is investigated experimentally, in section 2.3, for the transmission of multiple 201 MHz bandwidth 5G NR compatible universally filtered orthogonal frequency division multiplexed signals over a 25 km optical fibre. The permissible power difference between signal bands is also analysed in section 2.4 to emulate the uplink transmission scenario.

2.1 Fronthaul Possibilities

The distribution of wireless signals over optical fibre, to take the advantage of its low loss and broadband bandwidth property, has been a topic of interest for more than three decades. A subcarrier multiplexing (SCM) radio-over-fibre link based four-channel cordless telephony was demonstrated in 1990 [4]. The subsequent demonstrations used similar technology for delivering services for CATV [5], canister

transceivers and mobile telephony [6]. The radio frequency agnostic propagation loss offered by optical fibre led to its use for the transmission of millimetre wave frequency signals as well [7], [8]. In all these early demonstrations, the wireless signals were transmitted over the radio-over-fibre link in their original analogue form. The underdeveloped technologies, to overcome the impairments in the analogue optical links, and insufficient infrastructure at that time limited the reach of such systems. Meanwhile, the technological advances in various optoelectronics and optical components, digital signal processing techniques and optical transmission system, in general, has led to the widespread deployment of digital optical communication links, where binary or multi-level data signal is transmitted over thousands of kilometre of optical fibre [9]. Currently, digital data transmission is used in almost all systems ranging from long-distance subsea systems [10] to short-distance passive optical networks [11] and datacentre interconnects [12].

Digital data transmission is also adopted for carrying the backhaul and fronthaul data from the CO and C-BBU sites, respectively, to the remote antenna sites as mentioned in the first chapter. In various digital fronthaul standards, such as CPRI and OBSAI mentioned in chapter 1, the wireless standard specific waveforms (OFDM for 4G and 5G) need to be converted into 1's and 0's for transmission over the link [13]. The enormous line/data rate expansion, due to the quantization of the complex waveform (I-Q samples of OFDM), hindered the deployment of CPRI optical fronthaul link for the transport of the 4G and 5G signals [14]. The concurrent advances with RAN functional split options and the position of the CU and DU units led to various deployment scenarios as mentioned in the introduction chapter. While the RAN functional split is introduced to maintain the digital signal transmission over the fibre link, however, it leads to some signal processing functionalities being moved to the RU/RRH site at the expense of its increased remote site's complexity [2], [13]. It is necessary to consider the other fronthaul possibilities, involving the

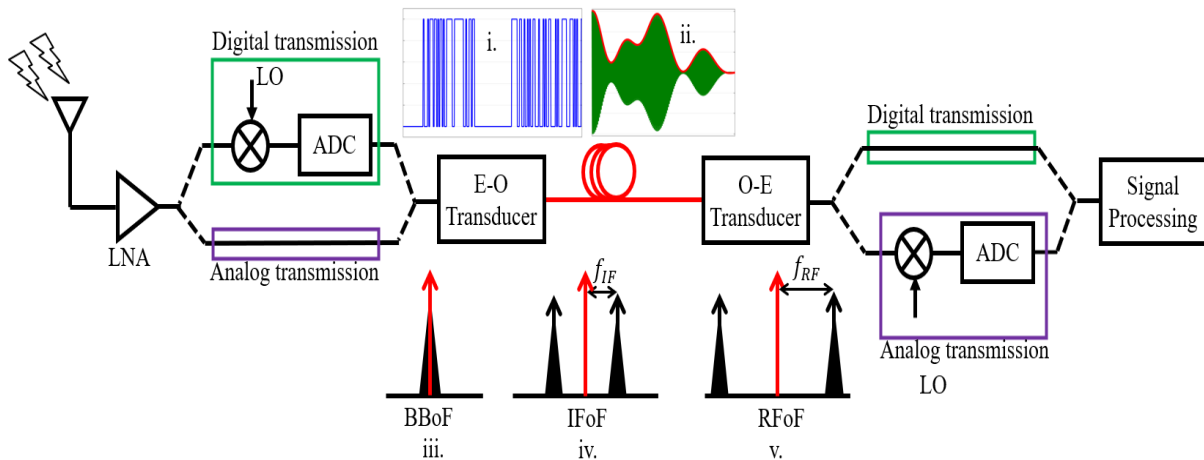


Fig. 2.1 Schematic of a general fronthaul link with (i) digital and (ii) analogue data modulation at (iii) baseband, (iv) intermediate and (v) radio frequency with respect to the optical carrier.

transmission of analogue signals at different frequencies with respect to the optical carrier, for the cost-efficient dense deployment of remote antenna sites.

Fig. 2.1 shows a general schematic of the optical fronthaul link, between the remote antenna unit and centralized BBU, with different transmission possibilities in terms of frequency (i.e. baseband, intermediate or radio frequency) and nature (i.e. analogue or digital) of the signal [3], [15]. This system maintains the general architecture of C-RAN, consisting of a co-hosted CU and DU (at the C-BBU site) with a fronthaul link connecting to the antenna RU/RRH site, and is considered for this work. The link shown in Fig. 2.1 demonstrates an uplink transmission scenario where a remote antenna unit receives the wireless signal at a standard specified radio frequency. The frequency of the carrier can be anywhere between 700 MHz to 6 GHz (sub-6 GHz systems only) in accordance with various wireless transmission standards. For 5G and 6G systems, the carrier frequency will be in the mm-wave/THz bands. The antenna captured RF signal needs to be sent to the C-BBU site for decoding and further processing – requiring both the frequency down-conversion and digitization operations to be performed on it. The choice of location for frequency down-conversion (using an RF mixer and external LO) and digitization (using ADC) operations decides the nature of the signal transmitted over the fronthaul link and the complexity of the remote antenna unit [15], [16].

2.1.1 Digital RoF Fronthaul Possibilities

In the case of D-RoF, the antenna captured signal is transmitted over the fronthaul link in the digital form - requiring ADC at the remote antenna site. The RF signal can be quantized directly or after frequency down-conversion to either IF or BB band leading to three different fronthaul possibilities namely digitized radio frequency over fibre (DRFoF), digitized intermediate frequency over fibre (DIFoF), and digitized baseband over fibre (DBBoF) [17]–[19]. The digitization of the baseband signal requires low sampling rate ADCs, while high and extremely high sampling rate ADCs and signal processing capabilities will be required for the DIFoF and DRFoF schemes respectively. It is not feasible to implement the quantization of RF signals directly, with the DRFoF scheme, as it requires high bandwidth components such as ADC, DAC, optical modulator and photodetector and leads to extremely high line rate requirements [19]. In the DIFoF, the required sampling rate of the ADC/DAC depends on the IF carrier frequency. The minimal value of the IF carrier that can be used should be slightly higher than the bandwidth of the antenna captured RF signal. A frequency down-conversion from the RF to IF maintains the real nature of the signal and enables the implementation of intensity modulation direct detection (IMDD) optical link without any signal processing requirements at the remote antenna site [3], [18], [19].

In the DBBoF scheme, the direct frequency down-conversion of RF signal to baseband results in a complex I-Q signal - which requires a phase modulation and coherent detection optical link deployment with increased complexity. In order to avoid this, a serialization technique is used to convert the complex

baseband signal into the real signal – enabling the use of a simple intensity modulation direct detection link for DBBoF fronthaul [14], [19]. Such serialization increases the line rate by a factor of two and requires a signal processing unit at the remote antenna site [14]. The serialized IQ samples are quantized and the generated 1's and 0's are transmitted over the fronthaul link. The CPRI standard, discussed in section 1.3.3 in chapter 1, also uses the DBBoF scheme for fronthaul link implementation. The scaling of bandwidth and signalling rate, over the fronthaul link, is proportional to the quantizer's resolution and the number of simultaneously transmitted signals [14]. A digital-to-analogue converter will be also required at the RRH site to convert the 1's and 0's into I & Q samples required for the downlink transmission to mobile units.

In our previous simulation work [19], the performance of DBBoF and DIFoF fronthauling schemes is analysed in terms of line rate/occupied signal bandwidth, received optical power and signal-to-noise ratio requirement for achieving below forward error correction limit performance for the transmission of 20 MHz bandwidth 4G LTE OFDM signals.

2.1.2 Analogue RoF Fronthaul Possibilities

In the case of the analogue RoF scheme, the antenna received RF signal is transported over the optical link in the original analogue form and then digitized at the C-BBU site for processing as shown in the purple-coloured path in Fig. 2.1. The analogue RF signal can be directly modulated on the optical carrier (using electric-to-optical (EO) transducer) or after down-conversion to the intermediate or baseband frequency leading to three different fronthaul schemes namely analogue radio frequency signal over fibre (ARFoF – Fig. 2.1(v)), analogue intermediate frequency signal over fibre (Fig. 2.1(iv)) and analogue baseband signal over fibre (ABBoF – Fig. 2.1(iii)) [3], [19]. In the case of ABBoF, the antenna captured RF signal is first frequency down-converted to baseband I-Q samples – requiring the use of optical phase modulation and coherent detection techniques for link implementation. The use of the coherent link for the transmission of small bandwidth (maximum 400 MHz for 5G) signals over short distances results in cost-inefficient system deployment. A simple IMDD link can be used for the implementation of both AIFoF and ARFoF fronthauling as they involve the intensity modulation of real signals. The photo-detected IF/RF signal, after transmission over the AIFoF/ARFoF link, is first frequency down-converted to the baseband and then digitized using ADC at the C-BBU site [3], [19].

As the wireless signals are transmitted in their original or frequency translated analogue form, over the ARFoF and AIFoF link respectively, their bandwidth remains the same as that of wireless RF signal (shown in the inset (ii) of Fig. 2.1) – leading to a spectrally efficient fronthaul implementation [19]. Also, these analogue links provide transparency for the transmission of different technology wireless signals with different bandwidths and signalling rates. The multiplexing of different signals, for transmission over the same fronthaul link, can be easily implemented by transmitting them at different IF/RF carrier frequencies.

The absence of the high speed ADC and DAC at the RRH antenna site reduces its power consumption and footprint. These advantages come at the cost of increased distortions and limited dynamic range - eventually reducing the reach of ARFoF and AIFoF links compared to digital counterparts [3], [15].

The bandwidth of optoelectronic and electronic components in the ARFoF link depends on the frequency of the wireless carrier and it increases with an increase in the carrier frequency. Even though the bandwidth of signals to be transported over the ARFoF fronthaul link is small (50 to 400 MHz - for 5G), the carrier frequency and in turn the bandwidth of various system components can be as high as 52 GHz for 5G and more than 100 GHz for 6G [20]– resulting in increased operational cost. Also, the effect of power fading introduced by fibre chromatic dispersion increases with an increase in the carrier frequency – leading to performance degradation [21]. In the case of the most commonly used MIMO antenna unit RRH site, the multiple antennas transmit a similar signal to users with some control information modifications. It is necessary to transmit these signals at different RF frequencies over the fronthaul network in order to avoid interference. This means a radio frequency correction stage will be required at the antenna site [19]. Even though the spectral efficiency of the wireless signal is preserved over the ARFoF link, these disadvantages hinder its deployment for carrying the signals between the remote antenna and C-BBU sites.

The transmission of signals at the intermediate frequency, instead of wireless radio frequency, over the AIFoF fronthaul link leads to the use of small bandwidth optoelectronic and electronic components while reducing the effect of fibre chromatic dispersion. It also provides the necessary flexibility for transporting the MIMO configuration signals over the fronthaul link at the expense of the need for a frequency up/down-conversion stage at the remote antenna site. The AIFoF link provides a simple, flexible and scalable solution for carrying the 5G signals between the C-BBU and remote RRH antenna site [15]. Various experiments [22]–[25] have demonstrated the feasibility of AIFoF fronthaul supporting the transmission of multiple signal bands over the same link. In the remainder of this chapter the analogue-IFoF technique is explored for providing fronthaul services for 5G systems. It is necessary to analyse the effect of various system parameters on the performance of the AIFoF link for the transmission of multiple 5G signals. Various components of the AIFoF fronthaul link are discussed in the next section.

2.2 Analogue Intermediate Frequency over Fibre Fronthauling and Components

In AIFoF fronthauling, the complex baseband signal is mixed with an intermediate frequency carrier at the C-BBU, as shown in Fig. 2.2, and transported over the intensity modulation direct detection optical link to the RRH antenna site. The IMDD links, in which the information is modulated on the intensity of the light [9], are a natural choice for the short-haul optical access links due to their low complexity and implementation costs. The I-Q mixing with an IF carrier converts the complex signal into the real one, which is the necessary condition for intensity modulation. This IQ mixing can be done either digitally in

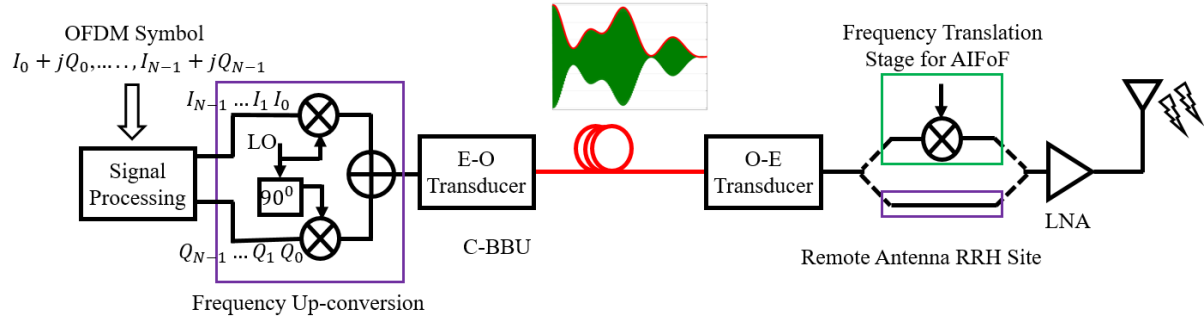


Fig. 2.2 Architecture of the ARFoF fronthaul link with data transmission between C-BBU and RRH site.

data processing software like MATLAB or electronically using an external local oscillator and electrical mixer. In the case of digital IQ mixing, the offline generated samples of the IF signals are loaded into DAC and then fed to an electric-to-optical conversion stage. The optically modulated signal, using either direct or external modulation at the C-BBU site, is sent to the remote antenna site over an optical fibre. The photo-detected IF signal can be transmitted to the end user after frequency translation as shown by the green-coloured box path in Fig. 2.2. In the case of uplink transmission, the antenna captured signal is first frequency down-converted to the IF band at the remote site and then transmitted to the C-BBU over fibre link. There is no need for a signal processing unit or DAC/ADC at the antenna site for the AIFoF scheme – providing a simple remote site architecture.

The choice of the IF carrier frequency needs to be made by considering the frequency response of the available components and the number of simultaneously transmitted signals over the link. The performance of the signal degrades over the AIFoF fronthaul link due to impairments introduced by E-O conversion, fibre transmission and O-E conversion processes [3]. The details of these AIFoF fronthaul link components along with the OFDM waveform are discussed in the next subsections.

2.2.1 Signals: Single Carrier and Multicarrier

The AIFoF fronthaul link provides transparency for the transmission of different generations of signals with variable modulation format and signalling rate. Typically single carrier or multicarrier waveforms are used for data transmission to the end users in different wireless standards [26]. In the case of single carrier waveforms, high baud rate wide bandwidth (50 to 400 Mbaud for 5G) digital signals such as on-off keying, M-ary quadrature phase shift keying (QPSK) or M-ary quadrature amplitude modulation are transmitted over the wireless channel after mixing with the RF carrier [26]. A representative spectrum of the single carrier signal is shown in Fig. 2.3(i) with the red bar corresponding to a low signal-to-noise ratio spectrum region. It is difficult to achieve a uniform and high SNR over the entire signal spectrum due to the frequency selective fading over the wireless channels [26]. In order to avoid such a scenario, the multicarrier waveforms divide the wideband signal into multiple low baud rate subcarriers and variable modulation

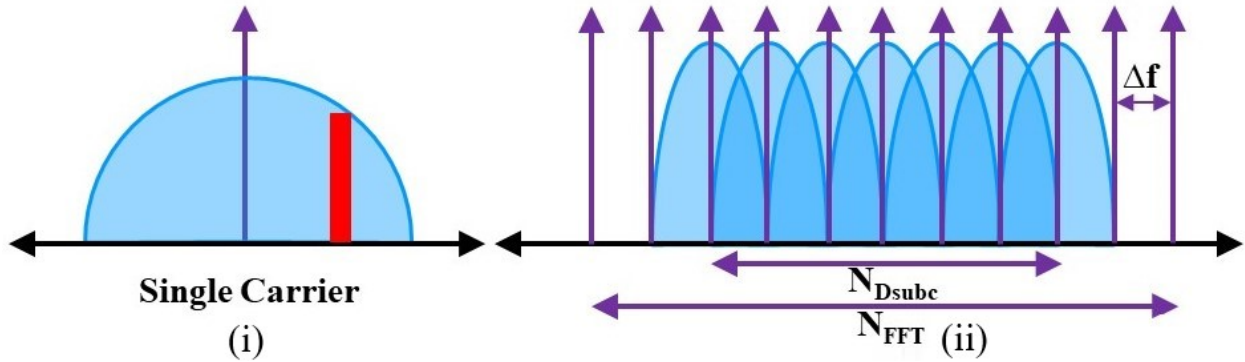


Fig. 2.3 Spectral representation of single carrier and multicarrier baseband signals.

format digital data can be modulated on each of these subcarriers [27] as shown in the spectral representation in Fig. 2.3(ii). Lower order modulation format data, for which the SNR requirements are not stringent, can be modulated on a low SNR subcarrier [27]. As mentioned in the first chapter, the 4G and 5G cellular standards have provisioned the use of OFDM multicarrier waveforms for data transmission to the end users. The higher mm-wave and THz frequency 6G system might adopt the use of both single carrier and multicarrier waveforms for data transmission to end users [20]. The details of the most commonly used OFDM waveform are provided in the next subsection.

Orthogonal Frequency Division Multiplexing

OFDM is a multi-carrier modulation technique in which wideband data is transmitted on the number of low data rate orthogonal overlapping sub-carriers as shown in Fig. 2.3(ii). A block diagram of the baseband OFDM transceiver is shown in Fig. 2.4. Initially, the serial input data (usually QPSK or M-QAM symbols) is divided into multiple parallel data streams and then shifted to the orthogonal frequencies [28] as shown in the figure. The data modulation and multiplexing operation can be performed by the Inverse Fast Fourier Transform (IFFT). IFFT multiples the incoming parallel data with orthogonal frequency sinusoids (subcarriers) and then add them to get one OFDM symbol [28]. Each IFFT operation results in one OFDM symbol and a number of such symbols are transmitted serially.

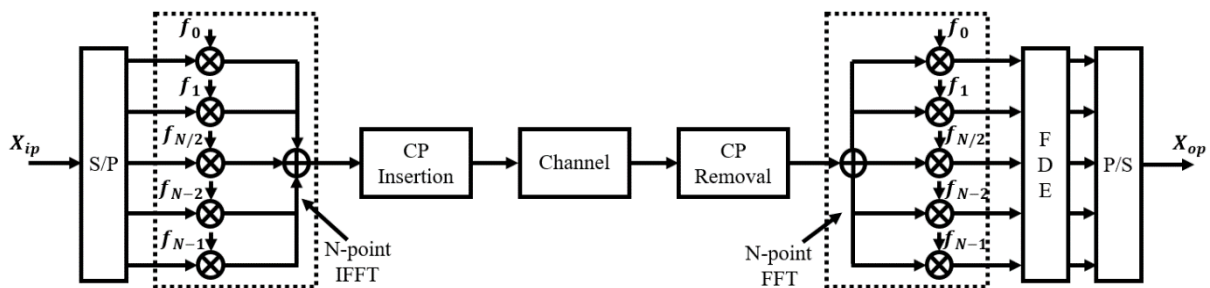


Fig. 2.4 Block diagram of baseband OFDM transceiver.

Mathematically the IFFT operation is represented as [28]

$$x_m = \frac{1}{\sqrt{N}} \sum_{k=0}^{N-1} X_k e^{j\frac{2\pi km}{N}} \quad \text{for } 0 \leq m \leq N - 1 \quad 2.1$$

where, in order to form the m^{th} OFDM symbol, N-point IFFT operation is done on the parallel X_k data symbols. Here each time domain sample, x_m contains information about each X_k data symbols. The period of each OFDM symbol is N times longer than the input data. In order to avoid the inter-symbol interference caused by the channel, a cyclic prefix (CP) is typically added to the serialized IFFT output [28]. For this, N_{CP} samples from the end of the OFDM symbol are appended at the beginning of the symbol. The addition of CP leads to a loss of bandwidth efficiency, but it allows the circular convolution of the transmit signal with channel impulse response resulting in a simple single-tap frequency domain equalizer at the receiver [28]. A number of such OFDM symbols are clubbed in a frame for transmission to the end user. The IFFT operation results in a complex signal, i.e. in-phase and quadrature-phase components, requiring two DACs for converting the samples into an analogue signal. Alternatively, techniques such as Hermitian symmetry or IQ mixing with an IF carrier can be implemented digitally to generate a real signal [29].

At the receiver side, the cyclic prefix samples are removed initially from the received signal after transmission over the channel and then an FFT operation is performed to demodulate the OFDM symbol as shown in Fig. 2.4. A single tap frequency domain equalization (FDE) is applied to the OFDM demodulated symbols to compensate for the linear impairments introduced by the channel [27], [28]. Parallel to serial conversion operation is performed to retrieve the data symbols and further process them for performance evaluation. The OFDM signal exhibits a large peak-to-average power ratio (PAPR), which creates significant chances of non-linear distortion from the amplifiers used in the system. More details of channel estimation and PAPR of OFDM signals are described in [28].

The numerical parameters of the OFDM signals can be understood from the 4G LTE standard specifications. The 4G standards, designed by 3GPP, define the transmission of OFDM signals over 1.25 MHz, 2.5 MHz, 5 MHz, 10 MHz and 20 MHz bandwidth channels [14]. The basic 1.25 MHz channel

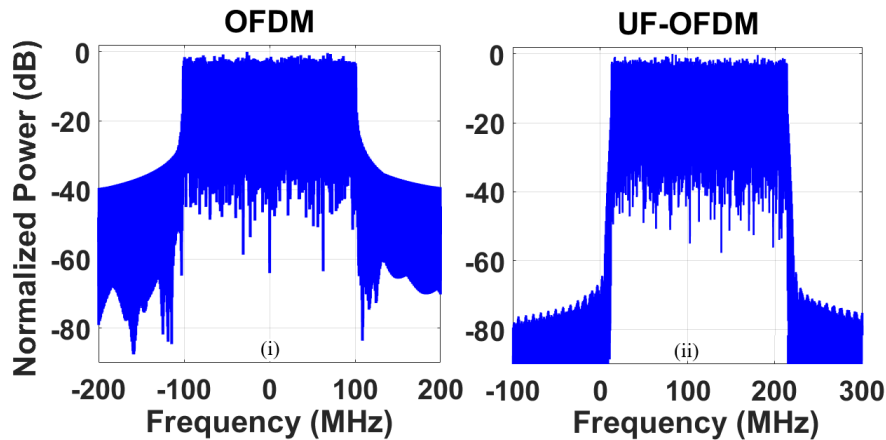


Fig. 2.5 Baseband spectra of 200 MHz BW (i) OFDM and (ii) UF-OFDM signals.

transmitted signal is generated by electronic chips operating at a sampling rate of 1.92 MSa/s (F_s) and contains 72 data modulated subcarriers (out of 128 – i.e. IFFT size N_{FFT}) at a spacing of 15 kHz (Δf) [14]. The increased bandwidth OFDM signals are generated by increasing the IFFT size, number of data modulated subcarriers and sampling rate by a factor of 2 with respect to previous bandwidth signal parameter values [14]. The data rate of such multicarrier signals can be calculated by multiplying the subcarrier spacing ($\Delta f = \frac{F_s}{N_{FFT}}$) with the number of data modulated subcarriers (N_{Dsubc}) and bits per symbol of the employed modulation format. The raw data rate carried by the 1.25 MHz channel transmitted OFDM signal is 72 (number of data subcarriers N_{Dsubc}) \times 15 kHz (Subcarrier Spacing) \times 4 (bits/symbol for 16-QAM data modulated subcarriers) = 4.32 Mb/s. This is a raw data rate without incorporating the cyclic prefix and other overheads. A similar topology is used throughout this thesis for mentioning the parameters of different multicarrier waveforms.

The sinc pulse shape of the OFDM subcarriers leads to larger out-of-band (OOB) emissions as seen from the spectrum of 200 MHz bandwidth OFDM signal shown in Fig. 2.5(i). This results in the requirement of a large guard band between adjacent OFDM signal bands transmitted over the same channel [27]. An additional filtering stage, at different subcarrier levels, is introduced in the new multicarrier waveforms such as filtered OFDM (f-OFDM), universally filtered OFDM (UF-OFDM) and generalized frequency division multiplexing (GFDM) in order to reduce the OOB emission and improve the performance in multiple signals transmission scenario [30]. Fig. 2.5(ii) shows a lower out-of-band noise in the baseband spectrum of the 200 MHz bandwidth UF-OFDM signal, in which filtering is performed on multiple sets of subcarriers before combination to form a symbol [31]. A summary of different multicarrier waveforms is given in [30]. In our previous work in [25], [32], the performance of some of these waveforms was compared over the AIFoF link. The lower OOB emission of UF-OFDM resulted in better performance compared to the OFDM and GFDM waveforms in a multiband transmission scenario [25], [32]. In this chapter, the transmission of multiple UF-OFDM signals is further explored to analyse the capacity of the AIFoF link.

2.2.2 Optical Modulation and Detection

In the AIFoF system, the complex baseband OFDM/UF-OFDM signal samples are converted to the real IF signal using IQ mixing with an IF carrier. The DAC output electric signal can be converted into the optical domain by either directly modulating the laser current or using an external modulator [9]. The choice of the optical modulation technique, i.e. either direct or external modulation, should be done considering the bandwidth and nature of the modulating signal. In general, direct modulation is preferred in the case of low bandwidth and short-reach applications, while external modulation is typically used for phase modulation and in the high bandwidth long haul systems.

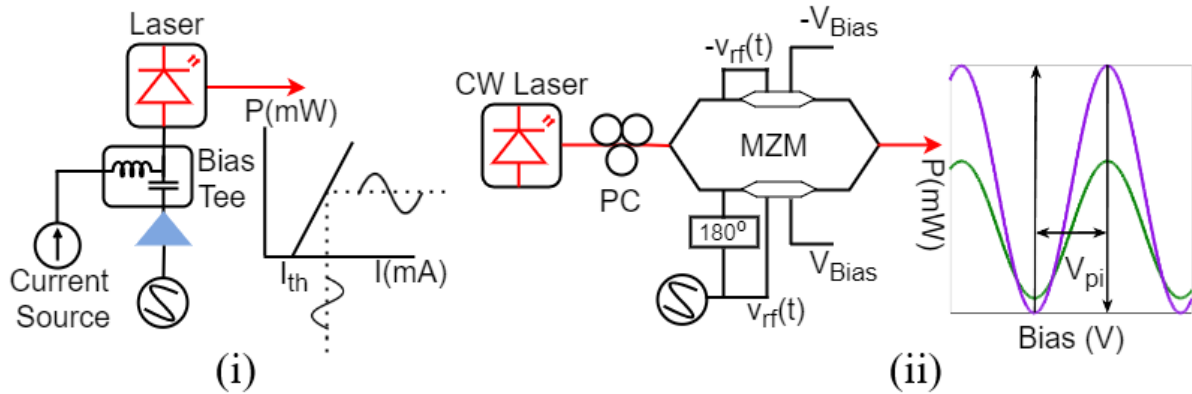


Fig. 2.6 Schematic of a (i) direct and (ii) external modulation system with respective P-I and P-V characteristics.

In the case of direct modulation, the carrier density and in turn the output intensity of a laser is modulated directly by modulating the drive current to the laser [9] – providing a simple implementation. The modulating signal is combined with a fixed bias current, typically using a bias tee, and the combined signal is applied to the laser as shown in the system of Fig. 2.6(i). The bias current to the laser and the swing of modulating signal should be adjusted in order to avoid amplitude nonlinearities. The swing of the modulating signal can be determined by observing the static characteristics of the laser obtained by measuring the output power with variable bias current [9], i.e. P-I curve shown in Fig. 2.6(i). The laser also exhibits frequency non-linearity in terms of relaxation oscillation, which arises from the nonlinear interaction between the photons and carriers in the laser cavity [9]. The relaxation oscillation peak frequency determines the modulation bandwidth of the laser and the maximum frequency of the signal that can be applied to the laser without exhibiting substantial power fading. The relaxation oscillation peak can be slightly changed by changing the bias current [9]. Directly modulated lasers (DMLs) with 15 to 20 GHz modulation bandwidth are commercially available. Injection locked vertical cavity surface emitting laser (VCSEL) diode with 50 GHz bandwidth is reported in the literature [33]. In order to avoid signal distortion, it is important to maintain the swing of the modulating signal within the linear region of the P-I curve and the signal's frequency should be less than the relaxation oscillation peak frequency. The semiconductor lasers also exhibit transient and adiabatic chirps, which can lead to significant performance change when interacting with the dispersion of optical fibre [34]. Also, the laser exhibits a relative intensity noise (RIN) [9], which should be minimum to avoid the amplitude noise in the system.

In the case of external modulation, a continuous wave (CW) laser light is modulated with the data signal using an external device, such as an electro-optic modulator (EOM) or electro-absorption modulator (EAM) [9], [35]. In the most commonly used Mach-Zehnder modulator (MZM) EOM, the input CW light is split into two paths and phase change is introduced in one or both arms in accordance with the modulating signal using a crystal as shown in Fig. 2.6(ii). These phase variations are converted into amplitude changes upon

combining the light from two paths [35]. The transfer characteristics of the MZM, obtained by varying the DC bias, are shown in Fig. 2.6(ii). For intensity modulation, the MZM should be biased at the $V_{\pi}/2$ quadrature point and the swing of the modulating signals should be adjusted such that it does not cross the nonlinear region of the DC characteristic curve [35]. V_{π} is the voltage required to produce a π phase change between the two arms of the MZM as shown in Fig. 2.6(ii). The MZMs suffer from higher insertion loss (3 to 5 dB) and lower extinction ratio (20 to 25 dB). It also requires a polarization controller (PC) at its input and a bias control mechanism – resulting in an increased transmitter footprint [9], [35]. Complex baseband signals can be modulated on the optical carrier using I-Q MZMs without the need of converting them into real IF signals. Plasmonic based MZM with up to 70 GHz bandwidth is reported in the literature[36].

Directly modulated laser systems are best suited for the wide deployment of short-haul AIFoF fronthaul links due to their simple architecture. DML does not require a strict bias control or a polarization controller. The effect of amplitude and frequency non-linearity can be mitigated by appropriately choosing the swing and IF carrier frequency of the modulating signal. A distributed feedback (DFB) laser diode exhibiting a relaxation oscillation peak at ~ 11.5 GHz was used in the AIFoF link experimental demonstration presented in this chapter.

The optical-to-electrical conversion is typically carried out using a square-law photodetector. PIN PDs and Avalanche PDs (APD) are most commonly used in optical communication systems [9]. The optical carrier's intensity detection is typically carried out with a single PD, while multiple PDs are required for phase information detection. The PDs add thermal noise, shot noise and dark current to the photo-detected signal resulting in performance degradation [9]. The square-law nonlinear response also leads to the mixing of various signal components upon detection resulting in the generation of additional beating components. The subcarriers of the multicarrier signals will also mix together in the case of single band transmission and additional mixing components between multiple signals will be generated in the case of multiband transmission over the AIFoF link [37].

2.2.3 Optical Fibre

The optically modulated IF OFDM signals are transmitted between the C-BBU and RRH site over several tens of kilometres of optical fibre. The length of the fronthaul link is primarily decided by the latency available for RAN processing. The 3 msec latency of 4G LTE signals results in the maximum recommended distance of ~ 25 km between the C-BBU and RRH site over a CPRI fronthaul link [38].

The optical signal gets impaired by the loss, chromatic dispersion and nonlinearities upon propagation through the standard single mode fibre (SSMF) resulting in performance degradation [9]. SSMF offers a low propagation loss (~ 0.2 dB/km) around 1550 nm wavelength and hence the laser sources around the

same wavelength are used for the experimental demonstration in this work. The chromatic dispersion of fibre leads to different frequency components of the modulated signal being propagated with different velocities over the optical fibre [9]. This results in different phase shifts for the upper and lower sideband of the optical double sideband (ODSB) signal (obtained after intensity modulation) leading to a reduction in the power of photo-mixing generated electrical signal at specific frequencies. The phase difference increases with an increase in frequency separation between the two sidebands for a given fibre length [21] and leads to a null response at specific frequencies with an 180° phase shift between the sidebands.

In the case of external modulation systems, the effect of fibre chromatic dispersion can be analytically given as [21]

$$H(f) = \cos^2(\sigma f^2); \quad \sigma = \frac{\pi D \lambda^2 L}{c} \quad 2.2$$

where f is the offset frequency of the signal from the optical carrier, D is the chromatic dispersion parameter, λ is the optical wavelength, c is the speed of light in vacuum and L is the length of the fibre. In the case of direct modulation systems, the interplay between the adiabatic and transient chirp of the laser and fibre chromatic dispersion result in different frequency response given as [34]

$$H(f) = \sqrt{\alpha^2 + 1} \cos(\sigma f^2 + \tan^{-1} \alpha) + j \frac{\alpha \kappa P_0}{2\pi f} \sin \sigma f^2; \quad 2.3$$

where α is the linewidth enhancement factor, κ is the adiabatic chirp parameter, P_0 is the output power of the laser and $\sigma = \frac{\pi D \lambda^2 L}{c}$ is the dispersion dependent parameter same as given in Eq. 2.2. The first and second terms, in Eq. 2.3, originate from the transient and adiabatic chirp of DML, respectively.

Fig. 2.7(i) and (ii) show the analytical power fading effect on the variable frequency microwave sinusoidal signal observed over the external modulated and directly modulated systems, respectively, due

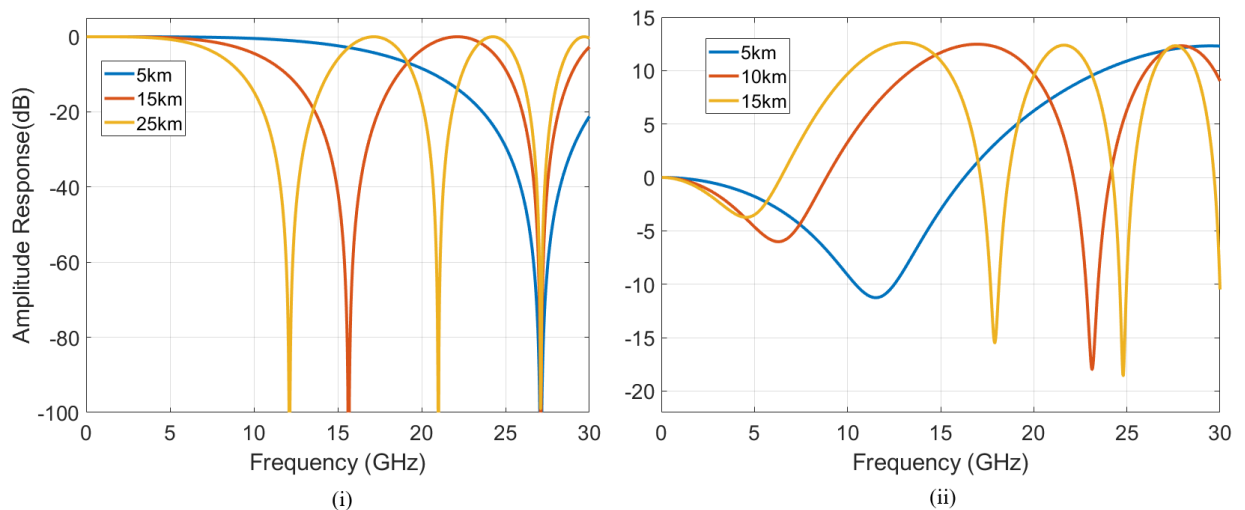


Fig. 2.7 Power fading introduced by optical fibre chromatic dispersion over (i) EML and (ii) DML systems.

to the effect of chromatic dispersion. In the case of an external modulated system, the power of the photo-detected signal has a cosine square relation with the frequency of the modulated microwave signal [21]. Complete extinction of the sinusoidal signal, with 180° phase shift between two sidebands, occurs at ~ 12.5 GHz and ~ 27.1 GHz frequencies after transmission over 25 km and 5 km length fibre, respectively, as shown in Fig. 2.7(i). Higher power degradation is observed for the same frequency microwave carrier as the fibre length is increased. In the case of direct modulation, a dip in the power of the photo-detected signals is observed as a result of the interplay between the laser's chirp and fibre dispersion. Results in Fig. 2.7(ii), obtained for the $\alpha = 3.25$ and $\kappa = 2.55 \text{ GHz/mW}$ values, shows that as the fibre length increases the first power cancellation point frequency reduces from more than 30 GHz (5 km) to 23.6 GHz (15 km) to 17.5 GHz (25 km). This clearly shows that the effect of the interplay between laser chirp and chromatic dispersion increases with an increase in fibre length. The results show higher power variations for small fibre lengths at lower frequencies within the first null point. The low-frequency power fading effect is dominated by the transient chirp of the laser, while power fading at a higher frequency is dominated by the adiabatic chirp.

The analytical results presented in Fig. 2.7 show significant degradation in the power of the microwave sinusoidal signal due to the fibre chromatic dispersion in both external and direct modulation cases. Techniques such as the transmission of optical single sideband (OSSB) signal, optical carrier suppression technique, using fibre nonlinearities or chirped fibre grating, or phase conjugation can be employed to mitigate the effect of chromatic dispersion [3], [39]. In this work, the most commonly used OSSB signal transmission technique is demonstrated. The fibre induced nonlinearities such as self-phase modulation and cross-phase modulation result in additional frequency components being generated [40]. In the case of AIFoF fronthauling, the optical power levels of the transmit signal are generally not high enough to trigger the nonlinearities in the optical fibre.

It is important to analyse the capacity of the AIFoF link considering the effect of loss, dispersion induced power fading and nonlinearities and bandwidth limitations of the various system components. In the next section, these components are put together to demonstrate an AIFoF fronthaul link and analyse its capacity for the transmission of 5G NR compatible signals.

2.3 Capacity of AIFoF Fronthaul Link

2.3.1 Experimental Setup

The schematic of the AIFoF experimental testbed is shown in Fig. 2.8. Initially, a complex baseband UF-OFDM signal, with 330 data modulated subcarriers (out of 1024), was generated offline in MATLAB at the transmitter. The 64 QAM data modulated subcarriers placed at a frequency spacing of ~ 610 kHz resulted

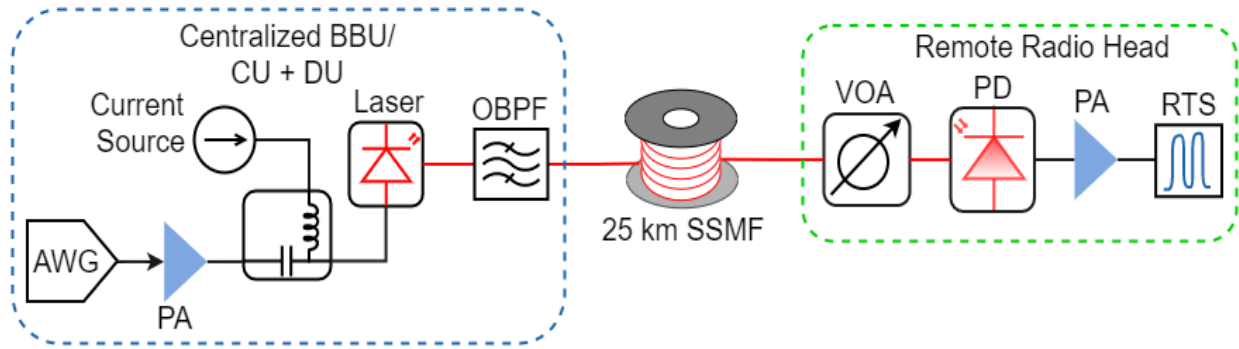


Fig. 2.8 Experimental setup to demonstrate the AIFoF fronthauling through the intensity modulation direct detection system.

in a signal bandwidth of 201 MHz and a raw data rate of 1.21 Gb/s. One training symbol was added to this signal for the estimation of channel response and subsequent equalization at the receiver side. The complex baseband UF-OFDM signal was mixed with an intermediate frequency carrier, in MATLAB, to generate a real IF signal. Hard clipping was applied on the IF signal to reduce its peak amplitude to 80% of the original maximum value resulting in a reduction of PAPR to $\sim 10 - 13$ dB. The performance of high PAPR signals gets affected by the nonlinearities introduced by the PA and it's essential to reduce it.

The samples of real IF signal were loaded into the arbitrary waveform generator (AWG), operated at a 20 GSa/s sampling rate, for generating the analogue electrical signal. The AWG7200, from Tektronix [41], had a maximum peak-to-peak output of 500 mV. This signal's voltage swing (in turn power) was increased, using an RF power amplifier (PA) as shown in the setup diagram, before directly modulating the laser. A

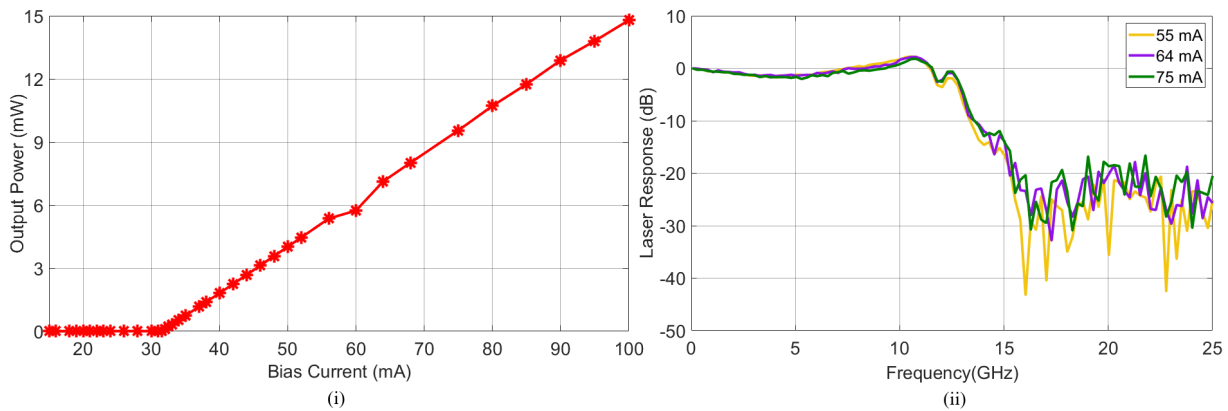


Fig. 2.9 (i) P-I characteristics and (ii) frequency response of the G&H DFB laser diode.

constant DC bias current was added, using a bias tee, to the IF signal for shifting it into the linear region of the laser P-I curve. The DC shifted IF signal was applied to a DFB laser, from G&H [42], for direct modulation - resulting in an optical double sideband signal. The P-I static characteristic of the laser, obtained by applying the dc bias only, is shown in Fig. 2.9 (i). It shows a threshold current of 32 mA and a linear slope efficiency of 0.222 W/A. In order to avoid the amplitude non-linearity arising from the laser,

the modulating signals swing was restricted to the linear region of the P-I curve. The laser was biased at 75 mA and a modulating signals swing was maintained at ~ 78 mA (corresponding to 16 dBm RF power). The laser emitted light at a wavelength of 1541 nm and had a resonance peak around ~ 11.5 GHz. Fig. 2.9(ii) shows the frequency response of the laser obtained using a vector network analyser (VNA). Changing the bias current to the laser did not result in the relaxation oscillation frequency change. The IF frequencies of modulating signals were chosen to be smaller than the resonance peak of the laser modulation response.

The optical signal from the laser output was transmitted over a 25 km SSMF with two different transmission scenarios. In the first case, the optical double sideband signal was transmitted over the fibre and the effect of the interplay between chromatic dispersion and lasers chirp was analysed by observing the photo-detected IF signals spectrum. In the second case, one of the sidebands was filtered first using a tuneable optical bandpass filter (OBPF) and the optical single sideband signal was transmitted over the fibre. The transmission of an OSSB signal helps to mitigate the effect of chromatic dispersion power fading as it avoids mixing of different phase data sidebands on the photodetector and results in a flat response for all the microwave carrier frequency signals [3], [21], [39].

The OSSB signal can be obtained by using bandpass filtering [43] or with external modulation using dual-drive MZM (DD-MZM) [44] or IQ MZM [45]. The passband profile of the OBPF, for eliminating one of the sidebands, needs to be sharp, especially for AIFoF systems where the signal is modulated close to the optical carrier. The passband profile of the filter needs to be selected appropriately while choosing the IF carrier frequency in an OSSB AIFoF link. There is no limitation on the choice of IF frequency for OSSB signal generation using DD-MZM or IQ-MZM, however, these techniques need an additional electrical phase shifter, bias control mechanism and polarization controller. The OSSB technique suffers from a 6 dB electric power loss, since half of the optical sideband power is removed in comparison to the optical double sideband signal, but it offers a simple way of mitigating the effect of chromatic dispersion. Also, a sufficient optical carrier-to-sideband power ratio needs to be maintained for optimal performance as it affects the SNR of the photo-detected signal [45], [46].

An OBPF, from EXFO [47], with a 4 GHz bandwidth and 5 pm wavelength tuning resolution was used in the experimental demonstration. The fine wavelength and bandwidth tuneability of the OBPF were used for adjusting the optical carrier to sideband power ratio. The filtered OSSB signal with a power of 4 dBm was transmitted through 25 km of SMF and detected using a PIN PD at the receiver RRH site. A photodetector with 20 GHz bandwidth was used for this experiment. A variable optical attenuator (VOA) was used to control the power falling on the PD. The detected signal was amplified and then captured using a real-time oscilloscope (RTS), from Tektronix [48], operating at a sampling rate of 50 GSa/s. Offline digital signal processing operations such as re-sampling, frequency down-conversion to baseband,

demodulation, channel estimation and equalization were performed on the captured signal. In the case of multiple signal transmission over the AIFoF link, a 12th-order Gaussian digital filter was used to filter and extract each IF signal band for demodulation and further processing. System performance was analysed by evaluating the error vector magnitude (EVM) and bit error rate (BER) in MATLAB.

2.3.2 Experimental Results and Discussion

The performance of the signals over the passive AIFoF fronthaul link degrades as SNR is degraded due to the nonlinearities from the E-O/O-E conversion process, chromatic dispersion induced fading and PD noise. Initially, a single band of 201 MHz bandwidth UF-OFDM signal centred at 4.5 GHz IF carrier was generated in Matlab and the generated ODSB signal was transmitted over the outlined AIFoF system. The effect of the above-mentioned impairments was minimal on the transmission of a single 201 MHz bandwidth UF-OFDM signal - resulting in a very good performance with EVM values of less than 4%. In order to analyse the capacity of the link, multiple signals were added on both sides of the 4.5 GHz IF signal band and the combined signal was transmitted over the link. The guard band between the signal bands was selected to minimize interference. A typical value of the spectral guard band specified in various standards is 10% of the signal bandwidth and the same was chosen here. IF carriers of the multiple signal bands were separated by 220 MHz as shown in the received signal spectrums in Fig. 2.10. The addition of more signals for simultaneous transmission over the link degrades the performance resulting from the SNR degradation due to power sharing between all signal bands.

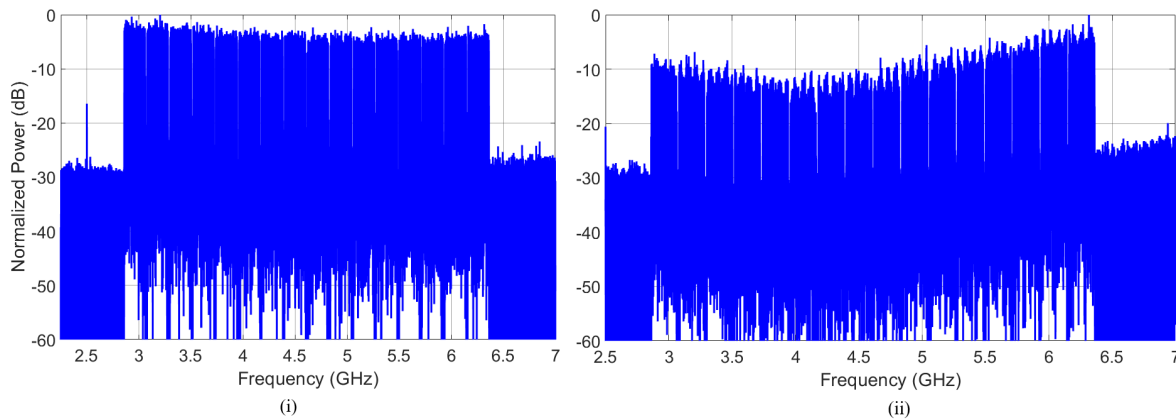


Fig. 2.10 Spectrum of the RTS captured 16 UF-OFDM signal bands after transmission over a 25 km SSMF AIFoF IMDD link using a DFB laser i) with and ii) without isolator.

In order to study the effect of the fibre chromatic dispersion and its interaction with the laser's chirp, initially optical double sideband modulated signals were transmitted over the 25 km IMDD AIFoF link. The schematic of this experimental setup is similar to the one shown in Fig. 2.8, except for the use of an optical bandpass filter. Two different lasers were used for studying the effect of chirp interaction with chromatic dispersion. Both these lasers, one had an internal isolator and another without an isolator, were

from the same manufacturer and exhibited approximately the same frequency response. Fig. 2.10(i) and (ii) show the spectrum of the RTS captured 16 UF-OFDM signal bands after transmission over a 25 km SSMF AIFoF IMDD link using two different DFB lasers for modulating the signal. Different chirp characteristics of these lasers resulted in different power fading effects on the received signals. As mentioned in section 2.2.3, the interaction between laser chirp and fibre chromatic dispersion results in a dip in the frequency response of the ODSB AIFoF link. A similar effect was observed from the received signal spectrum shown in Fig. 2.10. In the first case, a usual power fading effect was observed (in Fig. 2.10(i)) as a ~ 4 dB reduction in the power of signal bands was observed with increase in IF carrier frequency. In the second case with the use of laser without an internal isolator, exhibiting reflections and different chirp characteristics, more than 12 dB fluctuation in the power among signal bands was observed with a visible power dip at ~ 4.1 GHz (in Fig. 2.10(ii)). The power of higher IF frequency signal bands was observed to be increasing in this case – opposite of the observation from Fig. 2.10(i). A significant performance difference will be observed among the signal bands, after demodulation, in accordance with the power fading observed in both cases. In our previous ODSB AIFoF system demonstration [25] with 10 bands of 200 MHz BW 5G waveforms, a significant 2.5% to 3% EVM degradation was observed between the signals.

It is necessary to overcome the effect of chromatic dispersion and avoid its interaction with the laser chirp. As mentioned earlier, this can be achieved by removing one of the sidebands from the ODSB signal and transmitting the OSSB signal over the fibre. The OBPF was introduced to the link after the laser and one sideband was filtered out. In the remainder of this chapter optical single sideband signal transmission systems performance is analysed when using a laser with an internal isolator.

Initially, a single band of UF-OFDM signal centred at 4.5 GHz IF was transmitted over the OSSB AIFoF IMDD link. The performance of a single 201 MHz BW UF-OFDM signal does not degrade over the

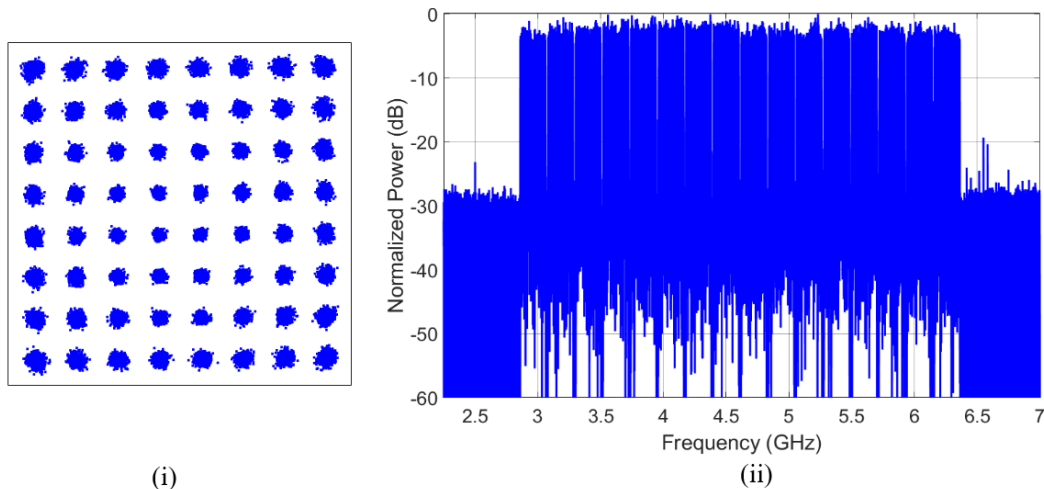


Fig. 2.11 (i) Constellation of the single UF-OFDM signal band and (ii) spectrum of the received 16 UF-OFDM signal bands after transmission over a 25 km SSMF OSSB AIFoF IMDD link.

25 km link and the same was observed from the constellation of the demodulated signal shown in Fig. 2.11(i). An excellent EVM of $\sim 3.7\%$, majorly due to the system noise floor, was observed at a received optical power of -2 dBm for a single UF-OFDM signal. Further, multiple 5G UF-OFDM signals modulated at different IF frequencies were generated and their performance was analysed in order to determine the maximum number of signal bands that can be simultaneously transmitted over the outlined link i.e. link capacity. Signal bands were added on both sides of the central band, at 4.5 GHz, with a guard band of 20 MHz and approximately equal power. 4, 8 and 16 signal bands were transmitted over the 25 km IMDD link and their EVMs are measured to be within the FEC limit.

Fig. 2.11(ii) shows the spectrum of the RTS captured 16 signal bands after transmission over a 25 km OSSB AIFoF link. The almost flat power across all the signal bands indicates the mitigation of the chromatic dispersion-induced power fading - previously observed for the ODSB system in Fig. 2.10. Fig.

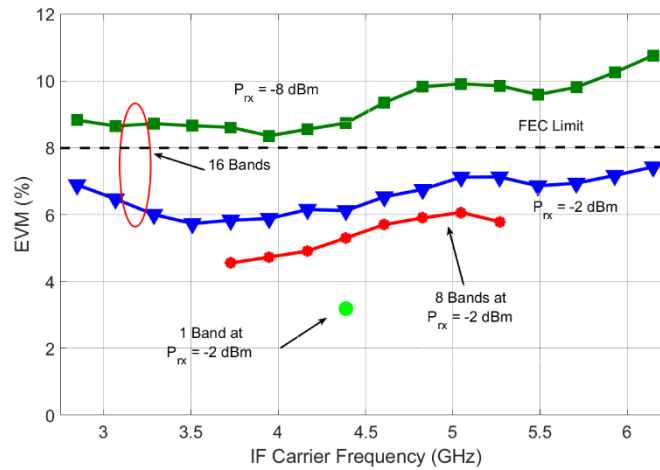


Fig. 2.12 EVM performance of 1 (flourecent green), 8 (red), and 16 (blue and green) UF-OFDM signal bands over OSSB AIFoF fronthaul link.

2.12 shows the EVM performance for the 1, 8 and 16 bands transmission over the outlined OSSB AIFoF system. The measured EVMs of the different signal bands are plotted against the corresponding IF carrier frequencies. The performance of all the mentioned transmission scenarios at -2 dBm received optical level was found to be within the FEC EVM limit of 8% for 64 QAM data modulated UF-OFDM signal bands. The approximate equal performance of all signal bands stems from the similar electrical power per band and in turn signal-to-noise ratio.

The successful simultaneous transmission of the sixteen UF-OFDM signals over 25 km of optical fibre, with all bands exhibiting below FEC limit EVM of 8% and BER of less than 3.3×10^{-3} , results in an aggregate data transmission rate of ~ 19.3 Gb/s (1.21 Gb/s $\times 16$). As the number of transmitted signal bands increased from 1 to 8 to 16, the overall performance starts to degrade as seen from the different EVMs of the central band in Fig. 2.12. The EVM of the central band, at the IF of 4.5 GHz, degrades from $\sim 3.7\%$ for

a single band to $\sim 5.5\%$ for eight bands and then to $\sim 6.3\%$ for sixteen bands at the same received power of -2 dBm. This degradation can be attributed to the reduction in signal-to-noise ratio resulting from the reduced power per band as the total power of the combined signal modulating the laser remains the same in the system (16 dBm). The number of successfully transmitted signals over the presented link is primarily limited by the power per band. The maximum output of the AWG is limited to 500 mV and as the number of bands increases the corresponding power per band, SNR and performance degrade. An additional RF amplifier can be used to boost the power of the combined signal, however, the nonlinearities in the amplifier will result in further performance degradation. In order to increase the power per band, different IF carrier signals need to be generated with different AWGs and then combine them externally using an RF coupler. Also, the RF power handling capabilities of the directly modulated laser limits the number of simultaneous signal bands that can be transmitted over the link. Furthermore, using multiple lasers to modulate multi-band signals and implementing a WDM system will also lead to increasing the capacity of the AIFoF link.

The results in Fig. 2.12 show that the performance across all signal bands is not constant and for the 16 band case it varies from $\sim 5.8\%$ to $\sim 7.4\%$. This variation can be attributed primarily to the non-flat modulation response of the laser diode shown in Fig. 2.9(ii). Fig. 2.12 also shows the performance of 16 bands when the optical power falling on the photo-detector was reduced from -2 dBm to -8 dBm. The performance degradation is observed with reduced optical power as a consequence of the degraded SNR. For -8 dBm and lower power levels, the EVM of all 16 bands goes above the FEC threshold limit. Using 16 -QAM modulated subcarriers, instead of 64 QAM, will result in the successful transmission of more than 16 bands over the presented O-SSB AIFoF link at this reduced received power, as the FEC limit increases with reduction in the order of modulation.

In the next section, the power difference penalty in the multiband transmission scenario is analysed to emulate the uplink scenario.

2.4 Power Difference Penalty over AIFoF Fronthaul Link

In the multiband transmission scenario, presented in the previous section, the performance of all the signal bands is similar as they exhibit the same power and SNR. Any difference in the powers, and the corresponding SNR, between simultaneously transmitted bands will result in performance variation. This is the most likely scenario for the uplink transmission [49], where multiple signals arrive at the RRH multi-sector antenna site with different powers and corresponding different SNRs owing to variations in the wireless transmission distance as depicted in the schematic of Fig. 2.13(i). All the antenna captured signals, with different powers and SNRs, need to be transported over the single fibre fronthaul link to the C-BBU without power equalization. As the simultaneously transmitted different power (and SNR) signal bands propagate through the AIFoF link they experience similar effects – resulting in approximately the same

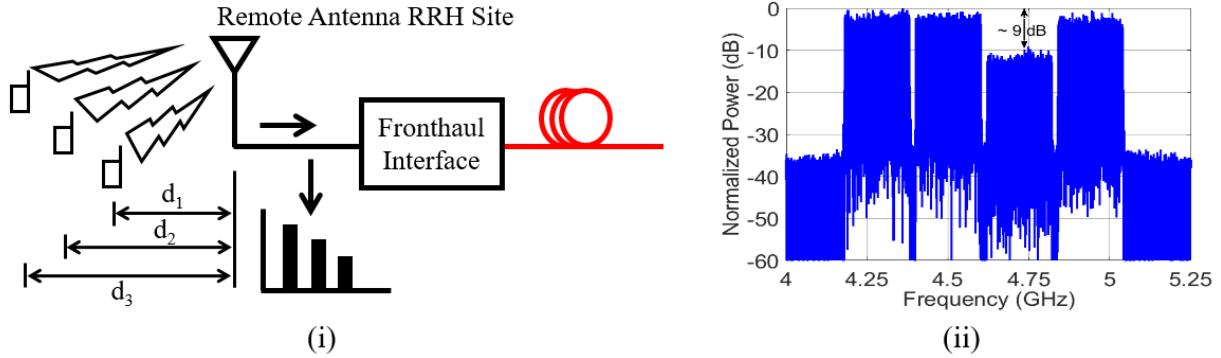


Fig. 2.13 (i) Schematic of uplink fronthaul transmission scenario and (ii) spectra of 4 UF-OFDM signal bands showing power difference between transmitted bands.

performance degradation. The permitted SNR difference (which is modelled as power difference) between the signal bands, so that their performance is within the FEC limit for uplink AIFoF transmission, varies with the total number of bands transmitted over the link. In order to design a robust fronthaul link, it is necessary to analyse the power difference penalty (PDP) (which ultimately translates to SNR penalty) over the presented AIFoF link for the transmission of multiple 5G signal bands.

In order to study the effect of power differences in a multi-band transmission scenario, the power of a signal band (at the IF of ~ 4.61 GHz) was varied by digitally attenuating it at the transmitter before combining it with other bands. The performance of this signal band was observed for variable power differences of 0 to 15 dB, with respect to the other bands, for the case of 2, 4 and 8 signal bands transmission over the OSSB AIFoF system. The experimental setup for this demonstration was the same as the one shown in Fig. 2.8, except for a change in the MATLAB code to emulate the power difference. The received signal spectra in Fig. 2.13(ii) shows one such scenario where the power of the signal band at ~ 4.61 GHz IF carrier was reduced by ~ 9 dB compared to other bands. Because of the reduced power per band, the tolerable power difference over the OSSB AIFoF link reduces as the number of bands increases and the results are presented in the next subsection. Similar to the previous experiment, 64 QAM modulated 201 MHz bandwidth UF-OFDM signals were transmitted over the multiband link.

2.4.1 Experimental Results and Discussion

Initially, the performance of two signal band transmission AIFoF link was analysed for the power difference penalty, with the power of the second band (at the IF carrier of ~ 4.61 GHz) being attenuated relative to the first band. Fig. 2.14(i) shows the measured EVM vs power difference performance of both bands in this scenario. The results show that the performance of the second band degrades as its power is reduced and it crosses the FEC limit EVM value at a power difference of ~ 10 dB. The performance of the first band improves slightly owing to the re-distribution of the total power but does not improve beyond the

system limit of $\sim 3\%$. This result indicates that the two signals with a 10 dB power difference between them can be successfully transmitted over the AIFoF fronthaul link.

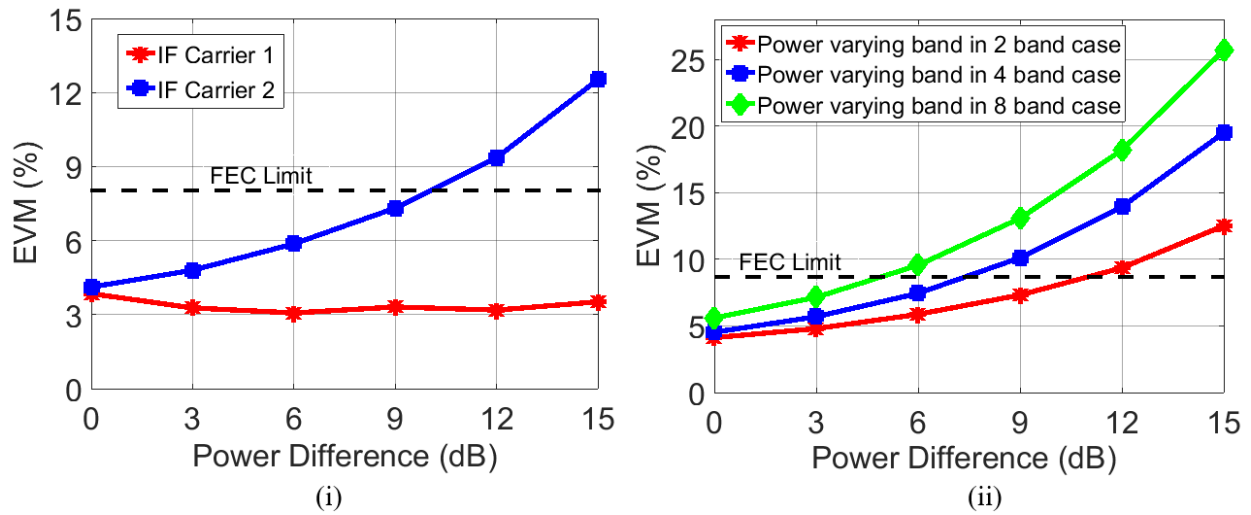


Fig. 2.14 EVM performance of (i) 2 band transmission with power difference and (ii) power varying band in 2, 4, and 8 band transmission scenarios over an O-SSB AIFoF uplink fronthaul link.

In order to analyse the PDP of the 4 and 8 band transmission, the power of the signal at the intermediate frequency of ~ 4.61 GHz was reduced compared to the other bands. EVM performance of the reduced power signal band is shown in Fig. 2.14(ii) for the transmission of 2, 4 and 8 bands over the OSSB AIFoF link. Results show that with an increase in the number of bands the power difference, at which performance goes above the FEC limit, reduces. Approximate power differences of 10 dB, 7 dB and 5 dB were observed for 2, 4 and 8 band cases respectively. This reduction in the tolerable power difference required for acceptable performance can be again attributed to the reduction in the power per band as the number of signal bands increases.

The power of an individual band can be increased by increasing the combined IF signal power, but the power handling capabilities of the directly modulated lasers (or external modulators) limit the amount of allowable RF power - eventually limiting the PDP. Digital signal processing algorithms can be used to equalize the power of all the signals received at the antennas, upon uplink transmission, but it will increase the complexity of the RRH site.

2.5 Conclusion

The introduction of C-RAN and higher channel bandwidths, in the 5G wireless systems, necessitates the implementation of a simple, spectrally efficient and cost-effective fronthaul network for transporting the data between C-BBU and remote antenna RRH site. Various fronthauling possibilities are summarized in this chapter along with the spectrally inefficient digital baseband over fibre. Two variants of analog-RoF, i.e. ARFoF and AIFoF, are discussed in detail along with their advantages and disadvantages for carrying

the 5G signals. The flexibility in the choice of the IF carrier frequency and the use of low bandwidth optical components makes the AIFoF link an ideal candidate for carrying the fronthaul data.

The capacity of the simple and spectrally efficient 25 km AIFoF link is experimentally analysed demonstrating the successful transmission of sixteen 201 MHz BW UF-OFDM signal bands carrying an aggregate data transmission rate of ~19.3 Gb/s. The number of successfully transmitted bands is limited by available power per signal band in the system and additional wavelength will be required to increase the overall network throughput. Nevertheless, the number of signal bands that can be successfully transmitted over the AIFoF link with a single wavelength is considerably higher than that can be achieved over the DBBoF based links. The RF power handling capabilities of the directly modulated laser limit the allowable power differences that 2, 4, and 8 band transmission systems can handle to 10 dB, 7 dB, and 5 dB, respectively.

References

- [1] A. Checko *et al.*, “Cloud RAN for Mobile Networks - A Technology Overview,” *IEEE Communications Surveys and Tutorials*, vol. 17, no. 1, pp. 405–426, Jan. 2015, doi: 10.1109/COMST.2014.2355255.
- [2] ITU-T, “5G wireless fronthaul requirements in a passive optical network context,” Sep. 2020.
- [3] C. Lim *et al.*, “Fiber-wireless networks and subsystem technologies,” *Journal of Lightwave Technology*, vol. 28, no. 4, pp. 390–405, Feb. 2010, doi: 10.1109/JLT.2009.2031423.
- [4] A. J. Cooper, “Fibre/radio for the provision of cordless/mobile telephony services in the access network,” *Electron Lett*, vol. 26, no. 24, p. 2054, 1990, doi: 10.1049/EL:1990132510.1049/EL:19901325.
- [5] D. M. Fye, “Design of fiber optic antenna remoting links for cellular radio applications,” *IEEE Vehicular Technology Conference*, pp. 622–625, 1990, doi: 10.1109/VETEC.1990.110394.
- [6] T. S. Chu and M. J. Gans, “Fiber Optic Microcellular Radio,” *IEEE Trans Veh Technol*, vol. 40, no. 3, pp. 599–606, 1991, doi: 10.1109/25.97514.
- [7] H. Ogawa, D. Polifko, and S. Banba, “Millimeter-wave fiber optics systems for personal radio communication,” *IEEE Trans Microw Theory Tech*, vol. 40, no. 12, pp. 2285–2293, 1992, doi: 10.1109/22.179892.
- [8] Schmuck H. and Heidemann R., “Hybrid fibre-radio field experiment at 60 GHz,” in *European Conference on Optical Communication*, 1996, pp. 59–62.
- [9] G. P. AGRAWAL, *FIBER-OPTIC COMMUNICATION SYSTEMS*, 5th ed. JOHN WILEY, 2021.
- [10] K. Balemarthy, “Long-Haul Optical Fiber Networks: 100Gbps and Beyond,” *International Conference on Fibre Optics and Photonics (2012)*, paper W2C.1, p. W2C.1, Dec. 2012, doi: 10.1364/PHOTONICS.2012.W2C.1.
- [11] T. Horvath, P. Munster, V. Oujezsky, and N. H. Bao, “Passive Optical Networks Progress: A Tutorial,” *Electronics 2020, Vol. 9, Page 1081*, vol. 9, no. 7, p. 1081, Jul. 2020, doi: 10.3390/ELECTRONICS9071081.
- [12] K. Bergman, M. Glick, M. Bahadori, Q. Cheng, and S. Rumley, “Recent advances in optical technologies for data centers: a review,” *Optica, Vol. 5, Issue 11, pp. 1354-1370*, vol. 5, no. 11, pp. 1354–1370, Nov. 2018, doi: 10.1364/OPTICA.5.001354.
- [13] P. Assimakopoulos, “Optical Fronthaul Options for Meeting 5G Requirements,” *International Conference on Transparent Optical Networks*, vol. 2018-July, Sep. 2018, doi: 10.1109/ICTON.2018.8473762.
- [14] A. de La Oliva, J. A. Hernandez, D. Larrabeiti, and A. Azcorra, “An overview of the CPRI specification and its application to C-RAN-based LTE scenarios,” *IEEE Communications Magazine*, vol. 54, no. 2, pp. 152–159, Feb. 2016, doi: 10.1109/MCOM.2016.7402275.

- [15] C. Lim, Y. Tian, C. Ranaweera, T. A. Nirmalathas, E. Wong, and K. L. Lee, "Evolution of Radio-Over-Fiber Technology," *Journal of Lightwave Technology*, vol. 37, no. 6, pp. 1647–1656, Mar. 2019, doi: 10.1109/JLT.2018.2876722.
- [16] C. Ranaweera, J. Kua, I. Dias, E. Wong, C. Lim, and A. Nirmalathas, "4G to 6G: Disruptions and drivers for optical access [Invited]," *Journal of Optical Communications and Networking*, vol. 14, no. 2, pp. A143–A153, Feb. 2022, doi: 10.1364/JOCN.440798.
- [17] A. Nirmalathas, P. A. Gamage, C. Lim, D. Novak, and R. Waterhouse, "Digitized radio-over-fiber technologies for converged optical wireless access network," *Journal of Lightwave Technology*, vol. 28, no. 16, pp. 2366–2375, 2010, doi: 10.1109/JLT.2010.2051017.
- [18] D. Novak *et al.*, "Radio-over-fiber technologies for emerging wireless systems," *IEEE J Quantum Electron*, vol. 52, no. 1, Jan. 2016, doi: 10.1109/JQE.2015.2504107.
- [19] A. Delmade, D. Venkitesh, and R. D. Koilpillai, "Performance comparison of optical fronthauling techniques for centralized radio access network," *2016 IEEE International Conference on Advanced Networks and Telecommunications Systems, ANTS 2016*, Jun. 2017, doi: 10.1109/ANTS.2016.7947836.
- [20] T. S. Rappaport *et al.*, "Wireless communications and applications above 100 GHz: Opportunities and challenges for 6g and beyond," *IEEE Access*, vol. 7, pp. 78729–78757, 2019, doi: 10.1109/ACCESS.2019.2921522.
- [21] U. Gliese, S. Norskov, and T. N. Nielsen, "Chromatic dispersion in fiber-optic microwave and millimeter-wave links," *IEEE Trans Microw Theory Tech*, vol. 44, no. 10 PART 1, pp. 1716–1724, 1996, doi: 10.1109/22.538964.
- [22] S. Noor, P. Assimakopoulos, and N. J. Gomes, "A Flexible Subcarrier Multiplexing System with Analog Transport and Digital Processing for 5G (and Beyond) Fronthaul," *Journal of Lightwave Technology*, vol. 37, no. 14, pp. 3689–3700, Jul. 2019, doi: 10.1109/JLT.2019.2918215.
- [23] H. Xin, H. He, K. Zhang, S. B. Hussain, and W. Hu, "Flexible Baseband-Unit Aggregation Enabled by Reconfigurable Multi-IF over WDM Fronthaul," *IEEE Photonics J*, vol. 10, no. 1, Feb. 2018, doi: 10.1109/JPHOT.2017.2780090.
- [24] S. H. Cho, H. S. Chung, C. Han, S. Lee, and J. H. Lee, "Experimental Demonstrations of Next Generation Cost-Effective Mobile Fronthaul with IFoF technique," *Optical Fiber Communication Conference (2015), paper M2J.5*, vol. 2015-June, p. M2J.5, Mar. 2015, doi: 10.1364/OFC.2015.M2J.5.
- [25] A. Delmade *et al.*, "Performance Analysis of Analog IF Over Fiber Fronthaul Link With 4G and 5G Coexistence," *Journal of Optical Communications and Networking, Vol. 10, Issue 3, pp. 174-182*, vol. 10, no. 3, pp. 174–182, Mar. 2018, doi: 10.1364/JOCN.10.000174.
- [26] Rappaport Theodore S., *Wireless Communications Principles and Practice*, Second. Pearson, 2001.
- [27] Christopher Cox, *An Introduction to LTE: LTE, LTE-Advanced, SAE, VoLTE and 4G Mobile*, 2nd ed. John Wiley & Sons Ltd, 2014.
- [28] T.-D. Chiueh and P.-Yun. Tsai, "OFDM baseband receiver design for wireless communications," p. 258, 2007, Accessed: Aug. 25, 2022. [Online]. Available: <https://www.wiley.com/en-us/OFDM+Baseband+Receiver+Design+for+Wireless+Communications-p-9780470822487>
- [29] J. Armstrong, "OFDM for optical communications," *Journal of Lightwave Technology*, vol. 27, no. 3, pp. 189–204, Feb. 2009, doi: 10.1109/JLT.2008.2010061.
- [30] B. Farhang-Boroujeny and H. Moradi, "OFDM Inspired Waveforms for 5G," *IEEE Communications Surveys and Tutorials*, vol. 18, no. 4, pp. 2474–2492, Oct. 2016, doi: 10.1109/COMST.2016.2565566.
- [31] V. Vakilian, T. Wild, F. Schaich, S. ten Brink, and J. F. Frigon, "Universal-filtered multi-carrier technique for wireless systems beyond LTE," *2013 IEEE Globecom Workshops, GC Wkshps 2013*, pp. 223–228, 2013, doi: 10.1109/GLOCOMW.2013.6824990.
- [32] C. Browning *et al.*, "5G wireless and wired convergence in a passive optical network using UF-OFDM and GFDM," *2017 IEEE International Conference on Communications Workshops, ICC Workshops 2017*, pp. 386–392, Jun. 2017, doi: 10.1109/ICCW.2017.7962688.
- [33] L. Chrostowski, Zhao X., Chang-Hasnain C. J., Shau R., Ortsiefer M., and Amann M., "50 GHz Directly-Modulated Injection-Locked 1.55 μm VCSELs," 2005.

- [34] S. H. Bae *et al.*, “Transmission of 51.56-Gb/s OOK signal using 1.55 μm directly modulated laser and duobinary electrical equalizer,” *Optics Express*, Vol. 24, Issue 20, pp. 22555–22562, vol. 24, no. 20, pp. 22555–22562, Oct. 2016, doi: 10.1364/OE.24.022555.
- [35] T. Kawanishi, *Electro-optic Modulation for Photonic Networks*. Cham: Springer International Publishing, 2022. doi: 10.1007/978-3-030-86720-1.
- [36] W. Heni *et al.*, “108 Gbit/s Plasmonic Mach-Zehnder Modulator with > 70-GHz Electrical Bandwidth,” *Journal of Lightwave Technology*, vol. 34, no. 2, pp. 393–400, Jan. 2016, doi: 10.1109/JLT.2015.2487560.
- [37] B. J. C. Schmidt, A. J. Lowery, and J. Armstrong, “Experimental demonstrations of electronic dispersion compensation for long-haul transmission using direct-detection optical OFDM,” *Journal of Lightwave Technology*, vol. 26, no. 1, pp. 196–203, Jan. 2008, doi: 10.1109/JLT.2007.913017.
- [38] Son H. J. and Shin S. M., “Fronthaul Size: Calculation of maximum distance between RRH and BBU,” Apr. 2014.
- [39] C. Lim, A. Nirmalathas, M. Bakaul, K. L. Lee, D. Novak, and R. Waterhouse, “Mitigation strategy for transmission impairments in millimeter-wave radio-over-fiber networks,” *Journal of Optical Networking*, Vol. 8, Issue 2, pp. 201–214, vol. 8, no. 2, pp. 201–214, Feb. 2009, doi: 10.1364/JON.8.000201.
- [40] G. Agrawal, *Nonlinear Fiber Optics*, vol. 5th Edition. Elsevier Inc., 2013. doi: 10.1016/C2011-0-00045-5.
- [41] Tektronix, “Arbitrary Waveform Generators: AWG7000 Series,” Jul. 2018.
- [42] Gooch and Housego, “High Bandwidth DFB Lasers: AA0701 Series,” Aug. 2016.
- [43] E. Vourch, D. le Berre, and D. Hervé, “Lightwave single sideband wavelength self-tunable filter using an InP:Fe crystal for fiber-wireless systems,” *IEEE Photonics Technology Letters*, vol. 14, no. 2, pp. 194–196, 2002, doi: 10.1109/68.980510.
- [44] G. H. Smith, “Overcoming chromatic-dispersion effects in fiber-wireless systems incorporating external modulators,” *IEEE Trans Microw Theory Tech*, vol. 45, no. 8 PART 2, pp. 1410–1415, 1997, doi: 10.1109/22.618444.
- [45] B. Hraimel *et al.*, “Optical single-sideband modulation with tunable optical carrier to sideband ratio in radio over fiber systems,” *Journal of Lightwave Technology*, vol. 29, no. 5, pp. 775–781, 2011, doi: 10.1109/JLT.2011.2108261.
- [46] C. Lim, M. Attygalle, A. Nirmalathas, D. Novak, and R. Waterhouse, “Analysis of optical carrier-to-sideband ratio for improving transmission performance in fiber-radio links,” *IEEE Trans Microw Theory Tech*, vol. 54, no. 5, pp. 2181–2187, May 2006, doi: 10.1109/TMTT.2006.872809.
- [47] EXFO, “XTM-50 Tunable filter with adjustable bandwidth,” Nov. 2020.
- [48] Tektronix, “Digital and Mixed Signal Oscilloscope: MSO/DPO 70000 Series,” Jan. 2015.
- [49] S. Berger, M. Danneberg, P. Zanier, I. Viering, and G. Fettweis, “Experimental evaluation of the uplink dynamic range threshold,” *EURASIP J Wirel Commun Netw*, vol. 2015, no. 1, pp. 1–9, Dec. 2015, doi: 10.1186/S13638-015-0447-6/FIGURES/5.

3. Optical Heterodyne Millimetre Wave Analogue Radio-over-Fibre Fronthauling with Free Running Lasers

Data transmission in the mm-wave (30 – 100 GHz), sub-THz (100 GHz – 300 GHz) and THz (300 GHz – 3 THz) frequency bands [1] and signal distribution over the optical fronthaul network [2] will be two key aspects of the future wireless communication system in order to meet the demand of high speed connectivity. The use of high frequency bands to facilitate wider channel bandwidths will represent a substantial technological shift from the current sub-6 GHz wireless systems. A simple and cost-efficient mm-wave signal generation and distribution technique, with minimal power consumption, must be employed for efficient system deployment. The complexity associated with the electronic generation of the mm-wave carriers hinders its deployment in the mobile network and hence photonic generation techniques such as optical heterodyning are being investigated for efficient and wide deployment. The optically compatible analogue radio-over-fibre fronthaul network can facilitate the distribution of mm-wave carriers to various remote radio head antenna sites through a fibre network [2] - leading the way for centralization of the resources with optical heterodyne analogue RoF link implementation. However, in such systems, the frequency fluctuations and phase noise in the photo-generated mm-wave carrier are shown to be performance limiting factors - especially for the transmission of small baud rate/subcarrier spacing multicarrier signals as provisioned in the 5G and beyond 5G wireless systems [3]. It is necessary to either reduce or compensate these impairments in some way for successful system deployment.

In this chapter, mm-wave signal generation is demonstrated over an optical heterodyne analogue RoF link using free-running laser sources. Two innovative techniques for the compensation of frequency offset and phase noise effect on the performance of low subcarrier spacing OFDM signals are presented. Initially, different components of a general optical heterodyne analogue RoF system with free running laser are discussed in section 3.1. The details of various components, RF frequency down-conversion techniques at the receiver and traditional frequency offset and phase noise compensation techniques are provided. A literature summary of various mm-wave or high frequency THz carrier generation demonstrations using independent lasers is also provided in section 3.1. Two new innovative compensation techniques, i.e. analogue mm-wave receiver and DSP receiver, are discussed in sections 3.2 and 3.3, respectively. The compensation mechanism and corresponding experimental results are presented by demonstrating successful transmission of 64-QAM data modulated 5G NR compatible low subcarrier spacing OFDM signals over a 25 km standard single mode fibre link. The advantages and limitations of these techniques are discussed in Section 3.4 with regard to the transmission of the 5G NR envisioned subcarrier spaced signals.

3.1 Optical Heterodyne Analogue RoF Link for Millimetre Wave/THz System

The beating of two optical carriers with the desired frequency spacing on a high speed photodetector results in the generation of a microwave/mm-wave/sub-THz/THz radio carrier. The schematic of a general optical heterodyne concept is shown in Fig. 1.12 (chapter 1, section 1.4.2) with two different types of sources, i.e. free-running lasers and an optical frequency comb source. The work presented in this chapter is focused on the use of free-running lasers in an optical heterodyne analogue RoF link for mm-wave carrier generation. The details of OFC based heterodyne system are presented in the next chapter.

3.1.1 A general schematic of Optical Heterodyne Analogue RoF Link

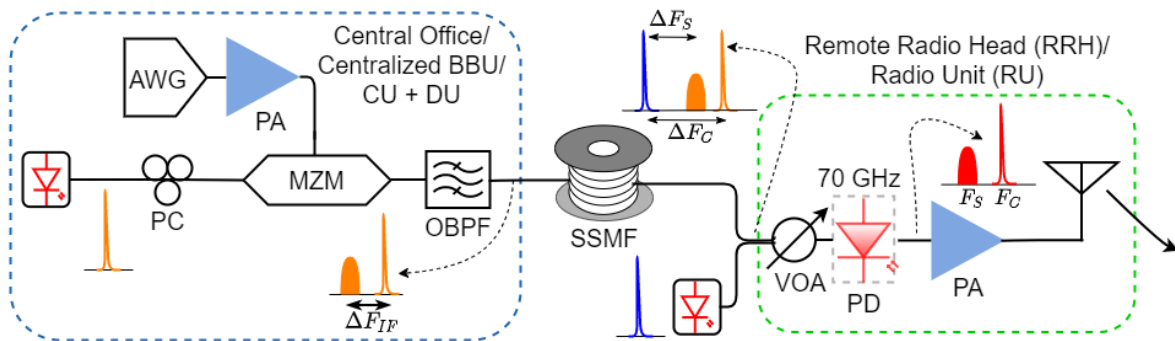


Fig. 3.1 A general schematic of Analogue RoF fronthaul link with remote optical heterodyning for mm-wave/THz frequency signal generation and distribution.

A general schematic of the optical heterodyne analogue radio over fibre link is shown in Fig. 3.1. An optically modulated intermediate frequency analogue data signal is transported over the AIFoF fronthaul link from the C-BBU to the remote antenna unit site. The data signal can be optically modulated using either a direct or external modulation technique, as mentioned in section 2.2.2 in chapter 2. A filtering stage, implemented using either an OBPF or DD-MZM or IQ MZM, is typically employed to generate an optical single sideband signal and avoid the power fading introduced by the effect of fibre chromatic dispersion. Any combination of data modulation stage and filtering can be used for the fronthaul link implementation. Fig. 3.1 shows one such possibility using a Mach-Zehnder modulator and OBPF. An optical carrier and data signal's sideband are transmitted to the antenna site over an optical fibre. The received signal is combined with another optical carrier, with desired mm-wave/THz carrier frequency difference, at the antenna site. The combined optical signal, consisting of an unmodulated carrier, modulated carrier and data sideband (as shown in the figurative spectra in Fig. 3.1), will beat on a high speed photodetector to generate the mm-wave/THz carrier and data signal.

The generated mm-wave/THz signal can be transmitted to the wireless end user after RF amplification. Such an optical heterodyne analogue RoF scheme facilitates the deployment of a simple remote RRH unit consisting of a laser, coupler, high speed PD, RF amplifier and antenna unit. The frequency of the generated

mm-wave signal can be tuned by changing the spacing between two lasers with IF tuning providing an additional degree of freedom. The fine frequency tuning of the laser placed at the remote RRH site will require an intelligence hardware unit – slightly increasing the system complexity. In order to avoid this, both lasers can be placed at the C-BBU site and a combined signal can be transported over the optical fibre to the RRH antenna site. In most of the experiments demonstrated in this thesis, both the optical carriers (modulated and unmodulated) and data signal's sideband are transmitted from the C-BBU to RRH site over an optical fibre.

Theoretically, RF carriers up to 10 THz frequency can be generated with the optical heterodyning technique, however, the practical limitation comes from the bandwidth of the photodetector required for beating the combined signal. Various photo-mixing technologies such as low temperature grown GaAs (LTG-GaAs) [4], PIN photodetector, uni-travelling carrier photodiodes (UTC-PDs) [5] and travelling wave UTC PDs [6] are typically used for the generation of high-frequency carriers. Photo-mixing up to 5 THz frequency is demonstrated using LTG-GaAs and distributed Bragg reflector (DBR) lasers operating in 780 – 850 nm window [4]. The detector used in this demonstration exhibits high power degradation beyond 3 dB bandwidth of 600 GHz and the detection in the non-telecom 780 nm wavelength range adds to its disadvantages. For operation in the optical fibre low loss 1550 nm window, the regular PIN PDs and UTC-PDs provide an excellent performance for mm-wave/THz generation. PIN PDs with up to 1 THz of bandwidth are reported in the literature [7], however, the low output power at such high frequencies can limit the performance of related wireless communication systems. The UTC-PDs offer higher bandwidths up to 2 THz [8], by overcoming the transit time limitations of PIN PDs, and offer two orders of magnitude increase in the detected power due to high output saturation current. Combining travelling wave (TW-UTC PD) and waveguide coupling with UTC-PDs can increase the detected power to 100s of micro watts [9]. Also, some antenna elements coupled with PDs have been developed [8] [10], [11] in order to minimize the waveguide losses and increase the radiating power. The experimental demonstrations reported in this thesis were limited to the 60 GHz band due to the availability of 70 GHz UTC-PD in our lab.

Two different types of user architectures are typically used for the frequency down-conversion and demodulation of the received mm-wave/THz signal as shown in Fig. 3.2. The first architecture depends on the use of an RF heterodyne receiver using an external LO and mixer [12], while the second direct detection receiver uses a diode to capture the envelope and frequency down-convert the received signal [12]. In the first heterodyne receiver architecture, the mm-wave/THz signal will be down-converted to either baseband or an intermediate frequency depending on the frequency of LO used for mixing. In practice, multiple down-conversion stages will be employed to bring back the antenna received signal to baseband frequency.

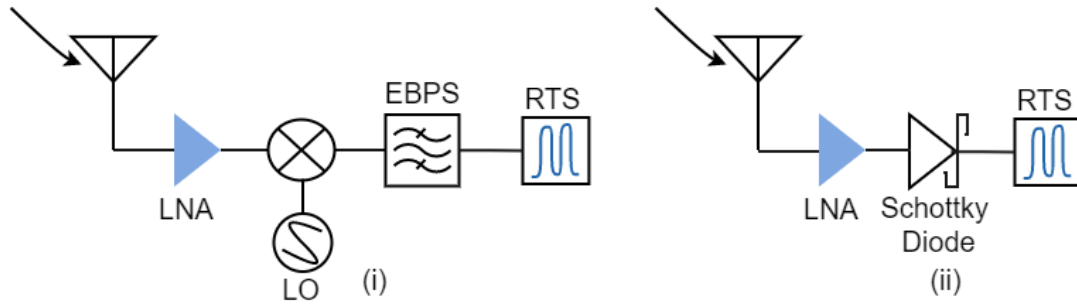


Fig. 3.2 Architecture of (i) a standard external local oscillator heterodyne receiver and (ii) direct detection diode receiver used in the wireless system for frequency down-conversion in the end user.

Additional filters and amplifiers will be required depending on the nature of frequency down-conversion used in the receiver. Alternatively, a direct frequency down-conversion can be achieved by RF direct detection diodes such as Schottky barrier diode (SBD), resonant tunneling diode (RTD), Fermi level managed barrier diode (FMBD) or envelope detector (ED) [13]. A summary of various types of diodes used for mm-wave/THz signal detection is provided in [13]. While the use of diode-based architecture reduces the receiver's complexity and achieves fluctuation-free envelope detection, the low conversion efficiency can reduce its suitability in practical systems relative to the heterodyne receiver approach. For the mm-wave optical heterodyne A-RoF experiments presented in this thesis, a single stage frequency conversion stage is used with an external LO frequency operating at the same frequency spacing between the beating optical carriers and resulting in mm-wave signals down-conversion to IF. The captured signal can be processed in real time using a processor or offline processing can be performed on the RTS captured signal to evaluate the system performance in terms of BER and EVM.

The random frequency fluctuations from the lasers used for heterodyning and the use of a fixed frequency LO for down-conversion at the receiver will result in a frequency offset in the captured IF signal. Fig. 3.3(i)

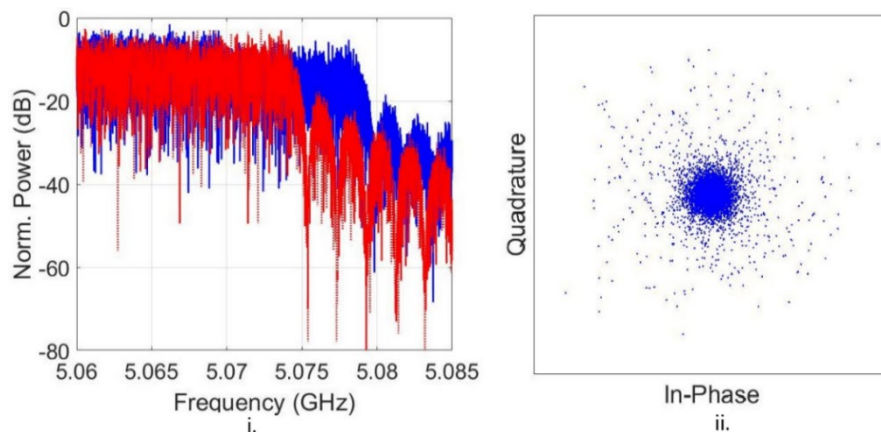


Fig. 3.3 (i) A portion of the transmitted (red) and received (blue) IF OFDM signal spectra showing non-overlap due to FO and (ii) Constellation of the demodulated signal in an optical heterodyne A-RoF link with free running lasers and fixed frequency external LO down-conversion receiver.

shows a non-overlapping spectrum between a portion of the transmitted (red) and received (blue) IF signal resulting from laser frequency fluctuations. Demodulation of such frequency-shifted IF OFDM signal, after capturing and offline processing using Matlab will result in the distorted constellation as shown in Fig. 3.3(ii). The level of performance degradation due to FO and PN varies with the nature of the waveform used for data transmission. For single carrier waveforms such as QPSK/QAM mixed with an IF carrier, the effect of FO and PN is minimal due to a relatively larger baud rate and smaller symbol duration [14]. In the case of multicarrier waveforms such as OFDM/UF-OFDM, the entire spectrum is divided into multiple subcarriers leading to a smaller baud rate or subcarrier spacing and larger symbol duration. In order to maintain the orthogonality of such multi-carrier signals, the FO should be less than 2% of the subcarrier spacing [15], [16], which goes as low as 60 kHz for 5G [17]. Also, the phase noise accumulates over time, as evident from the Weiner process representation, and the longer symbol duration of OFDM signals undergoes a larger impact from the phase fluctuations. A previous study in [3] has shown that a laser with less than 900 Hz linewidth will be required for the successful transmission of the 60 kHz subcarrier spacing 64-QAM data modulated OFDM signal over an optical heterodyne system.

Deploying lasers, with such stringent requirements of having frequency fluctuation in a few kHz range and linewidth below 900 Hz, is economically not viable. As shown in section 1.4.3 of chapter 1, commercial lasers exhibit frequency fluctuations in the order of several 10s of MHz to 100s of MHz and their linewidth ranges from several kHz to 10s of kHz. In order to avoid the FO, the external LO used for down conversion of the mm-wave OFDM data signal to IF, needs to replicate the laser frequency drift over time in order to reliably recover the data. Alternatively, the frequency and phase fluctuations of the beating optical carriers need to be correlated or some compensation technique needs to be employed for successful optical heterodyne analogue RoF system implementation. A summary of a few traditional frequency offset and phase noise compensation techniques is given in the next subsection.

3.1.2 Summary of frequency offset and phase noise compensation techniques

Traditionally techniques such as optical injection locking [18], optical phase locked loop [19] and optical injection phase-lock loop [20] are used for correlating the frequency and phase fluctuations of the free running lasers to achieve a stable mm-wave/THz carrier generation. Alternatively, correlated optical tones from an optical frequency comb (OFC) source [3], [21] can be also used for stable carrier generation. The details of OFC based system are presented in chapter 4. Fig. 3.4 shows the schematic of optical injection locking (OIL) and optical phase locked loop (OPLL) techniques. In the optical injection locking scheme [18], a master laser is directly modulated with a reference RF signal and the generated harmonic components, with desired mm-wave/THz carrier frequency difference, are injected into two slave lasers as

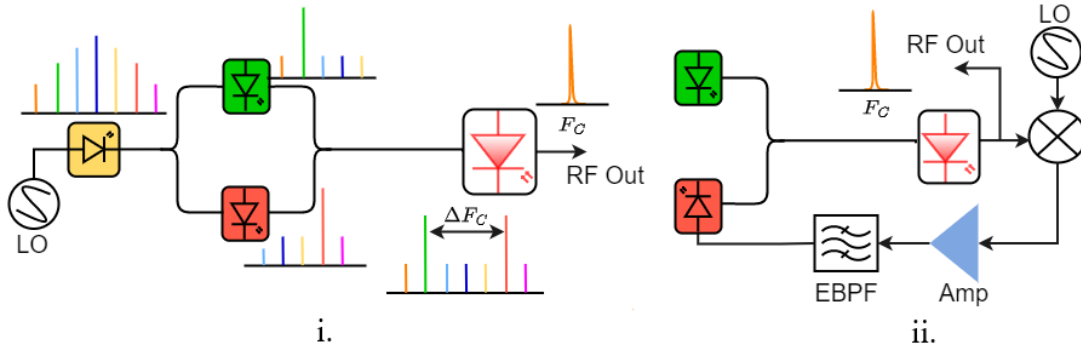


Fig. 3.4 Schematic of (i) Optical Injection Locking and (ii) Optical Phase-Locked Loop techniques for correlating the frequency and phase fluctuations of free-running lasers.

shown in Fig. 3.4(i). The frequency of the free-running slave lasers needs to be tuned close to the injected harmonics frequency for achieving stable locking and correlation. A frequency stable and low linewidth master laser might be required in this case to achieve stable locking and low phase noise carrier generation. Also, in order to generate higher frequency mm-wave/THz carriers, a higher number of harmonics need to be generated – requiring high power RF reference signal to modulate the master laser. The requirement of a low linewidth master and high power RF source puts the OIL at a disadvantageous position.

In the optical phase locked loop scheme [19], shown in Fig. 3.4(ii), the frequency error from the beating of heterodyne generated mm-wave carrier and a fixed frequency external local oscillator is fed to one of the free-running lasers – resulting in low phase noise and frequency fluctuation-free carrier generation. OPLL technique requires lasers with narrow linewidth limiting the phase fluctuations to low frequencies [19] and the frequency of reference LO used for frequency down-conversion should be close to the generated mm-wave/THz carrier frequency. While the OPLL technique has shown very promising results in mitigating the frequency fluctuations and phase noise, implementation of the feedback loop from RRH to the C-BBU site will need an additional link – increasing the latency and overall complexity of the system. In the optical injection phase locking (OIPL) scheme, OIL and OPLL are combined to improve both the frequency and phase correlation between the beating lasers by simultaneously injecting and modulating one of the slave lasers [20]. Such complex implementation requires two external LO sources, a feedback mechanism along with a low linewidth master laser in the system.

The techniques mentioned above demonstrate efforts for the correlation of optical tones from two free-running lasers used for heterodyning. These techniques achieve the correlation at the expense of increased optical/electrical complexity as seen in Fig. 3.4. Alternatively, some techniques which compensate for the effect of laser frequency fluctuations and phase noise are also used traditionally in an optical heterodyne system. As mentioned in section 3.1.1, the use of a direct frequency down-conversion receiver using diodes such as an envelope or Schottky barrier diode captures the envelope mm-wave signal and achieves

frequency fluctuation-free signal detection. The use of digital signal processing algorithms for FO and PN compensation is a well-explored topic in high baud-rate optical communication systems [22]–[24]. Traditionally, wireless systems also use different DSP algorithms to correct for the Doppler frequency shift [25] and phase noise from RF LO [26], [27].

In this thesis, two different techniques to mitigate the effect of laser frequency fluctuations (i.e. frequency offset) and phase noise/linewidth on the system performance are presented. The first approach advocates the use of an analogue mm-wave receiver [28], while the second approach uses digital signal processing algorithms [29]. Details and results related to these techniques are presented in sections 3.2 and 3.3. A summary of various mm-wave/THz optical heterodyne system demonstrations reported in the literature is provided in the next subsection.

3.1.3 Literature summary of Optical Heterodyne demonstrations using free-running lasers

Table. 3.1. Summary of various heterodyne demonstrations reported in the literature.

Author & Reference	Frequency (GHz)	Modulation, Baud Rate & Data Rate	mm-wave/THz Receiver Type	Compensation Mechanism
H. Y. Chen [30]	47.7	64-QAM OFDM, ~47 Mbaud, 24 Gbps	Harmonic Mixer	Injection Locking of FP modes
Javier Santacruz [31]	24.75	16-QAM OFDM, 60 kbaud, ~677 Mbps	Heterodyne Receiver	OPLL & DSP FO compensation
A. H. M. Razibul Islam [32]	35.75	OOK, 155 Mbaud, 155 Mb/s	Self Homodyne RF Receiver	RF self beating for compensation
Toshiaki Kuri [33]	59.6	OOK, 155.2 Mbaud, 155.2 Mbps	Square Law Detector and Mixer	Phase noise cancelling
Ramin Khayatzadeh [34]	95.5	OOK, 2 Gbaud, 2 Gbps 16-QAM, 200 Mbps	Envelope Detector	Envelope Detection
Andreas [35]	328	64-QAM OFDM, ~120 Mbaud, 59.06 Gbps	Schottky Barrier Diode	Envelope Detection
Sang-Rok Moon [36]	300	PAM-8; 30 Gbaud, 90 Gbps	Schottky Barrier Diode	Envelope Detection and DSP
Xinying Li, [37]	375 – 500	6 λ WDM PDM-QPSK, 5 Gbaud, 120 Gbps	Mixer, Amplifier, Multiplier Stages	Digital Signal Processing
Xinying Li [38]	124.5	4 \times 4 MIMO PDM 64-QAM PS 5.5; 24 Gbaud, 1 Tbps	Heterodyne Receiver with external LO	Look up table pre-distortion and receiver DSP

Table. 3.1 summarizes some of the optical heterodyne system demonstrations reported in the literature using free-running laser sources. The table highlights the frequency of generated mm-wave/THz signal,

type of modulation format used for the data transmission, baud rate and data rate of the signal, type of RF receiver architecture used for frequency down-conversion and the FO and PN compensation technique employed in these demonstrations.

The frequency of the generated mm-wave/THz signals in these demonstrations varies from 24.75 GHz to 500 GHz. In [37], authors generated THz signals between 350-500 GHz frequency range and achieved total data transmission rate of 120 Gbps with polarization division multiplexed quadrature phase shift keying (PDM-QPSK) data transmission on a six wavelength WDM optical fronthaul link. They further increased the data rates to 1 Tbps in [38] by transmitting PDM 64-QAM probabilistic shaped (PS) data over a 4×4 MIMO wireless link at 124.5 GHz mm-wave carrier generated using optical heterodyning. In most of the above mentioned demonstrations, single/multi-carrier waveforms with high baud rate (>100 Mbaud), were transmitted over an optical heterodyne link. As mentioned earlier, the effect of generated mm-wave carrier phase noise on high baud rate signals is minimal compared to the low baud rate multicarrier signals such as those provisioned in the 5G NR standard. The demonstrations in [34]–[36] used diodes to capture the envelope of mm-wave signal and achieve direct frequency down-conversion to the baseband/IF, while authors in [30], [31], [37], [38] used mixer and external LO based frequency down-conversion receiver. The optical injection locking technique was used in [30] for FO and PN compensation, while the authors in [31] used a combination of OPLL and DSP algorithms to mitigate the impairments. In the next two sections, we demonstrate two innovative techniques for the FO and PN compensation over an optical heterodyne analogue RoF link.

3.2 Analogue mm-wave Receiver for the FO and PN Compensation

3.2.1 Experimental Details

The schematic of the general optical heterodyne mm-wave A-RoF fronthaul link experimental setup using free-running lasers (with representative spectra along the transmission path) is shown in Fig. 3.5. The

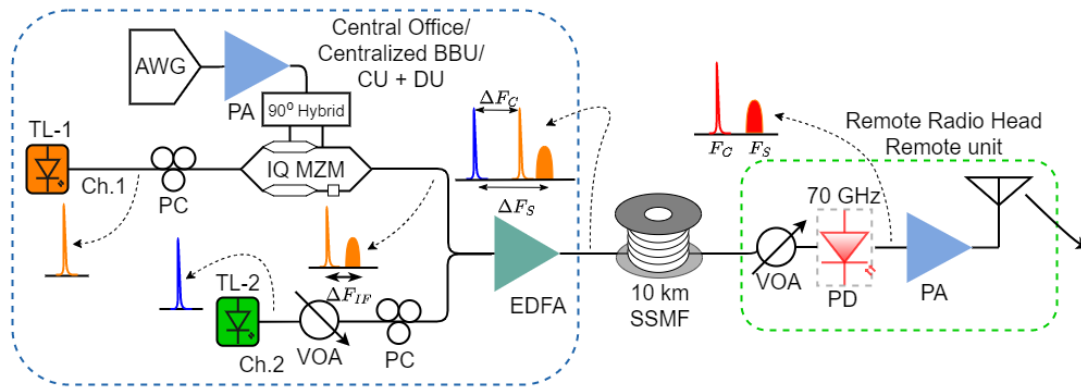


Fig. 3.5 Schematic of Optical heterodyne with analogue RoF fronthauling for remote mm-wave carrier generation and distribution.

system architecture is designed to replicate the future mobile fronthaul link wherein spectrally efficient signals are transported between C-BBU and RRH site over an analogue RoF link implemented using low bandwidth optical components. Optical heterodyning of the relevant optical data signal and carrier is then implemented at the RRH to achieve remote frequency up-conversion of the data to the mm-wave band. Two optical carriers with frequency spacing (ΔF_c) close to the desired mm-wave carrier frequency, 56 GHz in this case, from two free-running tuneable lasers (TL1 & TL2) were fed to the Ch. 1 and Ch. 2 of the transmitter. These optical carriers were obtained from two independent hybrid photonics integrated InP-Si₃N₄ micro ring resonator external cavity lasers (MRR-ECL) from LioniX International [39].

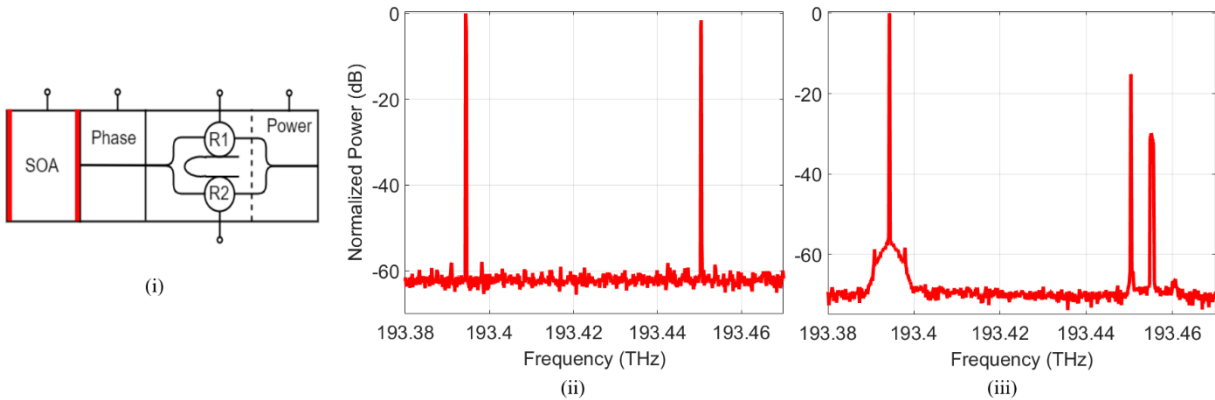


Fig. 3.6 (i) Schematic and (ii) combined spectrum of photonics integrated hybrid InP-Si₃N₄ micro ring resonator external cavity lasers and (iii) combined signal spectrum at the input of fibre.

The schematic of the hybrid photonic integrated circuit (PIC) lasers is shown in Fig. 3.6(i). It consists of an InP-based semiconductor optical amplifier (SOA) gain section coupled to a TriPleX (Si₃N₄-based photonic waveguide platform [40]) external cavity. The high and low reflectivity of the back and front facets of the InP gain section reduces the losses and imposes the lasing on the external cavity, respectively. The TriPleX waveguide external cavity consists of two cascaded MRRs with slightly different radii. This allows the exploitation of the Vernier effect to achieve discrete tunable single mode lasing across the C-band. The phase section, as shown in Fig. 3.6(i), can be used to tune the longitudinal modes and achieve fine wavelengths. The output power from the laser can be optimized by tuning the coupling coefficient in the power section. The laser exhibits an excellent linewidth of ~ 35 kHz; side mode suppression ratio (SMSR) of > 50 dB and maximum output power of +10 dBm over a discrete tuning range of 50 nm. The complete characterization of the device can be found in [39]. These lasers were tuned to operate at 193.394 THz and 193.45 THz frequencies, giving a frequency separation of 56 GHz. The combined spectrum of the two lasers is shown in Fig. 3.6(ii). The output power from each device was +10 dBm.

An optical single sideband modulated OFDM signal (orange signal in Fig. 3.5) is generated using an I/Q Mach-Zehnder Modulator and an electrical 90° hybrid coupler in Ch. 1. The OFDM signal was generated in the electrical domain, at an intermediate frequency of 5 GHz (F_{IF}), using an AWG. The OFDM signal

consists of 64-QAM modulated subcarriers at a spacing of 1.95 MHz. The flexibility in the choice of IF carrier results in relaxed constraints on the tunability of the lasers used for heterodyning. Also, the modulation bandwidth of the external modulator and AWG specifications need to be proportional to the IF carrier frequency. The OSSB modulated carrier was combined with the un-modulated carrier from Ch. 2 (blue carrier in Fig. 3.5) and transmitted through 25 km of SSMF after amplification by an EDFA. The combined optical signal spectrum is shown in Fig. 3.6(iii). A variable optical attenuator was used in Ch. 2 to equalize the optical power between the two paths due to different losses.

Two optical tones, separated by 56 GHz, and a data signal which is modulated 5 GHz away from one of the carrier tones, were transmitted together through the fibre to the RRH site transmit antenna. The photo-mixing of these three optical frequency components, on a 70 GHz PIN PD, generates the electronic copies of the mm-wave OFDM data signal at $F_S = 61 \text{ GHz}$ (from *un-modulated carrier* \times *OSSB data sideband* mixing) along with a mm-wave carrier at $F_C = 56 \text{ GHz}$ (from *carrier* \times *carrier* mixing). The strength of the generated mm-wave carrier and data signal will depend on the powers of all the beating terms, i.e. the modulated and un-modulated optical carriers as well as the OSSB modulated data signal. A relatively strong mm-wave data signal will be generated at F_S if the modulated carrier (orange carrier in Fig. 3.5) remains suppressed after OSSB modulation. The level of suppression on the modulated carrier can be changed by varying the bias applied to I-Q MZM. If the modulated carrier is un-suppressed after OSSB modulation, the beating between two optical carriers will produce a relatively high-powered mm-wave carrier at F_C . Such a strong mm-wave carrier can lead to saturation of the power amplifier used after the PD. A VOA was used at the RRH site to control the total optical power incident on the high-speed PD.

The photo-mixing generated 61 GHz OFDM signal can be directly transmitted to the wireless user using mm-wave antenna elements, after RF amplification, as shown in the RRH box of Fig. 3.5. It should be mentioned that the wireless transmission of the generated mm-wave signal was not carried out in this experiment. The output of PD was directly connected to the input of frequency down-conversion stage of user side receiver presented in Fig. 3.7.

3.2.2 Receiver Structure and Compensation Mechanism

The photo-mixing, at the RRH site, generates the electronic copies of the mm-wave OFDM data signal at $F_S = 61 \text{ GHz}$ and a mm-wave carrier at $F_C = 56 \text{ GHz}$. The frequency drift of the free-running lasers (TL1 & TL2) will result in the equal amount of frequency shift (say δF) in both F_C (will become $F_C \pm \delta F$) and F_S (will become $F_S \pm \delta F$), after the photo-detection. The frequency shift, δF , changes over time, but the difference between F_S and F_C will remain equal to F_{IF} . The frequency down-conversion of such mm-wave OFDM data signal, centred at $F_S \pm \delta F$, using a fixed frequency external LO and mixer (as shown in the architecture of Fig. 3.2(i)) results in the frequency shifted IF signal, with a spectrum as presented in Fig.

3.3(i). Demodulation of such frequency shifted IF signal, after capturing and processing using Matlab will result in the distorted constellation, due to FO and PN, as shown in Fig. 3.3(ii). Hence, the external LO used for down conversion of the mm-wave OFDM data signal to 5 GHz IF, needs to replicate the laser frequency drift over time in order to recover the data.

Regardless of the frequency drift of free-running tuneable lasers, the difference between $F_C \pm \delta F$ and $F_S \pm \delta F$ terms will always be equal to 5 GHz, which is the original IF. Hence, the mixing of these two mm-wave components can lead to frequency down-conversion of the mm-wave data signal ($F_S \pm \delta F$) to the original 5 GHz intermediate frequency - eventually making the system agnostic to the laser frequency drift. Achieving robustness to FO in this way negates the requirement for frequency correlation, or locking, between the laser sources - significantly reducing transmitter complexity. Also, the generated mm-wave carrier at $F_C \pm \delta F$ can be used as an external LO for the frequency down-conversion of the mm-wave data signal; achieving an external ‘LO-free’ frequency down-conversion. Eventually, this will necessitate the transmission of both photo-mixing generated mm-wave data signal and carrier over the wireless channel. This concept has led to the design of our analogue mm-wave receiver shown in Fig. 3.7.

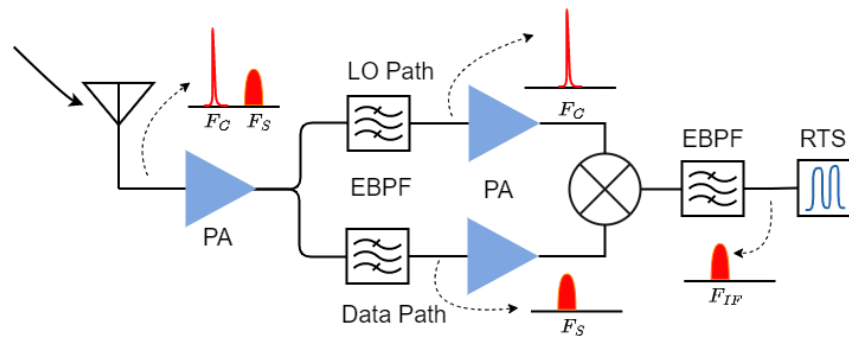


Fig. 3.7 Analogue mm-wave receiver architecture for FO & PN compensation over optical heterodyne A-RoF system using independent laser sources.

The signal captured by the antenna was split into two paths, the LO arm and data arms, to separate the mm-wave carrier and data signal, respectively, using electrical bandpass filters (EBPF). The centre frequencies and 3dB bandwidths of both EBPFs were chosen considering the frequency of IF data and frequency drifts of the commercially available tuneable lasers. EBPF with a centre frequency of $f = 56$ GHz and bandwidth of $BW = 500$ MHz was used in the LO arm, while the data arms filter centre frequency and bandwidth values were $f = 62$ GHz and $BW = 6$ GHz, respectively. The filtered mm-wave carrier and data signal were mixed together resulting in a data signal output at IF of 5 GHz. A real-time oscilloscope operating at 50 GSa/s was used to capture this IF signal. The captured signal was digitally resampled, frequency down-converted to the baseband and demodulated in Matlab. The bit error rate and error vector magnitude performance of the system were evaluated. The minimum power level, of the IF signal, on the

receiver side was limited to -28 dBm due to the significant effect of quantization noise introduced by the RTS below this power.

It is worth mentioning that the photo-mixing generated mm-wave carrier will have the same phase noise as that of the mm-wave data signal. Mixing of these phase noise correlated mm-wave frequency components, results in the cancellation of the RF phase noise, on the IF signal, upon frequency down-conversion. Achieving phase noise cancellation, in this manner, effectively removes the requirement for phase correlated or ultra-low linewidth laser sources which have been shown to be of paramount importance for heterodyne A-RoF systems. The presented architecture permits a significant reduction in the complexity of the C-BBU transmitter and RRH antenna site. It should be noted that these advantages come at the cost of a requirement for transmission of the mm-wave carrier over the wireless channel (after the PD) in tandem with the data signal.

The previous system demonstrations [41], [42] use a similar electronic phase noise cancellation mechanism, but the requirement of a correlated dual-mode optical source, for the de-multiplexing and cancellation operation, increases the receiver unit's optical complexity. A similar concept is demonstrated in [43] albeit with the use of square law non-linear device which potentially puts additional constraints on input (received) power.

3.2.3 System Performance

Initially, the mm-wave A-RoF heterodyne system using two hybrid photonic integrated InP-TriPleX tunable lasers at the transmitter was tested with a standalone 56 GHz external LO at the receiver. A universally filtered OFDM signal consisting of 76 subcarriers modulated with 64-QAM data symbols at a spacing of 1.95 MHz was generated offline. This signal, with a BW of ~148 MHz and a raw data rate of 0.89 Gb/s, was OSSB modulated on one of the optical carriers as explained in the previous subsection. The frequency offset between the generated mm-wave signal and fixed frequency external LO results in the non-overlapping transmitted (red) and received (blue) IF signal spectra as shown in Fig. 3.3(i). A maximum carrier frequency offset/spectrum non-overlap of ~10s of MHz was observed over several captures. As mentioned earlier, the captured OFDM signal could not be demodulated successfully due to the combined effects of FO and PN, resulting in the received noisy constellation presented in Fig. 3.3(ii).

The standalone external LO receiver was replaced by the analogue mm-wave receiver in order to test its capabilities for FO & PN compensation. A perfect overlap between a portion of the transmitted (red) and received (blue) IF signal electrical spectra, shown in Fig. 3.8(i), indicates that the implemented analogue mm-wave receiver was able to compensate for the frequency fluctuations between the two free running lasers. Moreover, the effect of phase noise, arising from the use of two ~35 kHz linewidth lasers, was also

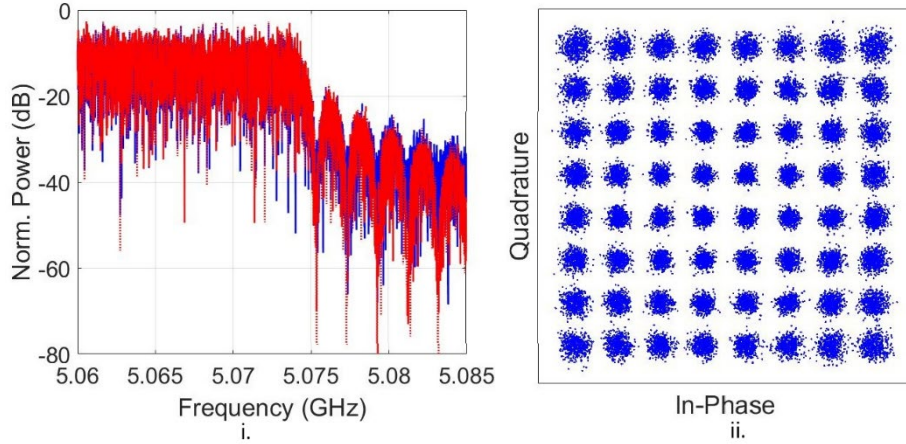


Fig. 3.8 (i) A portion of the transmitted (red) and received (blue) IF signal spectra showing exact overlap and (ii) Constellation of the demodulated signal in an optical heterodyne A-RoF link with free-running lasers source and standalone analogue mm-wave receiver.

compensated by the receiver as evident from the good constellation of the demodulated signal shown in Fig. 3.8(ii). Optical heterodyning, even with two low-linewidth (35 kHz) free running lasers, generates an mm-wave data signal with insufficient purity in order to support 64-QAM subcarrier modulation at a 1.95 Mbaud rate. However, by utilizing the proposed receiver architecture, the phase noise cancellation and successful demodulation of the UF-OFDM signal was achieved. The constellation shown in Fig. 3.8(ii) represents a measured EVM of 5.8% with a BER of 7.4×10^{-5} . Furthermore, the performance of the presented system was analysed with received optical power variations for single and five signal band transmission scenarios.

Fig. 3.9 (i) shows the received optical power versus BER performance for back-to-back and 25 km fibre transmission cases when a single band of UF-OFDM was transmitted over the presented optical heterodyne A-RoF link. No performance penalty was observed after 25 km optical fibre transmission. A BER value of

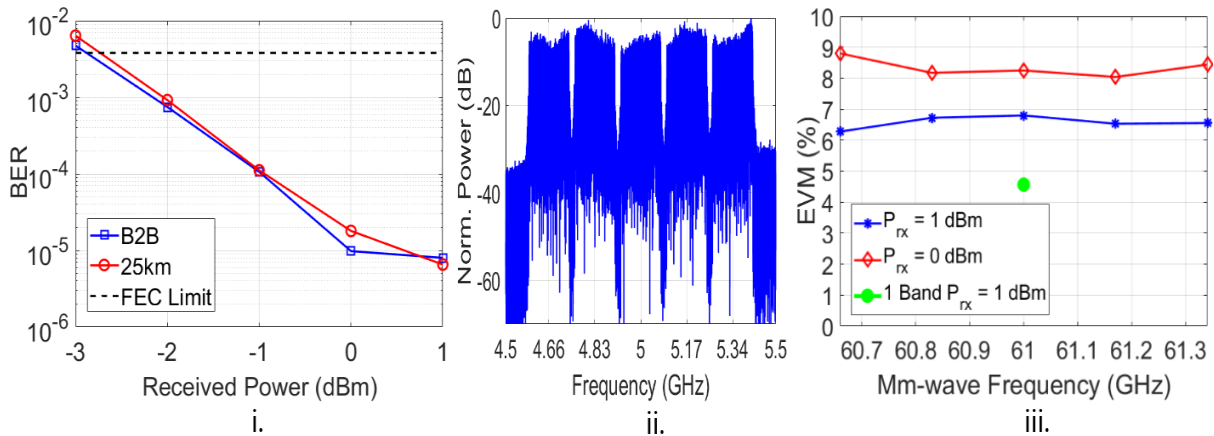


Fig. 3.9 (i) BER vs received optical power for a single UF-OFDM signal band; (ii) spectrum of captured 5 band signal and (iii) measured EVM for the five signal bands over an optical heterodyne A-RoF link with free-running lasers source and standalone analogue mm-wave receiver.

6.5×10^{-6} (EVM of $\sim 4.5\%$) was measured at the received optical power of +1 dBm. Performance just above the FEC limit BER of 3.8×10^{-3} was measured at -3 dBm received optical power and beyond which results are impacted by quantization noise introduced by the RTS. In order to demonstrate the capabilities of the presented optical heterodyne A-RoF system to serve multiple users simultaneously, 5 UF-OFDM signals modulated at different IF carriers were combined and OSSB modulation was performed on one of the optical carriers as explained in the previous subsection. A guard band of 20 MHz between each signal band was maintained. The heterodyning process will generate mm-wave data signals at 60.66, 60.83, 61, 61.17 and 61.34 GHz frequencies, with each signal band carrying the 64-QAM data at a rate of 0.89 Gb/s (total data rate: $0.89 \text{ Gb/s} \times 5 = 4.45 \text{ Gb/s}$). The spectrum of the frequency down-converted received signal is shown in Fig. 3.9(ii). The EVM of each received and frequency down-converted and demodulated UF-OFDM signal band after transmission over a 25 km optical heterodyne A-RoF link is shown in Fig. 3.9(iii). Results show performance degradation with a multi-band transmission scenario compared to the single-band case. This performance degradation can be attributed to the reduced RF power per band resulting from the use of a single RF amplifier at the output of the AWG – similar to the previous observation in the multi-band AIFoF link demonstration discussed in section 2.3.2 of chapter 2. Nevertheless, below FEC EVM limit performance was measured across all the bands with each received UF-OFDM signal exhibiting less than 7% EVMs values at +1 dBm received optical power. At 0 dBm power, EVMs between 8 and 9%, correspond to system performance just on or slightly below the FEC threshold. These performance levels are comparable to those achieved for similar multi-band transmission in a heterodyne system with correlated optical sources [44].

These experimental results highlight the proposed system's robustness to both frequency fluctuations and phase noise while facilitating a reduction in the optical complexity of the A-RoF heterodyne system - arising from the use of unlocked and un-correlated free-running lasers. The hybrid InP-TriPlex tunable lasers are inherently compatible with the photonic integration of optical modulators, amplifiers, and power combiners creating the possibility of a fully photonic integrated optical heterodyne A-RoF transmitter. Also, the fine and wide wavelength tunability capabilities of the deployed integrated laser provide an additional advantage while implementing a converged access network for wireline and wireless services. The implementation of the analogue mm-wave receiver increases the hardware complexity of the user-side receiver, and the requirement of photo-mixing generated mm-wave carrier transmission along with the data signal adds to its disadvantages. The current mobile communication systems do not have a provision for the transmission of an mm-wave carrier over the air. However, as deployed networks evolve to exploit the mm-wave technologies, the costs associated with the remote carrier generation at the user side make the concept of a centralized carrier distribution attractive. The line-of-sight nature of such mm-wave/THz wireless links, primarily due to the limited range and high beam directivity, will limit the effect of dispersive

fading, shadowing and jamming the other antenna elements. The compatibility of this receiver structure needs to be studied for advanced wireless systems consisting of MIMO and beamforming antenna structures used for achieving high data rate transmission. Meanwhile, this compensation mechanism can be used in applications where the constraints on the spectrum are not stringent. In the next section, receiver DSP-based FO and PN compensation is demonstrated over an optical heterodyne A-RoF system.

3.3 DSP Receiver for the FO and PN Compensation

The analogue mm-wave scheme demonstrated in the previous section uses a hardware-based approach and exploits the correlation between photo-mixing generated components for FO and PN compensation. It requires the transmission of the mm-wave carrier along with data signal – leading to a different network design from the current standard and practice. In order to avoid this, the DSP receiver approach uses a standard heterodyne receiver, with an external LO and mixer based receiver shown in Fig. 3.2(i), for mm-wave signals frequency down-conversion to IF. Standard digital signal processing algorithms were used for the FO and PN estimation and compensation. The hardware complexity of the analogue mm-wave receiver is transferred to the digital domain in this scheme. In the absence of a feedback mechanism to track the laser frequency fluctuations (or inability to transmit the photo-mixing generated carrier as presented earlier), a fixed frequency LO along with digital signal processing impairment compensation at the receiver side can lead to the deployment of simple and cost efficient mm-wave A-RoF system.

The fronthaul link and transmitter architecture used for this scheme remain the same as shown in Fig. 3.5, with the exception that the photo-mixing generated mm-wave carrier is suppressed. In this case, two low noise tunable fibre lasers, each with a linewidth of ~ 2 kHz, were used at the transmitter instead of the integrated lasers used in the previous scheme. The standard ‘Schmidl and Cox’ (S&C) [45] and decision directed least mean square (DD-LMS) algorithms were used for FO & PN compensation, respectively. The implementation of these DSP algorithms will not increase the processing complexity as these algorithms have been traditionally implemented in the wireless systems for RF FO & PN compensation at the mobile receivers. Robustness to timing and frequency offsets through digital means is a well-explored topic for high baud rate optically coherent OFDM systems [23], [24], which are inherently more tolerant to frequency and phase offsets compared to small baud rate A-RoF systems.

Initially, the FO and PN compensation is demonstrated by transmitting a ~ 200 MHz bandwidth OFDM signal with 100 subcarriers at a spacing of ~ 2 MHz over the link. The subcarrier spacing of the OFDM signal was varied from 2 MHz to 62.5 kHz in order to analyse the capabilities of the optical heterodyne analogue RoF link with DSP compensation for supporting 5G NR compatible low subcarrier spacing signal transmission. The compensation capability of the DSP algorithm was also analysed by varying the FO introduced with external LO frequency variation.

3.3.1 FO and PN Compensation Mechanism

Initially, an mm-wave carrier and data signal were generated at 56 GHz and 61 GHz frequencies, respectively, by beating two optical carriers and a data sideband on high speed PD after transmission over an optical heterodyne analog-RoF link as explained in section 3.1.1. The photo-mixing generated mm-wave data signal was frequency down-converted to the IF band at the user unit side, using an external LO and mixer. The IF signal was captured using the RTS and offline processing was performed for BER and EVM evaluation. The flow chart of the steps involved in offline processing is shown in Fig. 3.10. The spectrum of the captured IF signal resembles the one shown in Fig. 3.3(i), as relative frequency drift between the two

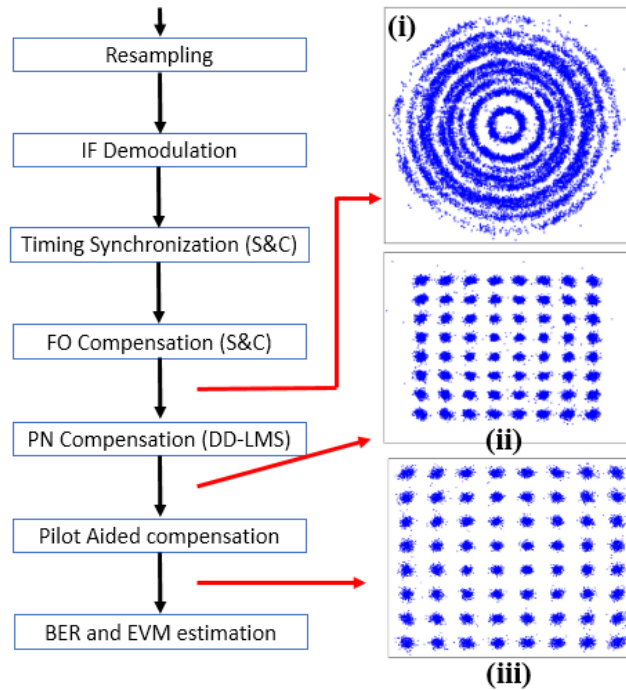


Fig. 3.10 The flow chart of offline DSP operations for demodulation of the signal; Constellation of the received signal after (i) FO compensation only (ii) FO & PN compensation and (iii) all the DSP processing.

fibres lasers prevents successful demodulation of the OFDM signal. The RTS captured OFDM signal, centred at $5 \text{ GHz} \pm \delta F$, was first frequency down converted to the baseband by mixing it with a 5 GHz IF carrier in Matlab. S&C and DD-LMS algorithms were then implemented digitally to help overcome the FO & PN, respectively. Aside from the phase noise, resulting from the linewidths of the lasers, the system will also produce random relative phase variations between the external LO used for down-conversion and the photo-mixing generated mm-wave signal. This additional PN also needs to be compensated for a reliable and successful data transmission.

Timing synchronization and FO estimation in the frequency down converted baseband signal were achieved by searching for an OFDM symbol with two identical halves. This special preamble, as defined

in the S&C algorithm, was transmitted at the start of the OFDM data from the transmitter. The integer (subcarrier index) FO was detected by cross correlation of the transmitted and received preamble, instead of using a second preamble as described in the S&C algorithm. The detected data was counter rotated in the frequency domain by a number of samples equal to the integer FO to correct for the FO. The same preamble was used for channel estimation. The fractional FO, which is less than the OFDM subcarrier spacing, manifests as phase rotation in the constellation. The frequency offset spanning multiple subcarriers can be corrected with the S&C algorithm.

Fig. 3.10(i) shows the constellation of the OFDM demodulated signal immediately after the FO compensation. The rotated constellation indicates the presence of phase noise in the signal, which needs to be corrected for successful signal demodulation. A decision directed least mean square algorithm was implemented in order to track phase rotation with respect to the ideal constellation point and a correction was applied to rotate the constellation points. Fig. 3.10(ii) shows the constellation of the OFDM demodulated signal after FO and DD-LMS PN compensation. Such a blind phase estimation based on the mean squared error with the ideal constellations leads to a phase ambiguity in terms of a fixed phase shift in the QAM symbols. Multiple pilot subcarriers were placed across the occupied OFDM spectrum to estimate this phase shift and the correction was applied to bring the constellation points to their original position. Fig. 3.10(iii) shows the constellation of the OFDM demodulated signal after employing all necessary digital processing for impairment compensation. These constellation results clearly indicate the capabilities of the DSP receiver to compensate the FO and PN completely.

3.3.2 System Performance

Initially, the performance of the outlined system with receiver DSP compensation was analysed with a variable received optical power falling on the PD under the influence of fluctuating frequency spacing

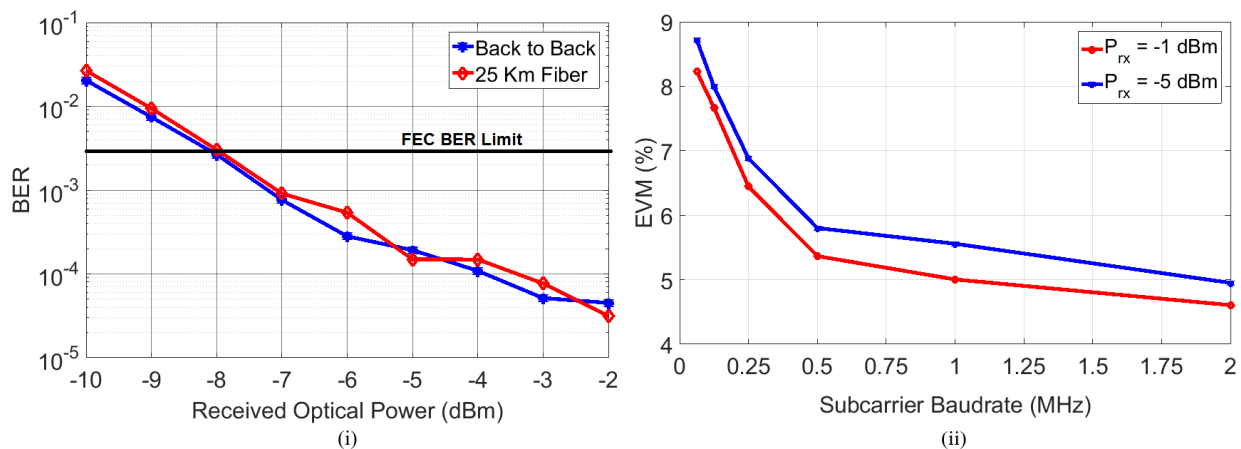


Fig. 3.11 (i) BER vs received optical power and (ii) EVM vs subcarrier spacing/ baud rate performance of the optical heterodyne mm-wave analogue RoF system with DSP impairment compensation.

between two carriers. Fig. 3.11(i) shows the BER performance of 200 MHz BW, ~ 2 MHz subcarrier spacing OFDM signal with variable received optical power for back-to-back and 25 km fibre transmission cases. The results show an excellent measured BER of 3.13×10^{-5} and EVM of 4.76% (represented by the constellation shown in Fig. 3.10(iii)) at a received optical power of -2 dBm. No performance penalty was observed after 25 km of fibre transmission. The excellent performance obtained at these lower power levels is attributed to the good quality of fibre lasers, with SMSR > 50 dB, and digital impairment compensation used for this experiment. Received optical power variations from -2 dBm to -10 dBm resulted in EVM variation from 4.76% to $\sim 12\%$, with performance hitting the hard decision FEC EVM limit of 8% at the received power as low as -8 dBm. The system's performance was limited due to the photodetector's sensitivity at lower power levels.

In order to analyse the system capabilities for 5G NR compatible subcarrier spacing signal transmission, variable subcarrier baud rate OFDM signals were generated by changing the IFFT size and keeping the baseband sampling rate constant. In order to keep the signal bandwidth constant, the number of 64 QAM data modulated subcarriers was increased in proportion to the IFFT size. 100 subcarriers out of 256 were modulated by 64 QAM data to get a baud rate of ~ 2 MHz resulting in a raw data rate of 1.2 Gb/s. Both IFFT size and the number of data subcarriers were increased by a factor of 2 with respect to previous values to reduce the baud rate by a factor of 2 each time. OFDM signals with subcarrier spacing/baud rate values of 2 MHz, 1 MHz, 500 kHz, 250 kHz, 125 kHz and 62.5 kHz were generated, and their performance was analysed after transmission over the presented mm-wave optical heterodyne analogue RoF system.

Fig. 3.11(ii) shows the EVM performance of 200 MHz bandwidth OFDM signals with variable subcarrier baud rates at received optical powers of -1 dBm and -5 dBm. The results show that the implemented system performance degrades as the OFDM signals subcarrier spacing/baud rate reduces. The phase noise of the generated mm-wave carrier does not significantly affect the performance of higher baud rate signals, but as the subcarrier baud rate reduces, the phase noise on the RF beat signal (due to the combined optical phase noise of the fibre lasers) starts to degrade the system performance. Performance goes above the FEC EVM limit of 8%, for 64-QAM modulated data, at the subcarrier spacing of 62.5 kHz and below. Less than 0.5% performance degradation in the EVM is observed when the power falling on the PD is changed from -1 dBm to -5 dBm.

It can be inferred from the results that for the successful transmission of the 62.5 kHz subcarrier baud rate OFDM signal, optical sources with a linewidth of < 2 kHz will be required. The linewidth (~ 2 kHz) of the lasers used in this experiment corresponds to $\sim 1.5\%$ of the lowest subcarrier baud rate (62.5 kHz) used. This is in agreement with the simulation results presented in our previous work [3]. It is important to note that the simulations presented in [3] do not consider the FO effect but our DSP compensation technique

was able to overcome the FO effect and achieve close to simulation performance. Lasers with linewidths of ~ 225 Hz will be required for the successful transmission of 64-QAM multi-carrier signals with the lowest subcarrier baud rates of 15 kHz suggested by 5G NR physical layer specifications [17], over an mm-wave A-RoF heterodyne system.

The fibre lasers used in the experimental setup drift by ~ 30 MHz over several captures, as seen from the max hold results discussed in section 1.4.3 of chapter 1. The DSP algorithms used here successfully mitigate the effect of FO over this range as evident from the constellation result shown in inset (iii) in Fig. 3.10 and the EVM performance of Fig. 3.11. This does not completely test the capabilities of the FO compensation algorithm. For this purpose, additional FO was introduced by changing the frequency of the external LO used for frequency down-conversion at the RRH site. Fig. 3.12 shows the EVM performance of the system with FO variations for three different subcarrier baud rates at a received power of -1 dBm. The results show

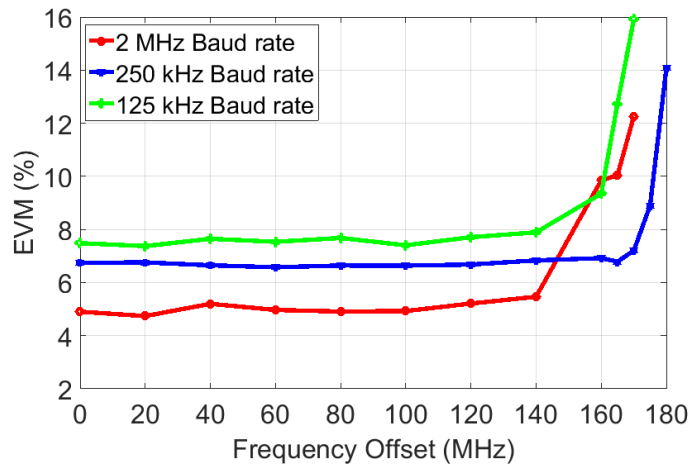


Fig. 3.12 EVM vs Subcarrier Spacing/Baud rate for DSP

compensation based Optical heterodyne mm-wave analogue RoF link.

that the LO induced frequency offsets of up to 140 MHz were successfully compensated digitally without any significant degradation in the system performance - and it is independent of the signal's subcarrier baud rate. The performance degradation observed for FOs beyond 140 MHz can be attributed to the limitations of the S&C algorithm [45]. Most of the commercial lasers exhibit FOs less than or close to 140 MHz – making them a candidate for use in the optical heterodyne A-RoF system with DSP compensation.

The S&C algorithm is typically used in wireless systems for the compensation of frequency offset in OFDM signals. In this work, the same set of algorithms were used to compensate for the impairments arising from the optical fronthaul system. A different set of algorithms can be also used in the demonstrated system as long as successful compensation is achieved for the 5G NR subcarrier spacing signals.

While the presented results show the FO and PN compensation capabilities of the system, however, the user side based compensation requires the transmission of frequency shifted mm-wave signal over the

wireless channel – increasing the probability of interference with the adjacent channels. This limitation of time varying frequency shift of the mm-wave signal can be eliminated by using commercially available lasers, whose frequency drift is limited within the guard bands of the wireless channels. The utilization of established DSP with ‘off-the-shelf’ commercial lasers paves the way for the deployment of a 5G compatible low subcarrier spacing multicarrier signals carrying optical heterodyne mm-wave A-RoF system.

3.4 Discussion

Spectrum and cost efficient front/back-haul networks and power efficient and simplistic mm-wave generation techniques are two key elements to the development of future high speed mobile communication systems. The fronthaul network should facilitate the centralization of resources along with simplifying the RRH antenna site architecture. In the currently employed CPRI or e-CPRI fronthaul links, digitization of the baseband signal increases the transmission rate over the link, while moving some of the functionalities to the RRH antenna site which requires high speed DAC/ADC. The digitized baseband implementation of current fronthaul transmission links requires remote frequency up-conversion, at the RRH site, for mm-wave operation – limiting the scope for cost saving through hardware centralization.

Meanwhile, with the optical heterodyne A-RoF technique, the RF data signal is directly generated in the mm-wave band as a result of the photodetection process. This simplifies the RRH site as it requires only one high speed photodetector, for mm-wave signal generation, while placing most of the processing components at the C-BBU, as shown in the architecture of Fig. 3.5. The optical heterodyne A-RoF link aids the centralization goal of the fronthaul network while retaining the spectral efficiency of the wireless signal over the optical fronthaul link. Also, a laser-free RRH site can be implemented by tapping and reusing the unmodulated carrier, in the optical heterodyne mm-wave A-RoF link, for carrying the uplink data to the C-BBU site as demonstrated in our previous work in [46].

In spite of these advantages, the frequency offset and phase noise on the photo-mixing generated mm-wave carrier remains one of the hindrances to the deployment of optical heterodyne A-RoF link capable of carrying the small baud rate/subcarrier spacing multicarrier signals that are compatible with the 5G standard. While such system implementation with free-running lasers requires an additional compensation technique, however, the fine and wide wavelength tunability offered by most commercial lasers makes the free-running laser based optical heterodyne analogue RoF system an attractive solution for deployment in wireless systems. The two schemes presented in sections 3.2 and 3.3 demonstrate the capabilities to compensate for the effect of laser frequency fluctuations and phase noise in an optical heterodyne mm-wave A-RoF system. In both the techniques (i.e. mm-wave analogue receiver and DSP receiver), FO and

PN are compensated at the user side receiver unit transferring most of the additional hardware/software complexity to the user unit.

The analogue mm-wave receiver compensates the FO and PN in the same operation using mm-wave cancellation architecture but increases the hardware complexity of the user side receiver unit. However, the “LO-free” frequency down-conversion of the mm-wave data signal reduces the cost of the receiver, while providing centralized control over most of the receiver operations. As the frequency shift in both the photo-mixing generated components (F_c and F_s) remains the same, irrespective of the beating laser’s relative fluctuations, the level of frequency offset compensated depends on the bandwidths of the EBPF used in the analogue mm-wave receiver architecture. Hence, for the presented system a frequency offset up to 500 MHz (BW of LO arm EBPF) can be compensated. Our latest work [47] on the analogue mm-wave receiver has shown that the PN capabilities of the receiver are greatly impacted by the chosen mm-wave (carrier and signal) filter design. With a 500 MHz bandwidth filter in the LO arm, phase noise arising from the interaction of two independent lasers, each exhibiting linewidths in the MHz range, can be compensated as demonstrated in our recent work in [47]. In the recent work [48], we tuned the wavelength of two optical carriers, obtained from an integrated dual-mode laser, across the C band and demonstrated the successful transmission of the 244 kHz subcarrier spacing 5G OFDM signals over the analogue mm-wave receiver-based optical heterodyne analog-RoF link.

Currently, the analogue mm-wave receiver can be used in systems with relaxed spectrum constraints and provision for transmission of the mm-wave carrier. It can be used in the systems providing wireless back/front-haul to the RRH antenna sites or fixed user wireless systems, using mm-wave signals which are generated using optical heterodyning of two free running lasers.

The digital compensation of the FO & PN at the receiver user unit, transfers the hardware complexity of the analogue mm-wave receiver to the digital domain, making the DSP receiver scheme well suited for deployment in mm-wave wireless systems. External LO induced frequency offset of up to 140 MHz can be compensated digitally with this technique, showing its capabilities to compensate for the FO induced by most of the commercial lasers. Our previous simulation study [3] has concluded that, for an optical heterodyne A-RoF link with independent tunable laser sources (that are frequency locked, but un-correlated in phase), the linewidths of the beating carriers should be less than $\sim 1.5\%$ of the subcarrier baud rate of the OFDM signal for 64-QAM modulated data. The S&C algorithm, used in the presented DSP receiver, compensates for the FO which is larger than the sub-carrier spacing while the residual FO is manifested as phase rotation in the constellation. This phase rotation is compensated using the DD-LMS algorithm. When both of these processing steps are applied to the received signal, the presented results follow these above mentioned trends. The DSP approach effectively compensates for phase rotations that are inherent to

OFDM transmission in the presence of FO, but the extent to which PN specifically attributed to intrinsic laser linewidth, can be overcome, warrants further experimental investigation - including the use of optical sources exhibiting higher linewidth values.

The successful transmission of the mm-wave OFDM signals, with subcarrier spacing as low as 125 kHz, over the DSP compensation link shows its capabilities to be used in the 5G and beyond 5G wireless systems. The reduced hardware complexity of the DSP receiver scheme makes it simple and most cost-efficient for deployment in most of the mm-wave wireless applications.

3.5 Conclusion

Optical heterodyning A-RoF links provide an efficient platform for the generation and distribution of mm-wave signals for wireless systems. The performance of a such system is mainly limited by the frequency drift and phase offset between the optical carriers, obtained from the use of free running lasers, - especially for the transmission of low subcarrier spacing signals as provisioned in the 5G NR standard. In order to facilitate the wide deployment of such fibre-wireless systems, techniques that ease restrictions on relative frequency drift and phase offset between the optical carriers, with minimal additional complexity, are of paramount importance.

The results presented in this chapter, demonstrate two specific schemes that compensate for the mm-wave signals performance limiting factors, i.e. FO and PN in an optical heterodyne A-RoF system using free-running lasers. The variable degree of compensation achieved, by these techniques, is demonstrated by successfully transmitting 5G compatible low subcarrier spacing OFDM signal over the link. The analogue mm-wave receiver exploits the correlation between the photo-mixing generated mm-wave carrier and data signal to compensate the FO and PN using a hardware based approach. The second approach used standard digital signal processing algorithms to compensate for the effect of FO and PN without increasing the hardware complexity of the optical heterodyne analogue RoF system. The choice of the compensation technique should be made by considering their limitations and the requirements of the application in which the mm-wave A-RoF system will be employed.

References

- [1] T. S. Rappaport *et al.*, “Wireless Communications and Applications Above 100 GHz: Opportunities and Challenges for 6G and Beyond,” *IEEE Access*, vol. 7, pp. 78729–78757, 2019, doi: 10.1109/ACCESS.2019.2921522.
- [2] P. T. Dat, A. Kanno, N. Yamamoto, and T. Kawanishi, “Seamless convergence of fiber and wireless systems for 5G and beyond networks,” *Journal of Lightwave Technology*, vol. 37, no. 2, pp. 592–605, Jan. 2019, doi: 10.1109/JLT.2018.2883337.
- [3] C. Browning *et al.*, “Gain-switched optical frequency combs for future mobile radio-over-fiber millimeter-wave systems,” *Journal of Lightwave Technology*, vol. 36, no. 19, pp. 4602–4610, Oct. 2018, doi: 10.1109/JLT.2018.2841365.
- [4] K. A. McIntosh, E. R. Brown, K. B. Nichols, O. B. McMahon, W. F. Dinatale, and T. M. Lyszczarz, “Terahertz photomixing with diode lasers in low-temperature-grown GaAs,” *Appl Phys Lett*, vol. 67, no. 26, p. 3844, Aug. 1998, doi: 10.1063/1.115292.

- [5] H. Ito, S. Kodama, Y. Muramoto, T. Furuta, T. Nagatsuma, and T. Ishibashi, "High-speed and high-output InP-InGaAs unitraveling-carrier photodiodes," *IEEE Journal on Selected Topics in Quantum Electronics*, vol. 10, no. 4, pp. 709–727, Jul. 2004, doi: 10.1109/JSTQE.2004.833883.
- [6] F. Bavedila *et al.*, "Development of a Millimeter-Long TravellingWave THz Photomixer," *Journal of Lightwave Technology*, vol. 39, no. 14, pp. 4700–4709, Jul. 2021, doi: 10.1109/JLT.2021.3078226.
- [7] S. Nellen, R. Kohlhaas, L. Liebermeister, S. Breuer, B. Globisch, and M. Schell, "Continuous Wave Terahertz Generation from Photodiode-Based Emitters with up to 200 μ W Terahertz Power," *International Conference on Infrared, Millimeter, and Terahertz Waves, IRMMW-THz*, vol. 2018-September, Oct. 2018, doi: 10.1109/IRMMW-THZ.2018.8509858.
- [8] H. Ito and T. Ishibashi, "Photonic terahertz-wave generation using slot-antenna-integrated uni-traveling-carrier photodiodes," *IEEE Journal of Selected Topics in Quantum Electronics*, vol. 23, no. 4, Jul. 2017, doi: 10.1109/JSTQE.2017.2657678.
- [9] A. J. Seeds, C. C. Renaud, D. G. Moodie, E. Rouvalis, and M. J. Robertson, "Traveling-wave Uni-Traveling Carrier Photodiodes for continuous wave THz generation," *Optics Express, Vol. 18, Issue 11, pp. 11105-11110*, vol. 18, no. 11, pp. 11105–11110, May 2010, doi: 10.1364/OE.18.011105.
- [10] K. Sun and A. Beling, "High-Speed Photodetectors for Microwave Photonics," *Applied Sciences 2019, Vol. 9, Page 623*, vol. 9, no. 4, p. 623, Feb. 2019, doi: 10.3390/APP9040623.
- [11] H. Ito *et al.*, "Continuous THz-wave generation using antenna-integrated uni-travelling-carrier photodiodes," *Semicond Sci Technol*, vol. 20, no. 7, p. S191, Jun. 2005, doi: 10.1088/0268-1242/20/7/008.
- [12] Q. Gu, "RF system design of transceivers for wireless communications," *RF System Design of Transceivers for Wireless Communications*, pp. 1–479, 2005, doi: 10.1007/B104642/COVER.
- [13] T. Nagatsuma, M. Fujita, and L. Yi, "Enabling Device Technologies for Photonics-Assisted Millimeter and Terahertz Wave Applications," *Technical Digest - International Electron Devices Meeting, IEDM*, vol. 2021-December, pp. 11.5.1-11.5.4, 2021, doi: 10.1109/IEDM19574.2021.9720521.
- [14] T. Pollet, M. van Bladel, and M. Moeneclaey, "BER Sensitivity of OFDM Systems to Carrier Frequency Offset and Wiener Phase Noise," *IEEE Transactions on Communications*, vol. 43, no. 234, pp. 191–193, 1995, doi: 10.1109/26.380034.
- [15] L. Wei and C. Schlegel, "Synchronization Requirements for Multi-user OFDM on Satellite Mobile and Two-path Rayleigh Fading Channels," *IEEE Transactions on Communications*, vol. 43, no. 234, pp. 887–895, 1995, doi: 10.1109/26.380121.
- [16] J. J. van de Beek, M. Sandell, and P. O. Börjesson, "ML estimation of time and frequency offset in OFDM systems," *IEEE Transactions on Signal Processing*, vol. 45, no. 7, pp. 1800–1805, 1997, doi: 10.1109/78.599949.
- [17] 3GPP, "5G Technical specification: NR and NG-RAN Overall Description," 2020.
- [18] K. Balakier *et al.*, "Optical injection locking of monolithically integrated photonic source for generation of high purity signals above 100 GHz," *Optics Express, Vol. 22, Issue 24, pp. 29404-29412*, vol. 22, no. 24, pp. 29404–29412, Dec. 2014, doi: 10.1364/OE.22.029404.
- [19] K. Balakier, L. Ponnampalam, M. J. Fice, C. C. Renaud, and A. J. Seeds, "Integrated Semiconductor Laser Optical Phase Lock Loops," *IEEE Journal of Selected Topics in Quantum Electronics*, vol. 24, no. 1, Jan. 2018, doi: 10.1109/JSTQE.2017.2711581.
- [20] L. A. Johansson and A. J. Seeds, "Millimeter-wave modulated optical signal generation with high spectral purity and wide-locking bandwidth using a fiber-integrated optical injection phase-lock loop," *IEEE Photonics Technology Letters*, vol. 12, no. 6, pp. 690–692, Jun. 2000, doi: 10.1109/68.849086.
- [21] V. Torres-Company and A. M. Weiner, "Optical frequency comb technology for ultra-broadband radio-frequency photonics," *Laser Photon Rev*, vol. 8, no. 3, pp. 368–393, Mar. 2014, doi: 10.1002/lpor.201300126.
- [22] K. Kikuchi, "Fundamentals of coherent optical fiber communications," *Journal of Lightwave Technology*, vol. 34, no. 1, pp. 157–179, Jan. 2016, doi: 10.1109/JLT.2015.2463719.
- [23] J. Wu *et al.*, "A robust and efficient frequency offset correction algorithm with experimental verification for coherent optical OFDM system," *Journal of Lightwave Technology*, vol. 33, no. 18, pp. 3801–3807, Sep. 2015, doi: 10.1109/JLT.2015.2445923.
- [24] H. Y. Rha, C. J. Youn, Y. H. Kwon, and H. W. Choi, "Real-Time Digital Signal Processing for High-Speed Coherent Optical OFDM Synchronization," *Journal of Lightwave Technology*, vol. 33, no. 11, pp. 2294–2302, Jun. 2015, doi: 10.1109/JLT.2015.2393304.

- [25] Jing Qingfeng and Guo Qing, "Adaptive compensating method for Doppler frequency shift using LMS and phase estimation," *Journal of Systems Engineering and Electronics*, Oct. 2009. <https://ieeexplore.ieee.org/document/6074525> (accessed Jul. 02, 2022).
- [26] A. Leshem and M. Yemini, "Phase Noise Compensation for OFDM Systems," *IEEE Transactions on Signal Processing*, vol. 65, no. 21, pp. 5675–5686, Nov. 2017, doi: 10.1109/TSP.2017.2740165.
- [27] I. M. Ngehani, J. M. Chuma, I. Zibani, E. Matlotse, and K. Tsamaase, "Joint Channel and Phase Noise Estimation in MIMO-OFDM Systems," *IOP Conf Ser Mater Sci Eng*, vol. 198, no. 1, p. 012007, May 2017, doi: 10.1088/1757-899X/198/1/012007.
- [28] C. Browning, A. Delmade, Y. Lin, J. Poette, H. H. Elwan, and L. P. Barry, "Phase noise robust optical heterodyne system for reduced complexity millimeter-wave analog radio-over-fibre," *IET Conference Publications*, vol. 2019, no. CP765, 2019, doi: 10.1049/CP.2019.0779.
- [29] A. Delmade, C. Browning, A. Farhang, R. D. Koilpillai, D. Venkitesh, and L. P. Barry, "OFDM Baud Rate Limitations in an Optical Heterodyne Analog Fronthaul Link using Unlocked Fibre Lasers," *2019 IEEE International Topical Meeting on Microwave Photonics, MWP 2019*, Oct. 2019, doi: 10.1109/MWP.2019.8892190.
- [30] H.-Y. Chen, Y.-C. Chi, G.-R. Lin, S. Kim, Y. Son, and S. Han, "Remote heterodyne millimeter-wave over fiber based OFDM-PON with master-to-slave injected dual-mode colorless FPLD pair," *Optics Express*, Vol. 23, Issue 17, pp. 22691–22705, vol. 23, no. 17, pp. 22691–22705, Aug. 2015, doi: 10.1364/OE.23.022691.
- [31] J. P. Santacruz *et al.*, "Experimental ARoF System Based on OPLL Mm-Wave Generation for Beyond 5G," *26th Optoelectronics and Communications Conference (2021), paper W2B.2*, p. W2B.2, Jul. 2021, doi: 10.1364/OECC.2021.W2B.2.
- [32] A. H. M. R. Islam, M. Bakaul, A. Nirmalathas, and G. E. Town, "Millimeter-wave radio-over-fiber system based on heterodyned unlocked light sources and self-homodyned RF receiver," *IEEE Photonics Technology Letters*, vol. 23, no. 8, pp. 459–461, 2011, doi: 10.1109/LPT.2011.2107894.
- [33] T. Kuri and K. I. Kitayama, "Optical heterodyne detection of millimeter-wave-band radio-on-fiber signals with a remote dual-mode local light source," *IEEE Trans Microw Theory Tech*, vol. 49, no. 10 II, pp. 2025–2029, Oct. 2001, doi: 10.1109/22.954825.
- [34] R. Khayat-zadeh, H. H. Elwan, J. Poette, and B. Cabon, "100 GHz RoF system based on two free running lasers and non-coherent receiver," *2015 International Topical Meeting on Microwave Photonics, MWP 2015 - Conference Proceedings*, Dec. 2015, doi: 10.1109/MWP.2015.7356689.
- [35] Andreas Stöhr, Maria Freire Hermelo, Matthias Steeg ZHO, Po-Tsung Boris Shih, and Anthony Ng'oma, "Coherent radio-over-fiber THz communication link for high data-rate 59 Gbit/s 64-QAM-OFDM and real-time HDTV transmission," *Optical Fiber Communications Conference and Exhibition (OFC)*, 2017. <https://ieeexplore.ieee.org/document/7937221> (accessed Jul. 02, 2022).
- [36] S. R. Moon, M. Sung, J. K. Lee, and S. H. Cho, "Cost-Effective Photonics-Based THz Wireless Transmission Using PAM-N Signals in the 0.3 THz Band," *Journal of Lightwave Technology*, vol. 39, no. 2, pp. 357–362, Jan. 2021, doi: 10.1109/JLT.2020.3032613.
- [37] X. Li *et al.*, "120 Gb/s wireless terahertz-wave signal delivery by 375 GHz–500 GHz multi-carrier in a 2×2 MIMO system," *Journal of Lightwave Technology*, vol. 37, no. 2, pp. 606–611, Jan. 2019, doi: 10.1109/JLT.2018.2862356.
- [38] X. Li *et al.*, "1-Tb/s Millimeter-Wave Signal Wireless Delivery at D-Band," *Journal of Lightwave Technology*, vol. 37, no. 1, pp. 196–204, Jan. 2019, doi: 10.1109/JLT.2018.2871472.
- [39] Y. Lin *et al.*, "Characterization of Hybrid InP-TriPleX Photonic Integrated Tunable Lasers Based on Silicon Nitride (Si₃N₄/SiO₂) Microring Resonators for Optical Coherent System," *IEEE Photonics J*, vol. 10, no. 3, Jun. 2018, doi: 10.1109/JPHOT.2018.2842026.
- [40] Y. Fan *et al.*, "Optically Integrated InP-Si₃N₄ Hybrid Laser," *IEEE Photonics J*, vol. 8, no. 6, Dec. 2016, doi: 10.1109/JPHOT.2016.2633402.
- [41] T. Kuri and K. I. Kitayama, "Optical heterodyne detection technique for densely multiplexed millimeter-wave-band radio-on-fiber systems," *Journal of Lightwave Technology*, vol. 21, no. 12, pp. 3167–3179, Dec. 2003, doi: 10.1109/JLT.2003.821729.
- [42] T. Kuri, T. Sakamoto, and T. Kawanishi, "Laser-Phase-Fluctuation-Insensitive Optical Coherent Transmission of 16-Quadrature-Amplitude-Modulation Radio-Over-Fiber Signal," *Journal of Lightwave Technology*, vol. 34, no. 2, pp. 683–690, Jan. 2016, doi: 10.1109/JLT.2015.2508441.
- [43] Y. Shoji, Y. Hashimoto, and H. Ogawa, "Fiber-optic broadband signal distribution link based on a millimeter-wave self-heterodyne transmission/optical remote heterodyne detection technique," *IEICE Transactions on Electronics*, vol. E88-C, no. 7, pp. 1465–1473, 2005, doi: 10.1093/IETELE/E88-C.7.1465.

- [44] C. Browning, E. P. Martin, A. Farhang, and L. P. Barry, "60 GHz 5G Radio-Over-Fiber Using UF-OFDM with Optical Heterodyning," *IEEE Photonics Technology Letters*, vol. 29, no. 23, pp. 2059–2062, Dec. 2017, doi: 10.1109/LPT.2017.2763680.
- [45] T. M. Schmidl and D. C. Cox, "Robust frequency and timing synchronization for OFDM," *IEEE Transactions on Communications*, vol. 45, no. 12, pp. 1613–1621, 1997, doi: 10.1109/26.650240.
- [46] A. Kaszubowska-Anandarajah; A. Delmade; E. Martin; P. Anandarajah; L. Barry; C. Browning, "Bidirectional Fiber Transmission of mm W Signals Using Remote Downconversion and Wavelength Reuse," in *Conference on Lasers and Electro-Optics (CLEO)*, 2019, pp. 1–2.
- [47] D. Dass, S. O'Duill, A. Delmade, and C. Browning, "Analysis of Phase Noise in a Hybrid Photonic/Millimetre-Wave System for Single and Multi-Carrier Radio Applications," *Applied Sciences 2020, Vol. 10, Page 5800*, vol. 10, no. 17, p. 5800, Aug. 2020, doi: 10.3390/APP10175800.
- [48] D. Dass, A. Delmade, L. Barry, C. G. H. Roeloffzen, D. Geuzebroek, and C. Browning, "Wavelength & mm-Wave Flexible Converged Optical Fronthaul With a Low Noise Si-Based Integrated Dual Laser Source," *Journal of Lightwave Technology*, vol. 40, no. 10, pp. 3307–3315, May 2022, doi: 10.1109/JLT.2022.3169446.

4. Optical Heterodyne Millimetre Wave Analogue Radio-over-Fiber Fronthauling with Optical Frequency Comb Sources

The frequency fluctuations and phase noise on the photo-mixing generated mm-wave carrier arising from the use of free-running lasers in an optical heterodyne analogue RoF link limits the performance of low subcarrier spacing multicarrier signals. The two new techniques demonstrated in chapter 3, i.e. analogue mm-wave receiver and DSP receiver, compensate for the effect of FO and PN at the user side. In order to reduce the probability of interference with adjacent channels, it is necessary to generate frequency fluctuation-free mm-wave signals over the optical heterodyne A-RoF link. The traditional correlation techniques such as OIL, OPLL and OPIL correlated the frequency and phase fluctuations of the beating optical carriers (obtained from free-running lasers) at the expense of increased system complexity. An alternative solution is to use an optical frequency comb source for optical heterodyning, which facilitates the generation of frequency fluctuation-free and low phase noise mm-wave carriers. Any level of decorrelation between the beating optical comb tones due to path length differences during optical fibre transmission (due to fibre dispersion) can lead to phase noise on the generated mm-wave carrier. It is necessary to analyse the effect of comb tone decorrelation on the performance of low subcarrier spacing multi-carrier signals for the successful deployment of an ARoF system that employs an OFC source.

In this chapter, mm-wave signal generation is demonstrated over an optical heterodyne analogue RoF link using two different types of OFC sources, i.e. gain switched laser and a passively mode-locked laser. Initially, the details of various types of OFC sources and their properties are provided in section 4.1. A general schematic of the OFC based heterodyne setup is discussed in section 4.2 along with the mathematical formulation for the phase noise of the generated mm-wave carrier. A literature summary of various mm-wave or high frequency THz carrier generation demonstrations using OFC sources is also provided in section 4.2. In section 4.3, the effect of comb tone decorrelation due to path length difference on the performance of 244 kHz subcarrier spacing 59 GHz OFDM signal is analysed over an optical heterodyne A-RoF link using a gain switched laser OFC source. Simulation and experimental analysis is presented to determine the level of path length mismatch by observing the spectrum of generated mm-wave carrier over the presented system. Furthermore, signal generation at 27 GHz, 43 GHz and 59 GHz frequencies using different pairs of GSL OFC tones for remote heterodyning is demonstrated in section 4.4. This shows that the OFC-based A-RoF optical/mm-wave system can support flexible and interoperable mm-wave functionality. In section 4.5, MLL OFC based heterodyne system's performance is analysed with variable subcarrier spacings of OFDM signals.

4.1 Optical Frequency Combs & Properties

An optical frequency comb source generates a number of equally spaced optical carriers from a single device or subsystem [1], [2]. The frequency and phase fluctuations of these carriers are strongly correlated – a property desired by most optical systems operating with multiple carriers. The precise spacing and correlation between the comb lines/tones have made the OFC sources an ideal choice for use in applications such as spectroscopy [3], atomic clock [4], metrology [5], astronomy [6], LIDAR (light detection and ranging) [7], optical communication [8] and microwave photonics [9]–[11]. The power consumption and complexity of the multi-wavelength system can be reduced by replacing multiple independent lasers with an optical frequency comb source. The use of optical carriers from an OFC source for the transmission of spectrally efficient waveforms over a WDM link allows the reduction or elimination of the guard band between adjacent channels [8] – increasing the overall data rate over the system. OFC sources are also used for performing different microwave photonics applications such as fixed frequency and low phase noise RF carrier generation [10], arbitrary waveform generation [12], RF transversal filtering [9] and true time delay beamforming [11] to name a few. As mentioned earlier, this work focuses on the use of OFC sources for the generation of mm-wave carriers capable of transmitting 5G NR compatible signals.

For an ideal OFC source, the comb lines can be viewed as a periodic train of impulses in the frequency domain with corresponding sinusoids in the time domain (from the Fourier transform). In deployable systems, it's impractical to generate a train of pulses to achieve an infinite number of comb lines [2]. Instead, periodic ultrashort pulses with a certain carrier envelope phase offset are generated in the time domain – resulting in a band limited optical frequency comb generation with shifted centre frequency [1] as shown in the time and frequency domain representation in Fig. 4.1. The frequency spacing between the comb lines, i.e. FSR (free spectral range; f_{rep}) of the OFC is equal to the inverse of pulse repetition rate (Δt), while the carrier envelope phase offset ($\Delta\phi_{\text{CE}}$) decides the centre frequency (f_{CEO}). The frequency of the n^{th}

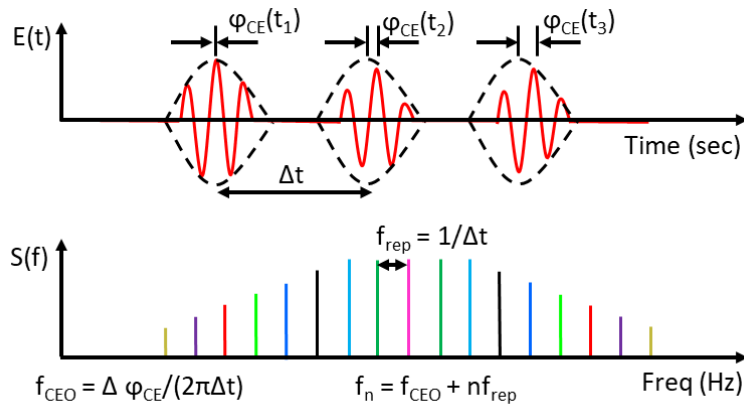


Fig. 4.1 Time and Frequency domain representation of an optical frequency comb.

comb line/tone can be given as $f_n = f_{\text{CEO}} + nf_{\text{rep}}$. The optical bandwidth of the comb source is inversely proportional to the temporal pulse width, i.e. the narrower the pulse the wider the comb spectrum.

Optical frequency combs can be generated by different techniques such as mode-locking of a semiconductor laser [2], [13], Kerr nonlinearities in micro-resonator [4], [14], parametric mixing of carriers using fiber nonlinearities [15], [16], external modulation using electro-optic modulator (EOMs) [8], [17], [18] and gain switched laser diodes [19]. The choice of type of OFC sources to be employed in the system should be made by considering their diverse spectral properties, noise performance and the requirements of the application. Typically, OFC sources with diverse spectral properties such as a large optical bandwidth (i.e. number of comb lines), good spectral flatness (i.e. low amplitude deviation among the comb tones), tuneable FSR and central wavelength and high optical power per comb line are required for the augmentation of the multiple applications in a flexible converged optical network [20]. In terms of noise characteristics, OFC sources with narrow optical linewidth or low phase noise, strong phase correlation, low RIN and high optical carrier-to-noise power ratio (OCNR) are required for efficient system implementation [20]. Furthermore, the practical implementation aspects such as long-term stability, compactness, the possibility of photonics integration, cost and power consumption need to be considered for commercial deployment.

4.1.1 Types of OFC Sources

A short description of the above-mentioned types of OFC sources is given in Fig. 4.2 along with the details of various properties. In MLLs, the phases of longitudinal modes of laser are correlated in the cavity in order to achieve comb generation [13]. Typically, active (by modulating modes with RF signal), passive

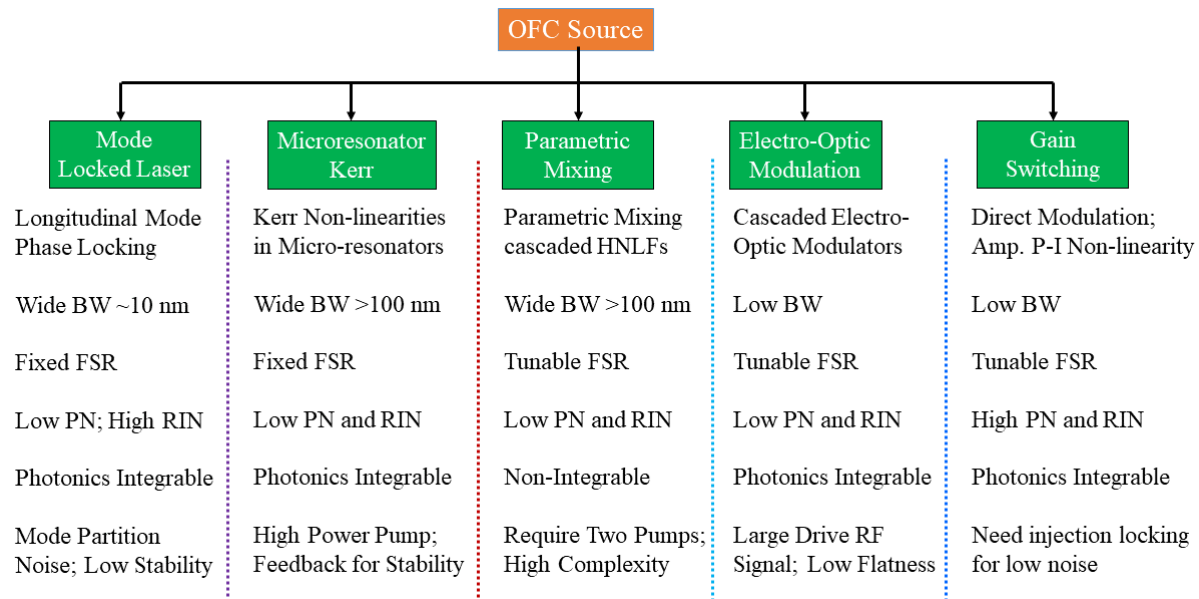


Fig. 4.2 Types of optical frequency comb sources and their properties.

(by introducing non-linearities in the cavity using a saturable absorber or special quantum structure design) or hybrid locking approaches are used to establish the phase correlation between the laser's longitudinal modes [20]. This results in MLL exhibiting wide bandwidth (around 10 nm) and good spectral flatness at low power consumption. While the MLLs are photonic-integrable, the fixed FSR and higher RIN hinder their deployment in the flexible optical network [20]. In section 4.5, millimetre-wave signal generation is demonstrated over an optical heterodyne A-RoF link using an InP based quantum dash passively mode locked laser OFC source.

The micro-resonator Kerr OFC [1], [4], [14] sources have attracted a lot of attention recently due to their ultra-wide bandwidth (more than 100 nm) spanning C and L bands and the photonics integrated nature of the resonator. The phases of the four wave mixing (FWM) components of the high power pump laser get locked with the resonator modes – resulting in the comb generation. The low phase noise and RIN properties of the pump get transferred to the OFC tones [20]. Despite the wide bandwidth, the fixed FSR and requirement of a feedback loop in some cases for stable operation impose practical limitations on the Kerr OFC sources. In the case of parametric mixing OFCs [15], [16], [20], a cascade of multiple highly non-linear and single-mode fibres is typically used to generate FWM components instead of micro-resonators. While the parametric OFC uses two pump lasers, the ultra-wide bandwidth of more than 100 nm, good OCNR, low RIN and PN (transferred from the seed laser) and tuneable FSR (an important characteristic lacked by MLL and Kerr OFCs) add to its advantages [20]. The use of a large number of components and the requirement of precise dispersion engineered fibres hinder the possibility of photonic integration and their use in field deployable systems.

In electro-optic modulator OFCs [8], [17], [18], [20], one or multiple modulators are modulated with a large amplitude RF sinusoidal drive signal – resulting in the comb tones generation from modulator non-linearity. The FSR and central wavelength tunability are afforded by the RF source and seed lasers, respectively. While the BW of the comb depends on the power of the applied signal to the modulators, the high insertion loss and low spectral flatness require the use of additional amplifiers and an amplitude flattening stage with power saturation [20]. The low phase noise and RIN provided by the seed laser and the possibility of photonics integration have promoted multiple optical communication [18] and optical heterodyne [21] system demonstrations with EOM combs.

The gain switched laser OFCs are also gaining importance due to their simple architecture and possible cost-efficient deployment through photonic integration [19], [20], [22]. This source exploits the amplitude P-I non-linearity of a semiconductor laser by quickly switching it below and above the threshold. The large driving RF signal is deliberately truncated to allow only the first spike of the relaxation oscillation to build in the laser [20]. An optical pulse train can be generated by periodically repeating this process at the rate

determined by the driving RF signal. FSR tunability (within the modulation bandwidth of the laser) can be achieved by changing the frequency of the driving signal, while limited wavelength tunability (< 3 nm) can be achieved by changing the bias and temperature currents [20]. The low BW and high phase noise properties can be improved by injection locking the gain switched laser with a low linewidth seed laser [23]. High-speed data transmission [20], [24], [25] and mm-wave generation [22], [23] have been demonstrated with injection-locked GSL OFC sources previously. In this work, a detailed analysis of phase noise from GSL OFC and its impact on the performance of low subcarrier OFDM signals is studied over an optical heterodyne link.

4.2 Optical Heterodyning with OFC Source

The beating of two optical carriers, obtained from an optical frequency comb source, on a high speed photodetector results in the generation of a frequency fluctuation-free mm-wave/sub-THz/THz radio carrier. The schematic of a general optical heterodyne concept with an OFC source is shown in Fig. 4.3. A

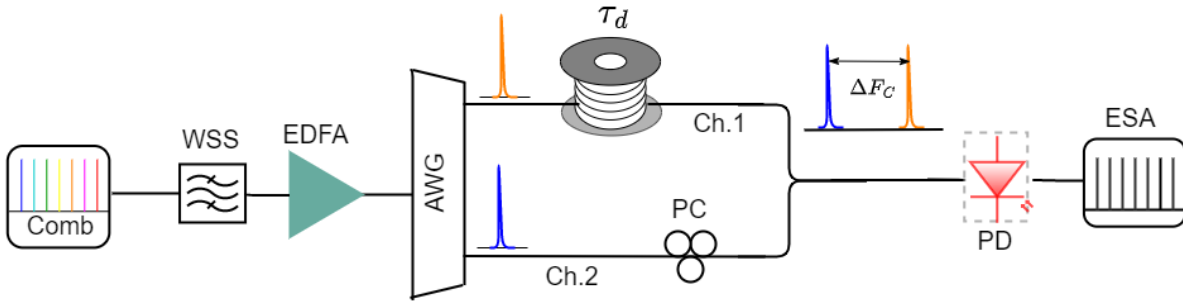


Fig. 4.3 OFC source based optical heterodyning with a delay between two optical carrier paths.

filtering stage, implemented using a programmable wave shaper (or wavelength selective switch) as shown in the figure, was used to filter out the two desired tones from the output of the OFC source. An erbium-doped fibre amplifier was also used to overcome the loss of power due to the dropping of multiple comb tones. An array waveguide grating or demultiplexer was used to further filter out the individual carriers and fed them to two channels (Ch.1 and Ch. 2). A path length difference between the two channels, which can arise from the use of various optical components with different length fibre pigtailed in both the channel paths, will lead to different phases of the optical carrier upon recombination. This path length difference ΔL , represented as a fibre in the figure, corresponding to the time delay of $\tau_d = \Delta L \times n/C$. C is the speed of light and n is the refractive index of optical fibre (1.4682).

The magnitude of the electric field of two OFC tones filtered by WSS can be mathematically represented as

$$E_1(t) = E_{01} \exp[j(2\pi f_1 t + \varphi_{OP}(t))] \quad 4.1$$

$$E_2(t) = E_{02} \exp[j(2\pi f_2 t + \varphi_{OP}(t))]$$

where, E_{01} and E_{02} are the amplitudes, f_1 and f_2 are the frequencies and φ_{OP} is the phase on all the comb tones at the output of the OFC device. The combined signal after considering the delay between the two channels can be expressed as

$$E_T(t) = E_1(t) + E_2(t - \tau_d) \quad 4.2$$

The beating of this signal on a high speed PD results in the generation of mm-wave carriers. The PD output current can be given as

$$\begin{aligned} I_{PD}(t) &= R(E_1(t) + E_2(t - \tau_d)) (E_1(t) + E_2(t - \tau_d))^* \\ &= 2R (E_{01}^2 + E_{02}^2 + 2E_{01}E_{02} \cos(2\pi f_{mmw}t + \Delta\varphi_{OP}(t, \tau_d))) \end{aligned} \quad 4.3$$

where, R is the responsivity of the PD. $f_{mmw} = |f_1 - f_2|$ is the frequency and $\Delta\varphi_{OP}(t, \tau_d) = \varphi_{OP}(t) - \varphi_{OP}(t - \tau_d)$ is the phase of the generated mm-wave carrier. $\Delta\varphi_{OP}(t, \tau_d)$ is typically assumed to be a zero mean Gaussian random variable, whose variance depends on the white noise component, i.e. linewidth, of the OFC tones. The variance of the photo-mixing generated mm-wave carrier's phase noise can be expressed as

$$\sigma^2_{\Delta\varphi_{op}}(t, \tau_d) = 2\pi\gamma_{op}|\tau_d| \quad 4.4$$

where, γ_{op} is the linewidth of the optical carriers. As mentioned earlier, τ_d is the time delay between the two optical carriers before photo-detection.

The expression for the autocorrelation function $R_I(\tau)$ and power spectral density (PSD) $S_I(f)$ of the photocurrent are derived in [26] and given as follows

$$R_I(\tau) = \begin{cases} R^2 E_1^2 E_2^2 \left[4 + 2 e^{(-2\pi\gamma_{op}|\tau|)} \cos(2\pi f_{mmw}\tau) \right] & \text{for } |\tau| \leq |\tau_d| \\ R^2 E_1^2 E_2^2 \left[4 + 2 e^{(-2\pi\gamma_{op}|\tau_d|)} \cos(2\pi f_{mmw}\tau) \right] & \text{for } |\tau| \geq |\tau_d| \end{cases} \quad 4.5$$

$$\begin{aligned} S_f &= 2 \left(\frac{\gamma_{op}}{\pi} \right) \exp(-2\pi\gamma_{op}|\tau_d|) \delta(f - f_{mmw}) \\ &\quad + \left[\exp(2\pi\gamma_{op}|\tau_d|) - \left(\frac{\gamma_{op}}{\pi(f - f_{mmw})} \right) \sin(2\pi(f - f_{mmw})|\tau_d|) \right. \\ &\quad \left. - \cos(2\pi(f - f_{mmw})|\tau_d|) \right] \left[\frac{\gamma_{op}^2 \exp(2\pi\gamma_{op}|\tau_d|)}{\pi[\gamma_{op}^2 + \pi^2(f - f_{mmw})^2]} \right] \end{aligned} \quad 4.6$$

The effect of the path length mismatch on the phase noise of the generated mm-wave carrier is analysed in the next subsection by simulating the power spectral density (Eq. 4.6) under different conditions.

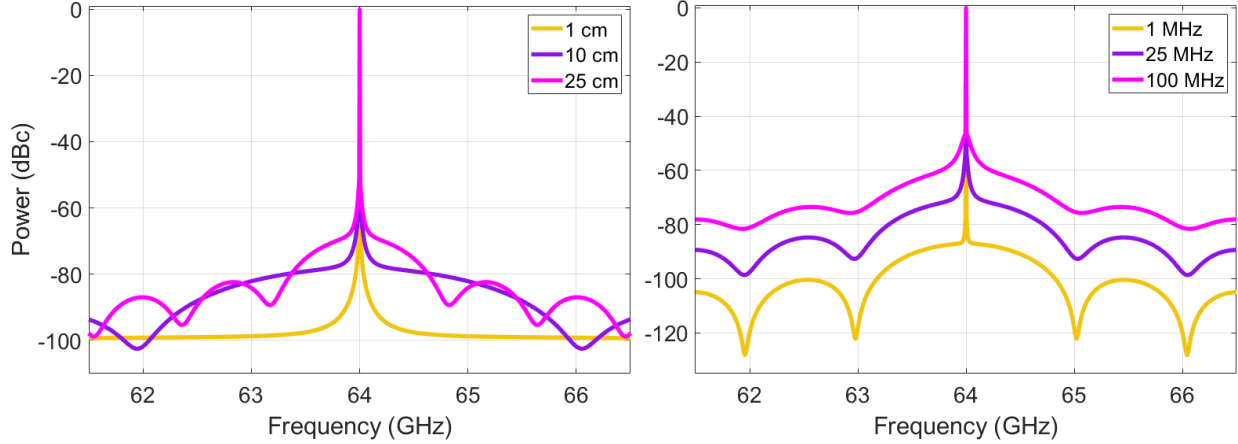


Fig. 4.4 Power spectral density of the heterodyne generated 64 GHz mm-wave carrier for the case of (i) different path length differences (25 MHz linewidth) and (ii) different linewidth OFC tones (20 cm path difference).

4.2.1 Phase Noise Analysis due to Path Length Mismatch

Fig. 4.4 shows the effect of path length mismatch and linewidth of the OFC tones on the PSD of the photo-mixing generated 64 GHz mm-wave carrier simulated using Eq. 4.6 and 4.4. Results show that the higher length difference between the beating optical carrier paths leads to a periodic increase in the noise floor. Also, the phase noise on the generated RF signal is observed to be increasing with an increase in the linewidth of the comb tones used for heterodyning. For a fixed linewidth OFC tones (25 MHz), the period of the main lobe (i.e. frequency difference between the nulls) is observed to be decreasing when the path length difference is increased from 1 cm to 10 cm to 25 cm as seen from mm-wave carriers PSD in Fig. 4.4(i). It is possible to determine the level of mismatch in the two paths by analysing the periodicity of the noise spectrum as the period remains the same irrespective of the linewidth of the beating tones [26]. It can be seen from the results of Fig. 4.4(ii) that the frequency separation between the nulls in the spectrum remains the same for a given path length difference (20 cm) irrespective of the linewidth of the beating tones. The 2.05 GHz difference between the first nulls in Fig. 4.4(ii) will result in τ_d of 0.976 ns and ΔL of 19.934 cm – which is the same as the value used for simulation. These simulation results are compared with the GSL OFC based optical heterodyne system experimental results in section 4.3.2. A detailed analysis of the effect of comb tone decorrelation due to path length difference on the performance of low subcarrier spacing OFDM signals is also presented in section 4.3.2.

The chromatic dispersion in optical fibres will also introduce the delay between the beating optical carriers and should result in additional phase noise on the photo-mixing generated mm-wave signal. The same power spectral density equation (Eq. 4.6) can be used to analyse the effect of chromatic dispersion induced phase noise with delay depending on the fibre dispersion coefficient, spacing between the carriers and fibre transmission distance. The chromatic dispersion induced delay between the carriers is given by

$\tau_d = D \Delta\gamma L$, where D is the dispersion coefficient of fibre given in ps/nm-km, $\Delta\gamma$ is the frequency spacing between the carriers (nm), and L is the length of fibre (km). The signal transmission over 10 km and 25 km fibre will introduce ~ 90 ps and 224 ps delay between the 64 GHz spaced optical carriers, respectively. A detailed evaluation of phase noise due to chromatic dispersion over different lengths of optical fibre can be found in [27].

4.2.2 Literature summary of Optical Heterodyne demonstrations using OFC Sources

Table. 4.1 summarizes some of the optical heterodyne system demonstrations reported in the literature using OFC sources. The table highlights the frequency of generated mm-wave/THz signal, type of OFC source, signal details such as modulation format, baud rate and data rate, type of RF receiver architecture used for frequency down-conversion and the PN compensation employed in these demonstrations.

Table. 4.1. Summary of various heterodyne demonstrations reported in the literature using OFC sources.

Author & Reference	OFC Type	Frequency (GHz)	Modulation, Baud Rate & Data Rate	Receiver Type & Compensation
Shi Jia [28]	EOM with 25 GHz FSR	425	16-QAM, ~ 32 Gbaud, 106 Gbps	Shottky Mixer; DSP
S. Koeing [29]	MLL OFC with 12.5 GHz FSR	237.5	16-QAM, 25 Gbaud, 100 Gbps	Heterodyne Receiver; DSP
Eduardo Saia Lima [30]	EOM with 2.6 GHz FSR	26	16-QAM, 5G NR, 900 Mb/s	Heterodyne Receiver
Andreas Stohr [31]	MLL with 58.8 GHz FSR	59.6	OOK, 5 Gbaud, 5 Gbps	Envelope Detector
Eamon Martin [32]	GSL with 18.1 GHz FSR	60	16-QAM OFDM, 97.7 Mbaud, 25 Gbps	Heterodyne Receiver
Colm Browning [33]	GSL with 18.7 GHz FSR	60.5	16-QAM OCDM, ~ 311 Mbaud, 16 Gbps	Heterodyne Receiver
Yitong Li [34]	EOM with 20 GHz FSR	150	16-QAM; 4 Gbaud, 16 Gbps	Heterodyne Receiver; DSP
Tong Shao [35]	GSL with 17 GHz FSR	170, 187 and 204	QPSK, 10 Gbaud, $3 \times 20 = 60$ Gbps	Heterodyne Receiver

The frequency of the generated mm-wave/THz signals in these demonstrations varies from 26 GHz to 425 GHz. While the table mentions the data transmission heterodyne demonstrations with the EOM, MLL and GSL OFC sources, the other two types of combs (i.e. Kerr and Parametric) are found to be used for the mm-wave/THz carrier generation only. In [28], the authors generated THz signals at 425 GHz frequency and achieved a total rate of 106 Gbps with 32 Gbaud 16-QAM data transmission over EOM OFC based

optical heterodyne system with digital signal processing impairment compensation. In [29], the authors successfully demonstrated a 100 Gbps data transmission rate at 237.5 GHz frequency generated using a 12.5 GHz FSR MLL OFC. Such high rates are achieved by modulating the data on both amplitude and phase of one of the OFC tones at the transmitter using an I-Q modulator and employing DSP at the receiver to retrieve the information. A combined data rate of 60 Gbps is reported in [35] by simultaneously generating the mm-wave signals at 170, 187 and 204 GHz frequencies by using different pairs of tones from a 17 GHz FSR GSL OFC source for heterodyning. The authors in these demonstrations, either operated the system at the exact path matched point or used DSP compensation to mitigate the effect of phase noise on the performance of the signal. Also, in most of these demonstrations, single/multi-carrier waveforms with a high baud rate (>90 Mbaud), were transmitted over an optical heterodyne link. The effect of phase noise on the performance of high baud rate signals is minimal compared to the low baud rate multicarrier signals. In the next section, we demonstrate mm-wave signal generation using a GSL OFC source over an optical heterodyne analog-RoF link.

4.3 Gain Switched Laser OFC Source based Optical Heterodyne A-RoF System

4.3.1 Experimental Details

A general schematic of the OFC based optical heterodyne mm-wave A-RoF fronthaul link (with representative spectra along the transmission path) is shown in Fig. 4.5. Similar to the system described in chapter 3, this system architecture is also designed to replicate the future mobile fronthauling wherein spectrally efficient wireless signals are modulated on one of the comb tones and transported between C-BBU and RRH site over an analogue RoF link implemented using low bandwidth optical components.

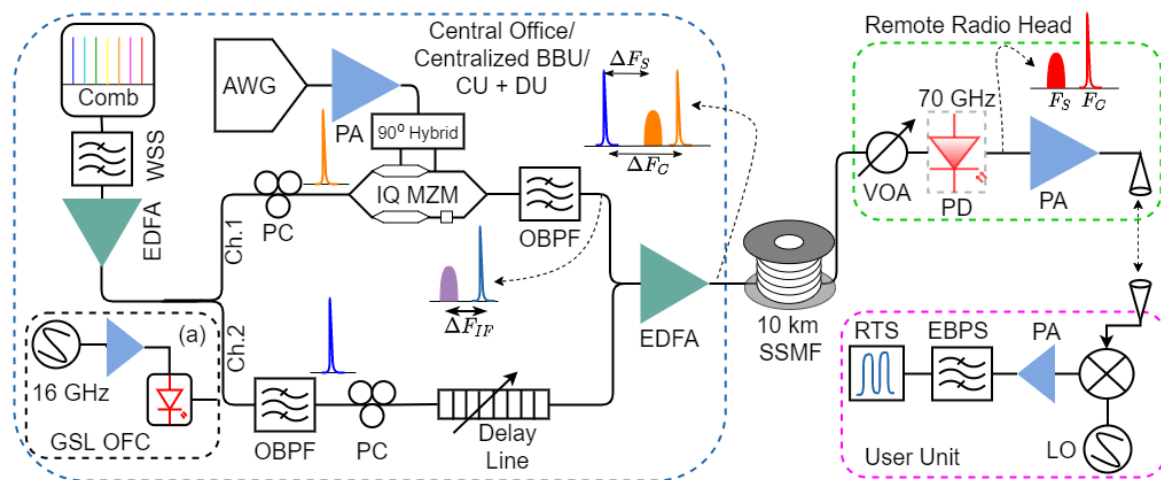


Fig. 4.5 OFC source based optical heterodyne mm-wave analogue RoF fronthaul link showing the C-BBU, RRH and user unit architecture along with GSL OFC schematic in inset (a).

Optical heterodyning of the relevant optical data signal and carriers, obtained from an OFC source, is then implemented at the RRH to achieve remote frequency up-conversion of data to the mm-wave band.

As mentioned earlier in section 4.1, the GSL OFC offers distinct advantages for use in the heterodyne system due to its simple architecture, precisely controlled channel spacing, and high phase coherence between the optical tones [11]. For this work, we used a gain switched laser comb source with an FSR of 16 GHz. The inset (a) in Fig. 4.5 shows the architecture of the GSL OFC source containing an RF sinusoidal signal source, RF amplifier and a free-running laser. The optical spectrum of the GSL OFC source containing 6 lines within 5 dB flatness is shown in Fig. 4.6(i). The number of comb lines generated directly from a gain switched laser depends on the bandwidth of the laser, bias current, and frequency and power of

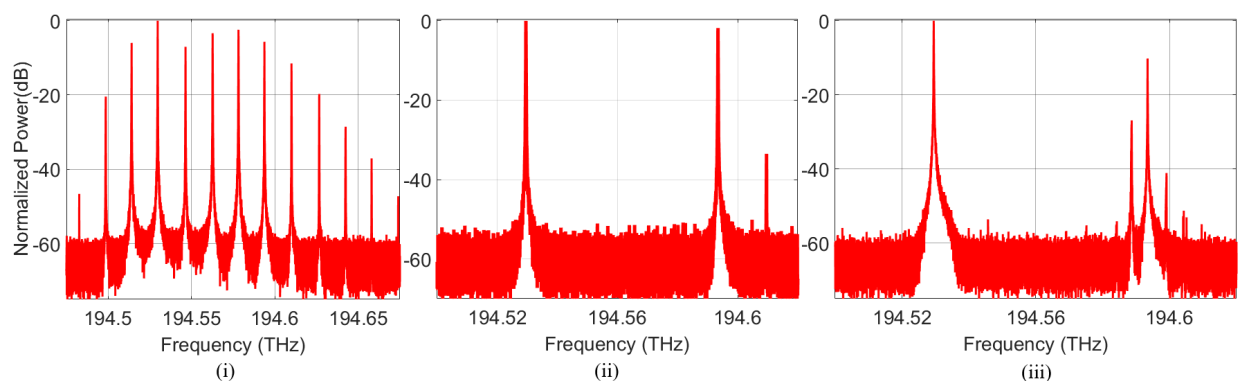


Fig. 4.6 Optical spectrum of (i) GSL OFC output, (ii) Two OFC tones filtered by WSS and (iii) Combined signal at the input of optical fibre.

the driving sinusoidal signal [22]. In this case, the gain switching of a DFB laser with a relaxation oscillation peak at ~ 17 GHz was achieved by applying an amplified 16 GHz sinusoidal signal (with 19 dBm RF power), with the DFB biased at 62.5 mA. As the gain switching process exploits the P-I curve amplitude non-linearity of the laser, the number of lines can be increased to some extent by either reducing the bias current or increasing the drive signal swing. It is worth noting that OFC expansion techniques that rely on the use of an external phase modulator [19] or dual-drive MZMs [36] (discussed in chapter 5, section 5.3) can also be used to achieve a greater number of flat comb lines.

The highest frequency of the generated mm-wave carrier in our setup was limited due to the bandwidth of the photodetector (70 GHz). Practically, in this case, this limitation means that only 5 flat comb lines with 16 GHz FSR are required. The total output power from the GSL was 6.5 dBm with individual comb lines exhibiting ~ 30 MHz linewidth.

Two optical tones with a frequency spacing (ΔF_c) - which was close to the target mm-wave data signal frequency of 59 GHz were filtered from the output of GSL OFC using a programmable WSS. The output spectrum of the WSS consisting of two tones separated by 64 GHz is shown in Fig. 4.6(ii). The insertion loss of the WSS, coupled with the rejection of other comb tones, reduced the total optical power to -6 dBm.

An erbium-doped fibre amplifier was used to boost the power of the filtered carriers before the optical path was split into two channels, as shown in the setup of Fig. 4.5. One of the optical carriers was modulated with a 5 GHz intermediate frequency (F_{IF}) OFDM signal in Ch. 1. In order to avoid the effect of dispersive fading, an optical single-sideband (orange signal in Fig. 4.5) signal was generated using an I/Q Mach-Zehnder Modulator and electrical 90° hybrid coupler.

The bias settings of the IQ-MZM were optimized to obtain the lower frequency data sideband. The 195 MHz bandwidth OFDM signal, consisting of 64-QAM modulated subcarriers at a spacing of 244 kHz (compatible with the 5G NR standard), was generated offline in Matlab at 5 GHz IF and loaded into an AWG which performed digital to analogue conversion at a sample rate of 20 GSa/s. The OSSB modulated carrier was combined with the un-modulated carrier from Ch. 2 (blue carrier in Fig. 4.5) and transmitted through 10 km of SSMF after amplification by an EDFA. A 300 ps tunable delay line was used in the unmodulated carrier arm to match the path lengths of two channels and avoid the decorrelation between comb tones. The effect of path length mismatch on the phase noise of the generated 64 GHz mm-wave carrier is analysed in detail in the next subsection. Power equalization, necessary to account for the difference in losses introduced through Ch. 1 and Ch. 2, was performed using the WSS. Optical bandpass filters were used in both paths to remove the unwanted signal/carrier components.

A combined signal consisting of two optical tones, separated by 64 GHz, and an IF data signal SSB modulated on one of the carriers, was transmitted through the fibre to the RRH site transmit antenna. The optical spectrum of the combined signal is shown in Fig. 4.6(iii). The photo-mixing of these three optical frequency components, on a 70 GHz PIN PD, generates the electronic copies of the mm-wave carrier at $F_C = 64$ GHz (from *carrier* \times *carrier* mixing) and a mm-wave OFDM data signal at $F_S = 59$ GHz (from *un-modulated carrier* \times *OSSB data sideband* mixing). The strength of the generated mm-wave carrier and data signal will depend on the powers of all the beating terms i.e. the modulated and un-modulated optical carriers as well as the OSSB modulated data signal. A VOA was used at the RRH site to control the total optical power incident on the high-speed PD.

The photo-mixing generated 59 GHz OFDM signal can be directly transmitted to the wireless user using mm-wave antenna elements, after RF amplification, as shown in the RRH box of Fig. 4.5. Wireless transmission of the data signal was not carried out in this experiment. The output of the PD was directly connected to the input of a frequency down-conversion stage at the user side receiver, highlighted by the magenta colour in Fig. 4.5. Here, an electrical heterodyne receiver with an external LO and mixer was used to down-convert the 59 GHz mm-wave OFDM signal back to 5 GHz IF. A real-time oscilloscope operating at 50 GSa/s was used to capture this IF signal. Then the signal was digitally resampled, frequency down-converted to the baseband and demodulated so that the bit error rate and error vector magnitude performance

could be evaluated. An intra-symbol frequency domain averaging (ISFA) channel estimation [37] was used to improve the system's performance.

4.3.2 Phase Noise Analysis and Effect of Path Length Difference

In the experimental setup shown in Fig. 4.5, the unmodulated carrier path (Ch. 2) has an optical bandpass filter and polarization controller, while the modulated path (Ch. 1) has additional IQ-MZM which results in path length mismatch. The extent of phase de-correlation between the comb lines due to this path mismatch depends on the coherence length, and hence the linewidth, of the beating optical carriers. A complete de-correlation of the tones will occur if the mismatch is more than the coherence length of the optical carriers, and in this case the linewidth of the generated mm-wave carrier will be equal to the sum of the beating optical carriers' linewidth – similar to the independent laser scenario discussed in chapter 3. In the case of correlated tones, the linewidth of the generated mm-wave carrier can be as low as several 10^3 Hz as shown in the beating signal spectrum in Fig. 1.14 in chapter 1.

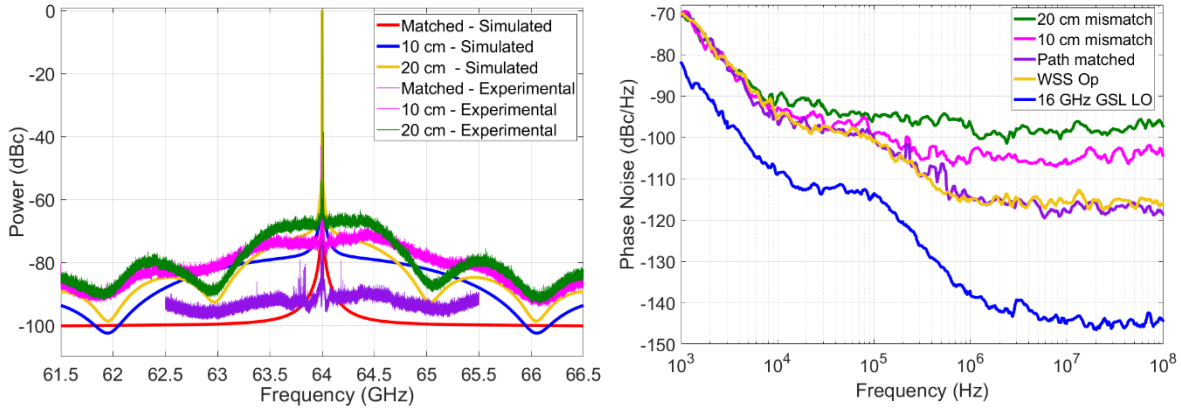


Fig. 4.7 (i) Simulated and experimental power spectral density and (ii) phase noise of the photo-mixing generated 64 GHz mm-wave carrier for the path matched and mismatched cases over an optical heterodyne A-RoF link

The effect of path length difference was analysed by observing the spectrum and phase noise of the generated 64 GHz carrier over the optical heterodyne A-RoF testbed. Fig. 4.7(i) shows the simulated and experimental spectrum of the generated 64 GHz carrier for the matched, 10 cm, and 20 cm path length differences. The experimentally generated 64 GHz carrier was frequency down-converted to 8 GHz using an external LO and mixer in order to observe its spectrum on the ESA. A close match is observed between the simulated and experimental spectra. It is clear from these spectral plots that the path length difference will result in an increased noise floor and its periodic nature can be attributed to the interferometric behaviour of the system. As mentioned earlier in section 4.2.1, the level of mismatch in the two paths can be analysed from the periodicity of the noise spectrum. The 2.05 GHz difference between the first nulls on either side of the central carrier on the green curve in Fig. 4.7(i) will result in τ_d of 0.976 ns and ΔL of 19.934 cm – which is similar to the measured 20 cm physical length difference introduced between the two

channel paths [26]. Similarly, the ~ 4 GHz difference between the nulls of the magenta coloured curve corresponds to the measured 10 cm path length difference. For a given path length difference, the frequency separation between these nulls in the received spectrum remains the same irrespective of the linewidth of the beating tones [30]. Hence, for a given system we can determine the level of path length mismatch, and required correction, by observing the spectrum of the generated mm-wave carrier.

In this experiment, we used a combination of different length patch chords and a 300 ps tunable optical delay line, corresponding to the length of 10 cm (free space tuning element), to achieve the exact path matching between two channels. The spectrum of the generated 64 GHz mm-wave carrier for the path matched case has a good carrier-to-noise ratio of >80 dB as seen in Fig. 4.7(i). In practical field-deployable photonic integrated circuit (PIC) based transceivers, such path length differences could be made negligible such that the phase noise of generated mm-wave carrier is minimised.

We also measured the phase noise of the generated 64 GHz mm-wave carrier after frequency down-conversion. Fig. 4.7(ii) shows the phase noise captured by the R&S spectrum analyser for the case of path matched, 10 cm and 20 cm path length difference. These results also indicate an increased phase noise with an increase in the path length difference. The power of the high frequency white noise component (beyond 1 MHz) is shown to increase as conditions vary from the path matched case to 10 cm and 20 cm delay cases. The figure also shows the PN of the 16 GHz RF source used for gain switching of the laser. Comparing this phase noise with the matched case indicates that the generated 64 GHz carrier has ~ 14 dB and ~ 24 dB higher phase noise power than the RF source at 1 kHz and 100 MHz offset frequencies from the carrier, respectively. This phase noise increase stems from the fact that the correlation between the GSL OFC tones is reduced with larger frequency spacing. The phase noise on the generated carrier scales by a factor of N^2 with respect to the RF LO phase noise [35], where N is the spacing between the two lines used for RF signal generation divided by the FSR. In this experiment, $N = 4$ (FSR = 16 GHz and line spacing for heterodyning set to 64 GHz), corresponds to a theoretical increase in the phase noise by a factor of 12.1 dB on the 64 GHz carrier relative to the RF LO. This closely matches with the ~ 14 dB experimentally measured value at 1 kHz offset as seen in Fig. 4.7(ii). A further increase in the phase noise at higher frequency offsets, which manifests as white noise components, can be attributed to the additional noise from the amplifier used after the PD and increased decorrelation at higher frequency offsets. In order to measure the phase noise in the absence of various system components, we directly beat the WSS filtered tones on PD and the generated 64 GHz mm-wave carrier. The yellow curve in Fig. 4.7(ii) indicates similar phase noise as that of the matched case – confirming close to ideal path matching in the system implementation. Additional phase noise analysis of mm-wave carriers generated using filtering of different comb tones is presented in section 4.4.1.

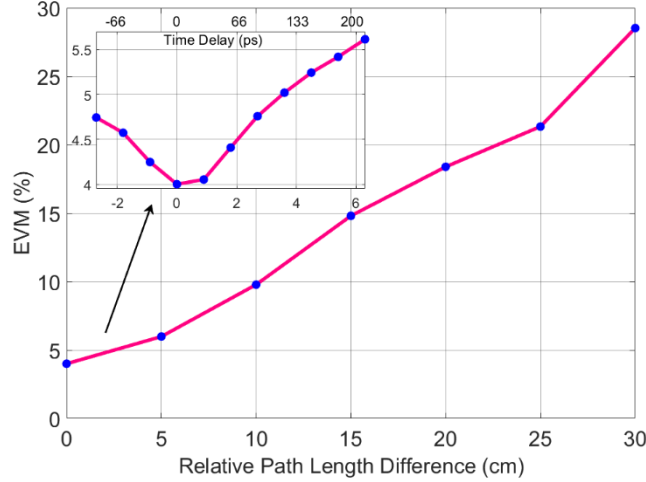


Fig. 4.8 EVM vs relative path length difference performance for 244 kHz subcarrier spacing 59 GHz mm-wave OFDM signal over an optical heterodyne A-RoF link.

We analysed the effect of phase noise, due to path length difference, on the performance of 5G NR compatible OFDM signal. Fig. 4.8 shows the EVM performance of 195 MHz bandwidth OFDM signal for different path length differences varied from the matched case to 35 cm at intervals of 5 cm. In the case of path length mismatch, the phase of the optical carriers from Ch. 1 and Ch. 2 are not correlated at the recombination point (see the setup of Fig. 4.5) – resulting in phase noise on the generated mm-wave carrier and reduced SNR on the IF signal. Increasing the path length difference will reduce the SNR further - degrading the performance of the demodulated signal as seen from the results of Fig. 4.8. The 64-QAM data modulated OFDM signals EVM increases from 4.1% to ~28% as the path length difference is changed from 0 to 35 cm. The results show that the performance above the 8% FEC EVM limit is observed within less than a 10 cm length difference between two channel paths. The inset in Fig. 4.8 shows the EVM as the unmodulated channel length is fine-tuned using the tuneable delay line shown in the experimental setup of Fig. 4.5. The measured EVM is observed to increase on both sides of the ideal path matching point – indicating the need for ideal path length matching to achieve optimum system performance. This highlights the critical importance of path matching requirements in such optical heterodyne analogue RoF systems, which can be readily achieved through the development of photonic integrated optical transceivers.

The high linewidth carriers, ~30 MHz in this case, exhibit low coherence length (2.17 m) and result in phase de-correlation within a short path length difference (fraction of coherence length) – as seen from the experimental results. Techniques such as injection locking the comb source with a low linewidth laser [23] can be implemented to reduce the linewidth of comb tones and increase the tolerance to de-correlation. In our previous work [22], we have shown the increased tolerance to path length difference upon injection of the comb source with low linewidth ECL. An alternate optical phase locked loop [38] technique can be used to lock the phase fluctuations of two beating optical carriers – requiring the implementation of a

feedback loop. The user site based compensation techniques such as the use of phase noise cancelling receiver [39] or advanced digital signal processing [40] can be used to relax the constraint on path length mismatch.

4.3.3 System Performance

Initially, the power budget of the presented system was analysed by observing the EVM performance of the photo-mixing generated 59 GHz mm-wave OFDM signal with variable received optical power falling on the PD. An exact path matching was maintained between ch.1 and ch.2 optical carrier paths in order to avoid the effect of comb tones decorrelation over the presented system. Fig. 4.9(i) shows the EVM vs

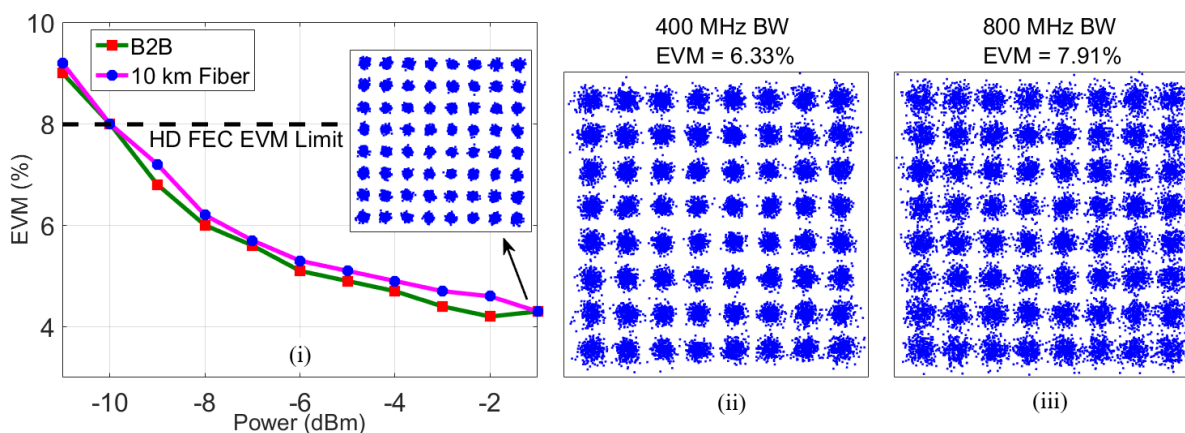


Fig. 4.9 (i) EVM vs received optical power performance of 200 MHz bandwidth 59 GHz mm-wave OFDM signal; Constellation of the (ii) 400 MHz and (iii) 800 MHz bandwidth 60.6 GHz mm-wave OFDM signals over a GSL OFC source based optical heterodyne A-RoF system.

received optical power performance for the 200 MHz bandwidth 244 kHz subcarrier spacing signal over the presented optical heterodyne mm-wave A-RoF system. An excellent EVM of 4.1%, as evident from the good constellation shown as an inset in Fig. 4.9(i), was measured at a received optical power of -1 dBm – signifying the successful generation, transmission and demodulation of the 59 GHz 5G NR compatible OFDM signal carrying raw data at the rate of 1.12 Gb/s. Received optical power variations from -1 dBm to -11 dBm result in EVM variation from 4.1% to ~9.25%, with performance hitting the 64-QAM modulation FEC EVM limit of 8% at the received power as low as -10 dBm. The system's performance was limited due to the photodetector's sensitivity at lower power levels. No performance penalty was observed due to 10 km fibre transmission over the back-to-back case. As mentioned in section 4.2.1, the 10 km fibre introduces ~90 ps delay between the 64 GHz spaced optical carriers - which can degrade the EVM by ~1% as seen from the results shown in the inset in Fig. 4.8. The tuneable delay line was tuned to compensate for fibre induced 90 ps delay between two optical carriers and avoid performance degradation.

In order to increase the data rate, higher bandwidth OFDM signals were transmitted over the presented link operating with an 18.6 GHz FSR gain switching OFC source [41]. Fig. 4.9(ii) and 4.9(iii) show the constellation of the demodulated 400 MHz and 800 MHz bandwidth 60.6 GHz mm-wave frequency OFDM signals at a received optical power of -1 dBm, respectively. The increase in OFDM signal BW from 200 MHz to 400 MHz degraded the EVM to 6.33% and further BW increase to 800 MHz degrades the EVM to 7.91% as a direct consequence of SNR degradation due to higher thermal noise and spreading of power over wider frequency. The measured BER values of 2.21×10^{-4} and 2.0×10^{-3} for 400 MHz and 800 MHz BW signals, respectively, were within the FEC limits, demonstrating the successful delivery of data at the rate of 2.4 Gb/s and 4.8 Gb/s over the optical heterodyne A-RoF system employing GSL OFC source.

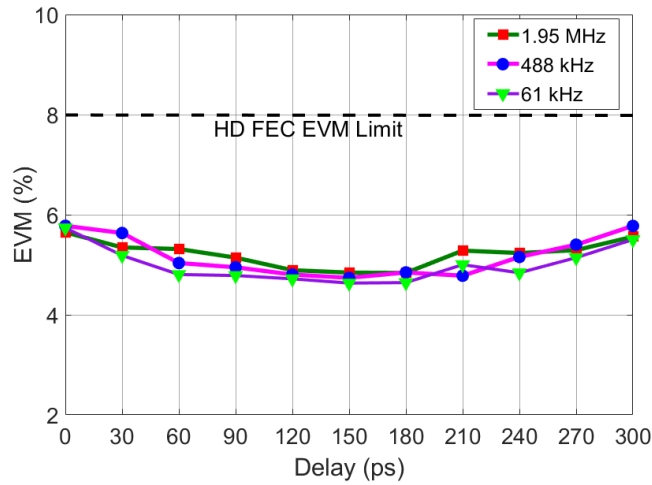


Fig. 4.10 EVM vs relative path length difference performance of 60.6 GHz mm-wave OFDM signal with variable subcarrier spacing over an optical heterodyne A-RoF link.

Furthermore, the subcarrier spacing of the OFDM signal was varied from 61 kHz to 1.95 MHz and the performance of the system with 18.6 GHz FSR GSL OFC was observed, with fine delay variation over 300 ps delay line, in order to test its capabilities for low subcarrier spacing signals transmission. As presented previously in chapter 3 section 3.3.2, the IFFT size and the number of data subcarriers were increased by a factor of 2 with respect to previous values to reduce the baud rate by a factor of 2 each time. The results, shown in Fig. 4.10, show the same performance for 61 kHz, 488 kHz, and 1.95 MHz subcarrier spacing OFDM signals exhibiting 4.5% EVM (close to current work) at path matched point. This shows the capabilities of the presented GSL OFC source based optical heterodyne A-RoF system to successfully generate and transmit 5G NR compatible low subcarrier spacing mm-wave OFDM signals. Contrary to this, in our work [34] with a passive MLL OFC source (discussed in section 4.5), the higher phase noise on the generated mm-wave carrier limited the successful transmission to 250 kHz and higher subcarrier spacing only.

To date, as evidenced by the works referenced above, our focus has been on the generation of mm-wave carriers at ~60 GHz capable of supporting A-RoF signals synonymous with 5G NR - with fine mm-wave carrier frequency tuning provided through the OFC's variable FSR. Broad mm-wave carrier tuning can also be supported through the selection of appropriate comb tones for heterodyne operation. This functionality offers the potential for the development of highly flexible system implementations capable of optically enabled mm-wave band interoperability. The following section demonstrates how the system outlined in section 4.3.1 is augmented to support mobile signal transmission at 32 GHz, 48 GHz and 64 GHz.

4.4 Multi-Frequency 5G NR mm-wave signal generation with GSL OFC

Future wireless broadband and mobile communications will be ultimately facilitated by a convergence of hybrid system implementations, different waveform types and cooperation of various wireless carrier frequency bands. It is clear that the optical domain advantages for these future systems - of high bandwidth transport and remote carrier generation - can only be fully exploited where they are enabled in a highly flexible and reconfigurable manner; providing support for heterogeneous signal transmission across various frequency bands. OFCs inherently provide multiple tuneable optical carriers from a single source and so have the potential to act as an excellent platform for the development of such systems.

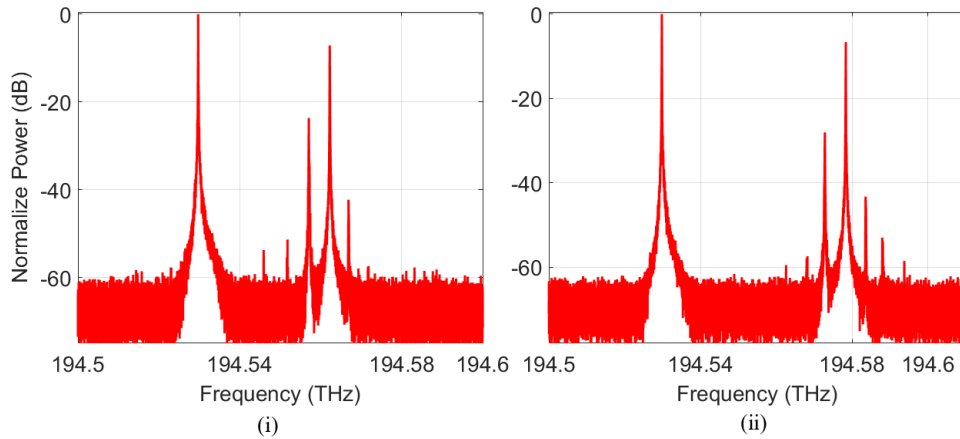


Fig. 4.11 Combined signal optical spectrums for the (i) 27 GHz and (ii) 43 GHz mm-wave signal generation case over an optical heterodyne A-RoF link.

To demonstrate the multi-frequency 5G NR signal generation from the same device, using the system outlines in section 4.3.1 as a basis, different pairs of optical carriers were filtered from the output of 16 GHz FSR GSL OFC using the WSS. To generate a data signal at 27 GHz, 43 GHz and 59 GHz, two carriers separated by 32 GHz, 48 GHz and 64 GHz were filtered and a 5 GHz IF OFDM signal was modulated onto the lower frequency sideband of one of the carriers as earlier described in section 4.3.1. The same GSL OFC tone was used for the unmodulated carrier while three different OFC carriers were used (separately) for data modulation; enabling multi-frequency mm-wave signal generation using the same source. The optical spectra showing the modulated carrier, IF data signal, and unmodulated carrier for 27 GHz and 43

GHz cases are shown in Fig. 4.11(i) and 4.11(ii), respectively. These optical signals were transmitted over 10 km SSMF separately and the photo-detection at the RRH side resulted in the generation of mm-wave OFDM signals at 27 GHz and 43 GHz frequencies. The performance of these mm-wave signals was evaluated after frequency down-conversion and demodulation as described earlier in section 4.3.1.

4.4.1 Phase Noise Analysis

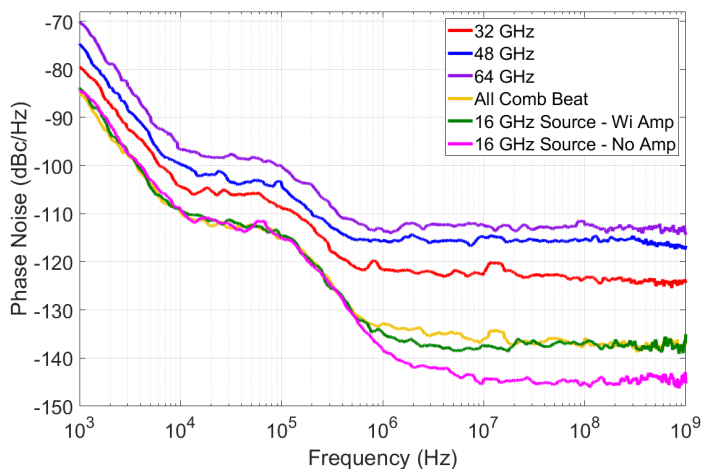


Fig. 4.12 Phase noise of the photo-mixing generated 32 GHz, 48 GHz and 64 GHz mm-wave carriers after beating different pairs of GSL OFC tones on the PD.

The phase noise analysis of the generated 32 GHz and 48 GHz mm-wave carriers was also performed. Fig. 4.12 shows the phase noise of the photo-mixing generated 32, 48 and 64 GHz carriers along with that of the RF source used for gain switching. Initially, we beat the entire optical frequency comb source (spectra shown in Fig. 4.6(i)) on the PD and observed the phase noise of the generated 16 GHz carrier after amplification. The result shows the same phase noise as that of the RF source used for gain switching (where an amplifier is employed between the RF source and ESA). The high frequency white noise component of the phase noise (above 1 MHz offset) increases in the presence of an amplifier, as seen from the different levels for pink and green curves in Fig. 4.12.

For the case of a 32 GHz carrier, a ~ 5.5 dB and ~ 15 dB increase in the phase noise was observed at 1 kHz and 10 MHz offset, respectively, compared to the RF source. At low frequency offset, the phase noise increases approximately by a factor of $10\log_{10}(N^2)$ as expected, while the further deviation in the white noise region can be attributed to the amplifier noise and reduced correlation at high offset frequencies. For the case of 32 GHz, 48 GHz and 64 GHz carriers, the phase noise at 1 kHz offset is observed to be increased by 5.5 dB ($\approx 10\log_{10}(4) = 6$ dB), 9.672 dB ($\approx 10\log_{10}(9) = 9.54$ dB) and 14 dB ($\approx 10\log_{10}(16) = 12.1$ dB) compared to the 16 GHz RF LO phase noise, respectively. The varying degree to which the white noise component increases, between 32 GHz and 48 GHz carriers and 48 GHz and 64 GHz carriers, respectively, can be attributed to the use of different RF amplifiers in these cases. We used a wideband amplifier from

SHF for the case of 32 GHz and 48 GHz and a 55 - 65 GHz amplifier from MI-wave for the 64 GHz carrier generation case. A detailed derivation of the $10\log_{10}(N^2)$ phase noise increase is given in [35].

This confirms our previous statement that the adjacent OFC tones separated by FSR are generally highly correlated and should result in the generation of a low phase noise carrier - the same as of RF source - while the correlation degrades with an increase in spacing between tones as seen from the increased phase noise in Fig. 4.12. Nevertheless, the measured phase noise values are sufficiently low to successfully transmit the 5G NR compatible low subcarrier spaced OFDM signals as evident from the results presented in previous section 4.3.3. The performance of the 27 GHz and 48 GHz signals is analysed in the next subsection.

4.4.2 System Performance

The results discussed in the previous subsection show that the phase noise on the photo-mixing generated mm-wave carrier increases with an increase in spacing between the OFC tones used for heterodyning. The effect of this increased phase noise on the system's performance was analysed by transmitting 244 kHz

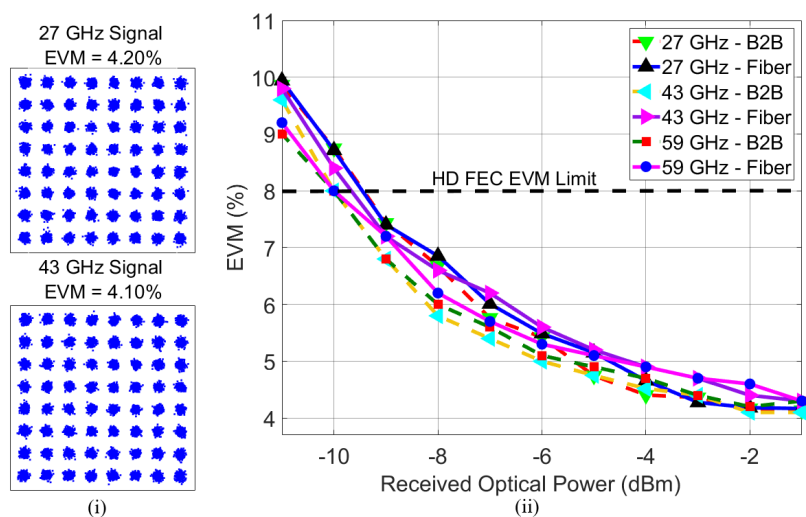


Fig. 4.13 (i) Constellations and (ii) EVM vs received optical power performance of the 27 GHz and 43 GHz mm-wave OFDM signal over a GSL OFC based optical heterodyne A-RoF link.

subcarrier spacing OFDM signals. The constellation of the demodulated 27 GHz and 43 GHz OFDM signals are shown in Fig. 4.13(i). The excellent measured EVM values of 4.2% and 4.1%, for the 27 GHz and 43 GHz signals respectively, at the received optical power of -1 dBm show that the phase noise increment by a factor of $10\log_{10}(N^2)$ has minimal impact on the performance of the presented system.

The performance of the generated 27 GHz, 43 GHz and 59 GHz signals with variable received optical power falling on the PD is shown in Fig. 4.13(ii). The results show that almost the same performance is achieved for all three cases which use different pairs of GS OFC tones. For all the signals, a best-case EVM, of close to 4.15%, is measured at -1 dBm of received optical power. The presented system exhibits a ~8 dB

power budget as the performance hits the FEC EVM limit of 8% at -9 dBm power. No performance penalty was observed after 10 km fibre transmission for all three cases. These results show the capability of the presented GSL OFC source based optical heterodyne analogue RoF system to successfully generate mm-wave signals across mm-wave bands, with the upper frequency bound limited only by the bandwidth of the receiver PD.

4.4.3 Simultaneous Multi-Frequency Signal Generation

While the above mentioned experimental work demonstrate the generation of three different mm-wave frequencies separately, it is possible to generate these signals simultaneously at the receiver by detecting the composite spectrum shown in Fig. 4.14. This scenario could be highly advantageous for remote antenna sites with multi-frequency mm-wave band capabilities.

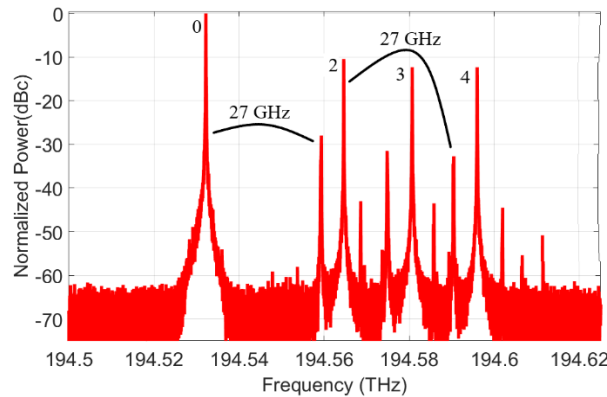


Fig. 4.14 Combined optical signal spectrum for simultaneous generation of mm-wave OFDM signals at 27 GHz, 43 GHz and 59 GHz frequencies over an optical heterodyne A-RoF system.

In this case, a single IQ-MZM was used to modulate the same IF OFDM data signal on three comb tones in Ch. 1 as shown in Fig. 4.5. Beating of all the spectral components, shown in Fig. 4.14, will result in the simultaneous generation of the mm-wave carrier at 32, 48 and 64 GHz and mm-wave signals at 27, 43 and 59 GHz. Additional beating terms, as shown for the case of 27 GHz, were generated from the photo-mixing of spectral components with the same frequency difference – creating interference at the desired signal frequencies and impacting the performance. In order to avoid such interference each OFC tone should be modulated separately with data signals at an IF frequency that is different from that assigned to other modulated tones. In this work, the simultaneous generation of mm-wave signals at different frequencies is not demonstrated due to the lack of multiple modulators in the lab. In practical OFC based systems, separate MZMs are usually employed for data modulation on individual comb lines - eliminating the problem of interference. Such a transceiver architecture, which is compatible with photonic integration, can lead to further centralization of the resources and efficient deployment of the RRH units capable of mm-wave interoperability, serviced by high bandwidth optical fronthaul. In the next section, a passively mode locked laser OFC source based optical heterodyne A-RoF system is demonstrated.

4.5 MLL OFC based Optical Heterodyne A-RoF System

The results presented in the previous sections 4.3 and 4.4 show the capabilities of the GSL OFC source for the generation of 5G NR compatible mm-wave signals over an optical heterodyne A-RoF system. The high linewidth (~ 30 MHz) of the GSL OFC tones results in phase de-correlation within a short path length difference and typically optical injection locking technique is employed to reduce the linewidth of comb tones – increasing the system complexity. Also, the power of RF signal required for exciting the P-I curve amplitude non-linearity increases in order to increase the number of comb tones. This increases the complexity of the GSL OFC based optical heterodyning system in addition to the power consumption. For the work presented in this section, an RF synthesizer-free low linewidth photonic integrated quantum dash passively mode locked laser (QD-P-MLL) OFC source was employed in the optical heterodyne mm-wave A-RoF link. In order to relax the constraints on the path matching and correlation of OFC tones, a digital phase noise compensation by the DD-LMS algorithm is used at the receiver user unit. Previous work with MLL OFC [42] has demonstrated the transmission of high baud rate single carrier signals, for which the impact of phase noise is minimal. Here, the transmission of 5G envisioned small subcarrier spacing multi-carrier signals is demonstrated.

4.5.1 QD-P-MLL OFC Source and System Description

A single-section photonic integrated MLL with the gain medium made of a few layers of InAs quantum dash, as shown in Fig. 4.15(i), was used in this experiment. A buried ridge structure guides a single transverse mode inside the Fabry-Pérot cavity. The laser mirrors were made with a cleaved facet and the length of the cavity was chosen to have a 32.5 GHz repetition rate. A threshold current of under 25 mA was measured at 20°C and a bias current of 300 mA resulted in ~ 9 dBm fibre coupled power. The OFC generated by the MLL laser has a 3 dB bandwidth of 11.8 nm resulting in ~ 45 flat comb lines (spectrum in Fig. 4.15(ii)). The optical linewidth of the comb lines is around 4 MHz and the RF linewidth of the beat signal

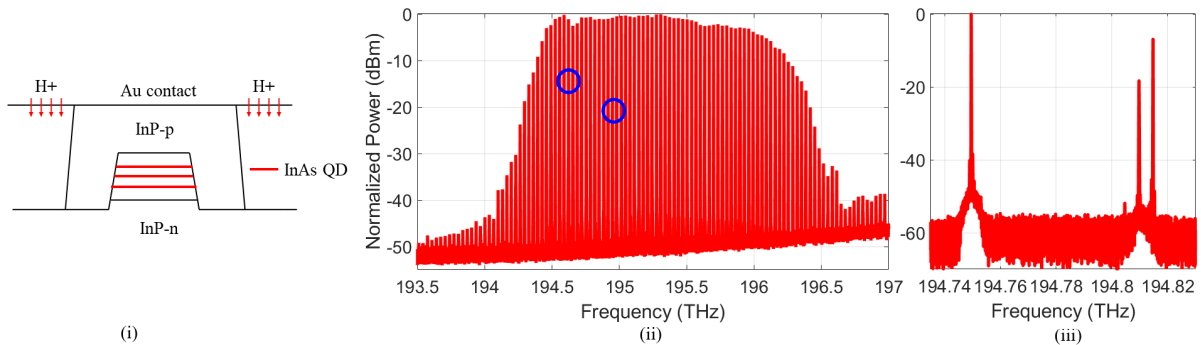


Fig. 4.15 (i) Schematic of a QD-MLL; (ii) Optical spectrum at the output of QD-MLL with blue circles showing different sets of operating frequencies used for the heterodyning, and (iii) combined optical signals spectrum at the input of optical fibre.

between comb lines is several 10's kHz, depending on operating conditions such as temperature, drive current and fibre coupling. The complete description of the device can be found in [43], [44]. An external free space cavity of approximately 30 cm in length was used in conjunction with the MLL to reduce the phase noise of both the optical lines and RF beat signal. The cavity consists of a collimating lens, a free space attenuator, and a mirror. The strength and phase of the optical feedback loop were controlled by tuning the position of the mirror with a piezo controller. The level of optical and RF beat signal linewidth reduction achieved depends on the strength and phase of the feedback [45]. Under coherent feedback conditions, both the optical linewidth and RF linewidth can be reduced by a factor of 10 [46].

The experimental testbed for this system was similar to the one shown in Fig. 4.5. The output of MLL OFC was fed to the WSS for filtering two optical carriers spaced by 65 GHz (twice the FSR of the OFC). Two different sets of comb tones with operating frequencies of 194.556 and 194.621 THz (first set) and 194.916 and 194.981 THz (second set), were separately selected for heterodyning in order to show the flexibility in the choice of the MLL OFC tones used for heterodyning. These tones are marked by the blue circles on the MLL output spectrum shown in Fig. 4.15(ii). The output of the WSS was amplified and sent to the two channels of the heterodyning system as shown in the system architecture in Fig. 4.5. Most of the remaining details of the experimental setup are the same as discussed in section 4.3.1. The 65 GHz spacing between the filtered optical carriers and a 5 GHz IF lower sideband data modulation resulted in the generation of a 60 GHz mm-wave OFDM signal over the MLL OFC based optical heterodyne A-RoF link.

A 195 MHz bandwidth OFDM signal, with a subcarrier baud rate of ~2 Mbaud, carrying a raw data rate of 1.12 Gb/s was initially transmitted over the link. Performance with variable subcarrier spacing is also analysed over the link. An RF heterodyne receiver consisting of an external standalone LO for frequency

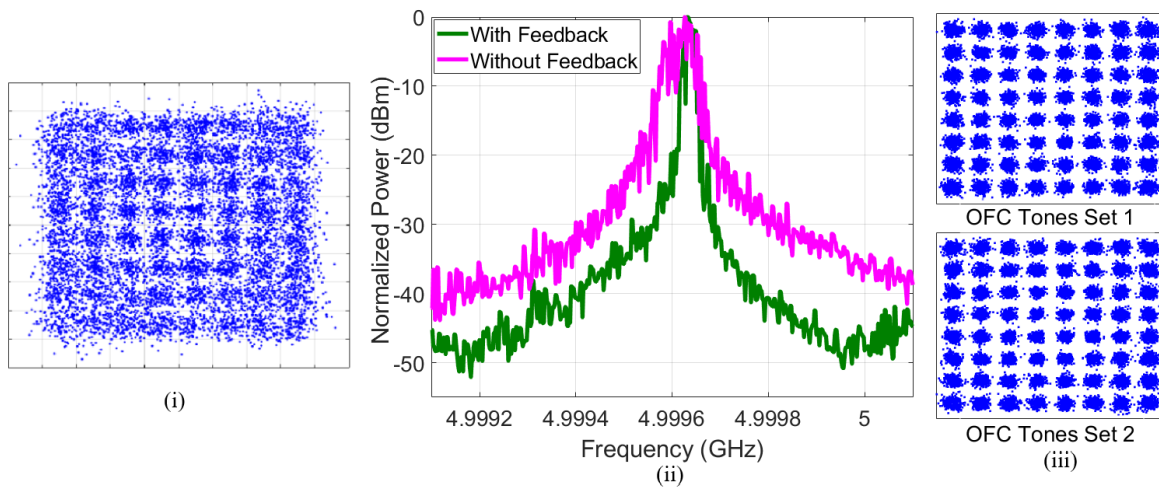


Fig. 4.16 Constellation of the demodulated OFDM signal over an mm-wave A-RoF heterodyne system employing a QD-P-MLL OFC (i) without and (ii) with a free space optical feedback; (iii) RF spectra of a frequency down-converted mm-wave carriers showing phase noise reduction with feedback.

down-conversion to IF was used in this system along with the DD-LMS DSP algorithms (discussed in chapter 3 section 3.4.1) for PN compensation.

4.5.2 Experimental Results – System Performance

Initially, the optical heterodyne system was tested without any feedback applied to the MLL OFC. The constellation of the 60 GHz mm-wave demodulated signal is shown in Fig. 4.16(i). The distorted constellation with a measured EVM of 13%, which is above the FEC EVM limit of 8%, indicates the unsuccessful data transmission over this link. The above FEC limit performance can be attributed to the higher phase noise on the generated mm-wave carrier, as seen from the higher linewidth of the RF beat tone in Fig. 4.16(ii). As mentioned earlier, the free space feedback to the MLL results in the reduction of the RF beat tone linewidth. The frequency down converted mm-wave carrier spectrum, shown in Fig. 4.16(ii), indicates the reduction in mm-wave carrier’s linewidth (eventually phase noise) from ~10 kHz without feedback to ~2 kHz with feedback case.

The performance of the presented optical heterodyne system was tested, when the MLL was operated with free space optical feedback, at the marked operating frequencies on the optical spectrum shown in Fig. 4.15(ii). The demodulated signals constellations are shown in Fig. 4.16(iii) for both the MLL OFC tone sets mentioned earlier. In both cases, an excellent EVM of ~6% was measured. A BER of $\sim 1.82 \times 10^{-4}$ was obtained, for both cases, with no penalty due to fibre transmission at a received optical power of 0 dBm. The improved performance upon reduction of the phase noise after applying the feedback shows the importance of generating a low phase noise (RF linewidth) mm-wave carrier.

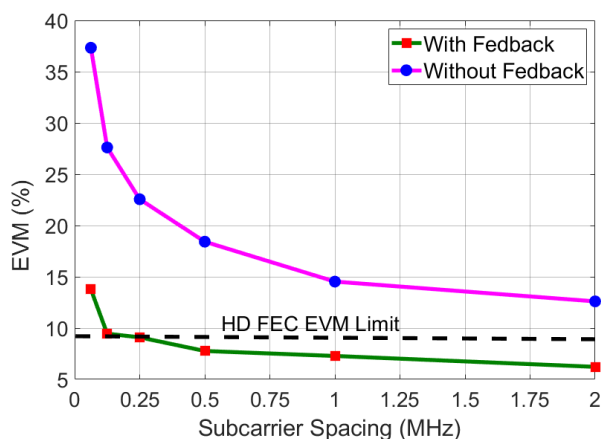


Fig. 4.17 EVM vs subcarrier baud rate performance for OFDM signals over a QD-MLL OFC mm-wave A-RoF system.

In order to analyse the QD-MLL OFC based optical heterodyne links capabilities for 5G NR compatible signals transmission, OFDM signals with different subcarrier spacing/baud rates were transmitted through the 25 km SSMF mm-wave A-RoF system. The presented link performance was analysed for the two

different laser conditions - with and without optical feedback. Fig. 4.17 shows the EVM vs subcarrier spacing performance of the system at the received optical powers of 0 dBm for the cases with and without free space feedback MLL OFC. The results show that the performance of the implemented system degrades, as the subcarrier spacing of the OFDM signal was reduced, for both the cases of with and without feedback MLL OFC. This degradation can be attributed to the increased effect of phase noise for lower subcarrier spacing OFDM signals. The phase noise on the heterodyne generated mm-wave carrier needs to be very low for the successful transmission of low subcarrier spacing signals. The passive mode-locking used in the employed OFC device generates tones with a low level of correlation as evident from the higher linewidth (10 kHz and ~ 2 kHz as shown in Fig. 4.16(ii)) of the frequency down-converted mm-wave carrier. In the case of the earlier demonstrated GSL OFC source, the use of an RF source for comb generation results in OFC tones with a good correlation, which eventually leads to the generation of mm-wave carriers with several 10's Hz linewidth (as shown in the spectrum in Fig. 1.14 in chapter 1) upon heterodyning.

In the case of MLL OFC without external free space feedback, the higher phase noise on the heterodyne generated mm-wave signal resulted in the EVM values above the FEC limit of 8% for all the subcarrier spacing values as seen from the pink curve in Fig. 4.17. OFDM signals with subcarrier spacing of 250 kHz and higher were successfully transmitted over the outlined system when the feedback was applied to the MLL OFC for linewidth and eventually phase noise reduction. This implies that the use of external free space feedback was also not sufficient to reduce the phase noise of the generated signal to the level such that it could support the transmission of signals with 125 kHz and lower subcarrier spacing. Nevertheless, the system still supports the transmission of a few 5G NR compatible subcarrier spacing OFDM signals and can support the transmission of single carrier waveforms. As the wireless network move towards the use of sub-THz and THz frequency bands, the subcarrier spacing of the signals will eventually increase to a few MHz. The demonstrated system with MLL OFC will be capable of successfully generating and transmitting such signals.

The use of a quantum dash MLL, with feedback, in the optical heterodyne mm-wave A-RoF system eliminates the requirement for an RF synthesizer at the transmitter. The higher bandwidth (11.8 nm with ~ 45 flat comb lines as shown in the optical spectrum in Fig. 4.15(ii)) of the employed MLL, makes it an ideal source for the generation of FSR order mm-wave/THz carriers up to 1.2 THz frequency by selecting the desired spacing tones for the heterodyning. The use of InP for the photonics integration of the demonstrated device increases the possibility of fully integrated optical heterodyne transmitter development by adding other system components. Also, the requirement of an external free space cavity, for phase noise reduction, can be eliminated by employing the recent advances in the QD MLL technology [47], which achieve lower linewidth RF beat tones without the requirement of free space feedback. The presented results

and stated advantages highlight the potential for the deployment of the passively mode-locked laser OFC source in an optical heterodyne mm-wave A-RoF system provisioned for the transmission of low subcarrier spacing multi-carrier signals compatible with future mobile services.

4.6 Conclusion

The use of an optical frequency comb source in the optical heterodyne A-RoF links facilitates the generation of frequency fluctuation-free mm-wave/THz carriers and data signals and eliminates the possibility of interference with adjacent wireless channels. A lower RF phase noise, paramount for the successful transmission of 5G provisioned low subcarrier spacing OFDM signals, can be achieved by operating the optical heterodyne A-RoF system at path matched point. The simulation and experimental analysis presented in this work allow the determination of the level of path length mismatch over the presented system and so, by appropriate correction, low phase noise 5G NR mm-wave signal generation can be achieved. The results presented in this chapter demonstrate the use of GSL OFC source for successful generation and transmission of 5G NR provisioned subcarrier spacing mm-wave OFDM signals carrying data at the rate of 1.12 Gb/s over an optical heterodyne A-RoF system. The successful demonstration of multi-frequency mm-wave signal generation at 27 GHz, 43 GHz and 59 GHz frequencies by using different pairs of tones from the same GSL OFC device shows how the presented A-RoF heterodyne fronthaul system can be used as a platform to reduce the complexity of future heterogeneous RRH antenna sites and further the centralization of resources.

Furthermore, replacing the GSL OFC with a photonic integrated QD-MLL eliminates the requirement of an RF source at the C-BBU site. This reduced complexity comes at the cost of increased phase noise on the heterodyne generated mm-wave signals as evident from the limitation of the presented system to restrict the successful transmission of the mm-wave OFDM signals with 250 kHz and higher subcarrier spacing only. The higher 3 dB bandwidth and flexibility in the choice of the frequency set for heterodyning make the MLL OFC based optical heterodyne A-RoF link more suitable for use in the high frequency wireless systems in convergence with the optical access networks, where the different sets of optical tones from the same MLL source can be used for various applications.

The potential for photonic integration and successful transmission of low subcarrier spacing OFDM signals makes both types of comb sources a good choice for use in the optical heterodyne A-RoF system. The choice of the employed OFC source should be done by considering the requirements of the particular system and the limitations of the comb.

References

- [1] S. A. Diddams, K. Vahala, and T. Udem, "Optical frequency combs: Coherently uniting the electromagnetic spectrum," *Science (1979)*, vol. 369, no. 6501, Jul. 2020, doi: 10.1126/SCIENCE.AAY3676/ASSET/B8B6CF9A-855D-4106-B6EA-89E0DD17420B/ASSETS/GRAPHIC/369_AAY3676_F6.JPEG.
- [2] T. Fortier and E. Baumann, "20 years of developments in optical frequency comb technology and applications," *Communications Physics 2019 2:1*, vol. 2, no. 1, pp. 1–16, Dec. 2019, doi: 10.1038/s42005-019-0249-y.
- [3] N. Picqué and T. W. Hänsch, "Frequency comb spectroscopy," *Nature Photonics 2019 13:3*, vol. 13, no. 3, pp. 146–157, Feb. 2019, doi: 10.1038/s41566-018-0347-5.
- [4] F. Quinlan *et al.*, "Microresonator frequency comb optical clock," *Optica, Vol. 1, Issue 1*, pp. 10-14, vol. 1, no. 1, pp. 10–14, Jul. 2014, doi: 10.1364/OPTICA.1.000010.
- [5] T. Udem, R. Holzwarth, and T. W. Hänsch, "Optical frequency metrology," *Nature 2002 416:6877*, vol. 416, no. 6877, pp. 233–237, Mar. 2002, doi: 10.1038/416233a.
- [6] Richard A. McCracken, Jake M. Charsley, and Derryck T. Reid, "A decade of astrocombs: recent advances in frequency combs for astronomy," *Opt. Express*, vol. 25, no. 13, pp. 15058–15078, 2017.
- [7] N. Kuse and M. E. Fermann, "Frequency-modulated comb LIDAR," *APL Photonics*, vol. 4, no. 10, Oct. 2019, doi: 10.1063/1.5120321.
- [8] L. Lundberg *et al.*, "Frequency Comb-Based WDM Transmission Systems Enabling Joint Signal Processing," *Applied Sciences 2018, Vol. 8, Page 718*, vol. 8, no. 5, p. 718, May 2018, doi: 10.3390/APP8050718.
- [9] M. Tan, X. Xu, J. Wu, R. Morandotti, A. Mitchell, and D. J. Moss, "RF and microwave photonic temporal signal processing with Kerr micro-combs," <https://doi.org/10.1080/23746149.2020.1838946>, vol. 6, no. 1, Jan. 2020, doi: 10.1080/23746149.2020.1838946.
- [10] V. Torres-Company and A. M. Weiner, "Optical frequency comb technology for ultra-broadband radio-frequency photonics," *Laser & Photonics Reviews*, vol. 8, no. 3, pp. 368–393, May 2014, doi: 10.1002/LPOR.201300126.
- [11] M. S. Alshaykh, J. D. McKinney, and A. M. Weiner, "Radio-Frequency Signal Processing Using Optical Frequency Combs," *IEEE Photonics Technology Letters*, vol. 31, no. 23, pp. 1874–1877, Dec. 2019, doi: 10.1109/LPT.2019.2946542.
- [12] P. J. Delfyett, J. Davila-Rodriguez, A. Klee, S. Bhoopapur, and C. Williams, "Optical frequency combs and their application in microwave photonics and coherent signal processing," *2013 Conference on Lasers and Electro-Optics, CLEO 2013*, 2013, doi: 10.1364/CLEO_SI.2013.CTU2G.1.
- [13] H. A. Haus, "Mode-locking of lasers," *IEEE Journal on Selected Topics in Quantum Electronics*, vol. 6, no. 6, pp. 1173–1185, Nov. 2000, doi: 10.1109/2944.902165.
- [14] T. J. Kippenberg, R. Holzwarth, and S. A. Diddams, "Microresonator-based optical frequency combs," *Science (1979)*, vol. 332, no. 6029, pp. 555–559, Apr. 2011, doi: 10.1126/SCIENCE.1193968/ASSET/C6C9738C-CD4D-4D1D-9F97-F433BFDD1359/ASSETS/GRAPHIC/332_555_F4.JPEG.
- [15] B. P. P. Kuo, E. Myslivets, V. Ataie, E. G. Temprana, N. Alic, and S. Radic, "Wideband parametric frequency comb as coherent optical carrier," *Journal of Lightwave Technology*, vol. 31, no. 21, pp. 3414–3419, 2013, doi: 10.1109/JLT.2013.2279540.
- [16] J. M. Chavez Boggio, S. Moro, N. Alic, M. Karlsson, J. Bland-Hawthorn, and S. Radic, "Nearly octave-spanning cascaded four-wave-mixing generation in dispersion optimized highly nonlinear fiber," *Frontiers in Optics 2009/Laser Science XXV/Fall 2009 OSA Optics & Photonics Technical Digest (2009), paper FTuD2*, p. FTuD2, Oct. 2009, doi: 10.1364/FIO.2009.FTuD2.
- [17] A. Parriaux, G. Millot, and K. Hammani, "Electro-optic frequency combs," *Advances in Optics and Photonics, Vol. 12, Issue 1*, pp. 223-287, vol. 12, no. 1, pp. 223–287, Mar. 2020, doi: 10.1364/AOP.382052.
- [18] B. Huang *et al.*, "Generation of coherent and frequency-lock multi-carriers using cascaded phase modulators and recirculating frequency shifter for Tb/s optical communication," *Optics Express, Vol. 19, Issue 14*, pp. 12891-12902, vol. 19, no. 14, pp. 12891–12902, Jul. 2011, doi: 10.1364/OE.19.012891.
- [19] R. Zhou, S. Latkowski, J. O'Carroll, R. Phelan, L. P. Barry, and P. Anandarajah, "40nm wavelength tunable gain-switched optical comb source," *Optics Express, Vol. 19, Issue 26*, pp. B415-B420, vol. 19, no. 26, pp. B415–B420, Dec. 2011, doi: 10.1364/OE.19.00B415.

- [20] Maria Deseada Gutierrez Pascual, "Development and Investigation of Optical Frequency Combs for Photonic Communication Systems," Dublin City University Ireland, 2017.
- [21] J. Beas, G. Castanon, I. Aldaya, A. Aragon-Zavala, and G. Campuzano, "Millimeter-wave frequency radio over fiber systems: A survey," *IEEE Communications Surveys and Tutorials*, vol. 15, no. 4, pp. 1593–1619, 2013, doi: 10.1109/SURV.2013.013013.00135.
- [22] C. Browning *et al.*, "Gain-switched optical frequency combs for future mobile radio-over-fiber millimeter-wave systems," *Journal of Lightwave Technology*, vol. 36, no. 19, pp. 4602–4610, Oct. 2018, doi: 10.1109/JLT.2018.2841365.
- [23] A. Kaszubowska, P. Anandarajah, and L. P. Barry, "Improved performance of a hybrid radio/fiber system using a directly modulated laser transmitter with external injection," *IEEE Photonics Technology Letters*, vol. 14, no. 2, pp. 233–235, Feb. 2002, doi: 10.1109/68.980532.
- [24] M. D. G. Pascual, V. Vujicic, J. Braddell, F. Smyth, P. Anandarajah, and L. Barry, "Photonic Integrated Gain Switched Optical Frequency Comb for Spectrally Efficient Optical Transmission Systems," *IEEE Photonics Journal*, vol. 9, no. 3, Jun. 2017, doi: 10.1109/JPHOT.2017.2678478.
- [25] T. Shao, R. Zhou, V. Vujicic, M. D. G. Pascual, P. M. Anandarajah, and L. P. Barry, "100 km Coherent Nyquist Ultradense Wavelength Division Multiplexed Passive Optical Network Using a Tunable Gain-Switched Comb Source," *Journal of Optical Communications and Networking, Vol. 8, Issue 2*, pp. 112–117, vol. 8, no. 2, pp. 112–117, Feb. 2016, doi: 10.1364/JOCN.8.000112.
- [26] T. Shao, M. Beltrán, R. Zhou, P. M. Anandarajah, R. Llorente, and L. P. Barry, "60 GHz radio over fiber system based on gain-switched laser," *Journal of Lightwave Technology*, vol. 32, no. 20, pp. 3695–3703, Oct. 2014, doi: 10.1109/JLT.2014.2308152.
- [27] T. Shao *et al.*, "Chromatic dispersion-induced optical phase decorrelation in a 60 GHz OFDM-RoF system," *IEEE Photonics Technology Letters*, vol. 26, no. 20, pp. 2016–2019, Oct. 2014, doi: 10.1109/LPT.2014.2344314.
- [28] S. Jia *et al.*, "0.4 THz Photonic-Wireless Link with 106 Gb/s Single Channel Bitrate," *Journal of Lightwave Technology*, vol. 36, no. 2, pp. 610–616, Jan. 2018, doi: 10.1109/JLT.2017.2776320.
- [29] S. Koenig *et al.*, "Wireless sub-THz communication system with high data rate enabled by RF photonics and active MMIC technology," *2014 IEEE Photonics Conference, IPC 2014*, pp. 414–415, Dec. 2014, doi: 10.1109/IPCON.2014.6995424.
- [30] L. ES, B. RM, A. N, C. E, C. G, and S. AC, "Integrated Optical Frequency Comb for 5G NR Xhuals," Apr. 2022, doi: 10.21203/RS.3.RS-1576950/V1.
- [31] A. Stohr *et al.*, "Millimeter-wave photonic components for broadband wireless systems," *IEEE Transactions on Microwave Theory and Techniques*, vol. 58, no. 11 PART 2, pp. 3071–3082, 2010, doi: 10.1109/TMTT.2010.2077470.
- [32] E. P. Martin *et al.*, "25-Gb/s OFDM 60-GHz radio over fiber system based on a gain switched laser," *Journal of Lightwave Technology*, vol. 33, no. 8, pp. 1635–1643, Apr. 2015, doi: 10.1109/JLT.2015.2391994.
- [33] C. Browning, D. Dass, P. Townsend, and X. Ouyang, "Orthogonal Chirp-Division Multiplexing for Future Converged Optical/Millimeter-Wave Radio Access Networks," *IEEE Access*, vol. 10, pp. 3571–3579, 2022, doi: 10.1109/ACCESS.2021.3137716.
- [34] Y. Li *et al.*, "D-Band mm-Wave SSB vector signal generation based on cascaded intensity modulators," *IEEE Photonics Journal*, vol. 12, no. 2, Apr. 2020, doi: 10.1109/JPHOT.2020.2974256.
- [35] T. Shao *et al.*, "Phase Noise Investigation of multicarrier Sub-THz Wireless Transmission System Based on an Injection-Locked Gain-Switched Laser," *IEEE Transactions on Terahertz Science and Technology*, vol. 5, no. 4, pp. 590–597, Jul. 2015, doi: 10.1109/TTHZ.2015.2418996.
- [36] A. Delmade *et al.*, "Power efficient optical frequency comb generation using laser gain switching and dual-drive Mach-Zehnder modulator," *Optics Express, Vol. 27, Issue 17*, pp. 24135–24146, vol. 27, no. 17, pp. 24135–24146, Aug. 2019, doi: 10.1364/OE.27.024135.
- [37] W. Shieh *et al.*, "Intra-symbol frequency-domain averaging based channel estimation for coherent optical OFDM," *Optics Express, Vol. 16, Issue 26*, pp. 21944–21957, vol. 16, no. 26, pp. 21944–21957, Dec. 2008, doi: 10.1364/OE.16.021944.
- [38] Y. Yoshimizu, S. Hisatake, S. Kuwano, J. Terada, N. Yoshimoto, and T. Nagatsuma, "Generation of coherent sub-terahertz carrier with phase stabilization for wireless communications," *Journal of Communications and Networks*, vol. 15, no. 6, pp. 569–575, 2013, doi: 10.1109/JCN.2013.000105.

- [39] D. Dass, S. O’Duill, A. Delmade, and C. Browning, “Analysis of Phase Noise in a Hybrid Photonic/Millimetre-Wave System for Single and Multi-Carrier Radio Applications,” *Applied Sciences* 2020, Vol. 10, Page 5800, vol. 10, no. 17, p. 5800, Aug. 2020, doi: 10.3390/APP10175800.
- [40] J. P. Santacruz, S. Rommel, U. Johannsen, A. Jurado-Navas, and I. T. Monroy, “Analysis and Compensation of Phase Noise in Mm-Wave OFDM ARoF Systems for beyond 5G,” *Journal of Lightwave Technology*, vol. 39, no. 6, pp. 1602–1610, Mar. 2021, doi: 10.1109/JLT.2020.3041041.
- [41] A. Delmade, C. Browning, and L. P. Barry, “5G New Radio Compatible Multicarrier Signals Delivery over an Optical/Millimeter-Wave Analog Radio-over-Fiber Fronthaul Link,” *2020 European Conference on Optical Communications, ECOC 2020*, Dec. 2020, doi: 10.1109/ECOC48923.2020.9333188.
- [42] H. H. Elwan, R. Khayatzaheh, T. Shao, J. Poette, B. Cabon, and L. P. Barry, “Impact of Laser Mode Partition Noise on Optical Heterodyning at Millimeter-Wave Frequencies,” *Journal of Lightwave Technology*, vol. 34, no. 18, pp. 4278–4284, Sep. 2016, doi: 10.1109/JLT.2016.2596381.
- [43] G. H. Duan *et al.*, “High performance InP-Based quantum dash semiconductor Mode-Locked lasers for optical communications,” *Bell Labs Technical Journal*, vol. 14, no. 3, pp. 63–84, Sep. 2009, doi: 10.1002/BLTJ.20388.
- [44] R. Rosales *et al.*, “High performance mode locking characteristics of single section quantum dash lasers,” *Optics Express*, Vol. 20, Issue 8, pp. 8649-8657, vol. 20, no. 8, pp. 8649–8657, Apr. 2012, doi: 10.1364/OE.20.008649.
- [45] A. Ramdane *et al.*, “Mode Locked Laser Phase Noise Reduction Under Optical Feedback for Coherent DWDM Communication,” *Journal of Lightwave Technology*, Vol. 38, Issue 20, pp. 5708-5715, vol. 38, no. 20, pp. 5708–5715, Oct. 2020, doi: 10.1364/JLT.38.005708.
- [46] K. Merghem, V. Panapakkam, Q. Gaimard, F. Lelarge, and A. Ramdane, “Narrow Linewidth Frequency Comb Source based on Self-injected Quantum-Dash Passively Mode-Locked Laser,” *Conference on Lasers and Electro-Optics (2017)*, paper SW1C.5, vol. 2017-January, p. SW1C.5, May 2017, doi: 10.1364/CLEO_SI.2017.SW1C.5.
- [47] C. Song *et al.*, “Passively mode-locked quantum dash laser with an aggregate 5.376 Tbit/s PAM-4 transmission capacity,” *Optics Express*, Vol. 28, Issue 4, pp. 4587-4593, vol. 28, no. 4, pp. 4587–4593, Feb. 2020, doi: 10.1364/OE.386266.

5. Advanced Optical Techniques for the Next Generation Millimetre-Wave Wireless Systems

The use of an optical frequency comb source for heterodyning facilitates the generation of frequency fluctuation-free and low phase noise mm-wave carriers. The simple and photonics-integrable architecture of the gain switched laser OFC with highly correlated comb lines makes it an ideal choice for deployment in the optical heterodyne mm-wave wireless systems for successful transmission of low subcarrier spacing OFDM signals provisioned in the 5G standard. However, the high linewidth of the GSL OFC tones, making it prone to path length mismatch induced decorrelation (as shown in chapter 4), adds to its disadvantages while extending its use beyond 5G systems. Also, the requirement of filtering and amplification stage, necessary for all types of OFC sources in the heterodyne system, increases the complexity of the C-BBU site architecture. It is necessary to reduce the linewidth of GSL OFC tones and further efficiently develop techniques which reduce the overall complexity of the optical heterodyne system.

In this chapter, advanced optical techniques such as active demultiplexing (for simultaneous filtering and amplification of OFC tones), injection locking with low linewidth laser (for reducing the linewidth of GSL OFC tones) and bi-directional mm-wave fronthaul link demonstration with remote frequency down-conversion are explored. Initially, a technique based on the injection locking and direct modulation of a DFB laser, with a combined data signal and RF LO, is demonstrated for reducing the complexity of the optical heterodyne A-RoF system in section 5.1. A technique based on the bi-directional signal propagation (downlink and uplink) through the same fibre is demonstrated, in section 5.2, with remote frequency down-conversion and reuse of one of the OFC tones for uplink data transmission. Active de-multiplexing was employed in this setup to filter the GSL OFC tones.

5.1 Millimetre-Wave A-RoF System employing Optical Injection Locking and Direct Modulation of a DFB Laser

The optical heterodyne analogue RoF system demonstrated in chapter 4 uses a programmable wave shaper (WSS), to filter two tones from the OFC source, and an optical amplifier to compensate for the power loss. It also requires additional optical bandpass filters (see Fig. 4.5 in chapter 4) to filter out one of the OFC tones in individual optical carrier paths i.e. unmodulated and modulated channels. These filters can be removed from the setup by filtering two OFC tones separately from two output ports of WSS, however, it will necessitate the use of two optical amplifiers to compensate for the excessive power loss – further increasing the complexity. Also, the use of amplifiers increases the noise in the system - resulting in performance degradation. The employed WSS, from Finisar [1] in our setup, was a sophisticated device

with minimum bandwidth of 10 GHz and a frequency resolution of 1 GHz. It's impractical and cost inefficient to use such an instrument in the field deployable systems. Typically, arrayed waveguide grating [2]–[4] or fibre Bragg gratings [5], [6] are used to filter out the OFC tones in optical systems. Most of the AWGs exhibits fixed channel spacing (mostly used for WDM systems), while the FBG's limited wavelength tunability hinders its use in the flexible optical heterodyne A-RoF systems deployment employing FSR tuneable OFC source. In this section, an active de-multiplexing technique [7], [8] and simultaneous data and RF LO modulation of the DFB laser are explored to simultaneously filter and amplify the OFC tones and further demonstrate the 5G NR mm-wave signal generation.

5.1.1 Active De-multiplexing and Simultaneous Data and RF LO modulation

An active de-multiplexing technique, which depends on the injection locking of a slave laser, has been demonstrated previously for filtering OFC tones [7]–[9]. Fig. 5.1(i) shows the schematic of the optical heterodyne system using active de-multiplexing for OFC tones filtering and subsequent mm-wave carrier generation. The output of a GSL OFC source, containing multiple correlated optical carriers, is injected

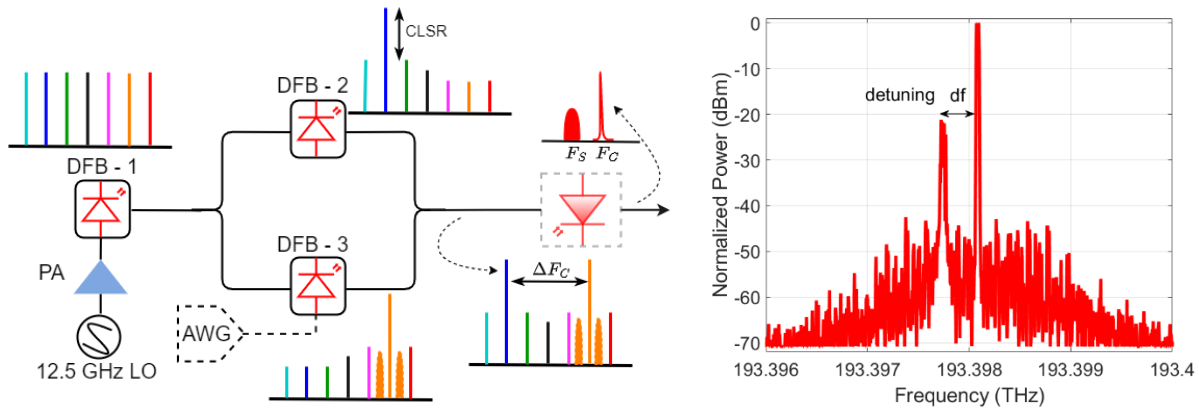


Fig. 5.1 (i) Schematic of an active de-multiplexer for simultaneously filtering and amplification of GSL OFC tones and (ii) combined optical spectrum of slave laser and OFC tone showing the detuning.

into two slave lasers. The frequency fluctuation and phase noise characteristics of two OFC tones, whose frequencies are close to the lasing frequencies of the slave lasers, will be imprinted on the output of slave lasers. As the spacing between OFC tones remains the same, the output of two slave lasers will also have a fixed spacing between them upon injection locking. While the slave lasers are operating independently, injection locking with the GSL OFC makes their frequency fluctuations correlated – leading to a fixed frequency mm-wave carrier generation upon heterodyning. The other OFC tones will be suppressed greatly from the output of the slave laser, as shown in the figurative spectrums in Fig. 5.1(i), – resulting in filtering [7], [10] Also, the power of the locked OFC tone will be the same as that of the slave laser – leading to amplification. The quality of locking and achieved level of OFC tones suppression (i.e. comb line suppression ratio (CLSR)) depends on multiple factors such as the ratio of slave laser power to injected

signal/tone power, the polarization of the injected signal and the frequency separation between the OFC tone to be locked and slave laser (i.e. detuning frequency) [7], [10].

If the power of injected OFC output signal is high, it can result in unstable oscillation and generation of nonlinear mixing components at the output of the slave laser [7]. Typically the power of OFC tones is considerably reduced before injecting it into the slave laser using a VOA, and amplification of the OFC tone whose frequency is close to the slave laser's lasing mode is achieved upon locking. A polarization controller will be used at the input of the slave laser to match the polarization state of the injected signal and slave laser. The detuning factor, i.e. the frequency spacing between the slave laser and the intended OFC tone to be locked, also plays an important role [7]. The spectrum in Fig. 5.1(ii) shows the detuning between a high-power slave laser and one of the GSL OFC tones. The higher detuning frequency leads to unstable locking and higher CLSR. Typically, a CLSR of 25 to 35 dB can be obtained by appropriately varying the power ratio and minimizing the frequency detuning [7], [10].

Fig. 5.1(i) also shows the possibility of data signal modulation (from AWG) on one of the slave lasers to achieve mm-wave signal generation. In the latest work in [10], [11], a GSL OFC source based optical heterodyne A-RoF system is demonstrated with active de-multiplexing and simultaneous data modulation on one of the slave lasers. It is possible to move this data modulation on the slave laser to the master laser being gain switched and reduce the system complexity. Also, the power of the RF signal used for gain switching can be reduced by modulating the laser at relaxation oscillation frequency. The higher amount of non-linearity at relaxation oscillation and the requirement of low injected tone power for active de-multiplexing can reduce the overall power consumption.

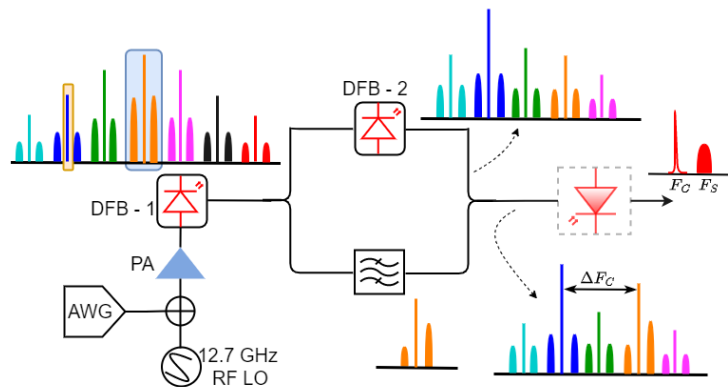


Fig. 5.2 A schematic of the optical heterodyne system based on simultaneous data and RF LO modulation and optical injection locking for mm-wave signal generation.

Fig. 5.2 shows the schematic of an optical heterodyne technique based on the simultaneous RF LO and data signal modulation. A distributed feedback laser was simultaneously modulated with a 5G compatible IF data signal and RF sinusoidal signal with a frequency close to the relaxation oscillation of the laser. The direct modulation of the laser at a nonlinear relaxation oscillation frequency point results in the generation

of optical carriers, separated by RF LO harmonics, along with a double sideband data signal on each harmonic as shown in the figurative spectra in Fig. 5.2. The output of DFB-1 was split into two paths, one for filtering and amplification of 2nd harmonic (shown by blue carrier in Fig. 5.2) with active de-multiplexing, and the other for direct filtering of the main carrier and data sideband (shown by the orange colour carrier and signal in Fig. 5.2). The lasing frequency of the DFB-2 was tuned to be close to the blue optical carrier from the output of DFB-1 in order to reduce the detuning frequency. Upon injection locking, this blue carrier gets amplified while the other frequency components get attenuated. The de-multiplexed blue carrier was combined with the optical bandpass filtered orange coloured main carrier and data signal sideband. The combined signal results in a low PN mm-wave signal generation after detection, at frequencies well above the modulation bandwidth of the DFB laser. Higher frequency signals can be generated by selecting the 3rd or 4th harmonics for active de-multiplexing and data signal from 0th or 1st harmonic copies for heterodyning. The de-multiplexing and filtering operations are shifted to the RRH remote antenna site in the demonstrated scheme here.

The successful generation of 5G compatible OFDM signals at 28.2 GHz and 35.1 GHz frequencies is demonstrated over the outlined optical heterodyne system with performance below the forward error correction limit after transmission over 10 km of single-mode fibre. A similar configuration is demonstrated in [10], where a master injected laser is gain-switched to generate an OFC source and its output tones were injected into two slave lasers. Here as well the laser is modulated with a sinusoidal signal, but rather than using high power RF signal to generate the OFC, the nonlinear modulation response of the laser is exploited to our advantage – resulting in power-efficient implementation. The simultaneous modulation of the IF data signal eliminates the need for an additional laser compared to the previous demonstration in [10].

5.1.2 Experimental Setup

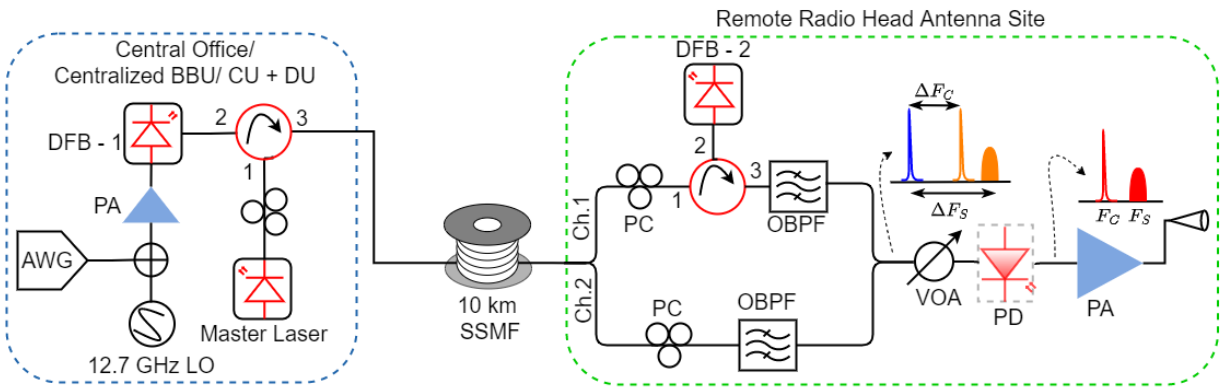


Fig. 5.3 Experimental testbed of the optical heterodyne A-RoF link based on simultaneous data and RF LO modulation and remote active demultiplexing for mm-wave signal generation.

The schematic of an optical heterodyne A-RoF system based on the OIL and DM of the DFB laser is shown in Fig. 5.3. A DFB laser with a relaxation oscillation peak of ~12.7 GHz was modulated

simultaneously with a 5G compatible IF signal and 12.7 GHz RF sinusoidal signal (~15 dBm power) at the CO. The RF signal modulation in the nonlinear region results in the generation of harmonic components as seen from the optical spectra of Fig. 5.4. The first-order modulation components (+1 and -1), at 12.7 GHz, have approximately the same power as the main optical carrier (0), while the second and third-order harmonics, at 25.4 GHz and 38.1 GHz, are approximately 10 dB and 25 dB lower than the main carrier, respectively. The power in the harmonic components depends on the depth of modulation and the nonlinearity of the laser response. 5G compatible 195 MHz BW OFDM signals with variable subcarrier

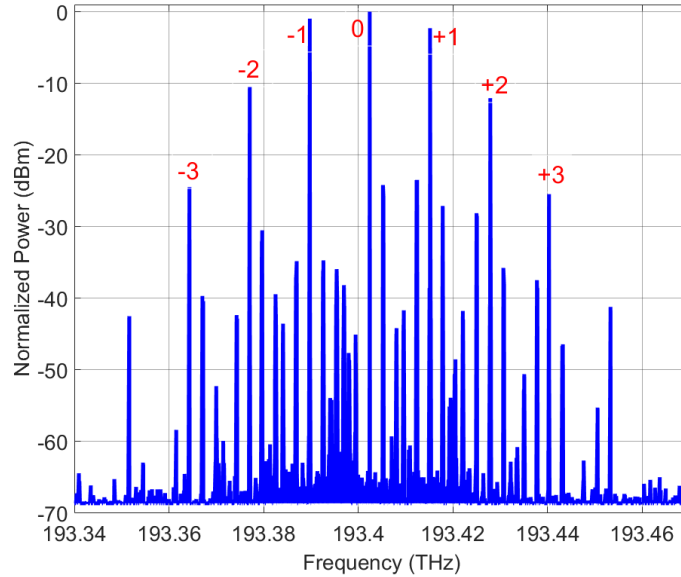


Fig. 5.4 Optical spectrum of the DFB laser simultaneously modulated with the data signal and RF LO. spacing were generated and frequency converted to the 2.8 GHz intermediate frequency in Matlab. The IF signal samples were loaded into the arbitrary waveform generator at the transmitter and the generated signal was combined with the RF sinusoidal signal before laser modulation. The direct modulation of the IF 5G data signal will generate a double-sideband signal around the main carrier and all of the harmonics as shown in the spectrum of Fig. 5.4. The second-order harmonics of the data signals will be also generated depending on the depth of modulation. A low linewidth master laser was injected into this DFB laser in order to stabilize the frequency and phase fluctuations of the DFB-1 laser. It's difficult to keep the detuning frequency minimal without injection of the DFB-1 with a stable master laser. The DFB-1 laser output was transmitted from CO to the RRH site through 10 km SMF.

At the antenna RRH side, the received signal was split into two channels – Ch. 1 to lock a free-running slave DFB laser 2 to the second harmonic (-2) of the RF carrier and Ch. 2 for filtering the IF data signal sideband and associated modulated carrier as shown in the experimental setup of Fig. 5.3. The locking of the DFB laser 2 by the second harmonic tone (-2) increases the optical power in this tone and suppress the

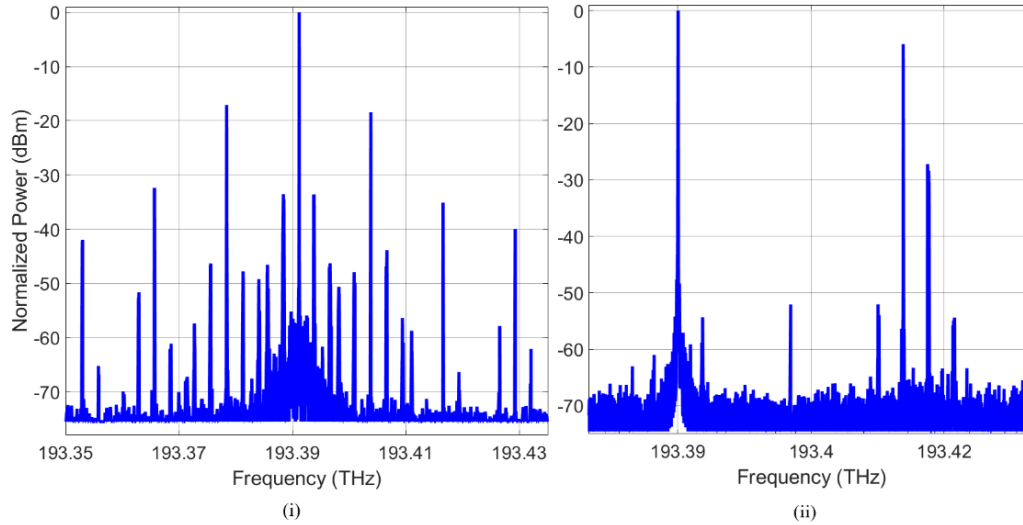


Fig. 5.5 Optical spectrum (i) at the output of slave laser (DFB-2) after injection locking and (ii) of a combined signal at the input of PD.

other signal components as shown in the slave laser output spectrum in Fig. 5.5(i). CLSR of close to 20 dB was measured as seen from the spectrum. The calibration error from the optical spectrum analyser resulted in different x-axis scales in Fig. 5.4 and 5.5. An additional filtering stage was required in Ch. 1 to filter out additional signal components passing through the slave DFB laser 2 after injection. In Ch. 2, the IF data signals sideband and the associated optical carrier were filtered using the OBPF. The combined signal from two channels, the spectrum of which is shown in Fig. 5.5(ii), beat on the PD to generate the mm-wave signal.

In the first case, the main carrier (0 harmonics) and associated IF data signals upper sideband were filtered from Ch. 2 and combined with an amplified second harmonic (-2 harmonic) carrier from Ch.1 to generate a 5G mm-wave signal at 28.2 GHz upon beating on the PD. In the second case, the first harmonic carrier on the upper side (+1 harmonic) and associated data signals lower sideband were filtered from Ch.2 and combined with an amplified second harmonic (-2) carrier from Ch.1 to generate a 5G mm-wave signal at 35.3 GHz frequency. This mm-wave data was captured using a real-time oscilloscope after frequency down-conversion to an IF band using an RF heterodyne receiver consisting of an external local oscillator and mixer. Offline processing including re-sampling, channel equalization, BER and EVM measurement was performed using Matlab. Moving the remote injection locking and data filtering stage (which has the potential to be integrated on a single chip) to the C-BBU site can further reduce the complexity of the RRH antenna site and improve network management.

The system's capabilities were investigated for the transmission of low subcarrier spacing multi-carrier signals by transmitting the OFDM signals with subcarrier spacing values of 2 MHz, 1 MHz, 500 kHz, 250 kHz, 125 kHz, and 62.5 kHz for both generated mm-wave frequencies. To keep the OFDM signal

bandwidth constant, the IFFT size and number of data subcarriers were changed by a factor of two with respect to the previous subcarrier spacing signal.

5.1.3 System Performance

Initially, two different mm-wave carriers at 25.4 GHz and 38.1 GHz frequencies were generated over the outlined optical heterodyne system. For the generation of the 25.4 GHz carrier, the main carrier (0 harmonic - filtered in Ch. 1) and -2 harmonic (from injected slave DFB laser 2 in Ch. 2) were combined for heterodyne

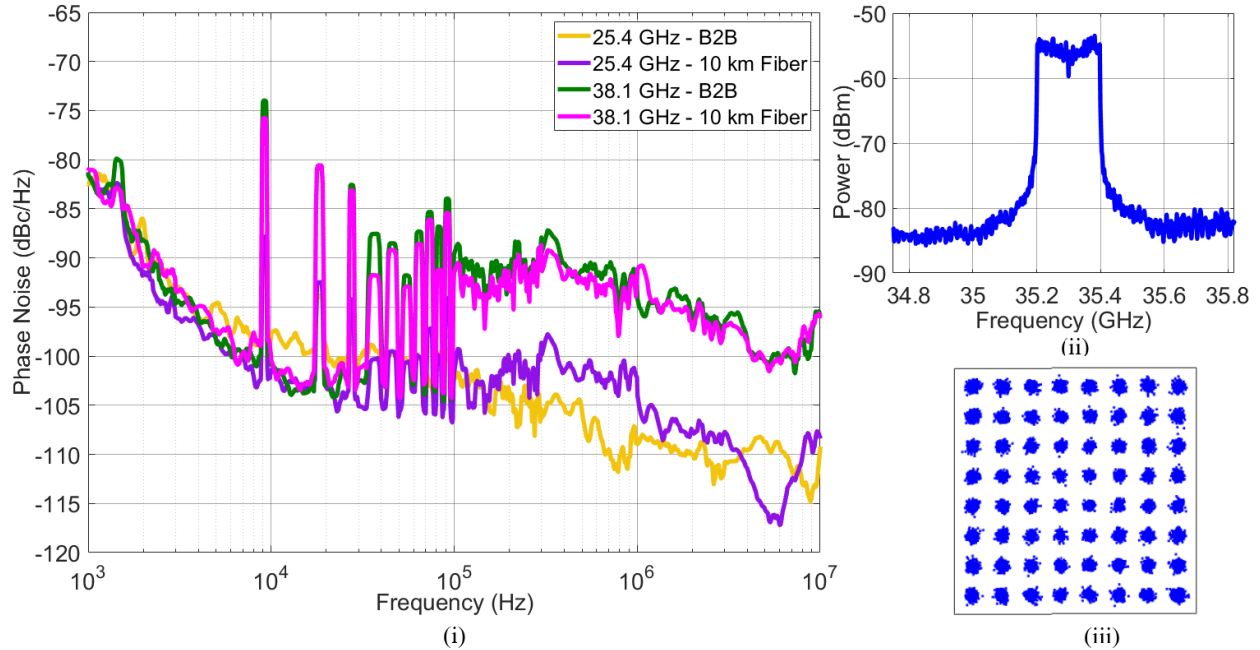


Fig. 5.6 (i) Phase noise of the photo-mixing generated 25.4 GHz and 38.1 GHz mm-wave carriers, (ii) RF spectrum of the generated 35.3 GHz mm-wave signals and (iii) constellation of the 28.2 GHz demodulated mm-wave signal over an optical heterodyne A-RoF system employing OIL and direct modulation of a DFB laser detection on the PD. For 38.1 GHz mm-wave carrier generation, the +1 RF signal harmonic (from Ch. 1) and -2 harmonic (from Ch. 2) were combined and beat on the high-speed PD. The PN of the generated carriers is shown in Fig. 5.6(i). Results show that both the generated carriers exhibit PN below -80 dBc/Hz at a 1 kHz frequency offset from the carriers. The PN of the 25.4 GHz carrier reduces further to -115 dBc/Hz at a 10 MHz offset, while that of the 38.1 GHz carrier reduces to -95 dBc/Hz only. The increase in the PN for the 38.1 GHz carrier at higher offsets stems from the use of a +1 harmonic modulated carrier, for beating, which is further away from the master laser than the main 0 order carrier used for 25.4 GHz carrier generation. The series of jumps observed in the phase noise plot arises from the feedback coming from the cavity created at the receiver for injection locking and filtering (see Fig. 5.3). The phase noise jumps are present for both the heterodyne generated 25.4 GHz and 38.1 GHz carriers and overlap at the same frequencies. The phase noise on the higher order harmonics of the RF LO increases with increasing spacing

between the optical carriers used for heterodyning – similar to the observation reported in chapter 4 for GSL OFC. Nevertheless, in both cases, the phase noise is low enough to produce a mm-wave signal with sufficient purity achieving the below FEC level performance. The PN of the beat signal is observed to be the same for the case of a back-to-back and 10 km fibre transmission, for a 38.1 GHz case. A slight deviation in the phase noise at high frequency offsets is observed for the case of a 25.4 GHz carrier.

To observe the system's performance, we modulated a 2.8 GHz IF OFDM data signal (with ~2 MHz subcarrier spacing) along with RF 12.7 GHz carrier on the first DFB laser 1. This resulted in the generation of mm-wave signals at 28.2 and 35.3 GHz frequencies as described in the above subsection. The RF spectrum of the generated signal at 35.3 GHz is shown in Fig. 5.6(ii), while the constellation of the demodulated signal, after frequency down-conversion, is shown in Fig. 5.6(iii). This constellation, with an EVM of ~4%, indicates the successful generation and transmission of mm-wave OFDM signal over a 10 km optical heterodyne A-RoF link resulting in data transmission at the rate of ~1.17 Gb/s. Finally, the outlined system's performance was analysed for the transmission of variable subcarrier spacing OFDM signals. The obtained results, shown in Fig. 5.7(i), indicate that for the implemented system, performance was almost the same at all the subcarrier spacing from 2 MHz to 62.5 kHz, for both the frequencies – showing its capabilities to successfully transmit the 5G NR compatible subcarrier spacing (60 kHz and

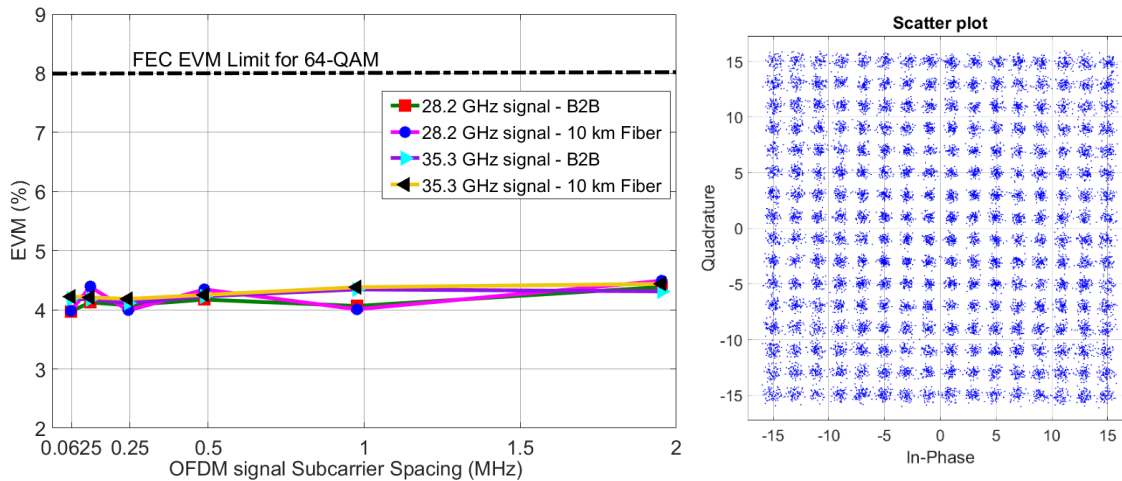


Fig. 5.7 (i) EVM vs subcarrier spacing and (ii) constellation of the 256-QAM data modulated OFDM signals over mm-wave A-RoF system employing OIL and direct modulation of a DFB laser.

higher) OFDM signals. Even though the phase noise of the 38.1 GHz carrier is slightly worse than the 25.4 GHz carrier (at higher frequency offsets as seen in Fig. 5.6(i)), it is sufficiently low to successfully demodulate the OFDM signals. The result shows no performance penalty after 10 km fibre transmission – similar to the PN findings. The obtained EVMs are well below the 8% FEC limit of 64-QAM data modulated signal. In order to increase the data rate over the outlined system, the order of QAM modulation on the OFDM subcarriers was increased from 64-QAM to 256-QAM and the constellation of the

demodulated signal is shown in Fig. 5.7(ii). A measured EVM of 3.8%, slightly above the FEC EVM limit of 3.5% for 256-QAM, was observed for the constellation shown in Fig. 5.7(ii) – indicating the need for further system optimisation.

The mm-wave system described here achieves excellent performance compared to our previous demonstrations using a mode-locked laser OFC source (discussed in chapter 4), while completely negating the requirement for optical amplification stages. The simultaneous direct modulation of the IF data and RF sinusoidal signal allows external modulation-free system implementation. Moving the remote injection locking and data filtering stage (which has the potential to be integrated on a single chip) to the CO can further reduce the complexity of the RRH antenna site. The low phase noise and constant performance over a wide range of OFDM subcarrier spacing highlight the potential of the outlined OIL and DM of the DFB laser based optical heterodyne A-RoF system for the mm-wave 5G and beyond 5G wireless systems. In the next section, a bidirectional mm-wave A-RoF link is demonstrated to further reduce the complexity of such systems.

5.2 Bidirectional Millimetre Wave Analog-RoF System employing Remote Down-Conversion and Wavelength Reuse

The implementation of a full duplex optical fronthaul link, for transferring data between the C-BBU/CO and RRH sites, is typically done with different optical fibre cables used for downlink and uplink data transmission [12]. Also, a laser and external modulator is typically used at the RRH site for carrying the uplink data to the C-BBU site. Furthermore, if the antenna received uplink signal from the mobile user is in the mm-wave or higher frequency bands, then an additional frequency down-conversion stage will be implemented at the RRH site - requiring an external LO and mixer. All these scenarios increase the complexity of the RRH antenna site and overall wireless system. It is necessary to reduce the complexity in order to facilitate a cost-efficient system implementation. In this section, a technique based on the bidirectional downlink and uplink signal transmission through the same fibre along with remote frequency down-conversion and wavelength reuse is demonstrated to reduce the complexity of the optical heterodyne mm-wave A-RoF system.

5.2.1 Experimental Setup and Details

The experimental setup of the bidirectional optical heterodyne A-RoF system is shown in Fig. 5.8. It consists of a C-BBU and RRH sites, connected by 12 km of fibre with both uplink and downlink signal passing through it in opposite directions. At the CO, highly coherent optical carriers were generated using an externally injected GSL OFC source [13]. An active optical demultiplexer [8], as shown in the setup, was used to simultaneously filter and amplify two of the comb lines, separated by 56 GHz. The

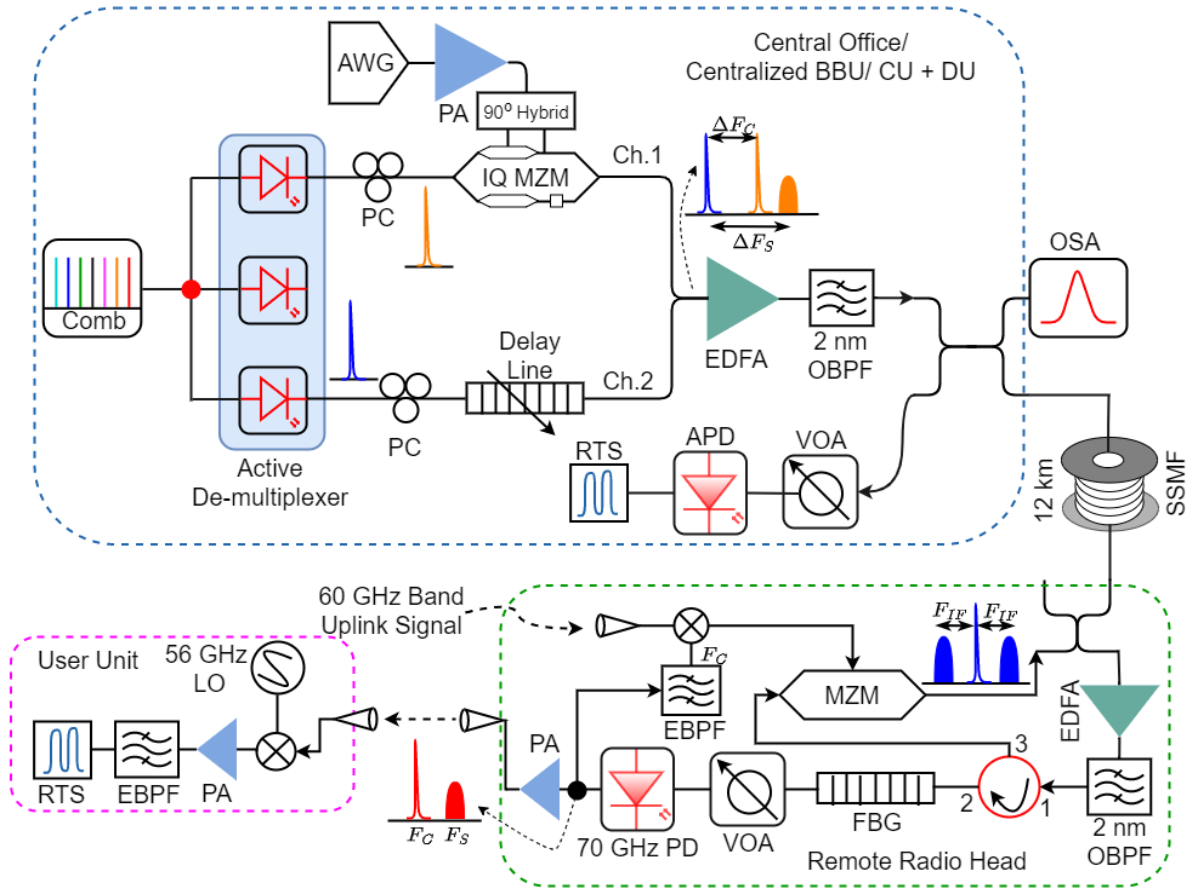


Fig. 5.8 Bidirectional mm-wave A-RoF systems experimental testbed with remote frequency down-conversion and wavelength reuse concept.

demultiplexed comb tones, with ~ 10 dBm power, were fed to two channels of the transmitter. An IQ Mach Zehnder Modulator and electrical 90° hybrid were used in Channel 1 to perform an optical single sideband data modulation, similar to the schemes discussed in chapters 3 and 4. A single band of universally filtered OFDM signal, centred at an intermediate frequency of 5 GHz, was generated using an AWG operating at 20 GSa/s. The 148.5 MHz bandwidth UF-OFDM signal, consisting of 76 64-QAM data modulated subcarriers spaced by 1.95 MHz, carried raw data at the rate of 0.89 Gb/s. The O-SSB data along with modulated optical carrier from Ch. 1 was combined with the unmodulated comb line from Ch. 2. The combined signal consisting of two optical carriers and one data sideband was first amplified by an Erbium doped fibre amplifier and then transmitted through a 12 km fibre with input power of 7.6 dBm.

At the RRH site, the received optical signal was again amplified ($P_{\text{avg}} = 18$ dBm) and passed through an optical circulator and FBG filter. This additional amplification stage was required to overcome the high loss offered by FBG used in the setup. The FBG was tuned to reflect a portion of the blue unmodulated optical carrier (Fig. 5.8), which was then fed as an input to the MZM used for modulation of the uplink signal (from the RRU to CO). The tuning of FBG slope resulted in a higher loss of ~ 8 dB ($\sim 16\%$ reflectivity)

for the reflected blue optical carrier. Such an arrangement simplifies the system, by removing the requirement of an optical source at the RRH site. The photo-mixing of the FBG transmitted signal components, after detection by a 70 GHz PIN PD, generated a downlink mm-wave data signal centred at 61 GHz along with a 56 GHz mm-wave carrier. This data signal can be directly transmitted to the end user after amplification as shown in the experimental setup of Fig. 5.8. Wireless transmission was not carried out for this experiment and the output of PD was directly connected to the RF heterodyne receiver for frequency down-conversion and subsequent signal demodulation. The 61 GHz mm-wave signal was mixed with a 56 GHz external LO and frequency down-converted to the original IF of 5 GHz.

The photo-mixing generated 56 GHz mm-wave carrier was used as an LO at the RRH site to frequency down-convert the antenna captured mm-wave uplink signal, transmitted by the user unit (64-QAM UF-OFDM signal at 61 GHz generated in a similar fashion as downlink), to an IF frequency, analogous to [14]. The IF uplink signal was then modulated, on the FBG reflected portion of the unmodulated optical carrier, using an MZM, and sent back to the CO through the same fibre. The 6 dB loss from the MZM used for the uplink data modulation and the 3 dB loss from the fibre resulted in the received power of +1 dBm at the C-BBU site. At the CO, the uplink data is detected using an APD with a multiplication factor of 3 and a saturation power of -8 dBm. Both, the uplink and downlink IF signals were captured using an RTS operating at 50 GSa/s. Offline processing, including re-sampling, channel estimation/equalization, BER and EVM calculations, was performed using Matlab.

5.2.2 System Performance

The performance of the system was analysed for two transmission scenarios. For the first scenario, the RRH and C-BBU site were connected by two separate fibres, one for uplink and one for downlink transmission, while in the second case both uplink and downlink signals were sent over the same fibre spool

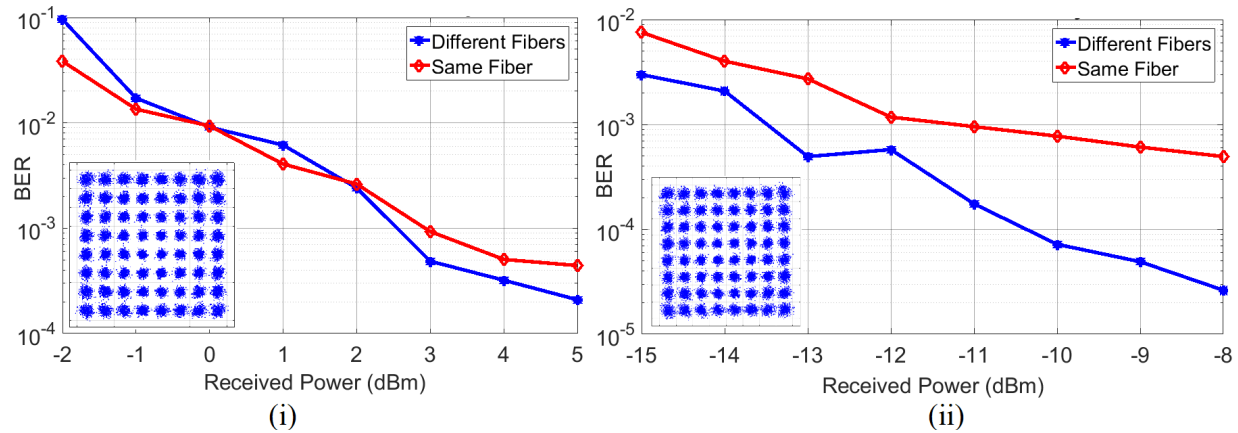


Fig. 5.9 BER vs received optical power performance of (i) 61 GHz mm-wave OFDM downlink signal and (ii) 5 GHz IF OFDM uplink signal for the cases of transmission through different (unidirectional) and same (bidirectional) optical fibre spools over an optical heterodyne A-RoF system.

(bidirectional transmission). The measured BER for each case and each direction, are shown in Fig. 5.9(i) and (ii). The results show that the below forward error correction limit (3.8×10^{-3}) BER values were obtained at the highest operating power for all the cases. For the downlink transmission, there was no power penalty due to the bidirectional transmission, while the uplink suffers a ~ 2 dB penalty at a BER of 1×10^{-3} . This performance degradation can be attributed to the Rayleigh backscattering and additional losses in the path, introduced by two 3 dB couplers needed to launch the signal into the fibre. In the bi-directional transmission through the same fibre scenario, the blue optical carrier (see Fig. 5.9) is transmitted in both directions and will see an increase in the total power throughout the length of the fibre. An increase in the power of the carrier will induce the Rayleigh backscattering nonlinearity and performance degradation. As the EDFA at the CO was operating at its maximum output power, this loss had to be compensated by increasing the gain of the RRH site EDFA. The reduced input power and increased gain of the RRH amplifier resulted in a degraded signal-to-noise ratio of the uplink signal. Using a higher output power EDFA at the CO would improve the performance of the uplink. A clearly defined constellation diagram of the received uplink and downlink signals, after the bidirectional transmission, are also shown in Fig. 5.9(i) and (ii) for the highest received optical power levels. The use of different sensitivity photodetectors for downlink (70 GHz PIN PD) and uplink (10 GHz APD) signals detection resulted in different power budgets for downlink and uplink transmission cases as evident from the received optical power levels in Fig. 5.9(i) and (ii).

The successful transmission of the OFDM signals over the outlined system with wavelength reuse shows that the optical source at the RRH unit can be eliminated by reusing a portion of the optical carrier from the downlink direction. In a heterodyne system, the unmodulated carrier experiences significantly less loss on its path than the modulated one (as it does not pass through an IQ-MZM). Thus, to maintain an optimum power distribution between the modulated and unmodulated lines, the unmodulated carrier is generally attenuated at the transmitter. In the demonstrated approach, rather than wasting this excess power, it is used for uplink transmission, improving the system's energy efficiency. The second benefit of the proposed scheme is that by down-converting the uplink signal to an IF using the photo-mixing generated mm-wave carrier at the RRH site, the necessity of modulating the uplink optical carrier with an mm-wave signal is eliminated. As a result, a high-speed electro-optic modulator is not required at the RRH site and dispersive fading problems [15], encountered when operating at high RF frequencies, are reduced. Furthermore, down-conversion and transmission of multiple uplink data signals can be carried out simultaneously, using the same wavelength. The effective utilization of the fibre infrastructure will become crucial as the density of small cells reaches its peak after mm-wave network deployment in the coming years. The solution proposed in this section, allows for the successful transmission of both the downlink and uplink signals over the same fibre, thus reducing the infrastructural requirements of the system.

5.3 Conclusion

A simple and cost efficient implementation of the impairment free OFC source based optical heterodyne analogue RoF link is paramount for the wide-scale deployment in the mm-wave wireless systems. In this chapter, two different optical techniques based on active demultiplexing along with simultaneous RF LO and data modulation and bidirectional signal transmission along with wavelength reuse are demonstrated in order to reduce the complexity of optical heterodyne systems and scale their deployment.

The need for an optical amplifier, essential for boosting the power of comb tones and further achieving higher SNR, is eliminated by employing active demultiplexing and simultaneous direct modulation of 5G NR compatible data signal and RF LO on the same laser. The successful generation and transmission of 28.2 and 35.3 GHz mm-wave OFDM signals is demonstrated over this system. The low phase noise of the generated carriers from the heterodyne system supports the transmission of 5G compatible OFDM signals with subcarrier spacing well down to 62.5 kHz – showing its potential for deployment in the 5G mm-wave wireless systems. Further, an optical source free RRH unit is demonstrated by employing wavelength reuse and remote frequency down-conversion over a GSL OFC based optical heterodyne A-RoF system. Excellent performance for both downlink (61 GHz mm-wave) and uplink (5 GHz IF) signals, propagating in opposite directions through the same fibre, over the demonstrated bidirectional scheme increases the possibility of further resource centralization and reduction of the number of system components.

References

- [1] Finisar, “WaveShaper 4000A Multiport Optical Processor.”
- [2] Y. Doi, “Applications of Arrayed Waveguide Gratings for 100GbE-and-Beyond Datacom Networks,” *Advanced Photonics 2015 (2015)*, paper NeT1D.2, p. NeT1D.2, Jun. 2015, doi: 10.1364/NETWORKS.2015.NET1D.2.
- [3] K. Fotiadis *et al.*, “16×16 silicon photonic AWGR for dense wavelength division multiplexing (DWDM) O-band interconnects,” <https://doi.org/10.1117/12.2543749>, vol. 11285, pp. 82–89, Feb. 2020, doi: 10.1117/12.2543749.
- [4] Y. Liu, H. Gao, Y. Chen, and P. Li, “Full-duplex WDM-RoF system based on OFC with dual frequency microwave signal generation and wavelength reuse,” *Optical Fiber Technology*, vol. 58, p. 102252, Sep. 2020, doi: 10.1016/J.YOFTE.2020.102252.
- [5] I. Navruz and N. F. Guler, “A novel technique for optical dense comb filters using sampled fiber Bragg gratings,” *Optical Fiber Technology*, vol. 14, no. 2, pp. 114–118, Apr. 2008, doi: 10.1016/J.YOFTE.2007.09.004.
- [6] S. Sengupta, “Ultra-Narrowband Optical Comb Filter Using Sampled Fibre Bragg Gratings,” *Photonics, Plasmonics and Information Optics*, pp. 213–239, Apr. 2021, doi: 10.1201/9781003047193-8.
- [7] Z. Liu and R. Slavik, “Optical Injection Locking: From Principle to Applications,” *Journal of Lightwave Technology*, vol. 38, no. 1, pp. 43–59, Jan. 2020, doi: 10.1109/JLT.2019.2945718.
- [8] F. Smyth, L. P. Barry, M. D. G. Pascual, P. M. Anandarajah, R. Zhou, and T. Shao, “Flexible wavelength de-multiplexer for elastic optical networking,” *Optics Letters*, Vol. 41, Issue 10, pp. 2241–2244, vol. 41, no. 10, pp. 2241–2244, May 2016, doi: 10.1364/OL.41.002241.
- [9] R. Zhou, T. Shao, M. D. Gutierrez Pascual, F. Smyth, and L. P. Barry, “Injection Locked Wavelength De-Multiplexer for Optical Comb-Based Nyquist WDM System,” *IEEE Photonics Technology Letters*, vol. 27, no. 24, pp. 2595–2598, Dec. 2015, doi: 10.1109/LPT.2015.2478791.

- [10] P. D. Lakshmijayasimha, S. T. Ahmad, E. Martin, A. M. Prince, and A. M. Kaszubowska-Anandarajah, "Tunable mm-wave A-RoF transmission scheme employing an optical frequency comb and dual-stage active demultiplexer," *Journal of Lightwave Technology*, 2021, doi: 10.1109/JLT.2021.3098949.
- [11] S. T. Ahmad *et al.*, "Active demultiplexer enabled mmW ARoF transmission of directly modulated 64-QAM UF-OFDM signals," *Optics Letters*, Vol. 45, Issue 18, pp. 5246-5249, vol. 45, no. 18, pp. 5246–5249, Sep. 2020, doi: 10.1364/OL.399418.
- [12] H. J. Kim and J. I. Song, "Full-duplex WDM-based RoF system using all-optical SSB frequency upconversion and wavelength re-use techniques," *IEEE Trans Microw Theory Tech*, vol. 58, no. 11 PART 2, pp. 3175–3180, Nov. 2010, doi: 10.1109/TMTT.2010.2074611.
- [13] P. M. Anandarajah *et al.*, "Generation of coherent multicarrier signals by gain switching of discrete mode lasers," *IEEE Photonics J*, vol. 3, no. 1, pp. 112–122, 2011, doi: 10.1109/JPHOT.2011.2105861.
- [14] A. Kaszubowska-Anandarajah and L. P. Barry, "Remote downconversion scheme for uplink configuration in radio/fiber systems," *Proceedings of 2005 7th International Conference on Transparent Optical Networks, ICTON 2005*, vol. 2, pp. 161–164, 2005, doi: 10.1109/ICTON.2005.1506123.
- [15] C. Lim, A. Nirmalathas, M. Bakaul, K. L. Lee, D. Novak, and R. Waterhouse, "Mitigation strategy for transmission impairments in millimeter-wave radio-over-fiber networks," *Journal of Optical Networking*, Vol. 8, Issue 2, pp. 201-214, vol. 8, no. 2, pp. 201–214, Feb. 2009, doi: 10.1364/JON.8.000201.

6. Conclusion and Future Work

6.1 Conclusion

The development of low-cost end user devices and reliable data transmission in the low to medium mobility scenario has made the cellular wireless system popular over the past two decades. The evolution of the cellular system from the 2nd to 4th generation technology increased data transfer speed which is sufficient to access standard definition and high definition videos, social media and general office work requirements. However, these speeds are not sufficient for data hungry applications such as virtual reality, live ultra-high definition/4K/8K videos and online gaming. The 5th and 6th generations of cellular systems aim to achieve such high data rates by transmitting data over higher bandwidth channels in the millimetre wave, sub-THz and THz frequency bands. While the move towards the use of high frequency carriers will help in terms of increased channel bandwidth, higher directivity due to smaller beamwidth and small antenna aperture, however, it will result in higher propagation and atmospheric losses; ultimately requiring a dense deployment of remote antenna sites [1]. A spectrally and cost-efficient fronthaul/backhaul network will be required to connect the centralized baseband unit - or co-located central and distributed units - with an increased number of remote radio head/radio units in a centralized radio access network [2]. An efficient mm-wave generation technique and fronthaul network proliferation are two important elements for future high-speed wireless communication systems and this thesis work focuses on both of these aspects. An analogue RoF fronthauling scheme is explored for the distribution of 5G and wireless signals, while a combined optical heterodyne analogue RoF link is explored to achieve remote mm-wave/THz carrier and signal generation.

- **Analogue RoF for Fronthauling of 5G Signals**

The functional split of a traditional base station with C-RAN and the use of higher signal bandwidths in 5G and 6G systems necessitate the implementation of a simple, spectrally and cost efficient fronthaul network for transporting the data between C-BBU (or co-hosted CU and DU) and remote antenna RRH (or RU) sites. The optical line rate explosion, due to signal quantization, hinders the deployment of digital-RoF CPRI fronthaul link for the 5G system. In the alternate analogue RoF scheme, the wireless signals are transmitted in their original form retaining their spectral efficiency over the fronthaul link. The flexibility in the choice of the intermediate frequency carrier and the use of low bandwidth optical components makes the AIFoF link an ideal candidate for carrying the fronthaul data.

The performance limiting factors of the AIFoF link, from various system components, are analysed in chapter 2 and the capacity of the directly modulated 25 km AIFoF link is investigated by demonstrating the successful transmission of sixteen 201 MHz BW UF-OFDM 5G NR compatible signals carrying an

aggregate data transmission rate of ~19.3 Gb/s. The number of simultaneously transmitted signals is limited by available power per signal band in the system. With the same bandwidth occupancy of less than 5 GHz of sixteen bands, the CPRI link will not be able to transmit one 200 MHz BW 5G signal between the C-BBU and RRH site – showing the spectral efficiency of the analogue RoF scheme. Furthermore, techniques such as signal amplification by separate amplifiers, the use of high power handling capacity lasers and WDM link implementation can be employed to further increase the overall throughput of the analogue RoF link. The use of analogue RoF and particularly AIFoF for fronthauling can enable ADC/DAC and signal processing free remote antenna site deployment with low bandwidth optoelectronic components.

- **Frequency Fluctuation and Phase Noise Impairment Compensation in Optical Heterodyning Analogue RoF Link with free running lasers**

The optical heterodyne A-RoF links provide an efficient platform for the generation and distribution of mm-wave signals for wireless systems. The performance of a such system is mainly limited by the frequency drift and phase offset between the optical carriers, obtained from the use of free running lasers, - especially for the transmission of low subcarrier spacing signals as provisioned in the 5G NR standard. In order to facilitate the wide deployment of such fibre-wireless systems, techniques that ease restrictions on relative frequency drift and phase offset between the optical carriers, with minimal additional complexity, are of paramount importance.

Two innovative techniques are introduced in chapter 3 to mitigate the effect of FO and PN impairment on the performance of low subcarrier spacing multicarrier mm-wave signals generated over an optical heterodyne analogue RoF link using free running lasers. The analogue mm-wave receiver exploits the correlation between the photo-mixing generated mm-wave carrier and data signal to compensate the FO and PN using a hardware based approach. The second approach used standard digital signal processing algorithms to compensate for the effect of FO and PN without increasing the hardware complexity of the optical heterodyne analogue RoF system. The successful generation and transmission of 2 MHz subcarrier spacing 60 GHz band mm-wave OFDM signals is demonstrated with both these techniques. The choice of the compensation technique should be made by considering their limitations and the requirements of the application in which the mm-wave A-RoF system will be employed.

- **Multi-frequency 5G NR Millimetre Wave Signal generation with OFC based Optical Heterodyne A-RoF link**

The use of an optical frequency comb source in the optical heterodyne A-RoF link facilitates the generation of frequency fluctuation-free and low phase noise mm-wave/THz carriers and data signals. However, path length mismatch and fibre dispersion can lead to the decorrelation of OFC tones and result

in phase noise on the generated mm-wave carrier – limiting the performance of low subcarrier spacing multi-carrier signals. The results presented in chapter 4 demonstrate the use of a gain switched laser OFC and photonics integrated mode locked laser OFC sources for successful the generation and transmission of 5G NR provisioned subcarrier spacing 60 GHz band mm-wave frequency OFDM signals over an optical heterodyne A-RoF system. The effect of path length mismatch on the phase noise of the generated 64 GHz mm-wave carrier and performance of the 59 GHz 61 kHz subcarrier spacing OFDM signal is analysed over a GSL OFC based system. A lower RF phase noise can be achieved by operating the optical heterodyne A-RoF system at path matched point, which can be determined by observing the spectrum of the generated mm-wave carrier.

The multi-frequency mm-wave signal generation capabilities of the optical heterodyne analogue RoF system are demonstrated by generating 5G NR compatible signals at 27 GHz, 43 GHz and 59 GHz frequencies using different pairs of tones from the same GSL OFC device – providing the flexibility and centralization capabilities for the implementation of the link. Additional flexibility can be conferred by using the photonics integrated MLL exhibiting higher 3 dB bandwidth and more than 40 comb lines. The choice of the frequency set for heterodyning, an RF LO free implementation and photonics integrated nature of the MLL OFC source make it more suitable for use in the optical heterodyne A-RoF system for the generation and transmission of 5G NR compatible high frequency mm-wave carriers.

- **Active Demultiplexing, Wavelength Reuse and Bi-directional transmission for Simplifying the Optical Heterodyning**

It is important to reduce the complexity of the OFC based optical heterodyne A-RoF link in order to achieve a cost efficient system deployment. Optical demultiplexing, a technique for filtering and amplification of OFC tones, and wavelength reuse and bi-directional transmission over the same fibre are explored in chapter 5. A 5G NR compatible subcarrier spacing mm-wave frequency signal generation and transmission is demonstrated by simultaneously modulating a DFB laser with OFDM IF data signal and RF sinusoidal LO in section 5.1. The relaxation oscillation non-linearity of the laser is exploited to reduce the power consumption, while the use of an active demultiplexing enabled amplifier free heterodyne system implementation. Furthermore, a passive FBG filter was employed to filter one of the optical carriers used for heterodyning and its reuse for the transmission uplink data is demonstrated in section 5.2. The deployment of such wavelength reuse can enable a laser free remote antenna site, while the bidirectional downlink and uplink signals transmission through the same fibre can lead to further cost savings.

In general, the work presented in this thesis supports the ongoing research being done across the world to employ various optical techniques for supporting the next generation of wireless systems and provide high speed connectivity for the progress of humanity.

6.2 Future Work

The research work presented in this thesis has shown the potential of optical heterodyne analogue RoF link to support the next generation wireless systems by enabling a simple and cost-efficient millimetre wave carrier generation and distribution using innovative optical techniques. However, many areas directly related to this work need further investigation to achieve field deployment.

- **Optical Heterodyne A-RoF Link Demonstration for Sub-THz and THz Frequency**

The maximum frequency of the generated mm-wave carrier in the various optical heterodyne analogue RoF experimental demonstrations presented in this thesis was limited to 64 GHz due to the availability of 70 GHz PD in our lab. The capabilities of the frequency offset and phase noise compensation techniques and OFC sources presented in this thesis need to be investigated for the generation of sub-THz and THz frequency carriers beyond 100 GHz. The presented results show that the phase noise of the generated carrier increases with an increase in the frequency spacing between the beating OFC tones. It will be interesting to analyse the effect of this increased phase noise on the performance of low subcarrier spacing multi-carrier signals. Also, the performance of higher bandwidth OFDM signals needs to be analysed over the optical heterodyne analogue RoF link for the sub-THz and THz wireless systems.

- **GSL OFC Comb Expansion for Sub-THz and THz Frequency Carrier Generation**

Optical heterodyne A-RoF link with two different types of comb sources, i.e. GSL OFC and MLL OFC, is presented in chapter 4 for the mm-wave carrier generation. While the latter source exhibits a high number of comb tones and can be used to generate higher frequency carriers, its fixed FSR and higher phase noise add to its disadvantages. The GSL OFC provides necessary FSR tuneability but has a limited number of comb tones. For the generation of high frequency sub-THz and THz carriers, it is essential to expand this comb and achieve more tones. In the recent work [3], we demonstrated a simple and power efficient technique where 3 tones with 9.5 GHz FSR from GSL OFC were expanded to 12 lines using a DD-MZM EOM. This technique needs to be further investigated for achieving more comb tones. Furthermore, the performance of such an expanded comb source needs to be analysed for use in the optical heterodyne system for the generation of low phase noise sub-THz and THz carriers.

- **Photonics Integration Transceiver Design**

An important step to take all these demonstrations towards practical implementation is the design of a photonics integrated circuit transceiver for optical heterodyne analogue RoF link. The systems demonstrated in this thesis used discrete components except for the free running lasers from LioniX and a passive MLL from III-V Labs as demonstrated in section 3.2 (chapter 3) and section 4.5 (chapter 4),

respectively. The use of discrete components, from different vendors, with varying loss, noise, linewidth, polarization and other characteristics in these experimental demonstrations required a lot of optimization to achieve a good performance. The use of photonics integrated transceivers can overcome these fluctuations from multiple components and lead to stable and efficient system implementation. Almost all the components, used in the demonstrated heterodyne setup, such as lasers, OFC sources, IQ-MZM, OBPF, amplifiers, VOA, delay line and couplers can be integrated using various PIC technologies such as SOI, InP and Si₃N₄. Also, the path length mismatch issue leading to higher phase noise in the OFC source based system, as discussed in chapter 4, can be eliminated by designing a transceiver PIC. Design and demonstration of an optical heterodyne PIC transceiver for the transmission of low subcarrier spacing multi-carrier mm-wave signals, for which the various characteristic requirements are stringent, will lead toward the deployment of cost-effective optical solutions for the next generation wireless systems.

- **Convergence of Fibre-Wireless System with Passive Optical Network**

The architecture of almost all the experimental testbeds presented in this thesis replicates the future mobile fronthauling wherein spectrally efficient wireless signals are modulated on an optical carrier at the C-BBU and optical heterodyning of the relevant optical data signal and carriers is then implemented at the RRH to achieve remote frequency up-conversion of data to the mm-wave band. Such architecture centralizes most of the resources at the C-BBU site and results in a simple remote antenna site. Further centralization can be achieved by converging the fronthaul link with the passive optical network to share some of the infrastructures and serve both the wireline and wireless end users through the same network. Such a link can be implemented using a WDM link with different wavelengths carrying the analogue fronthaul and digital PON data. Carrying both the wireline and wireless traffic on the same wavelength will be challenging given the different nature of data on the fronthaul (analogue) and PON (digital) networks. All such possibilities need to be analysed for the efficient implementation of a converged optical access network for serving both the wireline and wireless end users.

References

- [1] Rappaport Theodore S., *Wireless Communications Principles and Practice*, Second. Pearson, 2001.
- [2] A. Checko *et al.*, "Cloud RAN for Mobile Networks - A Technology Overview," *IEEE Communications Surveys and Tutorials*, vol. 17, no. 1, pp. 405–426, Jan. 2015, doi: 10.1109/COMST.2014.2355255.
- [3] A. Delmède *et al.*, "Power efficient optical frequency comb generation using laser gain switching and dual-drive Mach-Zehnder modulator," *Optics Express*, Vol. 27, Issue 17, pp. 24135-24146, vol. 27, no. 17, pp. 24135–24146, Aug. 2019, doi: 10.1364/OE.27.024135.

Appendix

List of Publications

The following is the list of publications yielded from this work.

Journal Publications

1. A. Delmade, M. Krstić, C. Browning, J. Crnjanski, D. Gvozdić, Liam Barry, “Power Efficient Optical Frequency Comb Generation using Laser Gain Switching and Dual-Drive Mach-Zehnder Modulator,” in *Opt. Express* 27, 24135-24146, 2019.
2. D. Dass, S. O’Duill, **A. Delmade**, C. Browning, “Analysis of Phase Noise in a Hybrid Photonic/Millimetre-Wave System for Single and Multi-Carrier Radio Applications,” *Appl. Sci.*, 10, 5800, 2020.
3. T. Verolet, G. Aubin, Y. Lin, C. Browning, K. Merghem, F. Lelarge, C. Calo, **A. Delmade**, K. Mekhazni, E. Giacomidis, A. Shen, L. Barry, A. Ramdane, “Mode Locked Laser Phase Noise Reduction Under Optical Feedback for Coherent DWDM Communication,” in *Journal of Lightwave Technology*, vol. 38, no. 20, pp. 5708-5715, Oct. 2020.
4. S. T. Ahmad, P. D. Lakshmi Jayasimha, C. Browning, P. M. Anandarajah, **A. Delmade**, L. P. Barry, and A. Kaszubowska-Anandarajah, “Active demultiplexer enabled mmW ARoF transmission of directly modulated 64-QAM UF-OFDM signals,” *Opt. Lett.* 45, 5246-5249, 2020.
5. **A. Delmade**, C. Browning, T. Verolet, J. Poette, A. Farhang, H. H. Elwan, R. D. Koilpillai, G. Aubin, F. Lelarge, A. Ramdane, D. Venkitesh, and L. P. Barry, “Optical Heterodyne Analog Radio-Over-Fiber Link for Millimeter-Wave Wireless Systems,” in *Journal of Lightwave Technology*, vol. 39, no. 2, pp. 465-474, Jan. 2021.
6. D. Dass, **A. Delmade**, L. Barry, C. GH Roeloffzen, D. Geuzebroek, C. Browning, “Wavelength & mm-Wave Flexible Converged Optical Fronthaul With a Low Noise Si-Based Integrated Dual Laser Source,” in *Journal of Lightwave Technology*, vol. 40, no. 10, pp. 3307-3315, May 2022.
7. H. Xu, **A. Delmade**, C. Browning, A. Atieh, Y. Yu, L. Barry “Demonstration of High Capacity Bidirectional A-RoF System Using Wavelength Reuse and Frequency Multiplexing,” in *Journal of Lightwave Technology*, December 2022.

8. **A. Delmade**, D. Dass, C. Browning, L. P. Barry, “Multi-Frequency 5G NR Millimeter-Wave Signal Generation over Analog RoF Link using Optical Frequency Combs,” under review in *Optics Communication*, 2022.

Conference Publications

1. C. Browning, **A. Delmade**, Yi Lin, D. H. Geuzebroek and L. P. Barry, “Optical Heterodyne Millimeter-Wave Analog Radio-over-Fiber with Photonic Integrated Tunable Lasers,” in *Optical Fiber Communications Conference (OFC)*, paper W11.4, March 2019.
2. A. Kaszubowska-Anandarajah, **A. Delmade**, E. Martin, P. Anandarajah, L. Barry and C. Browning, “Bidirectional fiber transmission of mm-wave signals using remote downconversion and wavelength reuse,” in *Conference on Lasers and Electro-Optics*, paper SM4G.2, May 2019.
3. **A. Delmade**, C. Browning, Yi Lin, A. Farhang, R. D. Koilpillai, D. Venkitesh and L. Barry, “Digital Frequency/Phase Offset Correction for 60 GHz OFDM Radio-over-Fibre with Unlocked Fibre Lasers,” in *2019 European Conference on Optical Communication (ECOC)*, paper P74, September 2019.
4. C. Browning, **A. Delmade**, Yi Lin, J. Poette, H. H. Elwan and L. P. Barry, “Phase Noise Robust Optical Heterodyne System for Reduced Complexity Millimeter-Wave Analog Radio-over-Fibre,” in *2019 European Conference on Optical Communication (ECOC)*, paper M.2.C.4, September 2019.
5. **A. Delmade**, C. Browning, A. Farhang, R. D. Koilpillai, D. Venkitesh and L. Barry, “OFDM Baud Rate Limitations in an Optical Heterodyne Analog Fronthaul Link using Unlocked Fibre Lasers,” in *2019 International Topical Meeting on Microwave Photonics (MWP)*, paper Th1.5, October 2019.
6. **A. Delmade**, C. Browning, P. Perry, R. D. Koilpillai, D. Venkitesh and L. Barry, “Performance analysis of multi-band Analog IF over Fibre Fronthaul Link for high capacity wireless networks,” in *POEM*, paper OFTu2A.5, November 2019.

7. **A. Delmade**, T. Verolet, C. Browning, Yi Lin, G. Aubin, F Lelarge, A. Ramdane and L. P. Barry, “Quantum Dash Passively Mode Locked Laser for Optical Heterodyne Millimeter-Wave Analog Radio-over-Fiber Fronthaul Systems,” *OFC*, paper W2A.41, March 2020.
8. P. Perry, **A. Delmade**, A. Peters, C. Browning, S. McClean, P. Morrow, B. Scotney, and L. Barry, “Comparison of Analogue and Digital Fronthaul for 5G MIMO Signals,” in *ICC*, Dublin, June 2020.
9. **A. Delmade**, C. Browning, L. P. Barry, “5G New Radio Compatible Multicarrier Signals Delivery over an Optical/Millimeter-Wave Analog Radio-over-Fiber Fronthaul Link,” in *2020 European Conference on Optical Communication (ECOC)*, 2020.
10. **A. Delmade**, C. Browning, L. P. Barry, “Optical Frequency Comb Sources for 5G New Radio Compatible Millimeter-Wave Signal Generation and Transmission,” in *2021 Photonics Ireland*, 2021.
11. D. Dass, **A. Delmade**, L. Barry, C. GH Roeloffzen, D. Geuzebroek and C. Browning, “Flexible Optical and Millimeter-Wave Analog-RoF Transmission with a Silicon-based Integrated Dual Laser Module,” in *2021 European Conference on Optical Communication (ECOC)*, 2021.
12. D. Dass, **A. Delmade**, L. Barry, C. GH Roeloffzen, D. Geuzebroek and C. Browning, “Flexible V-band mmWave Analog-RoF Transmission of 5G and WiGig signals using an InP-SiN Integrated Laser Module,” in *2021 International Topical Meeting on Microwave Photonics (MWP)*, 2021.
13. **A. Delmade**, E. Martin, C. Browning, L. P Barry, “5G Millimeter-Wave Analog RoF System employing Optical Injection Locking and Direct Modulation of DFB Laser,” in *2022 Optical Fiber Communications Conference and Exhibition (OFC)*, 2022.
14. L. P. Barry, **A. Delmade**, D. Dass, C. Browning, “Role of Analogue Radio-over-Fibre Technology Beyond 5G,” in *2022 Optical Fiber Communication Conference (OFC)*, 2022.